ON THE DEVELOPMENT OF A DYNAMIC CUTTING FORCE MODEL WITH APPLICATION TO REGENERATIVE CHATTER IN TURNING

A Dissertation
Presented to
The Academic Faculty

By

Adam A. Cardi

In Partial Fulfillment
Of the Requirements for the Degree
Doctor of Philosophy in Mechanical Engineering

Georgia Institute of Technology

May, 2009

ON THE DEVELOPMENT OF A DYNAMIC CUTTING FORCE MODEL WITH APPLICATION TO REGENERATIVE CHATTER IN TURNING

Approved by:

Dr. Steven Y. Liang, Co-Advisor
George W. Woodruff School of
Mechanical Engineering
Georgia Institute of Technology

Dr. Matthew T. Bement, Co-Advisor
Los Alamos National Laboratory

Dr. Shreyes N. Melkote
George W. Woodruff School of
Mechanical Engineering
Georgia Institute of Technology

Dr. J. Rhett Mayor
George W. Woodruff School of
Mechanical Engineering
Georgia Institute of Technology

Dr. Chen Zhou
H. Milton Stewart School of
Industrial and Systems Engineering
Georgia Institute of Technology

Dr. Paul M. Griffin
H. Milton Stewart School of
Industrial and Systems Engineering
Georgia Institute of Technology

Date Approved: March 9, 2009

ACKNOWLEDGEMENTS

Despite the fact that there is only one author of this thesis, it was far from an individual effort. Numerous people, both past and present have helped to shape my academic development. First, I extend my sincere thanks to my two co-advisors, Dr. Steven Liang and Dr. Matthew Bement for their financial and intellectual support over the last four years. They were able to strike a perfect balance between allowing my ideas to roam free and guiding me when I was truly stuck. In addition I am very appreciative of input from the other members on my thesis committee: Dr. Shreyes Melkote, Dr. Rhett Mayor, Dr. Chen Zhou, and Dr. Paul Griffin. Financial support through a Los Alamos National Laboratory LDRD research program as well as the GM Manufacturing Fellowship was also very much appreciated.

I am very thankful to Dr. Douglas Adams at Purdue University who first introduced me to research and gave me the opportunity to work in his laboratory. It was definitely the most memorable and worthwhile experience from my undergraduate career. I also benefited greatly from the knowledge that was instilled in me during my pre-college years–most notably by my high school chemistry teacher, Andrew Felczan. I have never met any person who was more passionate about education.

I am thankful for the many valuable discussions I have had with fellow students and staff at Georgia Tech since their inputs undoubtedly helped shape the course of my work. To my old officemates: Sivaramakrishnan Venkatachalam, Hyung-Wook Park, and Jiann-Cherng Su: thank you for showing me the ropes and helping me grasp some fundamental concepts in machining as well as putting up with my messy corner of the office. To my past and present lab group members: Quilin Xie, Sherry Huang, Binti Abraham, and Kuan-Ming Li, thank you very much for your valuable input at group meetings. To Steven Sheffield: thank you for training me in operating the equipment and providing machining-related input. To Marmar Mehrabadi and Konrad Rykaczewski: thanks for studying for the qualifying exams with me; it was grueling but we got through it together. To Matt Rogge, Aaron Enes, Shaohui Foong, Mike Damianakis, Dinesh Bansal, Patrick Opdenbosch, Farhad

Farzbod, and Longke Wang: thank you for providing me with many breaks from research over the years. I will always remember the time we spent talking about a wide range of intellectually stimulating topics.

I am grateful to my fiancé, Mu-Hung, for understanding my need to pursue this education and putting up with my odd sleep patterns and unpredictable work hours. Finally, I come to my parents. They knew what was best for me all along even if I did not. There are simply no words to do justice to all they have done for me.

TABLE OF CONTENTS

LIST OF TABLES

LIST OF FIGURES

NOMENCLATURE

$y(t)$, $\dot{y}(t)$	Relative tool-workpiece displacement and velocity in the radial direction, respectively, at time t
$z(t)$, $\dot{z}(t)$	Relative tool-workpiece displacement and velocity in the tangential direction, respectively, at time t
ζ	Damping ratio
ω_n	Natural frequency
RTWD	Relative tool workpiece displacement
SDOF	Single degree of freedom
$F(t)$	Generic dynamic force due to the cutting process
t_u	Undeformed chip thickness
ψ	A constant that reflects the stiffness of the vibrating body in a dynamic cutting simulation
$y_t(t)$, $\dot{y}_t(t)$	Absolute displacement and velocity of the cutting tool in the radial direction, respectively
$y_w(t)$, $\dot{y}_w(t)$	Absolute displacement and velocity of the workpiece in the radial direction, respectively
$z_t(t)$, $\dot{z}_t(t)$	Absolute displacement and velocity of the cutting tool in the tangential direction, respectively
$z_w(t)$, $\dot{z}_w(t)$	Absolute displacement and velocity of the workpiece in the tangential direction, respectively
f	Feed per revolution of the workpiece
d_c	The commanded depth of cut
μ_0	Overlap factor
ω_{crit} , τ_{crit}	The critical width of cut and workpiece revolution period for a classic linear chatter model [12]
w_{abs}	Absolute stable width of cut
k_1 , k_2 , k_3 , k_4 , k_5	Application-specific constants in the model proposed in [17]
$[t \quad t-\tau \quad \cdots \quad t-D\tau]$	Regenerative delay space
$[y(t) \quad y(t-\tau) \quad \cdots \quad y(t-D\tau)]$	Regenerative position space
D	The size of the regenerative delay (or position) space
$\mathbb{Z}$	The set of natural numbers

k_6 , k_7	Application specific constants in the model proposed in [20]
V_C , V_T	Components of $\vec{V}_C$ in the cutting and thrust directions, respectively
V_i	Interference volume
λ_w	Wavelength of the machined workpiece surface
$\bar{V}_C$	Commanded cutting velocity
C_1 , C_2	Dynamic cutting force coefficients used in [24]
$\overline{AB}$	Locates the shear plane in Oxley's orthogonal cutting force model
C - T	A reference frame that denotes the thrust and cutting directions
w	Width of cut
t_u	Undeformed chip thickness in an orthogonal cutting model
α_n , α_n^*	Actual and effective normal rake angles, respectively
$\vec{V}_C$, $\left\|\vec{V}_C\right\|$	A vector denoting the relative velocity between the workpiece and the cutting tool and its magnitude, respectively
γ	Clearance angle
ϕ	Shear angle
t'	Undeformed chip thickness in an orthogonal model referenced from the tip of the cutting tool
δ_s	Slope of the free workpiece surface in an orthogonal cutting force model
t_d	Deformed chip thickness in an orthogonal cutting force model
F_C , F_T	Orthogonal forces parallel and normal to the cutting direction, respectively
F , N	Frictional and normal forces at the cutting tool, respectively
R	Resultant force acting on the cutting tool in Oxley's cutting force model
λ	Friction angle
κ	Angle of the resultant force, R
k_{AB}	Flow stress along the shear plane
V , V_S	The velocity of the chip perpendicular and parallel to the shear plane, $\overline{AB}$
σ	Stress

ε_p , $\dot{\varepsilon}_p$	Plastic strain and strain rate, respectively
T , T_m	Temperature and melting point of the workpiece material, respectively
A , B , C , m , n , $\dot{\varepsilon}_0$	Johnson-Cook parameters
T_{AB}	Temperature rise along the shear plane, $\overline{AB}$
ε_{AB} , $\dot{\varepsilon}_{AB}$	Strain and strain rate along the shear plane, $\overline{AB}$, respectively
C_{Oxley}	Constant in Oxley's cutting force model
k_{AB}	Flow stress along the shear plane, $\overline{AB}$
h	Tool-chip contact length
τ_{int}	Shear stress along the tool-chip interface
k_{chip}	Average flow stress in the chip
ε_{int} , $\dot{\varepsilon}_{int}$	Average strain and strain rate in the chip, respectively
t_r	Ratio of the plastic zone thickness at the tool chip interface to t_d
S_{ϕ_N} , S_{f_C} , S_{f_T}	Regression surface fits to the Oxley cutting force model that describe the dynamic shear angle, cutting, force, and thrust force, respectively, as a function of t' , α_n , $\left\|\vec{V}_C\right\|$, and δ_s
A_i	Interference area
$\overline{\beta}_e$	Angle locating the material separation point along the tool edge for zero vibration orthogonal cutting
β_e	Angle locating the material separation point in orthogonal cutting with vibration
P_C , P_T	Interference forces in the cutting and thrust directions, respectively
μ	Coefficient of friction
K_{cf}	Force-interference volume constant
E	Young's modulus
ν	Poisson's ratio
ρ	Extent of the elastoplastic deformation zone beneath the cutting tool
r_e	Edge radius of tool
$\hat{\mathbf{y}}$ - $\hat{\mathbf{z}}$	A reference frame located at the center of curvature of the tool edge radius
$\hat{y}_{sur}(\hat{z})$	A polynomial in $\hat{z}$ representing the undeformed workpiece surface

a_0 , a_1 , a_2	Coefficients in the polynomial $\hat{y}_{sur}(\hat{z})$
$\hat{y}_t(\hat{z})$	Piecewise continuous function representing the boundary of the cutting tool
m_t , b_t	Slope and $\hat{y}$ intercept of the tool's clearance face, respectively
$\hat{z}_{te-cf}$	Transition point between the tool edge and the clearance face
$\hat{z}_{1-te}$, $\hat{z}_{2-te}$	Intersections between a semicircle coincident with the tool edge radius and the undeformed workpiece surface, $\hat{y}_{sur}(\hat{z})$
$\hat{z}_{1,quart}$, $\hat{z}_{2,quart}$	Real roots of a quartic equation in order to determine $\hat{z}_{1-te}$ and $\hat{z}_{2-te}$ when $a_2 \neq 0$
$\hat{z}_{1-cf}$, $\hat{z}_{2-cf}$	Intersections between a line coincident with the cutting tool's clearance face and the undeformed workpiece surface
$\hat{z}_1$, $\hat{z}_2$	The relevant z coordinates of intersection between the undeformed workpiece surface and the cutting tool
$\hat{z}_L$, $\hat{z}_U$	Lower and upper limits of integration, respectively
$A_{i-te}(\hat{z}_L, \hat{z}_U)$, $A_{i-cf}(\hat{z}_U)$	The interference area along the tool edge and clearance face respectively
γ^*	Effective clearance angle
$t_i(s)$	Local interference thickness as a function of path coordinate, s
$P(s)$	Pressure on the cutting tool as a function of path coordinate, s
K_p	Pressure coefficient
$\tilde{\mathbf{y}}$ - $\tilde{\mathbf{z}}$	Reference frame sharing an origin with the $\hat{\mathbf{y}}$ - $\hat{\mathbf{z}}$ and inclined at the clearance angle, γ
β	Angular coordinate along the tool edge in the $\hat{\mathbf{y}}$ - $\hat{\mathbf{z}}$ reference frame
$t_{i-te}(\beta)$	Interference along the tool edge as a function of angular coordinate, β
β_1 , β_2	Angles of intersection between the undeformed workpiece surface and semicircle coincident with the tool edge radius
$\tilde{z}_2$	Intersection between the undeformed workpiece surface and the clearance face of the cutting tool in the $\tilde{\mathbf{y}}$ - $\tilde{\mathbf{z}}$ reference frame
$\tilde{y}_{sur}(\hat{z})$	Undeformed workpiece surface in $\tilde{\mathbf{y}}$ - $\tilde{\mathbf{z}}$ coordinates
p'_C , p'_T	Interference forces per unit width of cut rotated by γ^*
p_C , p_T	Interference forces per unit width of cut
P_C , P_T	Interference forces
i , i^*	Actual and effective tool inclination angles, respectively

C_S , C_S^*	Actual and effective tool side cutting edge angles, respectively
r_n	Tool nose radius
$\overline{\Omega}$	Angle of the chip flow direction
XYZ	Reference frame that always is located a the center of curvature of the tool nose
$[\cdot]^*$	A quantity, $[\cdot]$, that exists in the tool nose radius cutting domain has an equivalent representation, $[\cdot]^*$, in the straight edge cutting domain
η_0	The chip flow direction measured relative to a normal vector to the straight side cutting edge
η_0'	The projection of η_0 on the tool rake face
η_c^*	The chip flow direction
w^* , t_u^*	The effective width and undeformed chip thickness, respectively
V_C^*	Effective total cutting velocity
F_R	The force perpendicular to F_C and F_T ,
F_Y , F_Z	The forces due to chip formation in the **Y** and **Z** directions, respectively
$\overline{\mathbf{XYZ}}$	Reference frame that is a distance of $-y(t)$ in the **Y** direction from the **XYZ** reference frame
θ	Angular coordinate in both the **XYZ** and $\overline{\mathbf{XYZ}}$ reference frames
θ_W	Angle of intersection between the unmachined workpiece surface and the tool nose radius at $y(t-W\tau)$
$\theta_{M,N}$	Angle of intersection between the tool nose radii at $y(t-M\tau)$ and $y(t-N\tau)$
$t_{u,A}(\theta,W)$, $t_{u,B}(\theta)$	Undeformed chip thickness in a type A or B region, respectively
$\left(x_{i-M,N}, y_{i-M,N}\right)$	coordinates of intersection between the M^{th} and N^{th} previous tool noses
Ang	A $(D+1)\times(D+1)$ real symmetric matrix that stores all angles of intersection
Ind	A $2\times Q$ matrix that references angles in Ang that are relevant to the description of the undeformed chip area
Q	The number of angles in Ang that are relevant to the deception of the undeformed chip area
j	$\sqrt{-1}$

δ_V	The angle of the net relative velocity between the workpiece and the cutting tool
F_C', F_T'	The cutting and thrust forces in the $\mathbf{C'}$ - $\mathbf{T'}$ reference frame
$\mathbf{C'}$ - $\mathbf{T'}$	A reference frame which is rotated by an angle of δ_V from the $\mathbf{C}$ - $\mathbf{T}$ reference frame to reflect dynamic effects
α_n^{**}	Velocity modified version of α_n^*
V_T^*	Effective velocity in the thrust direction
φ	Tool nose radius scaling factor
ϕ_V	The dynamic shear angle, denoted as the acute angle between the shear plane and the direction of net relative velocity with respect to the cutting tool
δ_s, δ_s^*	The actual and effective surface slope of the free workpiece surface
ϕ_0	The quasi-static shear angle, measure from the static $\mathbf{C}$ axis
$f_{C,\theta}$, $f_{T,\theta}$, $f_{R,\theta}$	Differential orthogonal cutting forces due to chip formation at a differential width of cut $r_n d\theta$ with dependence on θ, similar to their counterparts without a subscript θ (F_C, F_T, and F_R)
$\eta_{c,\theta}^*$, $\eta_{0,\theta}'$, $C_{S,\theta}^*$, $\alpha_{n,\theta}^*$, i_θ^*, $\eta_{c,\theta}^*$	Angles associated with an equivalent straight cutting edge tool geometry with a dependence on θ, similar to their counterparts without a subscript θ
$p_{C,\theta}$, $p_{T,\theta}$	Differential interference forces with a dependence on θ
t_θ', $\delta_{v,\theta}$	Similar to t' and δ_v, respectively, except evaluated at a particular value of θ along the cutting zone
$\delta_{s,comp}(\theta,W)$, $\delta_{s,comp}'(W)$	Intermediate angles used in the derivation of $\delta_s(\theta,W)$
$\delta_s(\theta,W)$	Similar to δ_s except now a function of θ and a past relative tool position at time $t-W\tau$
$\alpha_{n,\theta}^{**}$, $V_{C,\theta}^*$, $\phi_{0,\theta}$, $\phi_{V,\theta}$	Similar to α_n^{**}, V_C^*, ϕ_0, and ϕ_V except now a function of θ
$f_{C,\theta}'$, $f_{T,\theta}'$	Differential cutting and thrust forces in the $\mathbf{C'}$ - $\mathbf{T'}$ reference frame
$t_{pi}(\theta,a)$	The planar interference between the cutting tool and the workpiece
$\hat{y}_{sur,static}$	The equation describing the undeformed workpiece surface in $\hat{y}\hat{z}$ coordinates with zero relative tool-workpiece vibration
$a_{0,dyn}$	Component of a_0 due to dynamic effects
$\hat{y}_{sur,exact}(\theta,\hat{z})$	Mathematically exact representation of the undeformed workpiece surface in the refined cutting force model

$\hat{y}_{sur}(\theta,\hat{z})$	A polynomial in $\hat{z}$ which is an approximation to the undeformed workpiece surface in the refined cutting force model
$a_{0,\theta}$, $a_{1,\theta}$, $a_{2,\theta}$	Coefficients in $\hat{y}_{sur}(\theta,\hat{z})$, similar to a_0, a_1, and a_2 except with dependence on θ
$\beta_e(t)$, $\beta_e^*(t)$	Time varying angle of material separation in the refined and simplified dynamic cutting force models, respectively
$p'_{C,\theta}$, $p'_{T,\theta}$	Similar to p'_C and p'_T except with dependence on θ
γ^*_θ	Similar to γ^* except with dependence on θ
$t_{i-te}(\theta,\beta)$, $t_{i-cf}(\theta,\tilde{z})$	Similar to $t_{i-te}(\beta)$, $t_{i-cf}(\tilde{z})$ except with dependence on θ
$\hat{z}_{1,\theta}$, $\hat{z}_{2,\theta}$, $\tilde{z}_{2,\theta}$	Similar to $\hat{z}_1$, $\hat{z}_2$, and $\tilde{z}_2$, except with dependence on θ
$\beta_{1,\theta}$, $\beta_{2,\theta}$	Similar to β_1, β_2, except with dependence on θ
$A_{i,\theta}$	Similar to A_i except with dependence on θ
$A_{i-te}\left(\hat{z}_{1,\theta},\hat{z}_{te-cf},\theta\right)$	Similar to $A_{i-te}\left(\hat{z}_{1,\theta},\hat{z}_{te-cf}\right)$ except with dependence on θ
$A_{i-cf}\left(\hat{z}_{2,\theta},\theta\right)$	Similar to $A_{i-cf}\left(\hat{z}_{2,\theta}\right)$ except with dependence on θ
w_p, x_p	Weights and node points for Gaussian Quadrature on the interval [-1,1]
w'_p, x'_p	Weights and node points for Gaussian Quadrature on an arbitrary interval [a,b]
τ_1, τ_2	Delays corresponding to states used to curve fit the undeformed workpiece surface
$\hat{\mathbf{y}}_{\mathbf{sur}}$, $\hat{\mathbf{z}}_{\mathbf{sur}}$	Vectors containing points that define the undeformed workpiece surface in the $\hat{y}$ and $\hat{z}$ directions, respectively
$\mathbf{y}(t)$	Vector of states related to the vibration of the workpiece
Δt	Step size used in the numerical integration of the DDEs of motion
$\mathbf{y_n}$	The vector of states at the current time step
$\mathbf{y_{n+1}}$	The vector of states at the next time step
$\mathbf{k_1}$, $\mathbf{k_2}$, $\mathbf{k_3}$, $\mathbf{k_4}$	Vectors used in the Runge-Kutta integration of DDEs of motion
FRF	Frequency Response Function
$d_{c,\max}$	Maximum depth of cut that the proposed approach can model

SUMMARY

Turning is one of the most widely used processes in machining and is characterized by a cutting tool moving along the axis of a rotating workpiece as it removes material. A detrimental phenomenon to productivity in turning operations is unstable cutting or chatter. This can reduce the life of tooling, dimensional accuracy, and the quality of a part's surface finish because of severe levels of vibration. Ideally, cutting conditions are chosen such that material removal is performed in a stable manner. However, it is sometimes unavoidable because of the geometry of the cutting tool or workpiece. This work seeks to develop a dynamic cutting force model that can be used to predict both the point of chatter instability as well as its amplitude growth over time. Previous chatter models fail to capture the physics of the process from a first-principles point of view because they are oversimplified and rely on various "cutting force coefficients" that must be tuned in order to get a desired correlation with experimental results. The proposed approach models the process in a geometrically rigorous fashion, also giving treatment to the strain, strain rate, and temperature effects encountered in machining. It derives the forces encountered during a turning operation from two sources: forces due to chip formation and forces due to plowing and flank interference.

This study consists of a detailed derivation of two new cutting force models. One relies on careful approximations in order to obtain a closed-form solution; the other is more explicit and obtains a solution through numerical methods. The models are validated experimentally by comparing their prediction of the point of instability, the magnitude of vibration in the time and frequency domains, as well as the machined surface topography during chatter.

CHAPTER 1: INTRODUCTION

"Research is what I'm doing when I don't know what I'm doing."
–Wernher Von Braun

1.1 Overview and Motivation

Turning is one of the most common processes in machining and is characterized by a cutting tool moving parallel to the axis of a rotating workpiece as it removes material. This is known as the "feed" direction and as the cutting tool is fed it traces out a helix on the machined surface of the workpiece. One of the most detrimental phenomena to productivity in metal turning operations is unstable cutting or chatter. Characterized by large relative displacements between the cutting tool and workpiece, chatter can greatly reduce the life of tooling, dimensional accuracy, and the quality of a part's surface finish. Ideally, cutting conditions are chosen such that material removal is performed in a stable manner. However, chatter is sometimes unavoidable because of the inherent flexibility of the cutting tool or workpiece. An exaggerated version of chatter during a turning operation is shown in Figure 1-1 with the arrows indicating the motions of the cutting tool and workpiece that are not associated with chatter.

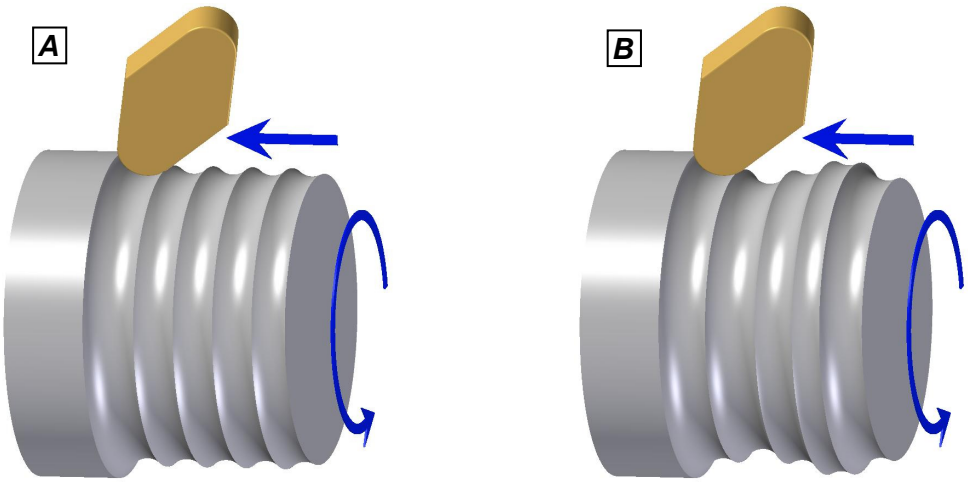

Figure 1-1: A workpiece and cutting tool with an exaggerated machined surface topography. (A), A stable cutting configuration characterized by relatively low levels of vibration; (B), a chattering cutting configuration characterized by relatively high levels of vibration.

Figure 1-1A depicts a case of stable cutting, characterized by minimal relative tool-workpiece vibration (typically assumed to be zero for modeling purposes). In Figure 1-1B large amounts of vibration are present, which would occur during chatter. Stable cutting is a dynamic problem that can be analyzed quasi-statically since the forces are theoretically in steady state with no time varying parameters. In contrast, chatter is an instance of dynamic cutting–a case where the cutting conditions are changing over time as the tool vibrates relative to the workpiece. Hence for the remainder of this dissertation the term "quasi-static cutting" will refer to cutting force modeling that assumes zero vibration, and "dynamic cutting" will denote modeling that accounts for vibration.

1.2 Research Goals and Objectives

This thesis concerns the development of a dynamic cutting force model for turning. It will incorporate the effects of vibration, tool geometry, and many other process parameters in order to accurately forecast both the occurrence and evolution of chatter though time. Other approaches to chatter prediction have previously been developed, but they are predicated on oversimplifications of the machining process and, often times, include coefficients that are based on curve fitting of experimental data. Some are able to make good predictions on the point of chatter instability during a turning machining operation; however, it is at the expense of a lack of physical understanding of the process. In short, the goal of the current approach is to predict the occurrence of chatter with a model derived from first-principles in order to *understand* rather than just simply *predict*. The model will be validated by many experimental cutting conditions as well as comparisons to experimental observations made previously in the literature.

1.3 Research Plan

This research aims develop a dynamic cutting force model that can be used to predict chatter instability in turning. The cutting process will be modeled in a geometrically rigorous fashion and will account for all the true process parameters that characterize a turning operation. For this study,

a chattering workpiece will be investigated. The chatter simulation developed as a part of this dissertation consists of two components: a dynamic cutting force model, and a dynamic model of the workpiece. During a turning simulation, the dynamic cutting force model produces forces that excite the workpiece, which in turn vibrates and changes the local machining conditions at the cutting zone. This change in state at the cutting zone affects the forces predicted by the dynamic cutting force model, and the process then repeats.

Figure 1-2 shows an overview of a chatter simulation and how the dynamic cutting force model is incorporated. True process conditions serve as the input to the analytical model; these include the cutting conditions, material properties, and the state of vibration of the workpiece. The next two elements that branch from the first block are both components of the dynamic cutting force model that predict forces in the machining process from two different sources. The first mechanism that creates forces during the cutting process is chip formation. This creates the forces that typically come to mind in a machining operation–the forces required to generate a level of stress in the material that causes it to flow up the rake face of the cutting tool to become a chip. The second contribution of forces is due to plowing and flank interference. Plowing forces arise because the workpiece material is forced to flow around the radius of the tool edge, and flank interference forces are caused when there is relative tool-workpiece vibration and the clearance face of the cutting tool collides with the machined surface.

Finally, a mathematical description of the workpiece (derived from experimental modal analysis in the current approach) is excited by the forces due to plowing and flank interference as well as chip formation. This formulation yields a set of ordinary differential equations that are solved numerically to find the states of the workpiece (position and velocity) at each time step. These states then are fed back to the first block in the flowchart (via the dotted line), the simulation moves forward in time, and the entire process repeats.

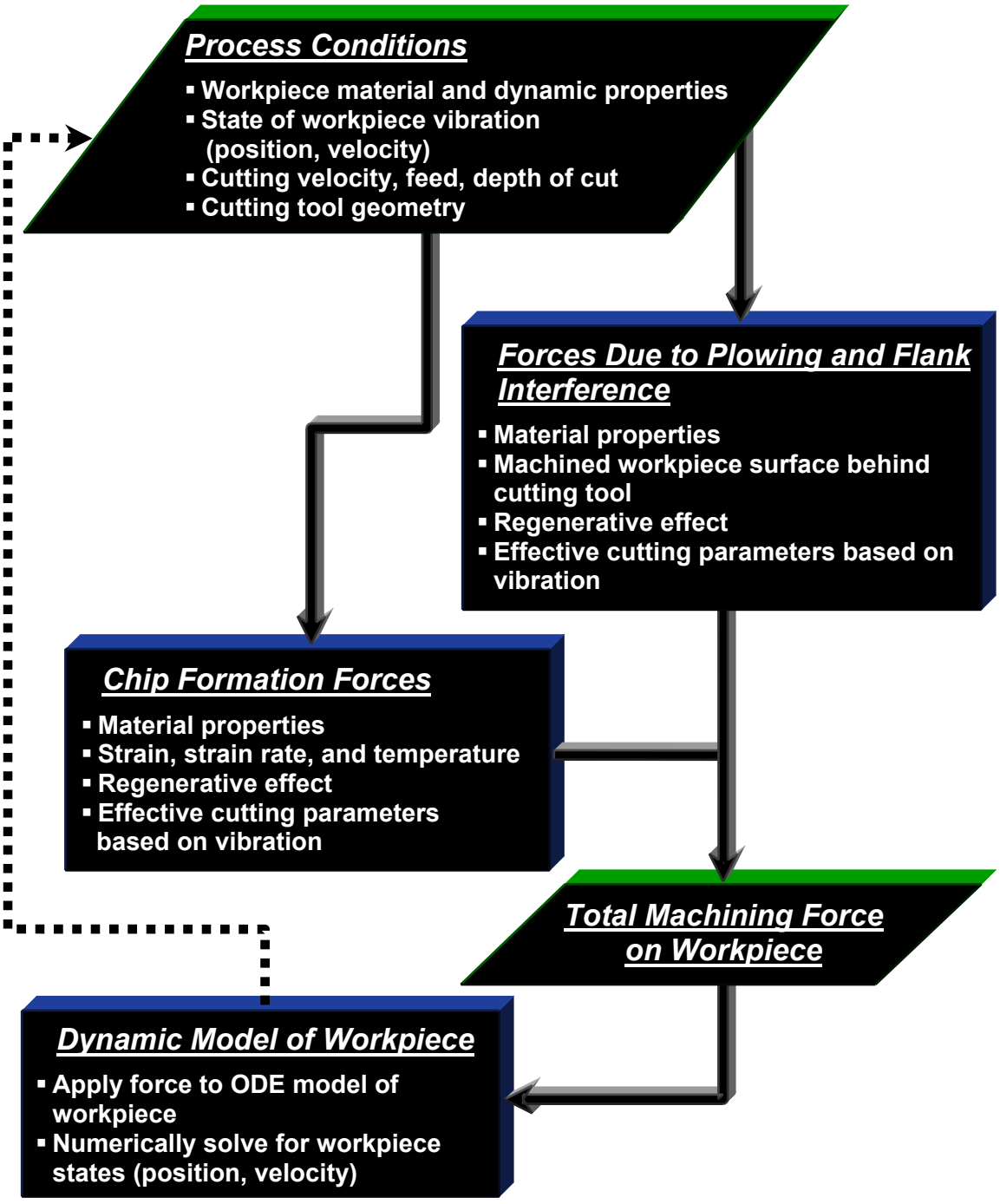

Figure 1-2: A flowchart showing how a dynamic turning process is simulated.

1.4 Overview of Thesis

This dissertation presents a method of predicting chatter in a turning operation from true process parameters. The techniques employed are extensions of work performed in quasi-static

cutting force modeling as well as dynamic cutting force modeling. Two models will be derived: a simplified model to describe dynamic cutting forces in turning in a closed-form manner, and a refined cutting force model, which utilizes a more rigorous formulation to describe dynamic cutting forces in a non-closed form fashion.

In Chapter 2 a background of chatter modeling work that has been performed for turning is given, and the departure and improvement that this work imposes upon these methodologies is presented.

In Chapter 3, two orthogonal cutting force models will be introduced. These will serve as the foundation upon which both the simplified and refined dynamic cutting force models are built. First, the Oxley orthogonal cutting force model will be introduced in order to describe the forces due to chip formation. This model captures the effect of strain, strain rate, and temperature on the chip formation forces. Additionally, the effects of a nonzero workpiece surface slope are incorporated such that these effects can be used in a cutting process with vibration. Next, forces due to plowing and flank interference are modeled in the orthogonal cutting domain. By tracking the vibration history of the workpiece, the amount of material displaced by the cutting tool's edge and clearance face can be determined. Through various geometric relations and assumptions made about the stress field around the tool edge, forces can be calculated based on the amount of displaced material.

Chapter 4 deals with capturing the influence that the tool geometry commonly used in practice and tool-workpiece vibration have on the machining forces. Effects such the oblique cutting geometry and the tool nose radius are incorporated into the model. The simplified cutting force model will be fully developed in this chapter by deriving a single equivalent orthogonal cutting representation for the forces due to chip formation and another orthogonal representation for the interference forces.

Comparisons between the current orthogonal cutting force modeling approach and previous experimental work in dynamic cutting analysis will be conducted in Chapter 5. The behavior of the

interference forces, forces due to chip formation, and the shear angle are explored as a function of the oscillation frequency of both the cutting tool and the unmachined workpiece surface.

In Chapter 6, the refined cutting force model is presented by deriving the geometry of the cutting process in a more rigorous fashion. Improvements will be made over the simplified cutting force model in the way that forces due to chip formation as well as plowing and flank interference are calculated by integrating an infinite number of cutting scenarios along the entire cutting zone.

Actual numerical implementation of both of the proposed dynamic cutting force models is presented in Chapter 7. The equations of motion will be developed and a Runge-Kutta integration solution procedure is presented. Additionally, methods for numerically evaluating integrals in the refined cutting force model will be given.

Finally in Chapter 8, both the simplified and refined dynamic cutting force models will be experimentally validated. Both will be used to predict the point of chatter instability along the workpiece and comparisons will be drawn over a wide range of cutting conditions. In addition, the refined cutting force model will be compared with experimental measurements of the workpiece vibration in the frequency and time domains. The experimentally machined surface topography of the workpiece will also be compared with that predicted by the numerical simulation of the refined cutting force model. A sensitivity study will be conducted whereby general trends in the refined cutting force model's output are explained and correlated with real-world machining observations and prior work in the literature.

CHAPTER 2: LITERATURE REVIEW

"If I have seen farther than others, it is because I was standing on the shoulders of giants."

–Isaac Newton

2.1 Early Chatter Modeling

A large body of work has been published in chatter modeling over the last fifty years. The vast majority of these investigations employ a single degree of freedom (SDOF), representing the lumped mass behavior of the cutting tool at the cutting zone, given as

$$\ddot{y}(t) + 2\zeta\omega_n \dot{y}(t) + \omega_n^2 y(t) = \psi F(t) \tag{2.1}$$

where y is the displacement, $F(t)$ is a time varying dynamic force due to the cutting process, ζ is the damping ratio, ω_n is the natural frequency, and ψ is a constant affected by the stiffness of the cutting tool. Typically, the workpiece is assumed to be rigid and the cutting tool to vibrate. However, it is mathematically unimportant which body undergoes motion; rather, the significance is the relative displacement between them. Equation (2.1) could describe the motion during cutting for a SDOF workpiece and a rigid cutting tool, or a SDOF cutting tool and a rigid workpiece (with appropriate values for ζ, ω_n, and ψ in each case). In this work $y(t)$ will denote the *relative* tool-workpiece displacement (RTWD) in the radial cutting direction, given as

$$y(t) = y_t(t) - y_w(t) \tag{2.2}$$

where $y_t(t)$ is the absolute displacement of the cutting tool, $y_w(t)$ is the absolute displacement of the workpiece, and the value of $-y(t)$ is the change in the depth that the tool is cutting in the workpiece. The radial cutting direction is perpendicular to the axis of the workpiece and is directed radially outwards towards the cutting tool. Motion in the radial cutting direction is the most intuitively obvious cause of chatter since it influences the amount that the cutting tool is engaged in the workpiece, and in turn the undeformed chip thickness. However, it will be shown later that

another degree of freedom (DOF) in the tangential cutting direction, $z(t)$, is necessary as well; this additional DOF is given as

$$z(t) = z_t(t) - z_w(t) \tag{2.3}$$

where the parameters follow the same pattern as they did for Equation (2.2). As the name suggests, the tangential cutting direction is tangent to the workpiece's surface at the tool-workpiece interface. The physical orientations of the radial and tangential cutting directions will be made apparent in Chapter 4. Equations (2.2) and (2.3) can be differentiated to give expressions for the relative velocities between the workpiece and the cutting tool, $\dot{y}(t)$ and $\dot{z}(t)$, given as

$$\dot{y}(t) = \dot{y}_t(t) - \dot{y}_w(t) \tag{2.4}$$

$$\dot{z}(t) = \dot{z}_t(t) - \dot{z}_w(t) \tag{2.5}$$

The difficulty in describing the chattering phenomenon is in the choice of the dynamic cutting force model $F(t)$ in Equation (2.1). The first milestone in solving this problem was the realization that in the case of turning, chatter onset is due to the so called "regenerative effect" [1]-[4]. Under this effect, the dynamics at the current time, t, are influenced by both the current displacement, $y(t)$, and the previous displacement, $y(t-\tau)$, where τ is the period of one workpiece revolution. This conceptually makes sense because if the tool "jumps" away from the workpiece at time $t-\tau$, there will be more material to cut and consequently a greater force developed at time t.

Early in chatter research, two common cutting scenarios were used to study the regenerative effect. One is similar to a parting operation, and is shown in Figure 2-1. The other one is referred to as a "tube cutting" operation, whereby a cutting tool is fed axially along a rotating tube, cutting its entire wall thickness. Both were used extensively with orthogonal cutting tools in order to accurately control the width of cut, w. With respect to the scenario in Figure 2-1, the tool is fed a nominal distance in the radial cutting direction each revolution of the workpiece. The workpiece revolution period is adjusted such that the cutting velocity at the nominal machined diameter, d_m, is constant.

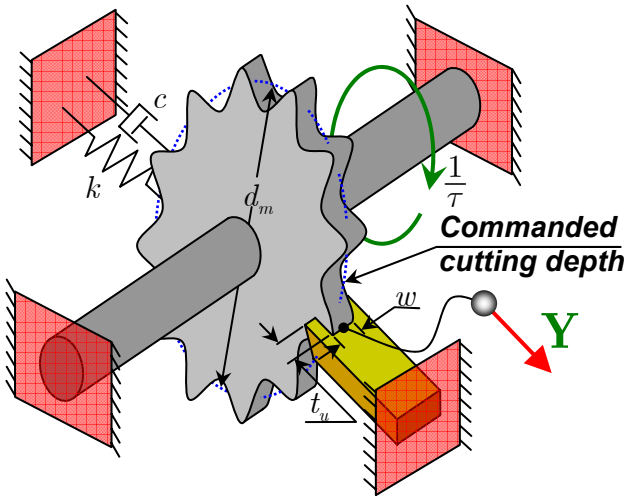

Figure 2-1: A schematic of an experimental configuration used to study regenerative chatter.

Based on the realization of the regenerative effect, some chatter models, such as in [5] and [6], employ a dynamic cutting force in Equation (2.1) having the form

$$F(t) = K_e w t_u \tag{2.6}$$

where w is width of cut, K_e is a application-specific cutting force coefficient with units of force/area and t_u is the undeformed chip thickness, given as

$$t_u = d_c + y(t-\tau) - y(t) \tag{2.7}$$

The quantity, $K_e\left(d_c + y(t-\tau) - y(t)\right)$ or just simply $K_e\left(y(t-\tau) - y(t)\right)$ is commonly referred to as the "regenerative cutting force."

It should be noted that the RTWD $y(t-\tau)$ influences the undeformed chip thickness to the same extent that $y(t)$ does since there is compete overlap in the tool passes from one revolution to another. For typical turning operations this is generally not the case because the tool is fed a relatively small distance along the axis of the workpiece each revolution. Therefore, this only results in partial overlap between the RTWDs at times t and $t-\tau$. In an effort to extend some of the models to more common machining scenarios such as turning and milling, where the overlap from one tool pass to another is partial, a parameter called an overlap factor was employed [7]-[10]. This results in the undeformed chip thickness in Equation (2.7) becoming

$$F(t) = K_e \left(d_c + y(t) - \mu_o y(t-\tau) \right) \tag{2.8}$$

where μ_o is referred to as the overlap factor and is generally is in the range [0,1]. $\mu_0 = 1$ would be for a threading operation and $\mu_0 = 0$ would reflect the complete overlap of successive tool passes, as is the case in the machining operation depicted in Figure 2-1. μ_o can be determined through geometric approximations, however its applicability over a wide range of input process parameters is relatively limited, as discussed in [10].

The most traditional way to validate dynamic cutting force models that are being used to predict chatter is to generate a "stability chart" or "stability lobe diagram" (owing to the many lobes that demark stable and unstable territory) [7],[11],[12]. The classic linear formulation for predicting the occurrence of chatter in turning is constructed by substituting the dynamic cutting force model in Equation (2.6) into Equation (2.1), which results in

$$\ddot{y}(t) + 2\zeta\omega_n \dot{y}(t) + \omega_n^2 y(t) = \psi K_e w t_u \tag{2.9}$$

and describes the system in Figure 2-1. The tool is considered to be rigid, and the workpiece has an effective mass for the single mode of vibration being modeled, m, damping coefficient, c, and a stiffness, k, that are related to the natural frequency, ω_n, damping ratio, ζ, and the factor, ψ, by

$$\omega_n = \sqrt{\frac{k}{m}} \tag{2.10}$$

$$\zeta = \frac{c}{2\sqrt{km}} \tag{2.11}$$

$$\psi = \frac{1}{m} \tag{2.12}$$

It should be noted that a system having a rigid workpiece and a compliant cutting tool can also be modeled in the same fashion. The workpiece revolution period, τ, is related to the machined workpiece diameter, d_m, and the commanded cutting velocity, $\bar{V}_C$, by

$$\tau = \frac{d_m \pi}{\bar{V}_C} \tag{2.13}$$

The ODE in Equation (2.9) can be transformed into the Laplace domain and is

$$\left(s^2 + 2\zeta\omega_n s + \omega_n^2\right) Y(s) = \psi K_e w \left(D_c(s) + \left(e^{-s\tau} - 1\right) Y(s)\right) \tag{2.14}$$

with the assumption of zero initial conditions. After some rearranging the transfer function relating the relative tool workpiece displacement to the instantaneous depth of cut is obtained as

$$\frac{Y(s)}{D_c(s)} = \frac{\psi K_e w}{\left(s^2 + 2\zeta\omega_n s + \omega_n^2 + \psi K_e w\left(1 - e^{-s\tau}\right)\right)} \tag{2.15}$$

where the characteristic equation of this transfer function is given by

$$s^2 + 2\zeta\omega_n s + \omega_n^2 + \psi K_e w\left(1 - e^{-s\tau}\right) = 0 \tag{2.16}$$

This equation is transcendental and hence has an infinite number of roots. However, the stability boundary for each root can be found by examining where the imaginary portion vanishes. Letting $s = j\omega$ and finding where the roots are purely imaginary and enforcing real-valued width of cut, the following expressions for the critical width of cut, w_{crit}, and critical workpiece revolution period, τ_{crit}, are obtained [12]:

$$w_{crit} = \frac{\left(\omega^2 - \omega_n^2\right)^2 + \left(2\zeta\omega_n\omega\right)^2}{2\psi K_e\left(\omega^2 - \omega_n^2\right)}, \quad \omega > \omega_n \tag{2.17}$$

$$\tau_{crit} = \frac{1}{\omega}\left((2n+1)\pi + \tan^{-1}\left[\frac{2\zeta\omega_n\omega}{\omega^2 - \omega_n^2 - 2\psi K_e w_{c,crit}}\right]\right), \quad n = 0,1,2,\ldots \tag{2.18}$$

These two values are parameterized in ω, and by letting $n = 0,1,2,\ldots$ each branch of the stability lobe diagram can be generated. Using ω_n = 4000 rad/s, ζ = 0.01, ψ = 1 kg^{-1}, and K_e = 8 × 10^5 N/mm^2, the stability lobe diagram in Figure 2-2 is obtained.

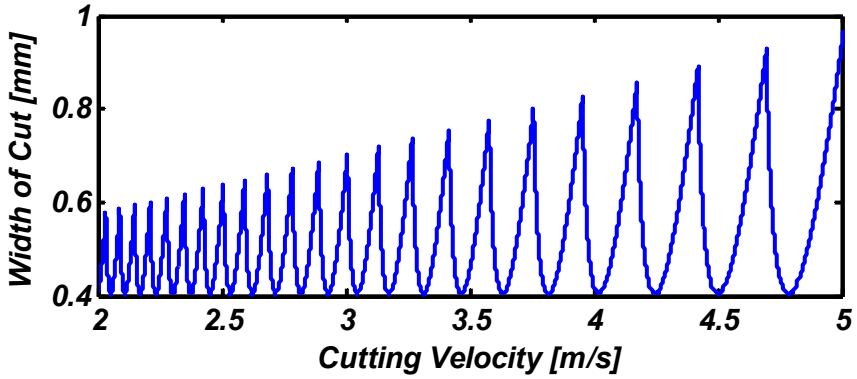

Figure 2-2: Classical stability lobe diagram resulting from the formulation in Equation (2.9).

It should be noted that the stability lobes in Figure 2-2 were plotted against the cutting velocity, $\bar{V}_C$, instead of the critical workpiece revolution period, τ_{crit}. To do this, a workpiece with a 37.31 mm diameter was assumed and $\bar{V}_C$ was found using Equation (2.13) by letting $\tau = \tau_{crit}$. This linear formulation of chatter in Equation (2.9) predicts unbounded vibration for combinations of cutting velocity and width of cut above the stability lobes. It can be shown that the minima of all the lobes occur at the same width of cut, w_{abs}. This is referred to as the absolute stable width of cut since any width of cut less than this value is stable regardless of the cutting velocity. It is given as

$$w_{abs=} \frac{2\omega_n^2 \zeta (1+\zeta)}{\psi K_e} \tag{2.19}$$

which, for the parameters used in this example, gives $w_{c,abs} = 0.404$ mm.

Investigation into the dynamics resulting from the forcing function in Equation (2.6) used in Equation (2.1) reveals a significant shortcoming in that it predicts unbounded exponential growth in the RTWD, $y(t)$, when chatter occurs. Analyses of simple non-linear models of the cutting process have suggested that the onset of chatter represents a sub-critical Hopf bifurcation from a stable fixed point to an unstable fixed point and a stable limit cycle [13]-[15]. This notion has also been upheld through qualitative experimental observations [16].

In an effort to address the limitations of a linear description, investigators such as Hanna and Tobias [17] developed a highly-cited model which has the general form of

$$\begin{aligned} &\ddot{y}(t) + 2\zeta\omega_n \dot{y}(t) + \omega_n^2 \left(y(t) + k_1 y(t)^2 + k_2 y(t)^3 \right) = \\ &k_3 \left(y(t-\tau) - y(t) \right) + k_4 \left(y(t-\tau) - y(t) \right)^2 + k_5 \left(y(t-\tau) - y(t) \right)^3 \end{aligned} \tag{2.20}$$

where k_1, k_2, k_3, k_4, and k_5 are application-specific constants. This model includes a cubic nonlinear structural stiffness as well as a cubic nonlinear regenerative cutting force. However in practice a chattering tool holder or workpiece is well-described by a linear structural stiffness, since the displacements during chatter are typically relatively small in comparison with the length scales associated with the workpiece [18]. The important contribution of this model is that it could finally reproduce the bounded nature of vibration during chatter.

For the common case of turning with significant overlap between successive tool passes, relatively large amounts of vibration can cause influence from many previous RTWDs at integer multiples of the workpiece revolution period before the current time, t, at the cutting zone. Collectively, these times will be referred to as the "regenerative delay space," and are given as

$$[t \quad t-\tau \quad \cdots \quad t-D\tau]_{1\times(D+1)}$$

where $D \geq 1$ and $D \in \mathbb{Z}$, where $\mathbb{Z}$ is the set of natural numbers. Similarly the "regenerative position space" is comprised of all the RTWDs at times in the regenerative delay space, given as

$$[y(t) \quad y(t-\tau) \quad \cdots \quad y(t-D\tau)]_{1\times(D+1)}$$

The precise value of D that is needed will depend on the depth of cut, feed rate, tool nose radius, and expected relative tool-workpiece vibration amplitude (e.g., a small feed rate and large amounts of vibration would necessitate a larger value of D). Efforts to capture this "multiple regenerative effect," that is dependence of the undeformed chip area on more than just the RTWDs $y(t)$ and $y(t-\tau)$, have been described by the investigators in [19]. However, they only considered $D=2$ and the possibility of only one previous RTWD influence. It will be shown in later chapters that there can be multiple previous RTWDs that can influence the state of cutting at a given time, t. In [20] multiple previous delays were assumed ($D=2$) and in this case the dynamic cutting force, $F(t)$, would have the general form

$$F(t) = k_6\left(y(t)-y(t-\tau)\right) + k_7\left(y(t)-y(t-2\tau)\right) \tag{2.21}$$

where k_6 and k_7 are application-specific constants. The problem with such a description is that it suggests that the two previous regenerative terms, $y(t)-y(t-\tau)$ and $y(t)-y(t-2\tau)$, exist for all time. In fact, it will be shown that the regenerative terms' influence is intermittent in time and hence cannot be represented by a simple polynomial. It is even possible that influence from the regenerative term $y(t)-y(t-\tau)$ can vanish.

The general structure of all these relatively simple formulations for chatter are attractive for analysis using bifurcation theory or perturbation techniques. Hence, they have been the source of

many papers in the last thirty to forty years, especially from applied mathematician (e.g. in ref. [20]-[23]). However they are all reverse-engineered (i.e. adding a cubic nonlinearity to get a bounded response during chatter) and overly simplistic, offering little physical insight into the underlying physics of machining. Surprisingly, there have been fewer attempts to apply the knowledge gained from metal cutting theory to the physics of regenerative chatter. And even those fall short of a complete description of chatter as it is encountered in a real-world turning operation. In the words of Moon and Kalmar-Nagy [18], "Fascination with time-delay differential equations has often overshadowed the physics of material processing." The complex mechanics of cutting and many process parameters are often reduced to a constant, such as K_e in Equation (2.6), and consequently the models associated with such an approach must certainly only be valid in a small subset of machining conditions.

2.2 Modeling of Low-Speed Chatter Stability

One true test of a chatter model's accuracy lies in its ability to predict increased stability at low cutting velocities, since this has been observed experimentally in many reports [24], [25]. Despite this, many chatter models continue to be developed that generate stability lobe diagrams where each lobe touches an asymptote at a constant value, as suggested by Equation (2.19) and shown in Figure 2-2. This added stability is due to process damping from interference between the cutting tool and the machined workpiece surface [26],[27]. For a given oscillation frequency and amplitude of the RTWD, the effect of cutting velocity on the amount of interference between the workpiece and the cutting tool is qualitatively depicted in Figure 2-3. It should be noted that the radius of the cutting edge, r_e, has been increased dramatically for clarity. In each case a volume of workpiece material, V_I, a so-called "interference volume," is displaced because it has to flow around the cutting tool's edge and clearance face. The size and orientation of this interference volume changes based upon the recent relative vibration history; this in turn affects the forces imparted on the workpiece and the cutting tool. In both Figure 2-3A and B, the instantaneous velocity of the cutting tool relative to the

workpiece in the thrust direction, V_T, (the direction into the workpiece) is the same. However, since the magnitude of the slope of the machined workpiece surface is generally larger for the low-velocity cutting case, larger interference volumes can be developed, shown in Figure 2-3B. This adds increased damping and in turn more stabilization at low cutting velocities. This will be explained in more detail in Chapter 5.

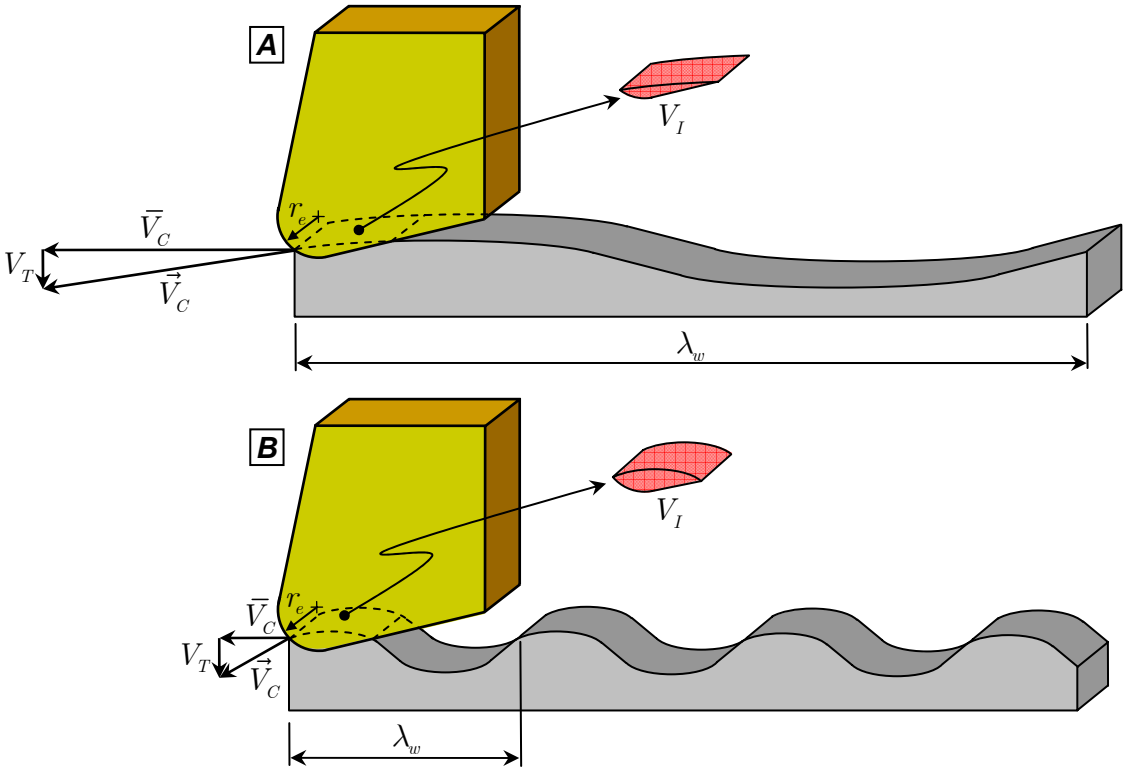

Figure 2-3: The effect of cutting velocity on the interference volume between the workpiece and an oscillating cutting tool. (A) High cutting velocity; (B) low cutting velocity.

In an effort to obtain a chatter model that can accurately describe stability at low cutting velocities an interesting turning experiment was conducted by Altintas et al. in [24]. They identified dynamic cutting force coefficients, C_1 and C_2, that are proportional to the velocity and acceleration of the cutting tool, respectively, by measuring cutting forces while using a fast tool servo oscillating at known frequencies and magnitudes. In this way they were able to construct a model of the form

$$\ddot{y}(t)+2\zeta\omega_n\dot{y}(t)+\omega_n^2 y(t)=\psi K_e\left(d_c+y(t-\tau)-y(t)\right)-\frac{C_1\dot{y}(t)}{\bar{V}_C}-\frac{C_2\ddot{y}(t)}{\bar{V}_C^2} \tag{2.22}$$

and reproduce the increased stability encountered at low cutting velocities. This represents an important step forward in chatter modeling, but it is at the cost of a lack of physical insight into the effect of true process parameters such as the cutting tool geometry and material properties. The results of their chatter stability prediction are graphically re-presented in Figure 2-4. There are three traces shown on the figure. One uses both the velocity and acceleration terms (C_1 and C_2), one uses only the velocity term, C_1, and the remaining one represents the classical solution, i.e. Equation (2.16).

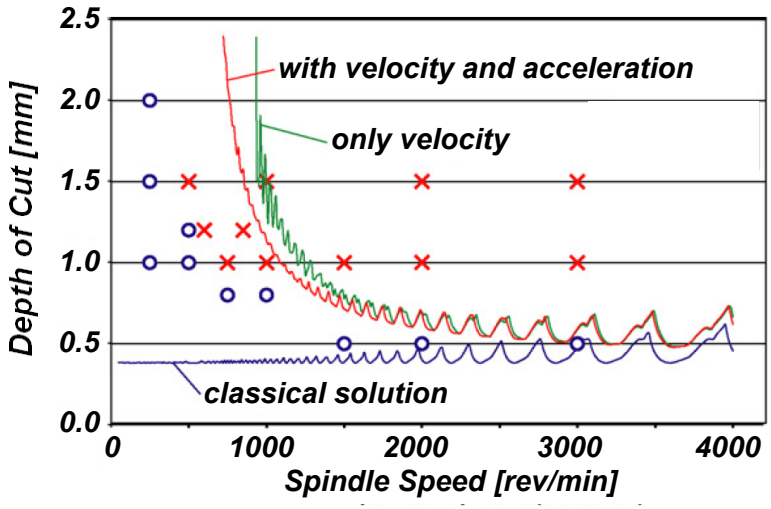

Figure 2-4: A re-presentation of the results in [24] showing the low-speed chatter stability predicted by Equation (2.22). ×, cutting condition producing chatter; ○, stable cutting condition.

Chiou and Liang derived an orthogonal model with a relatively coarse approximation of the interference volume when the tool has wear along its flank [26]. They assumed that the clearance face of the tool never makes contact with the machined workpiece surface during vibration–only the worn portion on the flank does. Consequently the model predicted no increase in stability at low cutting velocities for a perfectly sharp tool, despite their experimental data showing otherwise. This is because with no flank wear their predictions were essentially reduced to the classical solution in Equation (2.16). However, when interference between the workpiece and the cutting tool as a result of flank wear was simulated in their model and compared with machining tests using worn tools, an accurate prediction of the increase in stability at low cutting velocities was obtained. This represents

an important contribution to dynamic cutting force modeling, since low-speed chatter stability was predicted by a physics-based model.

2.3 Chatter Models That Incorporate True Process Parameters

Two efforts stand out from other previous works in dynamic cutting force modeling by attempting to include the cutting geometry that is typically used in practice. Rao and Shin [29] incorporated the effect of a nonzero tool inclination angle (termed oblique machining) and a tool nose radius into a 3D dynamic cutting force model used to predict chatter in turning. However, they failed to model any plowing forces or process damping between the cutting tool and the workpiece. Later, Clancy and Shin [30] appear to have revised the same model and applied it to a facing operation. They added process damping due to the interference between the clearance face of the cutting tool and the workpiece in the manner that was developed by Chiou and Liang [26]. However, the stability lobe diagrams they generated appear qualitatively very similar to those resulting from the linear formulation in Equation (2.9) in that there is no increase in stability at low cutting velocities. Also, in both [29] and [30], the only cutting parameter that changed with time was the undeformed chip area. As will be shown later on, the effective cutting parameters (rake angle, cutting velocity) change over time when there is relative tool-workpiece vibration.

Ozlu and Budak [31]-[33] have presented a 2D model that incorporates tool nose radius and regenerative effects; however it is still a linear model and reduces to an eigenvalue value problem in order to find regions of stable and unstable machining. They make the claim that the tangential cutting force "does not contribute to the regeneration mechanism [33]". They are correct in that it does not contribute *directly* to the undeformed chip thickness, and in turn the regenerative effect. However, as demonstrated by Cardi et al. [34] and Marui et al. [27], the majority of the vibration energy is typically in the tangential cutting direction since the cutting force is largest along that axis. It will be shown later that this vibration is coupled to the vibration in the radial cutting direction and in turn influences the occurrence of chatter. Therefore, forces in the tangential direction can not be

neglected. Finally, this model failed to address the interference between the cutting tool and the workpiece, which has been shown to influence process damping, and in turn stability–especially at lower cutting velocities [24].

2.4 Identification of a Research Direction Based on Prior Work

This literature review shows that a cutting force model has yet to be developed to predict chatter in turning that simultaneously and accurately captures the two most important mechanisms during dynamic cutting: the regenerative effect and the interference between the cutting tool and the workpiece. This work seeks to develop a fully comprehensive dynamic cutting force model for turning by using physical insight and extending orthogonal models used in quasi-static cutting force modeling to the current application of predicting chatter. The model will also consider material property effects such as the strain, strain rate and temperature dependence on the flow stress of the workpiece material during machining.

This work is written from an engineer's perspective, not an applied mathematician's. Consequently, there is no treatment of topics such as chaos, bifurcations, or perturbation solution techniques. These types of investigations are still important, since regenerative chatter is a good real-world example of a system with pure delays that exhibits chaos. However, the field has seen an explosion of these papers in recent years and needs to become more rigorous from a first-principles point of view. This is what will ultimately help the machining community to better understand why chatter occurs and to advance process monitoring and control.

Because of the geometric complexity of the current approach, a decision was made to only consider machining conditions where the nose of the cutting tool is engaged in the workpiece. In other words, the model cannot immediately deal with larger depths of cut that have both the tool nose and the side cutting edge in contact with the workpiece. It is not to say that this effect cannot be incorporated, but since it introduces a cutting edge that cannot be described by a smooth function with a finite number of terms, the equations needed would become considerably more complicated

and greater in number. The author feels that this increase in complexity to an already geometrically rigorous methodology would preclude the contribution of the present approach without contributing any new fundamental understanding. In addition the commanded feed rate, f, nominal cutting velocity, $\bar{V}_C$, and commanded depth of cut, d_c, are all assumed to be held constant. Once again, the model could be modified to deal with these parameters if they were time varying; however it would just add complexity to the proposed approach and is not necessary in determining its validity. Finally, owing to the nature of the dynamic properties inherent to the workpiece used in the experimental validation portion of this work in Chapter 8, vibration along the axis of the workpiece is neglected.

Two dynamic cutting force models will be presented in this dissertation. One termed the "simplified cutting force model", resolves the cutting condition at every time step of a dynamic simulation into a single equivalent orthogonal cutting scenario and solves for the forces in closed-form. The other approach derives the cutting forces in a more precise manner by using a geometrically rigorous representation with some elements that cannot be evaluated in closed-form and is termed the "refined cutting force model."

It should be noted that there is nothing inherently "chatter specific" about the following approach. The subject of chatter is just an obvious context to demonstrate the validity of the proposed modeling methods. The experimental system under study is a compliant workpiece machined by a relatively rigid cutting tool (assumed rigid for modeling purposes). Therefore in Equation (2.2) $y_t(t)$ will always be zero in this analysis. However, all subsequent equations are developed around the use of RTWDs, which would facilitate modeling a vibrating cutting tool as well.

It is the author's opinion that in order to make a truly accurate dynamic cutting force model that is used to predict chatter the following components must be incorporated:

- Forces due to chip formation along the undeformed chip area, taking into account influence of relative tool workpiece vibration at the current time, and at previous times, $t-\tau$, $t-2\tau$,…

- Plowing forces
- Forces caused by interference between the machined workpiece surface and the clearance face of the cutting tool
- For a chattering workpiece in a turning operation, a model with at least two degrees of freedom is required (recommended for a chattering tool holder as well)

The necessity of the aforementioned components will be substantiated in later chapters. With a truly accurate model for chatter, the following four items should be able to be predicted:

- Frequency content of chatter vibration
- Stability lobe diagrams with increased stability at lower cutting velocities
- Chatter amplitude vibration growth over time
- Machined surface topography (chatter marks)

These four aspects are arranged in increasing level of difficultly since each successive one requires a more accurate model. To the author's knowledge the last two items, chatter amplitude growth and machined surface topography, have never been compared with experimental measurements in turning. The most rigorous method of comparison would be a combination of the third and fourth objectives, since if they are predicted adequately the model is able to reproduce both the amplitude and the nature of the growth of vibrations during chatter. It is the goal of this thesis to accurately predict all four of these aspects from a physics-based dynamic cutting force model that excites a model of the workpiece.

CHAPTER 3: ORTHOGONAL CUTTING FORCE MODELING

"The usual approach of science of constructing a mathematical model cannot answer the questions of why there should be a universe for the model to describe. Why does the universe go to all the bother of existing?"

-Stephen Hawking

3.1 Forces Due to Chip Formation

As identified in the literature review there are two sources of forces in machining: those due to chip formation and those due to plowing and flank interference. In this section, the forces due to chip formation will be modeled in the orthogonal cutting domain with the Oxley cutting force model [35]. It is a slip-line cutting force model derived from experimental observations in metal cutting. One of the assumptions is the existence of steady-state, plane-strain conditions; another is a perfectly sharp tool. Clearly this is at odds with its present application in predicting forces during chatter in turning–a scenario where the depth of cut is changing over time as the workpiece vibrates relative to the cutting the tool. Despite this it has been shown for a milling operation, where the effective depth of cut at each flute is changing over time, that the Oxley cutting force model can be applied instantaneously at points in time, as in the investigations in [36] and [37]. In these cases, 40 Hz was the dominant frequency that the undeformed chip thickness was changing. This is far below the 600 Hz chatter frequencies encountered in this work.

In [38] a shear plane model was used to predict forces during chatter in turning, which just like Oxley's theory is meant for steady-state, plane-strain conditions. In this case the chatter frequency is much higher at 1200 Hz, and although the force predictions have a higher average value than the measurements, the force variation is similar. In analytical chatter modeling, if the workpiece is assumed to respond linearly, it is not the mean level of force that is of interest but rather the variation of the force. One factor contributing to the error could be that the dynamometer used to measure the forces had internal dynamics. There was no make or model number specified, but dynamometers are typically large, relatively massive devices. They can contribute significant phase lag and attenuation or amplification in measurements at frequencies as low as about 1 kHz,

depending on how they are mounted. There was no mention in the paper of any attempt to compensate for this. If a piezoelectric dynamometer is to be used for dynamic cutting force measurement, it is necessary to compensate for its internal dynamics by deriving a transfer function matrix for the dynamometer and using the inverse of that matrix as a prefilter on the output of the dynamometer [39].

Typically, models developed for quasi-static cutting with constant cutting conditions are used to describe a dynamic cutting process with time-varying cutting conditions. Often times, the assumption that this aforementioned approach is valid is never directly stated or justified. One work that explicitly states this assumption is in [40] where tool vibration frequencies of 100 Hz are considered. What is really being assumed when applying quasi-static cutting force models to dynamic scenarios is that the mechanics of the cutting process are not dependant on past inputs or outputs. In signal processing it is said that such a system is *memoryless*. With this assumption the system will exhibit zero transient response, and the Oxley model can be applied at instants in time during a dynamic simulation. This work makes no attempt to prove the validity of this assumption.

A brief overview of the constitutive equations and method for implementing a modified version of Oxley's cutting force model will now be given. The theory analyzes the stresses developed along $\overline{AB}$ and the tool-chip interface, as shown in Figure 3-1.

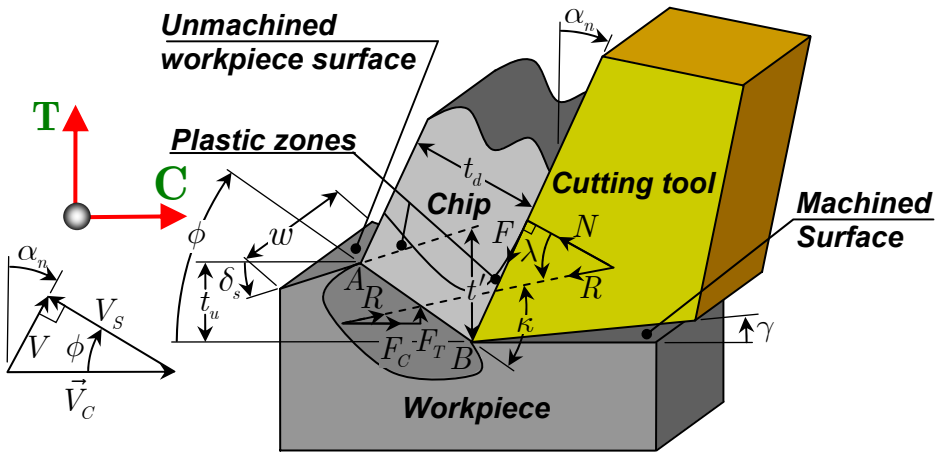

Figure 3-1: An orthogonal cutting configuration with consideration of nonzero workpiece slope, δ_s.

The directions typically referred to as "cutting" and "thrust" are denoted by the **C** and **T** axes, respectively. The cutting direction is parallel to the machined workpiece surface and the thrust direction is perpendicular to it. These are terms used in many other reports concerning orthogonal cutting models and are presented here for consistency. In this work, the orientation of the **C** and **T** axes is the important feature, not the position of their origin in space.

All annotations in Figure 3-1 are in the plane of the page except for w. The given parameters are the undeformed chip thickness, t_u, the width of cut, w, the normal rake angle, α_n, and $\vec{V}_C$, the relative velocity between the cutting tool and workpiece. It is important to note that $\vec{V}_C$ is a vector in order to reflect that its orientation and magnitude can change during vibration. In a turning operation the commanded cutting velocity is usually a constant and will be denoted by $\bar{V}_C$. In general, $\vec{V}_C$ will only equal $\bar{V}_C$ when there is zero relative tool-workpiece vibration, as will be shown in Chapter 4. The clearance angle, γ, although not a part of Oxley's cutting force model, is a given parameter as well and will be used in subsequent force modeling from mechanisms not due to chip formation. The clearance angle has been shown not to significantly influence forces due to chip formation [41] and hence can be neglected. In this investigation, the effect of the workpiece surface slope, δ_s, will be incorporated as well. For stable cutting force modeling, the surface slope is typically considered to be zero. However, it will be shown in Chapter 4 that a nonzero workpiece surface slope is needed when there is significant relative tool-workpiece vibration.

Measured clockwise from the direction of the negative **C** axis, one of the outputs of the Oxley cutting force model is the shear angle, ϕ. It defines the orientation of the shear plane, $\overline{AB}$, which is the region where workpiece material abruptly changes direction by a shearing force and flows up the rake face of the tool to become a chip. In Figure 3-1, this plane would be defined by line segment $\overline{AB}$ and the width of cut, w. In reality, steel is a rigid-plastic hardening material and hence can not change direction instantaneously. Owing to this, parallel sided shear zone theory is employed which considers a shear zone inclined at an angle, ϕ, and not a shear plane.

It should be noted that in Figure 3-1 there are two undeformed chip thicknesses, t_u and t'. Typically, orthogonal cutting models have zero workpiece slope; therefore the undeformed chip thickness can be uniquely defined by t_u –the distance between a line coincident with the machined workpiece surface and a line parallel to the unmachined workpiece surface. This description is valid because t_u is invariant under the shear angle, ϕ. However, for a given nonzero workpiece slope t_u will change with varying shear angle. To address this, the undeformed chip thickness is uniquely defined by two quantities: t' and δ_s. As shown in Figure 3-1, t' is measured perpendicularly from a line coincident with the machined workpiece surface at the tip of the cutting tool to a line extended along the unmachined workpiece surface. In terms of t' and δ_s the length of the shear plane, $\overline{AB}$, is given as

$$\overline{AB} = \frac{t' \cos[\delta_s]}{\sin[\phi + \delta_s]} \tag{3.1}$$

and the undeformed chip thickness is given by

$$t_u = \overline{AB} \sin[\phi] = \frac{t' \cos[\delta_s] \sin[\phi]}{\sin[\phi + \delta_s]} \tag{3.2}$$

It should be noted that for $\delta_s = 0$, $t_u = t'$ for all $\phi \in [0, \pi/2]$ in Equation (3.2) and is thereby consistent with the previous claim that t_u is invariant under shear angle for workpiece surface slope of zero. With this modification to the length of the shear plane and the undeformed chip thickness in Equations (3.1) and (3.2), respectively, the rest of the equations presented in [35] can be used to describe the forces due to chip formation.

The shear angle, ϕ, is selected such that the resultant forces transmitted along the shear plane are in equilibrium. It is formed by the line segment, $\overline{AB}$, and the cutting width, w. It should be noted that the cutting width does not affect the predicted shear angle since this a planar analysis.

Once ϕ is determined, the deformed chip thickness, t_d, and all forces in Figure 3-1 are simply

$$t_d = \frac{t_u \cos[\phi - \alpha_n]}{\sin[\phi]} \tag{3.3}$$

$$F_C = R\cos[\lambda - \alpha_n] \tag{3.4}$$

$$F_T = R\sin[\lambda - \alpha_n] \tag{3.5}$$

$$F = R\sin[\lambda] \tag{3.6}$$

$$N = R\cos[\lambda] \tag{3.7}$$

where

$$R = \frac{F_S}{\cos[\kappa]} = \frac{k_{AB} t_u w}{\sin[\phi]\cos[\kappa]}$$

t_d is the deformed chip thickness, F_C and F_T are the forces due to chip formation parallel and normal to the cutting direction, respectively, F and N are the frictional and normal forces at the cutting tool, respectively, λ is the friction angle, k_{AB} is the flow stress along the shear plane, R is the resultant force acting on the cutting tool, F_S is the shear force, and κ is the angle of the resultant force. To facilitate future developments where the chip formation forces per unit width of cut are required, f_C and f_T are defined as

$$f_C = \frac{F_C}{w} = \frac{t_u k_{AB} \cos[\lambda - \alpha_n]}{\sin[\phi]\cos[\kappa]} \tag{3.8}$$

and

$$f_T = \frac{F_T}{w} = \frac{t_u k_{AB} \sin[\lambda - \alpha_n]}{\sin[\phi]\cos[\kappa]} \tag{3.9}$$

The velocities of the chip perpendicular and parallel to $\overline{AB}$, V and V_S, respectively, are defined in Equations (3.10) and (3.11) as

$$V = \frac{\left|\vec{V}_C\right| \sin[\phi]}{\cos[\phi - \alpha_n]} \tag{3.10}$$

$$V_S = \frac{\left|\vec{V}_C\right| \cos[\alpha_n]}{\cos[\phi - \alpha_n]} \tag{3.11}$$

where $\left|\vec{V}_C\right|$ denotes the magnitude of $\vec{V}_C$. One of the earliest analyses of cutting forces was performed by Merchant [42], who assumed that the shear angle, ϕ, adjusts itself to minimize the F_C and F_T. The outcome of this assumption results in the following formulation for the shear angle

$$\phi = \frac{\pi}{4} + \frac{\alpha_n}{2} - \frac{\lambda}{2} \tag{3.12}$$

which has been used by many investigators due to its simplicity. The problem with Equation (3.12) is that it tends to overestimate the shear angle because it fails to capture many effects in the machining process: the high strains, strain rates, and temperatures developed in the cutting zone. To reflect this, a Johnson-Cook model is adopted to describe the flow stress as function of strain, strain rate, and temperature [43]. The general form of the equation describing this relationship is given as

$$\sigma = \left(A + B\varepsilon_p^n\right)\left(1 + C\ln\left[\frac{\dot{\varepsilon}_p}{\dot{\varepsilon}_0}\right]\right)\left(1 - \left(\frac{T - T_0}{T_m - T_0}\right)^m\right) \tag{3.13}$$

where σ is the flow stress, ε_p is the effective plastic strain, $\dot{\varepsilon}_p$ is the effective plastic strain rate, T is the temperature of the material, T_m is the melting point of the material, T_0 is the reference temperature, and A, B, C, m, n, $\dot{\varepsilon}_0$, are material-specific constants.

The Oxley cutting force model will be used in this study to predict forces due to chip formation with relative tool-workpiece vibration. To do this the model needs to be applied over a wide range of cutting parameters. In the experimental validation portion of this dissertation, given in Chapter 8, AISI 1018 steel is used during all machining tests. Johnson-Cook parameters for AISI 1018 were not able to be found in any published data, so coefficients for another material had to be used to approximate the behavior of AISI 1018 steel. When trying many other sets of Johnson-Cook parameters, it was found that the Oxley cutting force model was not able to converge to a solution for many of the cutting conditions used in this study. It was later discovered that when using the Johnson-Cook coefficients for AISI 4340 steel in [43] the Oxley model performed very well over a wide range of cutting conditions. AISI 4340 is an alloy steel with a higher yield strength than AISI 1018, a low carbon steel. However in dynamic cutting force modeling, it is the changes in the force

that matter, not the mean value. Consequently, if the strain, strain rate, and temperature sensitivity of AISI 4340 are assumed to be similar to those of AISI 1018, then the Johnson Cook coefficients for AISI 4340 can be used. The coefficients for AISI 4340 are given in Appendix A.

It is noteworthy that some approaches to modeling cutting forces abuse Equation (3.13). All of the aforementioned coefficients should be determined directly from a test that isolates the strain, strain rate, and temperature effects such as a Hopkinson bar test [43]. Some researchers choose to develop a cutting force model that is oversimplified, and they incorporate the Johnson-Cook flow stress equation. Then with experimental data they perform a regression analysis to solve for all the Johnson-Cook coefficients in Equation (3.13). The problem with this method is that in the machining tests there are so many complicated mechanisms interacting that it is difficult to isolate them, as opposed to a Hopkinson bar test which does a better job of isolating the parameters that it models. In other words they overcome the oversimplifications in their cutting force model by using Equation (3.13) to curve-fit experimental data. By doing this they open up a philosophical debate about whether the true physics of the process are being captured or whether the model is essentially being used as a curve-fitting device. This issue was presented in order to underscore the precise goal of this work; that is, to be as geometrically rigorous as possible and only resort to experimentally derived coefficients when absolutely necessary. It should be noted that the Johnson-Cook coefficients used in this investigation were derived from Hopkinson bar testing.

The key parameter in the Oxley cutting force model is the shear angle, ϕ, which must be found iteratively. First, the temperature rise in the shear plane along $\overline{AB}$, T_{AB}, is computed in order to predict the flow stress, k_{AB}, the details of which can be found in [35]. The strain along AB is

$$\varepsilon_{AB} = \frac{\cos[\alpha_n]}{2\sqrt{3}\sin[\phi]\cos[\phi - \alpha_n]} \tag{3.14}$$

and the strain rate is given by

$$\dot{\varepsilon}_{AB} = \frac{C_{Oxley} V_s \sin[\phi]}{\sqrt{3} t_u} \tag{3.15}$$

The flow stress along $\overline{AB}$ is

$$k_{AB} = \frac{1}{\sqrt{3}}\left(A + B\varepsilon_{AB}^{n}\right)\left(1 + C\ln\left[\frac{\dot{\varepsilon}_{AB}}{\dot{\varepsilon}_{0}}\right]\right)\left(1 - \left(\frac{T_{AB} - T_{0}}{T_{m} - T_{0}}\right)^{m}\right) \tag{3.16}$$

With the flow stress determined, all the forces given in Equations (3.4)-(3.7) can now be found. The friction angle, λ, is given by

$$\lambda = \kappa + \alpha_{n} - \phi \tag{3.17}$$

where the inclination angle of the resultant force is described by

$$\kappa = \tan^{-1}\left[1 + 2\left(\frac{\pi}{4} - \phi\right) - Cn\right] \tag{3.18}$$

In Equation (3.18), the n term is a strain-hardening coefficient used in [44] that allows the Johnson-Cook flow stress model to be incorporated into the cutting force model. It is given as

$$Cn = C_{Oxley} n \frac{B\varepsilon_{AB}^{n}}{A + B\varepsilon_{AB}^{n}} \tag{3.19}$$

With the angles determined, the tool-chip contact length is computed by

$$h = \frac{t_{u}\sin[\theta]}{\cos[\lambda]\sin[\phi]}\left(1 + \frac{Cn}{3\tan[\kappa]}\right) \tag{3.20}$$

Assuming the stress distribution along the tool chip contact length is constant, the shear stress along the tool-chip interface is

$$\tau_{int} = \frac{F}{hw} \tag{3.21}$$

The temperature rise in the chip is then computed using a method detailed by Oxley in [35]. The resulting expression for the average flow stress in the chip is given as

$$k_{chip} = \frac{1}{\sqrt{3}}\left(A + B\varepsilon_{int}^{n}\right)\left(1 + C\ln\left[\frac{\dot{\varepsilon}_{int}}{\dot{\varepsilon}_{0}}\right]\right)\left(1 - \left(\frac{T_{int} - T_{0}}{T_{m} - T_{0}}\right)^{m}\right) \tag{3.22}$$

where the average value of the strain and strain rate is given in Equations (3.23) and (3.24), respectively

$$\varepsilon_{int} = 2\varepsilon_{AB} + \frac{h}{\sqrt{3}\delta t_{d}} \tag{3.23}$$

$$\dot{\varepsilon}_{int} = \frac{\left|\vec{V}_C\right|}{\sqrt{3} t_r t_d} \tag{3.24}$$

and t_r is the ratio of the thickness of the plastic zone at the tool-chip interface to the deformed chip thickness, t_d.

To solve for ϕ, all of the previous computations are made to determine τ_{int} and k_{chip} over a range of possible shear angles, typically evenly distributed between 5° and 45°. In keeping with the principle of minimum work, the largest shear angle value where $\tau_{int} = k_{chip}$ is taken as the actual shear angle. Since a discrete number of shear angles is evaluated, linear interpolation of this intersection is used to increase accuracy. Herein lies the power of using the Oxley cutting force model–the fact that no knowledge of the deformed chip thickness, t_d, is required (the shear angle can easily be determined with knowledge of t_u and t_d via Equation (3.3)). It is a simple task to determine t_d experimentally for a small number of orthogonal cutting conditions; however, the present investigation searches a parameter space too large to make this practical.

For the remainder of this investigation, when using the Oxley cutting force model a regression surface for each one of its outputs, f_C, f_T, and ϕ_V, will be used instead. ϕ_V is the shear angle chosen by the Oxley model out of all potential shear angles, ϕ. Regression surfaces are used because the algorithm is computationally inefficient in finding the shear angle due to its iterative nature. The regression surfaces are a function of four independent parameters, and are given as

$$S_{f_C}\left(t', \alpha_n, \left|\vec{V}_C\right|, \delta_s\right) \approx f_C \tag{3.25}$$

$$S_{f_T}\left(t', \alpha_n, \left|\vec{V}_C\right|, \delta_s\right) \approx f_T \tag{3.26}$$

$$S_{\phi_V}\left(t', \alpha_n, \left|\vec{V}_C\right|, \delta_s\right) \approx \phi_V \tag{3.27}$$

where the relations are given as approximate since there will inevitably be some error between the exact outputs from the Oxley cutting force model, f_C, f_T, and ϕ_V, and the outputs from the

regression surfaces, S_{f_C} , S_{f_T} , and S_{ϕ_V} . The exact details of the computation of these regression surfaces will be given in Chapter 7.

3.2 Plowing and Flank Interference Forces

In addition to the contribution from the forces due to chip formation, there are forces due to the fact that the tool edge is not perfectly sharp (the cutting edge would be located at point B in Figure 3-1, extending into the page). These forces are termed plowing forces because some material is "plowed" into the workpiece due to the nonzero radius on the edge of the cutting tool. The need to address these forces has been considered by many other researchers [45],[46]. In addition, there are forces due to contact between the machined workpiece surface and clearance face of the cutting tool when there is relative vibration between them. The clearance face can also be referred to as the flank and would be located on the underside of the cutting tool above the machined workpiece surface, as indicated in Figure 3-2B.

An interesting set of experiments performed by Marui et al. shows that forces due to plowing and flank interference are intimately linked with chatter stability in turning processes [27]. In this work they turned a square-threaded workpiece with a straight edge cutting tool. The feed rate per revolution was equal to the thread pitch, and in this way the regenerative effect was completely eliminated. Despite this, chatter was still produced with much larger vibration in the tangential cutting direction than in the radial direction. Efforts in explaining the effect of flank wear on the stability of the turning process have also been conducted in [26]. It was shown that increasing flank wear stabilized the cutting process, especially at low cutting velocities. In other reports, by investigating the surface profile after a turning operation where chatter was present, it was clear that the flank of the cutting tool was impacting the workpiece surface as it advanced [27]. Clearly there is interaction between the clearance face of the cutting tool and the machined workpiece surface; therefore any chatter model for turning that is meant to explain the process from a first-principles point of view must include forces due to plowing and flank interference.

Figure 3-2A is an orthogonal cutting scenario with zero relative tool-workpiece vibration and a constant commanded cutting velocity, $\bar{V}_C$. As the material approaches the tool edge, it either moves upwards to become a chip, or is plowed as it flows around the tool's edge of radius, r_e . As a simplification, the material is considered to be elastic in that it makes a full recovery to its machined height after it passes beneath the cutting tool. Therefore an "undeformed workpiece surface," as indicated in the figure, represents the machined surface of the workpiece that would exist if somehow machining could progress without interference from the edge or clearance face of the cutting tool. In reality plowing is characterized by plastic deformation of the workpiece material, which would result in an inelastic and therefore incomplete recovery.

A technique was developed by Wu in [47] where the forces due to plowing and contact along the clearance face can be resolved simultaneously. The amount of force developed by such a process is proportional to the amount of workpiece material that is displaced by the cutting tool, a so-called "interference volume." In an orthogonal cutting scenario the interference volume is the product of the interference area, A_i , and the width of cut, w . The interference area is the region defined by the boundary of the cutting tool and the undeformed workpiece surface, as shown in Figure 3-2.

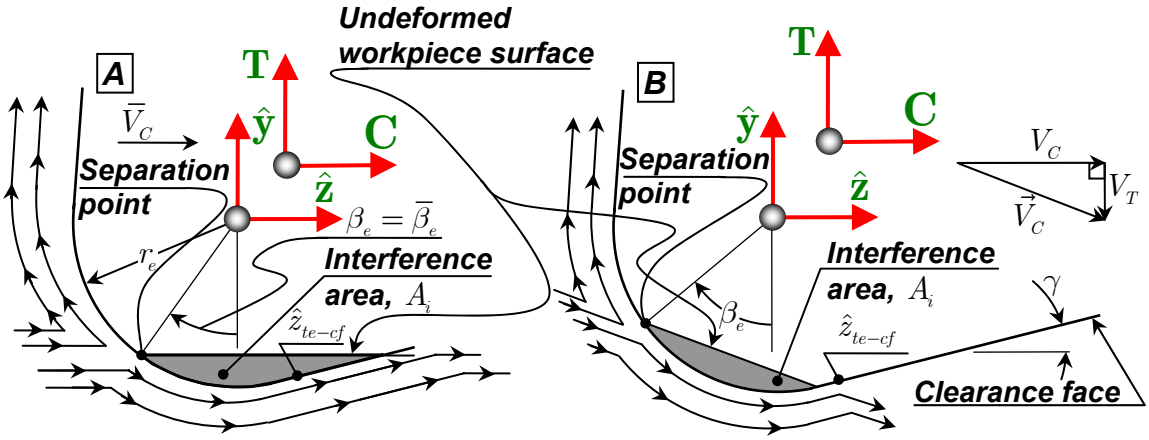

Figure 3-2: Two orthogonal cutting scenarios with different relative vibration and interference areas. (A) Cutting with zero relative tool-workpiece vibration; (B), cutting with nonzero relative tool-workpiece vibration.

In Figure 3-2B a different case arises when there is relative vibration between the cutting tool and the workpiece. In this case there could be an instantaneous velocity in the cutting direction, V_C , and an instantaneous velocity in the thrust direction, V_T , of the workpiece material. In the

specific case pictured, there is only contact between the machined workpiece surface and edge radius portion of the cutting tool. For the case where there is vibration during cutting, the interference area, and in turn the interference volume can be larger or smaller and have a different orientation than in the case of zero vibration cutting.

A critical parameter in this model is the material separation point, or the cutting edge contact point. It can be defined as the point of intersection between a ray at an angle of $\overline{\beta}_e$ measured clockwise from the negative thrust direction and the cutting edge. In [48] $\overline{\beta}_e$ was determined empirically; however in this case it is taken to be 30°, a value determined by the experimental results in [49]. The angle of material separation, β_e, is valid for all time in the case of stable cutting, but in dynamic cutting it is assumed to change based on the components of the velocity in the thrust and cutting directions, as given by

$$\beta_e = \overline{\beta}_e - \tan^{-1}\left[\frac{V_T}{V_C}\right] \tag{3.28}$$

In Figure 3-2B β_e is larger than it is in Figure 3-2A as a result of a negative velocity of the cutting tool relative to the workpiece in the thrust direction, V_T.

With all of these assumptions the problem of finding the plowing and flank interference forces has essentially been reduced to an exercise in geometry. This was also adopted in [47] and [48], however the approach in [48] was far more rigorous and will serve as the foundation for later developments. For conciseness, the forces due to plowing and flank interference will now be termed "interference forces."

As in [47], the interference forces will have a component in the thrust direction, P_T, and in the cutting direction, P_C, and are proportional to the interference volume, V_i, as given by

$$P_C = \mu K_{cf} V_i \tag{3.29}$$

$$P_T = K_{cf} V_i \tag{3.30}$$

where μ is the coefficient of friction and K_{cf}, the force-interference volume constant, derived in [50] to be

$$K_{cf} = \frac{0.775E}{\rho(1-2\nu)} \tag{3.31}$$

where E is Young's modulus, ν is Poisson's ratio, and ρ is the extent of the elastoplastic deformation zone beneath the cutting tool.

A relatively coarse approximation for the interference area, A_i, was developed in [47]. It relied on the assumption of a sinusoidal signal-frequency, constant-amplitude relative velocity between the workpiece and the cutting tool in the thrust direction in addition to a constant velocity in the cutting direction. A more accurate model for describing the interference area, A_i, and resulting forces was developed by Endres in [48], with a more detailed account given in his thesis [51]. It operates from the assumption that discrete data points describing the position of the workpiece relative to the cutting tool are the output of a numerical simulation. Based on linear interpolation between the data points at times, k, $k-1$,…, the interference area is given in the way depicted in Figure 3-3A.

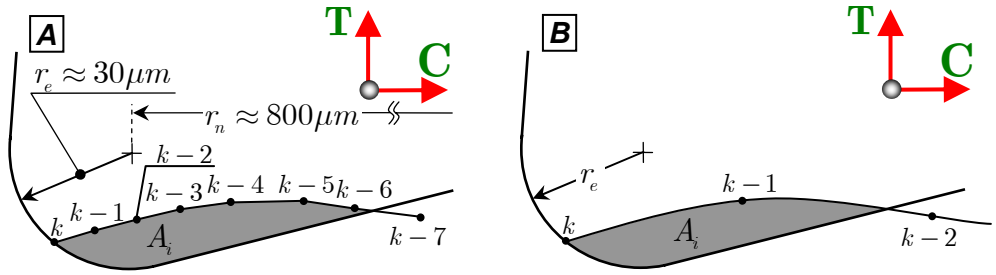

Figure 3-3: Two scenarios where data points from a numerical simulation are used to find the interference area, A_i. (A), Many data points spaced closely together with linear interpolation of the undeformed workpiece surface; (B), data points spaced far apart with polynomial interpolation of the undeformed workpiece surface.

To get a sense of scale in Figure 3-3 the edge radius, r_e, is typically around 30 µm. Considering the common frequency range that chatter typically occurs ($\leq$ 1500 Hz) and the cutting velocities used in practice, a chatter simulation would not typically need to output points with the fine spatial resolution shown in Figure 3-3A. To force the simulation to take time steps that small would increase the computational time drastically while obtaining a solution that is much more

accurate than necessary. In reality, the time steps needed for an accurate simulation are much more coarsely spaced, as depicted qualitatively in Figure 3-3B. Since the data points are now much further apart it would be desirable to interpolate with a higher order polynomial to capture the curvature of the workpiece surface that is generated during dynamic cutting. In addition, it is desirable to have a single polynomial represent the undeformed workpiece surface, as opposed the piecewise linear formulation in Figure 3-3A, because it will facilitate the evaluation of various integrals to find the interference volume in a more concise manner. The following approach for describing the interference area is inspired by the work of Endres in [48], however most of the equations are different since a polynomial representation of the undeformed workpiece surface is used instead of a piecewise linear one.

An approach for finding the volume of interference in an orthogonal cutting configuration will now be presented. A local $\hat{\mathbf{y}}$ - $\hat{\mathbf{z}}$ reference frame with an angular coordinate, β, measured CCW from the positive $\hat{\mathbf{z}}$ axis is used in the following derivation, as depicted in Figure 3-4. It should be noted that quantities denoted in red will be used in the simplified cutting force model, quantities in blue are modified versions that will be used in later developments of the refined cutting force model, and quantities in black are not specific to either approach.

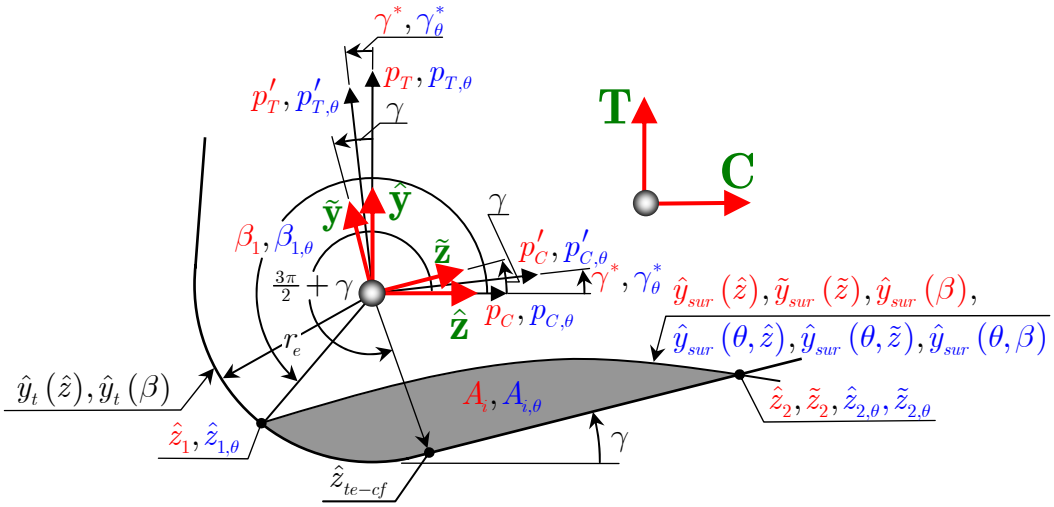

Figure 3-4: The reference frames and quantities used to find the interference area and effective clearance angle. Quantities in **red** are used for the simplified dynamic cutting model, quantities **blue** are used for the refined dynamic cutting model, and quantities in **black** are shared by both models.

The undeformed workpiece surface, $\hat{y}_{sur}(\hat{z})$, as shown in Figure 3-4, can be represented in the $\hat{\mathbf{y}}$ - $\hat{\mathbf{z}}$ reference frame by the following second order polynomial:

$$\hat{y}_{sur}(\hat{z}) = a_0 + a_1\hat{z} + a_2\hat{z}^2 \tag{3.32}$$

where the coefficients, a_0, a_1, and a_2 are determined via least squares based on the relative vibration history between the cutting tool and the workpiece during the chatter simulation. In the following analysis there will be numerous instances where equations are presented for both the case where $a_2 = 0$ and $a_2 \neq 0$. In reality, since the proposed method will be numerically simulated, $a_2 = 0$ really means $a_2 \approx 0$. If $a_2 \approx 0$, then some equations will be modified to reflect solutions assuming that Equation (3.32) does not posses the a_2 term. The boundary of the cutting tool can be represented by the piecewise continuous function, $\hat{y}_t(\hat{z})$, as

$$\hat{y}_t(\hat{z}) = \begin{cases} -\sqrt{r_e^2 - \hat{z}^2} & 0 \le \hat{z} < \hat{z}_{te-cf} \\ m_t\hat{z} + b_t & \text{otherwise} \end{cases} \tag{3.33}$$

where m_t is the slope of the line representing the cutting tool clearance face, and is given as

$$m_t = \tan[\gamma] \tag{3.34}$$

and b_t is its $\hat{y}$ intercept, expressed as

$$b_t = \frac{-r_e}{\cos[\gamma]} \tag{3.35}$$

and $\hat{z}_{te-cf}$ is the point of transition from the curved tool edge to the straight clearance face, given as

$$\hat{z}_{te-cf} = r_e \sin[\gamma] \tag{3.36}$$

The interference area, A_i, is simply the area bounded by the undeformed workpiece surface and the boundary of the cutting tool, given by

$$A_i = \int_{\hat{z}_1}^{\hat{z}_2} \int_{\hat{y}_t(\hat{z})}^{\hat{y}_{sur}(\hat{z})} d\hat{y}d\hat{z} \tag{3.37}$$

where $\hat{z}_1$ and $\hat{z}_2$ are the limits on the integration defined by the intersection of the undeformed workpiece surface and the boundary of the cutting tool.

There are two possibilities for intersections between the undeformed workpiece and the cutting tool. Either both intersections can occur along the tool edge, as in Figure 3-2B, or one intersection can occur along the tool edge and the other along the clearance face, as in Figure 3-2A. In order to determine which case is present, all intersections between the undeformed workpiece surface and the constituent functions repressing the boundary of the cutting tool ($\hat{y}_t(\hat{z}) = -\sqrt{r_e^2 - \hat{z}^2}$ and $\hat{y}_t(\hat{z}) = m_t\hat{z} + b_t$) must be determined. A total of three or four unique intersections will be calculated (depending on whether $a_2 = 0$ or $a_2 \neq 0$), but only two of them will be relevant to the bounds of the interference area in the $\hat{z}$ direction. The intersections are compared to the transition point between the tool edge and the clearance face, $\hat{z}_{te-cf}$, in order to determine which ones are relevant.

The two $\hat{z}$ coordinates of intersection between undeformed workpiece surface and the portion of the cutting tool boundary representing the tool edge, $\hat{y}_t(\hat{z}) = -\sqrt{r_e^2 - \hat{z}^2}$, is given as

$$\hat{z}_{1-te} = \begin{cases} \hat{z}_{1,quart} & a_2 \neq 0 \\ \dfrac{-a_0a_1 - \sqrt{r_e^2\left(1+a_1^2\right) - a_0^2}}{1+a_1^2} & \text{otherwise} \end{cases} \tag{3.38}$$

$$\hat{z}_{2-te} = \begin{cases} \hat{z}_{2,quart} & a_2 \neq 0 \\ \dfrac{-a_0a_1 + \sqrt{r_e^2\left(1+a_1^2\right) - a_0^2}}{1+a_1^2} & \text{otherwise} \end{cases} \tag{3.39}$$

where $\hat{z}_{1,quart}$ and $\hat{z}_{2,quart}$ are the roots of a quartic equation and $\hat{z}_{1-te} \leq \hat{z}_{2-te}$. A closed-form solution exists, but is quite lengthy and given in Appendix A. The intersections between the undeformed workpiece surface and the clearance face of the cutting tool, defined by $\hat{y}_t(\hat{z}) = m_t\hat{z} + b_t$, are given as

$$\hat{z}_{1-cf} = \begin{cases} \dfrac{1}{2a_2}\left(m_t - a_1 - \sqrt{\left(a_1 - m_t\right)^2 + 4a_2\left(b_t - a_0\right)}\right) & a_2 \neq 0 \\ \dfrac{b_t - a_0}{a_1 - m_t} & a_2 = 0 \end{cases} \tag{3.40}$$

$$\hat{z}_{2-cf} = \begin{cases} \dfrac{1}{2a_2}\left(m_t - a_1 + \sqrt{\left(a_1 - m_t\right)^2 + 4a_2\left(b_t - a_0\right)}\right) & a_2 \neq 0 \\ \dfrac{b_t - a_0}{a_1 - m_t} & a_2 = 0 \end{cases} \tag{3.41}$$

Finally, the relevant $\hat{z}$ coordinates of intersection between the undeformed workpiece surface and the boundary of the cutting tool are described by

$$\hat{z}_1 = \hat{z}_{1-te} \tag{3.42}$$

$$\hat{z}_2 = \begin{cases} \hat{z}_{2-te} & \hat{z}_{2-te} < \hat{z}_{te-cf} \\ \hat{z}_{1-cf} & \hat{z}_{1-cf} > \hat{z}_{te-cf} \cup \hat{z}_{1-cf} < \hat{z}_{2-cf} \\ \hat{z}_{2-cf} & \text{otherwise} \end{cases} \tag{3.43}$$

In the case of interference only along the tool edge, the interference area becomes $A_{i-te}\left(\hat{z}_L, \hat{z}_U\right)$ and is given by

$$A_{i-te}\left(\hat{z}_L, \hat{z}_U\right) = \int_{\hat{z}_L}^{\hat{z}_U} \int_{\hat{y}_t(\hat{z})}^{\hat{y}_{surr}(\hat{z})} d\hat{y}d\hat{z} = \frac{1}{6}\left(\hat{z}\left(6a_0 + 3a_1\hat{z} + 2a_2\hat{z}^2 + 3\sqrt{r_e^2 - \hat{z}^2}\right) + 3r_e^2 \tan^{-1}\left[\frac{\hat{z}}{\sqrt{r_e^2 - \hat{z}^2}}\right]\right)\Bigg|_{\hat{z}_L}^{\hat{z}_U} \tag{3.44}$$

where $\hat{z}_L$ and $\hat{z}_U$ are the appropriate lower and upper limits of integration, respectively. The second possibility is the one depicted in Figure 3-4, a case where one intersection occurs along the tool edge and the other along the clearance face. In this case there will be a contribution to the interference area along the tool clearance face, $A_{i-cf}\left(\hat{z}_U\right)$, given as

$$A_{i-cf}\left(\hat{z}_U\right) = \int_{\hat{z}_{te-cf}}^{\hat{z}_U} \int_{\hat{y}_t(\hat{z})}^{\hat{y}_{surr}(\hat{z})} d\hat{y}d\hat{z} = \frac{\hat{z}}{6}\left(6a_0 - 6b_t + \hat{z}\left(3a_1 - 3m_t + 2a_2\hat{z}\right)\right)\Bigg|_{\hat{z}_{te-cf}}^{\hat{z}_U} \tag{3.45}$$

It should be noted that there is only one limit of integration that needs to be specified in this case since the integration always begins at the transition point between the tool edge and the clearance face, $\hat{z}_{te-cf}$. Equation (3.37) can be expressed as a piecewise continuous function, described by

$$A_i = \begin{cases} A_{i-te}\left(\hat{z}_1, \hat{z}_2\right) & \hat{z}_2 \leq \hat{z}_{te-cf} \\ A_{i-te}\left(\hat{z}_1, \hat{z}_{te-cf}\right) + A_{i-cf}\left(\hat{z}_2\right) & \text{otherwise} \end{cases} \tag{3.46}$$

Now that the interference area, A_i, has been described the concept of an effective clearance angle, γ^*, will be introduced. It is defined as the effective orientation angle of the cutting tool

surface in contact with the machined workpiece surface. This angle accounts for the cutting edge radius, the slope of the clearance face and the shape of the undeformed workpiece surface. This idea is once again extended from the work of Endres in [51] to a scenario where there is a simple polynomial representation of the undeformed workpiece surface.

The pressure distribution at a given point along the boundary of the cutting tool is assumed to be proportional to the local interference thickness, $t_i(s)$, where s is the position along a path defined by the boundary of the cutting tool. This is depicted in Figure 3-5A for a case where the undeformed chip thickness is decreasing and in Figure 3-5B for a case where it is increasing.

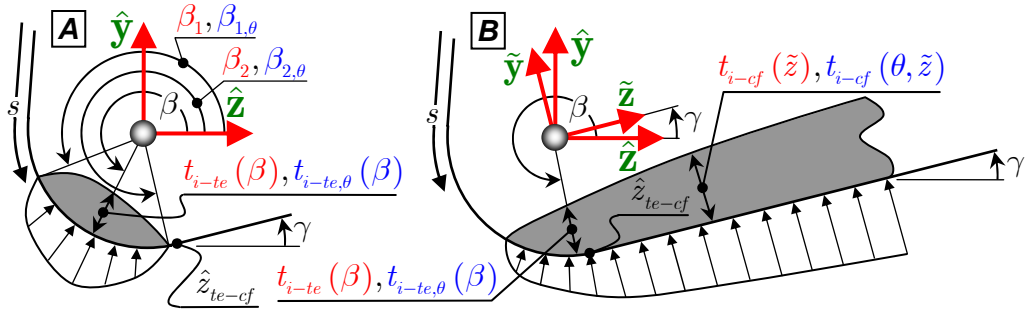

Figure 3-5: Qualitative pressure distributions along the boundary of the cutting tool for various undeformed workpiece surfaces. Quantities in **red** are used for the simplified dynamic cutting force model, quantities **blue** are used for the refined dynamic cutting force model, and quantities in **black** are shared by both models. (A), Decreasing chip thickness; (B), increasing chip thickness.

In a manner similar to that described in [51], the effective clearance angle is given as

$$\gamma^* = \frac{\int_{te+cf} P(s)\,\gamma(s)\,ds}{\int_{te+cf} P(s)\,ds} \tag{3.47}$$

where $P(s)$ and $\gamma(s)$ are the pressure and clearance angle as a function of the path variable s, and the limit $te+cf$ means "the path defined by the tool edge and the clearance face of the cutting tool". As an approximation, the pressure at a point along the portion of the cutting tool in contact with the workpiece is assumed to be the product of some pressure constant, K_p, and the local interference thickness, $t_i(s)$. In this way Equation (3.47) now becomes

$$\gamma^* = \frac{\int_{te+cf} K_p t_i(s)\,\gamma(s)\,ds}{\int_{te+cf} K_p t_i(s)\,ds} \tag{3.48}$$

Clearly with the aforementioned assumption, the pressure constant, K_p, will conveniently cancel out in the calculation of γ^* in Equation (3.48). In order to facilitate the description of the clearance angle as a function of position along the tool boundary a change of variables is used. Along the tool edge, ds becomes $r_e d\beta$, and along the clearance face ds becomes $\tilde{z}$, where the $\tilde{\mathbf{y}}$-$\tilde{\mathbf{z}}$ reference frame is inclined at an angle of γ from the $\hat{\mathbf{y}}$-$\hat{\mathbf{z}}$ reference frame, as shown in Figure 3-5B. With this change of variables, the effective clearance angle becomes

$$\gamma^* = \begin{cases} \dfrac{\overbrace{\int_{\beta_1}^{\beta_2} t_{i-te}(\beta)\left(\beta - \dfrac{3\pi}{2}\right) r_e d\beta}^{\text{tool edge}}}{\underbrace{\int_{\beta_1}^{\beta_2} t_{i-te}(\beta)\, r_e d\beta}_{\text{tool edge}}} & \hat{z}_2 < \hat{z}_{te-cf} \\ \dfrac{\overbrace{\int_{\beta_1}^{3\pi/2+\gamma} t_{i-te}(\beta)\left(\beta - \dfrac{3\pi}{2}\right) r_e d\beta}^{\text{tool edge}} + \overbrace{\int_0^{\tilde{z}_2} t_{i-cf}(\tilde{z})\,\gamma d\tilde{z}}^{\text{clearance face}}}{\underbrace{\int_{\beta_1}^{3\pi/2+\gamma} t_{i-te}(\beta)\, r_e d\beta}_{\text{tool edge}} + \underbrace{\int_0^{\tilde{z}_2} t_{i-cf}(\tilde{z})\, d\tilde{z}}_{\text{clearance face}}} & \text{otherwise} \end{cases} \tag{3.49}$$

and depends on whether $\hat{z}_2 < \hat{z}_{te-cf}$. If this is true then the integration is only performed along the tool's cutting edge and gives rise to a single integral in the numerator and denominator. Now $\gamma(s)$ along the cutting edge becomes $\beta - \frac{3\pi}{2}$, and $t_i(s)$ becomes $t_{i-te}(\beta)$, which is given by

$$t_{i-te}(\beta) = \begin{cases} r_e - \dfrac{1}{2a_2\cos^2[\beta]}\left(\sin[\beta] - a_1\cos[\beta] + \sqrt{\left(\sin[\beta] - a_1\cos[\beta]\right)^2 - 4a_0a_2\cos^2[\beta]}\right) & a_2 \neq 0 \\ r_e - \dfrac{a_0}{\sin[\beta] - a_1\cos[\beta]} & \text{otherwise} \end{cases} \tag{3.50}$$

where β_1 and β_2 are the limits on the integration and are related to the points of intersection between the undeformed workpiece surface and the boundary of the cutting tool, $\hat{z}_1$ and $\hat{z}_2$, by

$$\beta_1 = c_1\left(\hat{z}_1\right) \tag{3.51}$$

$$\beta_2 = c_1(\hat{z}_2) \tag{3.52}$$

where $c_1(\hat{z})$ is essentially a quadrant-conscious tan^{-1} function, defined as

$$c_1(\hat{z}) \equiv \begin{cases} \pi + \tan^{-1}\left[\dfrac{-\sqrt{r_e^2 - \hat{z}^2}}{\hat{z}}\right] & \hat{z} < 0 \\ 2\pi + \tan^{-1}\left[\dfrac{-\sqrt{r_e^2 - \hat{z}^2}}{\hat{z}}\right] & \text{otherwise} \end{cases}$$

If interference occurs along both sections of the cutting tool, i.e. $\hat{z}_2 \geq \hat{z}_{te-cf}$, then it is necessary to evaluate the integrals separately for each region. As previously mentioned, a $\tilde{\mathbf{y}}$ - $\tilde{\mathbf{z}}$ reference frame is employed in order to facilitate the integration along the clearance face. Because it is inclined at the same angle as the clearance angle, the integration is from 0 to $\tilde{z}_2$, where $\tilde{z}_2$ is related to $\hat{z}_2$ by

$$\tilde{z}_2 = \hat{z}_2 \cos[\gamma] + (m_t \hat{z}_2 + b_t)\sin[\gamma] \tag{3.53}$$

In order to operate in the $\tilde{\mathbf{y}}$ - $\tilde{\mathbf{z}}$ reference frame, the polynomial representing the workpiece surface in Equation (3.32), $\hat{y}_{sur}(\hat{z})$, must undergo a rotation transformation to become $\tilde{y}_{sur}(\tilde{z})$ in the $\tilde{\mathbf{y}}$ - $\tilde{\mathbf{z}}$ reference frame, the results of which are expressed by

$$\begin{aligned} \tilde{y}_{sur}(\tilde{z}) = \csc^2[\gamma]\big(&\cos[\gamma] + a_1 \sin[\gamma] + a_2 \tilde{z} \sin[2\gamma] - \\ &\sqrt{(a_1 \sin[\gamma] + \cos[\gamma])^2 + 4a_2\left(\tilde{z}\sin[\gamma] - a_0 \sin^2[\gamma]\right)}\big) \end{aligned} \tag{3.54}$$

and is valid for any value of a_2.

Regardless of the nature of the interference area, there will always be an integration performed along the tool edge in both the numerator and denominator of Equation (3.49). The limits on these integrals are from β_1 to $\frac{3\pi}{2} + \gamma$, where β_1 was given in Equation (3.51). These integrals have no closed-form solution for $a_2 \neq 0$, and for $a_2 = 0$ only the integral in the denominator has a closed from solution. In all cases for a_2, it is in fact computationally more efficient to numerically evaluate each integral in the numerator and denominator simultaneously in a

vectorized fashion since they have the same limits. In contrast, the integration performed along the clearance face has a closed-form solution and is given as

$$\int_0^{\tilde{z}_2} t_{i-cf}(\tilde{z})\,d\tilde{z} = \frac{1}{4}\left[4r_e\tilde{z} + \frac{2\tilde{z}^2}{\tan[\gamma]} + \frac{2\tilde{z}\left(\cos[\gamma] + a_1 \sin[\gamma]\right)}{a_2 \sin^2[\gamma]} - \frac{\left(1 + a_1^2 - 4a_0a_2 + \left(1 - a_1^2 + 4a_0a_2\right)\cos[2\gamma] + 8a_2\tilde{z}\sin[\gamma] + 2a_1\sin[2\gamma]\right)^{3/2}}{6\sqrt{2}a_2^2 \sin^3[\gamma]} \right]_0^{\tilde{z}_2} \tag{3.55}$$

for $a_2 \neq 0$, and for $a_2 = 0$ it is

$$\int_0^{\tilde{z}_2} t_{i-cf}(\tilde{z})\,d\tilde{z} = \frac{\tilde{z}_2\left(2a_0 + \cos[\gamma](2r_e + a_1\tilde{z}_2) + \sin[\gamma](2a_1r_e - \tilde{z}_2)\right)}{2\left(\cos[\gamma] + a_1\sin[\gamma]\right)} \tag{3.56}$$

where the lower limit in Equation (3.56) always gives a value of zero so therefore only $\tilde{z}_2$ appears above.

Equation (3.55) is the antiderivative of the integral in the denominator of Equation (3.49) along the clearance face. For the integral along the clearance face in the numerator, the result is the same as in Equation (3.55) except that it is multiplied by the clearance angle, γ, since the inclination of the interference thickness is constant in this region.

With the description of the interference area and the effective clearance angle complete, the equations for the forces per unit width of cut due to the interference between the cutting tool and the workpiece can be evaluated. As in Figure 3-4, the interference forces on the cutting tool, p'_C and p'_T are orthogonal and inclined at an angle of γ^* from the $\hat{\mathbf{y}}$ - $\hat{\mathbf{z}}$ and $\mathbf{T} - \mathbf{C}$ axes, and are given as

$$p'_C = \mu K_{cf} A_i \tag{3.57}$$

$$p'_T = K_{cf} A_i \tag{3.58}$$

Applying a rotation transformation, the interference forces in the thrust and cutting directions per unit width of cut are simply

$$p_C = -p'_T \sin[\gamma^*] + p'_C \cos[\gamma^*] = K_{cf} A_i \left(\mu \cos[\gamma^*] - \sin[\gamma^*]\right) \tag{3.59}$$

$$p_T = p'_T \cos[\gamma^*] + p'_C \sin[\gamma^*] = K_{cf} A_i \left(\cos[\gamma^*] + \mu \sin[\gamma^*]\right) \tag{3.60}$$

The final step in describing these forces is the recognition that for an orthogonal cutting scenario the width of cut is simply w. Therefore the forces due to plowing and flank interference between the cutting tool and the workpiece are the product of Equations (3.59) and (3.60) with w, and are given as

$$P_T = w p_T \tag{3.61}$$

$$P_C = w p_C \tag{3.62}$$

In order to keep the solution in the simplified cutting force model in closed-form, γ^* is taken to be 0° since for stable cutting with γ usually having a value of about 10°, it is a good approximation for the very low levels of vibration present before chatter materializes. Therefore, it shouldn't significantly limit this approach's ability to predict the onset of chatter, which is the most important output of a chatter simulation. Later in the development of the refined cutting force model in Chapter 6, γ^* is found numerically and thereby permitted to vary with time during a simulation.

To illustrate the effect of tool vibration on the interference area, consider Figure 3-6. In Figure 3-6A, a sinusoidal displacement applied to the cutting tool in the thrust direction is shown with interference areas at certain points in time given in Figure 3-6B-I. As one would intuitively expect, when the relative motion of the tool is towards the workpiece, e.g. points C, D, and E in Figure 3-6A, the interference area is the largest and γ^* is positive. Conversely, when the tool is moving away relative to the workpiece, e.g. points F, G, and H in Figure 3-6A, the interference area becomes smaller and γ^* is negative. At points B and I, the rate of change of the RTWD is approximately zero. This causes the interference area to be similar to that during zero vibration cutting and γ^* to be close to zero.

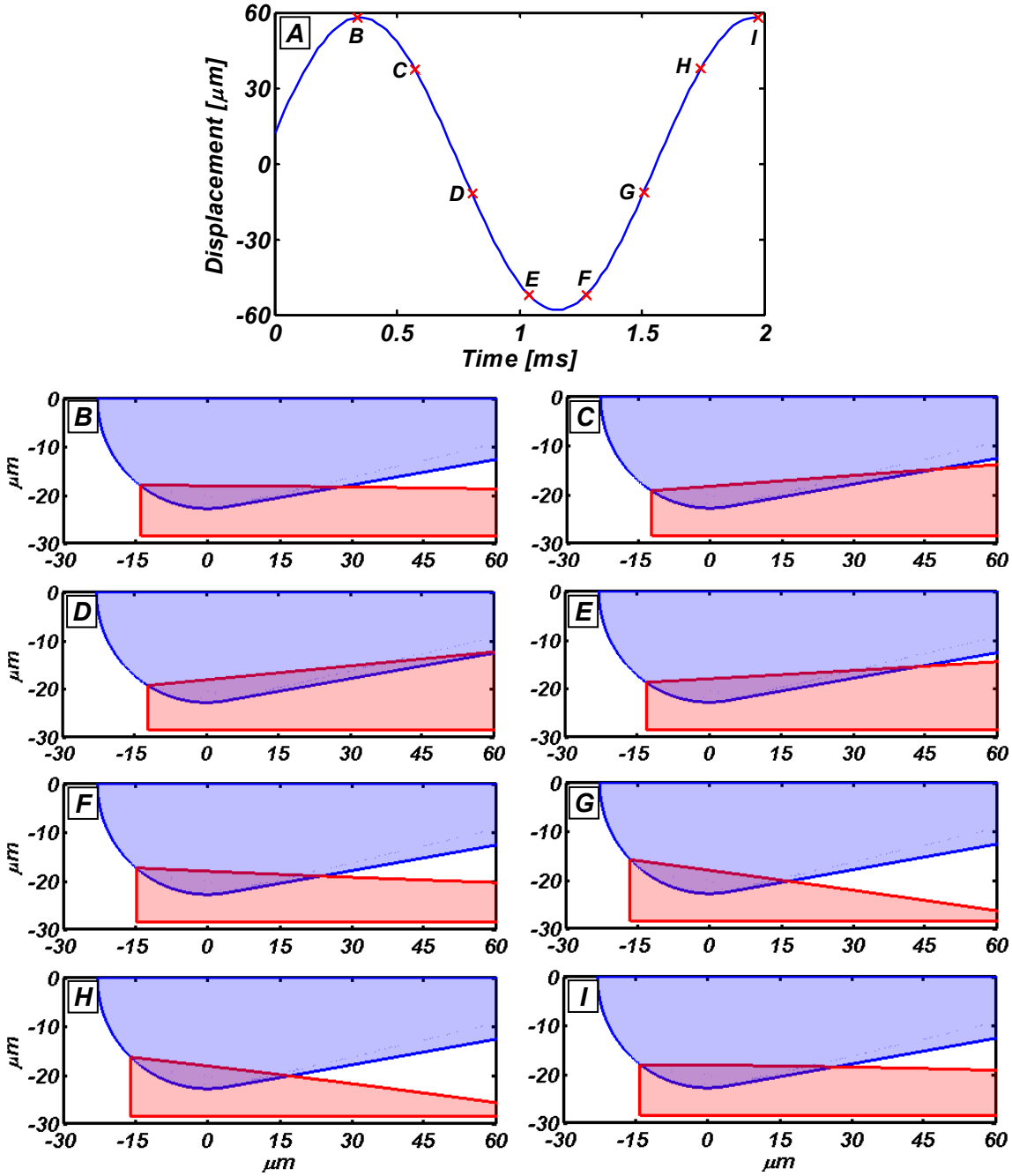

Figure 3-6: The change in the interference area when the tool is vibrating in the thrust direction (positive displacement is oriented away from the workpiece). The cutting tool is shaded in blue and the undeformed machined workpiece surface is shaded in red. (A), A sinusoidal RTWD in the thrust direction; (B)-(I), the interference area at points in time denoted in (A), e.g. the interference area in (E) occurs at the time where point E is located in (A).

CHAPTER 4: THE SIMPLIFIED DYNAMIC CUTTING FORCE MODEL

"The important thing in science is not so much to obtain new facts as to discover new ways of thinking about them."

–William Lawrence Bragg

4.1 Modified Tool Angles and the Development of an Equivalent Straight Edge Cutting Tool

In the previous chapter, models in the orthogonal cutting domain were presented that can describe forces due to chip formation as well as plowing and interference between the machined workpiece surface and the cutting tool. Both are two-dimensional models and therefore are not immediately applicable to the three-dimensional turning scenarios normally encountered in practice. This chapter will introduce the "simplified dynamic cutting force model," which makes careful approximations to the three-dimensional nature of the cutting zone in order to generate equivalent cutting scenarios that can be modeled by the orthogonal models developed in Chapter 3. For fast computational time, care is taken to develop a formulation for the dynamic cutting forces in the simplified cutting force model that can be solved in closed-form. Later in Chapter 6, a "refined cutting force model" is developed that is more computationally intensive and describes the cutting process in a more geometrically rigorous manner.

As previously mentioned, metal cutting scenarios used in practice typically rely on a tool whose cutting edge is curved and in a plane that is not coincident with the axis of the workpiece, like that pictured in Figure 1-1. Collectively these two properties are known as oblique nose radius machining. Oblique machining with a nose radius is a three-dimensional process. Plastic flow problems of this dimension are extremely complicated and generally lack closed-form solutions. Typically to solve problems of such a scale FEA techniques are employed. However, the large computation time associated with this approach disqualifies it as an option because millions of cutting conditions need to be evaluated over the course of a single turning simulation. Fortunately there are methods that predict forces by using a transformation to obtain an equivalent oblique straight cutting edge process, invoking some assumptions to make the process orthogonal, predicting

forces in the orthogonal cutting domain, and then transforming those forces back into the oblique cutting domain [52]. The cutting tool geometry shown in Figure 4-1 will be used to illustrate this procedure.

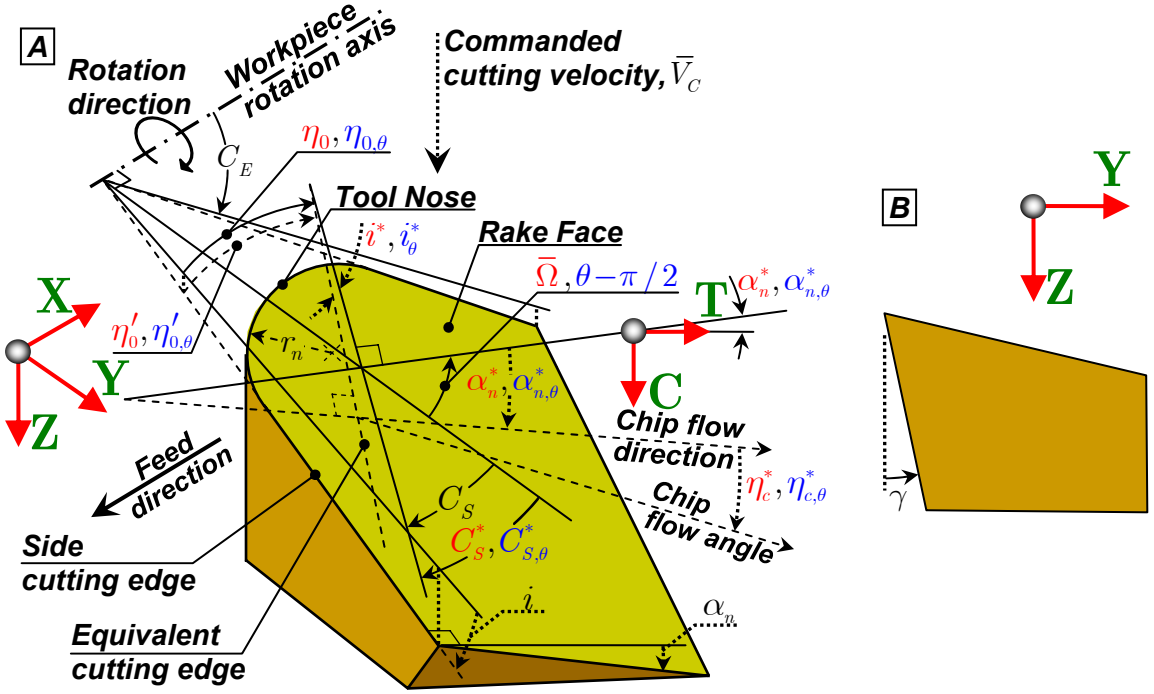

Figure 4-1: An oblique nose radius cutting tool with input tool geometry shown in **black**, equivalent tool geometry for the simplified cutting force model shown in **red**, and equivalent tool geometry for the refined cutting force model shown in **blue**. Solid (—) and dash-dotted lines (– · –) lie in the **X - Y** plane; dashed lines (– – –) lie in a plane defined by the tool rake face; dotted lines (···) lie in a plane parallel to the **Z** axis. (A) Isometric view; (B) planar view showing the location where the clearance angle is measured.

The given values of the tool geometry in Figure 4-1 are the inclination angle, i, rake angle, α_n, clearance angle, γ, side cutting edge angle, C_S, end cutting edge angle, C_E, and the tool nose radius, r_n. There are two types of geometric factors that affect the transformation into a roughly equivalent orthogonal cutting representation: the angles associated with the tool orientation and a single angle associated with the size and orientation of the undeformed chip area. The latter of the two is termed the angle of the chip flow direction, $\bar{\Omega}$. This angle is measured from the **Y** axis in the counter-clockwise direction about the **Z** axis and locates the direction that the chip exits the cutting zone. $\bar{\Omega}$ is influenced by the tool nose radius, feed, depth of cut, and RTWDs in the regenerative position space. The method for finding $\bar{\Omega}$ will be introduced in the next section and is required to

determine the rest of the angles in Figure 4-1. Much of the following analysis involves deriving an effective quantity in the straight cutting edge domain, g^*, based on an original quantity in the tool nose radius cutting domain, g. As for the diagrams associated with the interference force model in the previous section, in Figure 4-1 input tool geometry has been color coded in black, equivalent tool geometry for the simplified dynamic cutting force model in red, and equivalent tool geometry for the yet-to-be introduced refined cutting force model in blue.

The angle of the chip flow direction can also be measured relative to a normal vector to the straight side cutting edge, and is given as

$$\eta_0 = \frac{\pi}{2} - C_S - \overline{\Omega} \tag{4.1}$$

The projection of η_0 on the tool rake face, η_0', is given as

$$\eta_0' = \cos^{-1}\left[\frac{\cot[\eta_0] - \tan[\alpha_n]\sin[i]}{\sqrt{\left(\cot[\eta_0]\sin[i] - \tan[\alpha_n]\right)^2 + \left(\csc[\eta_0]\cos[i]\right)^2}}\right] \tag{4.2}$$

and the remaining effective straight cutting edge geometry can be shown to be

$$C_S^* = C_S + \eta_0 \tag{4.3}$$

$$i^* = \sin^{-1}\left[\cos\left[\eta_0'\right]\sin[i] - \sin\left[\eta_0'\right]\sin[\alpha_n]\cos[i]\right] \tag{4.4}$$

$$\alpha_n^* = \sin^{-1}\left[\frac{\sin[i] - \sin[i^*]\cos\left[\eta_0'\right]}{\sin\left[\eta_0'\right]\cos[i^*]}\right] \tag{4.5}$$

The chip flow angle, η_c^*, is given as

$$\eta_c^* = i^* \tag{4.6}$$

Equation (4.6) is known as Stabler's flow rule and is derived from the experimental observation that the chip flow angle, η_c^*, which is measured from a normal vector to the equivalent cutting edge in the rake face plane is approximately equal to the effective inclination angle, i^* [53]. Equations (4.1)-(4.6) are a well-accepted approach in the machining research community to describe machining with a tool nose radius by deriving equivalent parameters [52].

With these angular transformations, the oblique nose radius cutting configuration in Figure 4-1 has been transformed to the equivalent oblique straight cutting edge configuration in Figure 4-2. It should be noted that the same convention for line styles in Figure 4-2 is used as in Figure 4-1. In Figure 4-2A and B, the translucent tool is the relative position of the cutting tool one workpiece revolution period back in time, and the opaque tool is its current position. Additionally the effective width of cut, w^*, and effective undeformed chip thickness, t_u^*, are shown and will be derived in a later section.

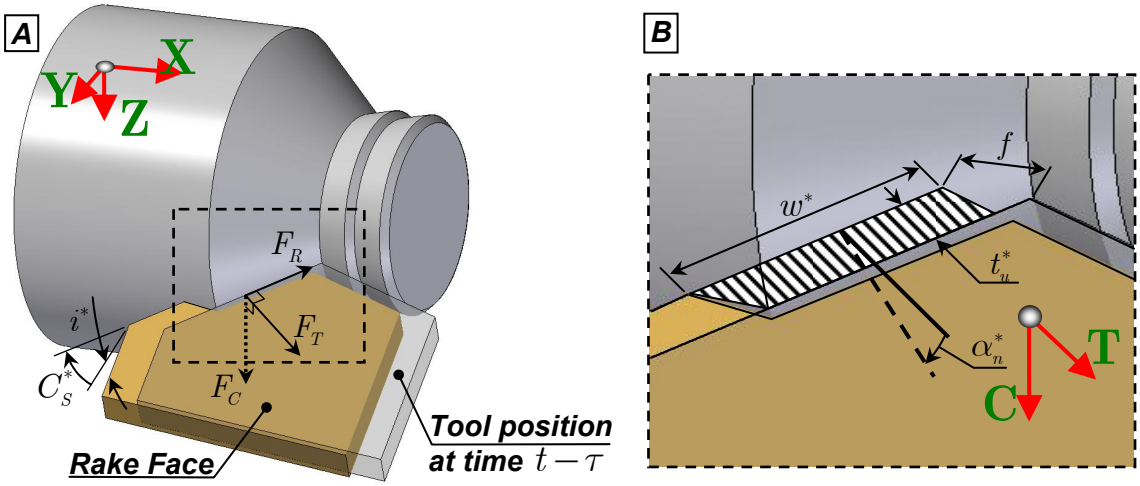

Figure 4-2: An equivalent straight cutting edge representation annotated with relevant forces and angles. (A), An oblique straight cutting edge process; (B), a close-up view of the undeformed chip area.

In the case of static cutting, the forces due to chip formation, F_C and F_T in Figure 4-2, can be determined directly from the aforementioned Oxley orthogonal cutting force model using the parameters α_n^* for α_n, t_u^* for t_u, and w^* for w. It has been shown that these forces are nearly independent of i^* [54]. In the case of dynamic cutting, where there can be relative tool velocity in the radial (**Y**) or tangential (**Z**) cutting directions, another transformation is needed in order to find F_C and F_T, as will be outlined in the next section. Also needed in the case of dynamic cutting is the effective cutting velocity, V_C^*, which will be used in place of $\left|\vec{V}_C\right|$ in previous developments. t_u^*, w^*, and V_C^* will all be derived in the next section, along with the angle of the chip flow direction, $\bar{\Omega}$, for the general case where there is relative tool-workpiece vibration.

The force perpendicular to F_C and F_T, F_R, which results from a nonzero inclination angle is found using the following equation regardless of whether there is relative tool vibration or not:

$$F_R = \frac{F_C\left(\sin[i^*] - \cos[i^*]\sin[\alpha_n^*]\tan[\eta_c^*]\right) - F_T\cos[\alpha_n^*]\tan[\eta_c^*]}{\sin[i^*]\sin[\alpha_n^*]\tan[\eta_c^*] + \cos[i^*]} \tag{4.7}$$

Once F_C, F_T, and F_R are determined, the forces due to chip formation on the cutting tool in the **Y** and **Z** directions, F_Y and F_Z, respectively, for the simplified cutting force model are given as

$$F_Y = F_T\sin[C_S^*] - F_R\cos[C_S^*] \tag{4.8}$$

$$F_Z = F_C \tag{4.9}$$

4.2 Consideration of Tool Nose Radius and Vibration Effects

4.2.1 Influence of the relative tool-workpiece displacement and tool nose radius on the chip flow direction

It is a well-known fact that the tool nose radius plays an important role in chatter stability [55]. Therefore, any physics-based chatter model must capture this effect. In Figure 4-3 is a model that will be used to derive the angle of the chip flow direction, $\bar{\Omega}$, which will follow a similar philosophy as the commonly accepted method in [35] for zero vibration cutting force modeling. The effective width of cut and undeformed chip thickness, w^* and t_u^*, respectively, will also be derived.

Figure 4-3 depicts the RTWD of the nose of the cutting tool relative to the workpiece, y, at four times in the regenerative delay space: t, $t-\tau$, $t-2\tau$, and $t-3\tau$. However, the generic paradigm in which this approach is formulated allows for an arbitrary number of relative tool-workpiece positions to be considered in the regenerative position space. In Figure 4-3, a $\overline{\mathbf{X}}\overline{\mathbf{Y}}\overline{\mathbf{Z}}$ reference frame is used, which differs from the **XYZ** reference frame introduced earlier in Figure 4-1. The **XYZ** reference frame moves with the cutting tool, always having its origin located at the center of curvature of the tool nose radius. On the other hand, the $\overline{\mathbf{X}}\overline{\mathbf{Y}}\overline{\mathbf{Z}}$ reference frame only tracks the tool in the feed ($\overline{\mathbf{X}}$) direction. If there is any relative vibration present, such as in Figure 4-3, the origin of $\overline{\mathbf{X}}\overline{\mathbf{Y}}\overline{\mathbf{Z}}$ will not generally coincide with that of **XYZ**. However, based on the fact that the **XYZ** and $\overline{\mathbf{X}}\overline{\mathbf{Y}}\overline{\mathbf{Z}}$ reference frames are parallel to one another, and the fact that relative

displacements between the cutting tool are used, $y(t)$ and $z(t)$ can be used in either reference frame interchangeably. The current and previous RTWDs in the regenerative position space are represented by small shaded circles, each coinciding with the center of curvature of a tool nose radius at a time in the regenerative delay space. Due to the constant feed per revolution of the workpiece, f, assumed throughout this investigation each tool position is spaced by a distance of f in the $\overline{\mathbf{X}}$ direction. For future developments, let the free boundary of the undeformed chip area be given as the portion that is not defined by the position of the tool nose radius at the current time, $y(t)$.

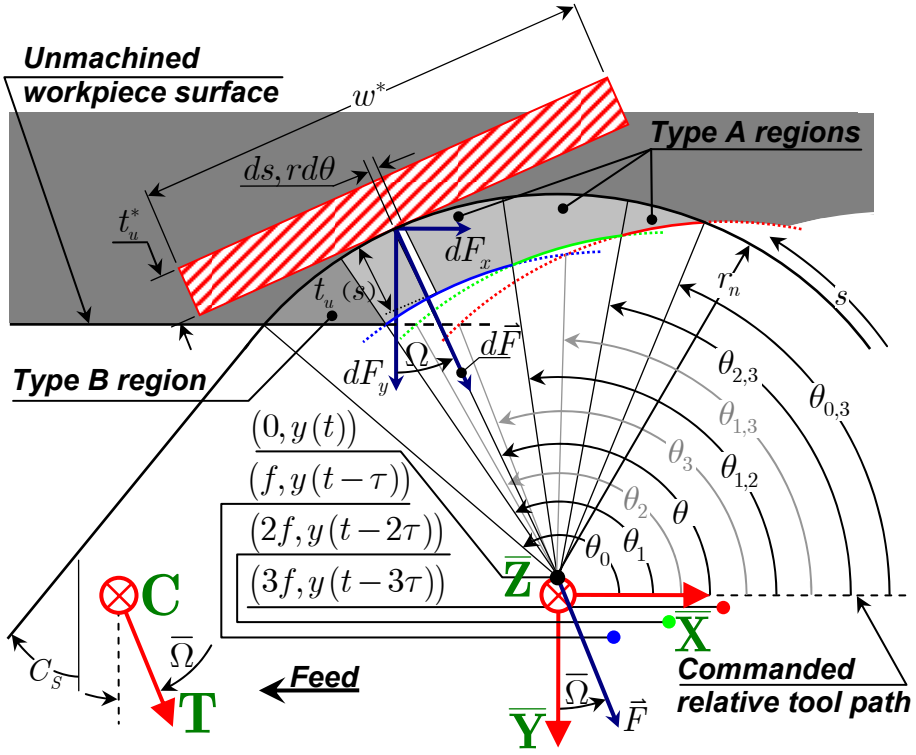

Figure 4-3: A schematic showing the relationship between all the angles of intersection between tool nose radii in the regenerative position space, the angle of the chip flow direction, $\overline{\Omega}$, the effective width of cut, w^*, and the equivalent undeformed chip thickness, t_u^*. The angles of intersection irrelevant to the description of the undeformed chip area are shown in grey and all relevant angles are shown in **black**.

Before presenting the constitutive equations needed to find the angle of the chip flow direction, a 3D visualization is presented in Figure 4-4 that shows how the regenerative position space can influence the undeformed chip area over time. This was generated in CAD software and not dictated by an actual computer simulation of chatter. The cutting tool is not pictured in order for the undeformed chip area (shaded in dark red) and the machined surface topography to be seen

more clearly. Figure 4-4A-F are ordered in time as machining progresses with Figure 4-4A occurring at the earliest time. It can be seen that the influence from a given tool position in the regenerative position space is intermittent as cutting progresses, which is contrary to approaches that consider influence from a RTWD in the regenerative position space to be persistent in time, e.g. in Equation (2.21).

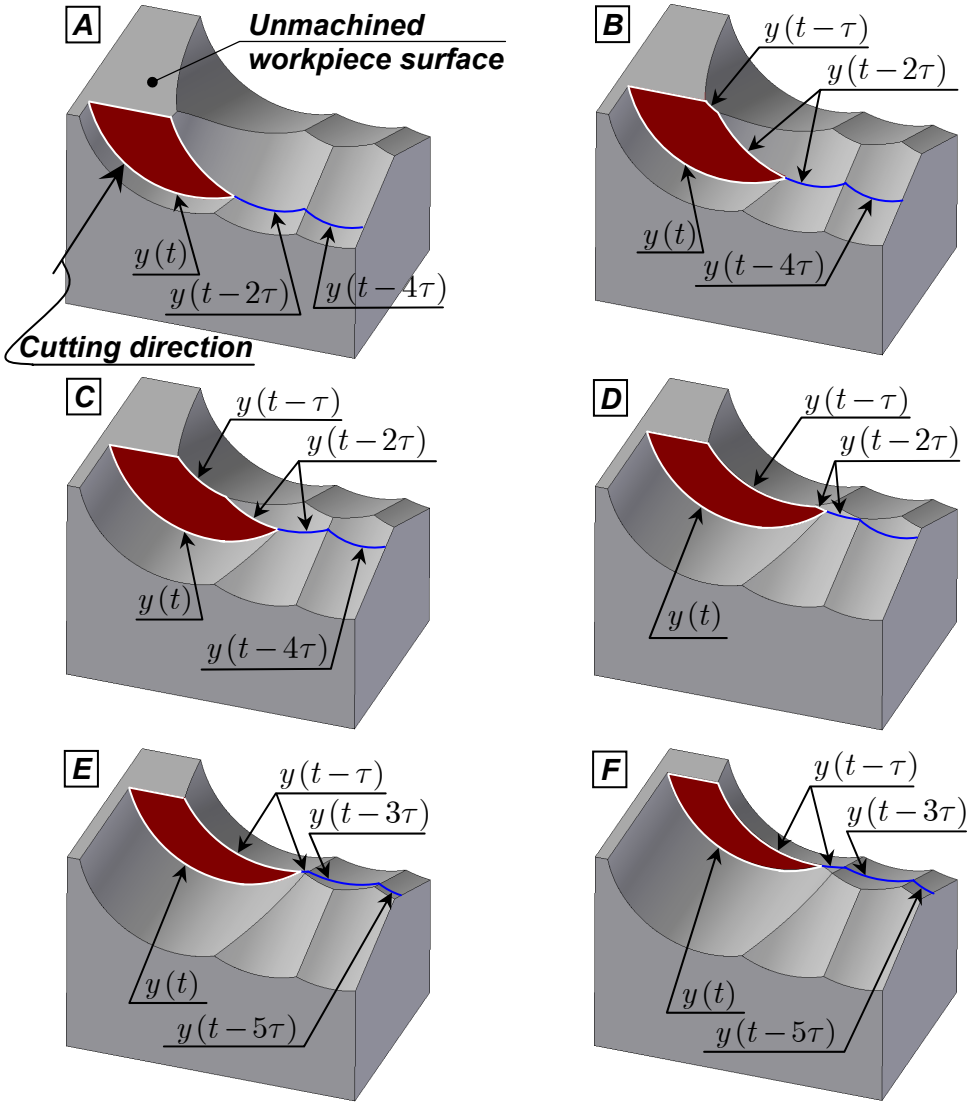

Figure 4-4: A demonstration showing how RTWDs in the regenerative position space can influence the undeformed chip area in an intermittent fashion as cutting progresses in time. (A) Influence from the RTWD $y(t-2\tau)$; (B) Influence from the RTWDs $y(t-\tau)$ and $y(t-2\tau)$; (C) Influence from the RTWDs $y(t-\tau)$ and $y(t-2\tau)$; (D) Influence from the RTWDs $y(t-\tau)$ and $y(t-2\tau)$; (E) Influence from the RTWD $y(t-\tau)$; (F) Influence from the RTWD $y(t-\tau)$.

The boundary of the undeformed chip area defined by the current and previous tool positions in the regenerative position space is denoted by solid white lines. The blue lines indicate portions of previous tool positions in the regenerative position space that do not influence the free boundary of the undeformed chip area. All of these lines exist in the same plane, and would be present in a 2D view like that pictured in Figure 4-3. Just as in Figure 4-3, a tool nose radius at a relative tool position in the regenerative position space can have a portion of it that influences the current undeformed chip area and part of it that does not, e.g. $y(t-2\tau)$ in Figure 4-4A. As long as cutting is taking place, there is always influence from $y(t)$. Additionally, as time progresses there can be intermittent influence from a RTWD in the regenerative position space. For instance, the RTWD $y(t-2\tau)$ defines a free boundary of the undeformed chip area in Figure 4-4A-D but not in Figure 4-4E and F.

Returning now to Figure 4-3, it should be noted that there are more angles shown than are needed to find $\overline{\Omega}$ because of the possibility that the undeformed chip area could be influenced by multiple previous RTWDs in the regenerative position space in an intermittent fashion as cutting progresses in time (this was just made evident in Figure 4-4). This differs from the case of quasi-static cutting force modeling with assumed zero vibration where the cutting region is only influenced by tool positions at t and $t-\tau$ in a consistent way for all time. For this analysis, all angles are depicted in their positive senses, measured counterclockwise from the positive $\overline{\mathbf{X}}$ axis. The convention used in this investigation is that θ_W is the angle of intersection between a line coincident with the undeformed workpiece surface in the $\mathbf{XY}$ plane and the tool position at $y(t-W\tau)$ where

$$0 \le W \le D,\ \mathrm{W} \in \mathbb{Z} \tag{4.10}$$

and $\theta_{M,N}$ is the intersection between tool nose radii at positions $y(t-M\tau)$ and $y(t-N\tau)$, where

$$0 \le M \le D,\ M \in \mathbb{Z} \tag{4.11}$$

$$0 \le N \le D,\ N \in \mathbb{Z} \tag{4.12}$$

and as previously mentioned, D is the number of delays to consider in the regenerative delay space.

Referring to Figure 4-3, assuming that the friction force on the undeformed chip area varies linearly with the local undeformed chip thickness [56], and temporarily assuming α_n and i to be zero [35], the friction force per unit of elemental undeformed chip area is a constant, u. The magnitude of that friction force acting over an area, dA, is given as

$$\left|d\vec{F}\right| = udA = ut_u(s)\,ds \tag{4.13}$$

where ds is the differential chip width, and $t_u(s)$ is the local undeformed chip thickness. The net force on the entire undeformed chip area in Cartesian coordinates is therefore

$$\vec{F} = \left(u\int \sin[\Omega]\,dA\right)\vec{\mathbf{i}} + \left(u\int \cos[\Omega]\,dA\right)\vec{\mathbf{j}} \tag{4.14}$$

where the angle that $\left|d\vec{F}\right|$ makes with the positive $\overline{\mathbf{Y}}$ axis, Ω, is described by

$$\Omega(s) = \theta(s) - \frac{\pi}{2} \tag{4.15}$$

The velocity with which the chip exits the cutting zone is assumed to be coincident with the net force exerted upon it, which is located in the $\overline{\mathbf{X}}\overline{\mathbf{Y}}$ plane at an angle of $\bar{\Omega}$ from the positive $\overline{\mathbf{Y}}$ axis (keeping with convention in the literature), and is given by

$$\bar{\Omega} = \tan^{-1}\left[\frac{\vec{F}\cdot\vec{\mathbf{i}}}{\vec{F}\cdot\vec{\mathbf{j}}}\right] = \tan^{-1}\left[\frac{\int \sin[\Omega]\,dA}{\int \cos[\Omega]\,dA}\right] \tag{4.16}$$

It should be noted that the friction force per unit of elemental chip area, u, has conveniently cancelled in Equation (4.16).

There are two types of cutting areas whose contributions need to be addressed by different formulae: those that have free boundary defined by the unmachined workpiece surface (type B regions) and those that do not (type A regions). Each region is defined by a portion of the undeformed chip area that has a smooth free boundary. For example, as annotated in Figure 4-3, the undeformed chip area is comprised of three type A regions and one type B region. Substituting $rt(\theta)\,d\theta$ for dA, Equation (4.16) may be expressed as contributions from potentially multiple type A regions and a single type B region, given as

$$\bar{\Omega} = \tan^{-1}\left[\frac{\overbrace{\sum_{A}\left[\int \sin\left[\Omega t_{u,A}(\theta)\right]d\theta\right]}^{\text{Type A Region(s)}} + \overbrace{\int_{B} \sin\left[\Omega t_{u,B}(\theta)\right]d\theta}^{\text{Type B Region}}}{\underbrace{\sum_{A}\left[\int \cos\left[\Omega t_{u,A}(\theta)\right]d\theta\right]}_{\text{Type A Region(s)}} + \underbrace{\int_{B} \cos\left[\Omega t_{u,B}(\theta)\right]d\theta}_{\text{Type B Region}}}\right] \tag{4.17}$$

where $t_{u,A}(\theta)$ and $t_{u,B}(\theta)$ denote the undeformed chip thickness in a type A or B region, respectively, and $\sum_{A}$ means to sum over the number of type A regions, and $\int_{B}$ means to integrate over the range of angles in a type B region. In order to perform the integrations in Equation (4.17) two types of information must be determined: the undeformed chip thickness variation, $t_{u,A}(\theta)$ and $t_{u,B}(\theta)$, and the angles of intersection between all the current and previous tool nose radii in the regenerative position space (although not all of the angles of intersection will be pertinent).

Consider the intersection of a line and three circular arcs, which represent the unmachined workpiece surface, the position of the center of curvature of the tool nose at its current position in time, $(0, y(t))$, one previous one located at $(x_1, y_1) = (Mf, y(t - M\tau))$, and another previous one located at $(x_2, y_2) = (Nf, y(t - N\tau))$, as shown in Figure 4-5. The same $\bar{\mathbf{X}}\bar{\mathbf{Y}}\bar{\mathbf{Z}}$ reference frame in Figure 4-3 is used in Figure 4-5, thereby making its origin a distance of $-y(t)$ in the $\bar{\mathbf{Y}}$ direction from the current tool position, $(0, y(t))$.

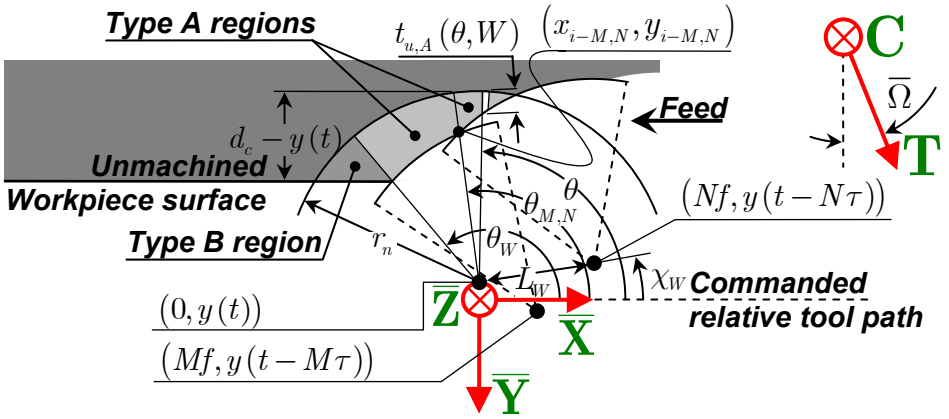

Figure 4-5: The geometry used to find all the angles of intersection and the undeformed chip thickness variation, $t_{u,A}(\theta, W)$ and $t_{u,B}(\theta)$.

The undeformed chip thickness in a type A region, $t_{u,A}(\theta)$, depends not only on θ, but also on which RTWD in the regenerative position space is defining the free boundary of the undeformed chip area at that particular value of θ. Owing to this, $t_{u,A}(\theta)$ becomes $t_{u,A}(\theta,W)$ to reflect dependence on the W^{th} previous relative tool position in the regenerative position space, and can be expressed as

$$t_{u,A}(\theta,W) = r_n - \sqrt{L_W}\cos[\theta-\chi_W] - \sqrt{r_n^2 - L_W\sin^2[\theta-\chi_W]} \tag{4.18}$$

where

$$\chi_W = \tan^{-1}\left[\frac{y(t)-y(t-W\tau)}{Wf}\right] \tag{4.19}$$

$$L_W = (Wf)^2 + [y(t)-y(t-W\tau)]^2 \tag{4.20}$$

The subscript W is used for conciseness and denotes a dependence on W, where W corresponds to the W^{th} previous tool nose position in the regenerative position space that defines the free boundary of a type A region (e.g. $t_{u,A}(\theta,2)$, L_2 and χ_2 are associated with the tool position at time, $t-2\tau$, in a type A region). It should be noted that the evaluation of $t_{u,A}(\theta,W)$ will be inaccurate if W corresponds to a RTWD that does not define the undeformed chip area or the value of θ is incorrect for the particular value of W. It could even potentially take on negative or imaginary values, which clearly is nonsensical. For example in Figure 4-3, in the range $\theta_{2,3} < \theta < \theta_{1,2}$, it would be incorrect to use $t_{u,A}(\theta,1)$ or $t_{u,A}(\theta,3)$ since in that angular range the boundary of the undeformed chip area is defined by the tool position at time $t-2\tau$ and hence $t_{u,A}(\theta,2)$ is to be used in this range of angles. The undeformed chip thickness in a type B region can be shown to be

$$t_B(\theta) = r_n - \frac{r_n + y(t) - d_c}{\sin[\theta]} \tag{4.21}$$

where d_c is the nominal depth of cut. Just like $t_{u,A}(\theta,W)$, $t_{u,B}(\theta)$ must be defined over a valid range of angles in order to make physical sense. However unlike $t_{u,A}(\theta,W)$, it only depends on θ since its free boundary is always the unmachined workpiece surface. As an aside, this work has been

careful in distinguishing the nominal depth of cut from the undeformed chip thickness since in nose radius machining they are two different quantities. This is true even when there is no relative tool-workpiece vibration, as suggested by Equation (4.21).

In order to find all the angles of intersection between the tool nose radii with centers of curvature at positions in the regenerative position space, $\theta_{M,N}$, the Cartesian coordinates of intersection between them, $\left(x_{i-M,N}, y_{i-M,N}\right)$, must be found first. The unknown coordinate of intersection, $x_{i-M,N}$, between the M^{th} and N^{th} previous tool nose positions is

$$x_{i-M,N} = \begin{cases} \frac{1}{2}\left(f(M+N) - \Delta_{y-M,N}\sqrt{\frac{4r_n^2}{\Delta_{x-M,N}^2 + \Delta_{y-M,N}^2} - 1} \right) & \Delta_{y-M,N} > 0 \\ \frac{1}{2}\left(f(M+N) + \Delta_{y-M,N}\sqrt{\frac{4r_n^2}{\Delta_{x-M,N}^2 + \Delta_{y-M,N}^2} - 1} \right) & \text{otherwise} \end{cases} \tag{4.22}$$

where

$$\Delta_{x-M,N} \triangleq Mf - Nf$$

$$\Delta_{y-M,N} \triangleq y(t - M\tau) - y(t - N\tau)$$

Once $x_{i-M,N}$ is found, $y_{i-M,N}$ is simply

$$y_{i-M,N} = -\sqrt{r_n^2 - \left(x_{i-M,N} - Mf\right)^2} + y(t - M\tau) \tag{4.23}$$

Finally, the angle of the intersection between the M^{th} and N^{th} previous tool nose radii is found to be:

$$\theta_{M,N} = \begin{cases} \tan^{-1}\left[\frac{y(t) - y_{i-M,N}}{x_{i-M,N}}\right] & x_{i-M,N} \geq 0 : M \neq N \\ \pi + \tan^{-1}\left[\frac{y(t) - y_{i-M,N}}{x_{i-M,N}}\right] & x_{i-M,N} < 0 : M \neq N \end{cases} \tag{4.24}$$

Equation (4.24) is solved for all previously discussed combinations of M and N, where $M \neq N$, and by the symmetry of the problem $\theta_{M,N} = \theta_{N,M}$. Next, the intersection between the W^{th} previous

tool nose radius and a line coincident with the unmachined workpiece surface in the **XY** plane, θ_W, is located at an angle of

$$\theta_W = \begin{cases} \pi - \tan^{-1}\left[\dfrac{r_n + y(t) - d_c}{c_{2,W}}\right] & c_{2,W} \geq 0 \\ -\tan^{-1}\left[\dfrac{r_n + y(t) - d_c}{c_{2,W}}\right] & c_{2,W} < 0 \end{cases} \tag{4.25}$$

where

$$c_{2,W} \triangleq \sqrt{\left(d_c - y(t - W\tau)\right)\left(2r_n + y(t - W\tau) - d_c\right)} - Wf$$

If any values of θ_W are imaginary it means that the cutting tool has moved so far relative to the workpiece in the **Y** direction that the tip did not cross the level of the unmachined workpiece surface at time $t - W\tau$. For future developments, these imaginary angles should be set equal to zero in computer code implementation for the purpose of using an algorithm that will determine the angles of intersection relevant to the undeformed chip area. If there are large amounts of vibration during the simulation the tool can momentarily lose contact with the workpiece, and the cutting forces will go to zero. To check if cutting is taking place, the following inequality is evaluated

$$\theta_0 > \theta_T, \quad \forall T \in \mathbb{Z} \text{ and } 1 \leq T \leq D \tag{4.26}$$

If the inequality if true for all values of T then cutting is taking place. The inequality is checking whether any of the angular intersections between tool nose positions at times in the regenerative delay space and the level of the unmachined workpiece surface are greater than the one at the current time, θ_0. If this is true, then cutting is not taking place.

4.2.2 An algorithm to determine the relevant angles of intersection pertaining to the undeformed chip area

As previously mentioned, there are many more angles of intersection calculated by Equations (4.24) and (4.25) than are needed to define the undeformed chip area. Owing to this, an algorithm will now be presented which will find which of these angles are relevant. First a $(D+1)\times(D+1)$ real symmetric matrix, Ang, that stores all angles of intersection is constructed as

$$Ang = \begin{bmatrix} \theta_0 & \theta_{1,0} & \cdots & \theta_{D,0} \\ \theta_{0,1} & \ddots & & \theta_{D,1} \\ \vdots & & \ddots & \vdots \\ \theta_{0,D} & \theta_{1,D} & \cdots & \theta_D \end{bmatrix}_{(D+1)\times(D+1)} \tag{4.27}$$

where the diagonal terms come from Equation (4.25) by considering all values of W defined in Equation (4.10) and the off-diagonal terms are symmetric and come from Equation (4.24) by considering all combinations of M and N, defined in Equations (4.11) and (4.12). Not counting the entries along the diagonal, the $(S+1)^{\text{th}}$ row of Ang corresponds to the angles of intersection between the tool position at time $t - S\tau$ and all other tool positions (and likewise for the $(S+1)^{\text{th}}$ column due to the fact that Ang is symmetric). A term along the diagonal, located at either the $(S+1)^{\text{th}}$ row or column, is the intersection between a line coincident with the unmachined workpiece surface in the **XY** plane and the tool position at time $t - S\tau$.

With the matrix Ang constructed, the algorithm shown in Figure 4-6 can be implemented in order to find the angles of intersection relevant to the undeformed chip area. This approach is valid when the inequality in Equation (4.26) is satisfied. First a positive integer, L, is chosen in the range $2 \le L \le (D+1)$ such that $Ang(L,L)$ is as large as possible. This integer corresponds to the previous tool position whose intersection with the free workpiece surface is relevant to the description of the undeformed chip area (e.g. in Figure 4-3 L would equal 2). Next a $2\times(D+1)$ matrix, Ind, is created in order to store matrix indices corresponding to angles in Ang that are relevant to the undeformed chip area. The indices are arranged such that their corresponding angles are in order, with the index of the largest angle stored in the first column, and that corresponding to the smallest angle stored in the last column. At most there can be $D+1$ relevant angles of intersection for the undeformed chip area, and at the least there will be two (e.g. in quasi-static cutting force modeling, where the relevant angles are always θ_1 and $\theta_{1,0}$). The first column is assigned the value of $[L \quad L]^T$ indicating that $Ang(L,L)$ is the first and largest angle relevant to the undeformed chip area, where

$[\cdot]^T$ denotes the transpose of a matrix. The convention of storing indices in Ind is best explained by the following example:

$$Ind = \begin{bmatrix} 2 & 2 & 3 & 4 \\ 2 & 3 & 4 & 1 \end{bmatrix} \rightarrow \begin{bmatrix} \theta_1 & \theta_{1,2} & \theta_{2,3} & \theta_{3,0} \end{bmatrix}_{1\times Q}$$

where the "$\rightarrow$" means that the indices in the first matrix imply the angles listed in the second.

In this example, the values in Ind correspond to the vibration history depicted in Figure 4-3. The largest relevant angle to the undeformed chip area is θ_1 (besides θ_0, which is *always* relevant as long as there is cutting), and hence the first column is $[2 \;\; 2]^T$. The chip area is then defined by the tool position at $t-\tau$ until it intersects the previous tool boundary at time $t-2\tau$; hence the next column entry in Ind is $[2 \;\; 3]^T$. Next, the chip area is defined by the tool boundary at time $t-2\tau$ until it intersects the previous tool boundary at time $t-3\tau$, reflected by the column entry of $[3 \;\; 4]^T$ in Ind. Finally, the chip area is defined by the tool position at time $t-3\tau$ until it intersects the tool position at the current time, t, which explains the final entry of $[4 \;\; 1]^T$ in Ind.

A pattern now emerges, as indicated by each identical pair of numbers enclosed in dotted lines. The indices for the second column have to correspond to an angle of intersection that lies along the tool boundary at time $t-\tau$, since the indices in the first column correspond to an intersection between the free workpiece surface and the tool position time $t-\tau$. Therefore, a search is conducted along the 2nd row of Ang for the next relevant angle, and this explains why the "2" is carried from entry $(2,1)$ to entry $(1,2)$ in Ind (indicated by the arrow). Likewise when the indices in the third column are being found, they must correspond to an angle in Ang that lies along the tool boundary at time $t-2\tau$ since the last relevant angle of intersection was between a tool position at time $t-\tau$ and time $t-2\tau$. This explains why the "3" is carried from entry $(2,2)$ to entry $(1,3)$ in Ind. A similar argument holds for the "4" being carried from entry $(2,3)$ to entry $(1,4)$ as well.

Returning to the flowchart in Figure 4-6, the final step of the initialization process, shown in the first block, consists of assigning a counter variable, p, with the value of 2. p corresponds to the

column number of Ind for which index values are currently being solved. Since the first column was already assigned values of $[L \quad L]^T$, it starts by referencing the second column of Ind. Next, the algorithm enters the outer loop by first guessing the p^{th} column of Ind and assigning it the value of $\left[Ind(2,p-1) \quad 1\right]^T$. The first entry in this column, $Ind(2,p-1)$, is due to the observation in the previous example that the number in the first row of every pair of indices in all columns > 2 of Ind corresponds to the number in the second row of the previous column. However, the value of 1 for the second entry is only an initial guess and could possibly be overwritten. Another variable, q, will reference the q^{th} entry of the $Ind(1,p)^{\text{th}}$ row of Ang. It starts at the value of $Ind(2,p-1)+1$ and tests the two statements in the decision block for each entry. Collectively the two statements check to see if the current angle being evaluated, $Ang\left(Ind(1,p),q\right)$, is smaller than the angle in Ang corresponding to the last relevant indices that were found, $Ang\left(Ind(1,p-1),Ind(2,p-1)\right)$, and larger than the current guess, $Ang\left(Ind(1,p),Ind(2,p)\right)$. If this is true then the current value of q is assigned to $Ind(2,p)$ and the iteration along the $Ind(1,p)^{\text{th}}$ row of Ang continues.

Eventually q will reach the $(D+1)^{\text{th}}$ entry in the $Ind(1,p)^{\text{th}}$ row of Ang and the algorithm will check to see if $Ind(2,p)$ is still equal to 1, as this was the initial guess when iteration began in the inner loop. If this true then the last relevant angle in the chip area has been found and the algorithm terminates, since the last intersection must be between the RTWD at the current time and a previous one. Just like in the previous example, the second row of the last column of a completed matrix, Ind, will always be equal to one. If $Ind(2,p)$ is not equal to 1 than p is incremented and another relevant intersection angle in the chip area will be found the next iteration. It is possible that the algorithm will terminate and less than $D+1$ angles of intersection describing the chip area will have been found, thereby resulting in some columns of Ind containing zeros. In this event, Ind should be truncated to only have columns with nonzero values. Finally, a the current value of q is stored in

the variable Q, which represents the number of columns in Ind, or more specifically the number of angle intersections found to be relevant to the free boundary of the undeformed chip area.

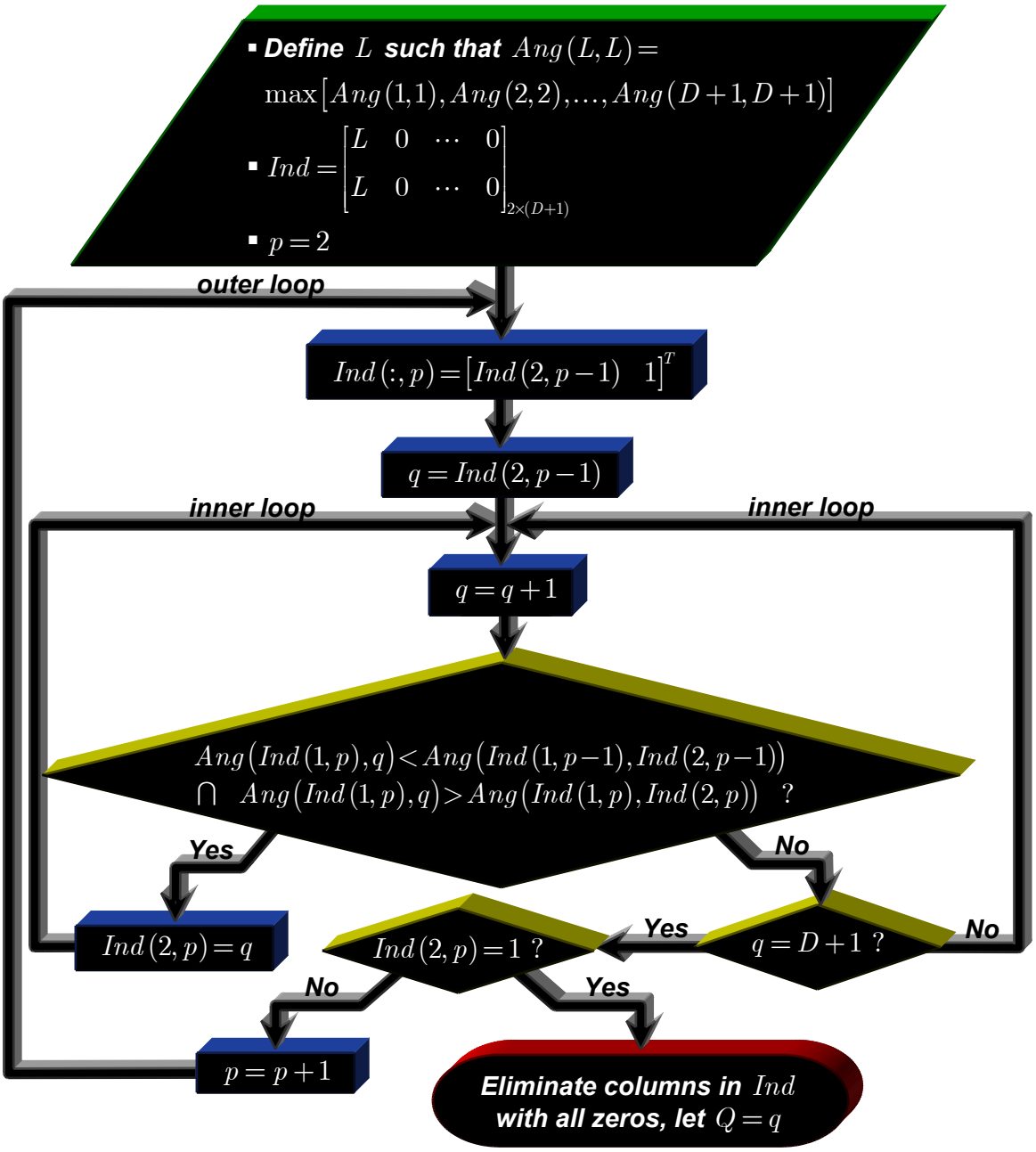

Figure 4-6: An algorithm for determining the angles of intersection relevant to the undeformed chip area.

4.2.3 Exact formulation of the angle of the chip flow direction

With the matrix, Ind, referencing the angles of intersection in the matrix, Ang, that are relevant to the undeformed chip area, Equation (4.17) can now be evaluated using these angles as the

integration limits in conjunction with the previously derived expressions for $t_{u,A}(\theta,W)$ and $t_{u,B}(\theta)$. It is rewritten in a new form in order to facilitate implementation in computer code, given as

$$\overline{\Omega} = \tan^{-1}\left[\frac{\overbrace{\sum_{q=1}^{Q-1}\int_{Ang(Ind(1,q+1),Ind(2,q+1))}^{Ang(Ind(1,q),Ind(2,q))}\sin\left[\left(\frac{\pi}{2}-\theta\right)t_{u,A}\left(\theta,Ind(1,q)-1\right)\right]d\theta}^{\text{Type A Region(s)}} + \overbrace{\int_{Ang(Ind(1,1),Ind(2,1))}^{\theta_0}\sin\left[\left(\frac{\pi}{2}-\theta\right)t_{u,B}(\theta)\right]d\theta}^{\text{Type B Region}}}{\underbrace{\sum_{q=1}^{Q-1}\int_{Ang(Ind(1,q+1),Ind(2,q+1))}^{Ang(Ind(1,q),Ind(2,q))}\cos\left[\left(\frac{\pi}{2}-\theta\right)t_{u,A}\left(\theta,Ind(1,q)-1\right)\right]d\theta}_{\text{Type A Region(s)}} + \underbrace{\int_{Ang(Ind(1,1),Ind(2,1))}^{\theta_0}\cos\left[\left(\frac{\pi}{2}-\theta\right)t_{u,B}(\theta)\right]d\theta}_{\text{Type B Region}}}\right] \tag{4.28}$$

The form of Equation (4.28) is the same as Equation (4.17) in that there are contributions from type A and B regions in both the numerator and denominator of the fraction inside the $\tan^{-1}$ function. The contribution from type A regions involves a summation of various integrals, each one being evaluated over θ in the range $\left[Ang\left(Ind(1,q+1),Ind(2,q+1)\right),\ Ang\left(Ind(1,q),Ind(2,q)\right)\right]$ as q varies from 1 to $Q-1$, where Q is the number of angular intersections associated with the description of the undeformed chip area. In each integration, $t_A(\theta,W)$ is also passed the value of $Ind(1,q)-1$ for W, since $y\left(t-\left(Ind(1,q)-1\right)\tau\right)$ corresponds to the previous tool position that is defining the free boundary of the undeformed chip area in the current range of θ. For conciseness, only the results of a single integration over a type A region are presented for the numerator and denominator of Equation (4.28) (i.e. the summation has been dropped) in order to show the form of the result, and the generic $t_A(\theta,W)$ has been used in place of $t_A\left(\theta,Ind(1,q)-1\right)$. The integral along a type A region in the numerator is given by

$$\begin{aligned}\int \sin\left[\left(\tfrac{\pi}{2}-\theta\right)t_{u,A}(\theta,W)\right]d\theta = \frac{1}{4\sqrt{A_W}}\Bigg(&L_W\sin\left[2\theta-\chi_W\right]+\sqrt{L_W}\left(c_{3,W}\sqrt{2}-4r_n\right)\sin\left[\theta\right]+\\ &2\cos\left[\chi_W\right]\left(r_n^2\tan^{-1}\left[\frac{\sqrt{2L_W}\sin\left[\theta-\chi_W\right]}{c_{3,W}}\right]+L_W\left(\theta-\chi_W\right)\right)+\\ &2\left(r_n^2-L_W\right)\ln\left(\sqrt{2L_W}\cos\left[\theta-\chi_W\right]+c_{3,W}\right)\sin\left[\chi_W\right]\Bigg)\end{aligned} \tag{4.29}$$

when neglecting the constant of integration (it would cancel when the above result is evaluated over the appropriate integration limits). The integral along a type A region in the denominator is given by

$$\int \cos\left[\left(\tfrac{\pi}{2}-\theta\right)t_{u,A}(\theta,W)\right]d\theta = \frac{1}{4\sqrt{L_W}}\Bigg(L_W\cos[2\theta-\chi_W]+\sqrt{L_W}\left(c_{3,W}\sqrt{2}-4r_n\right)\cos[\theta]- 2\sin[\chi_W]\left(r_n^2\tan^{-1}\left[\frac{\sqrt{2L_W}\sin[\theta-\chi_W]}{c_{3,W}}\right]-L_W(\theta-\chi_W)\right)+ 2\left(r_n^2-L_W\right)\ln\left(\sqrt{2L_W}\cos[\theta-\chi_W]+c_{3,W}\right)\cos[\chi_W]\Bigg) \tag{4.30}$$

where

$$c_{3,W} \triangleq \sqrt{2r_n^2+L_W\left(\cos\left[2(\theta-\chi_W)\right]-1\right)}$$

In Type B regions the integrals are each only evaluated once with the upper limit always being θ_0. This is because if cutting is taking place, θ_0 must be the largest angle associated with the undeformed chip area. The results of these integrations in the numerator and denominator of Equation (4.28) are

$$\int_{Ang(Ind(1,1),Ind(2,1))}^{\theta_0}\sin\left[\left(\tfrac{\pi}{2}-\theta\right)t_{u,B}(\theta)\right]d\theta = \left(r_n-d_c+y(t)\right)\ln\left[\sin[\theta]\right]-r_n\sin[\theta]\Big|_{Ang(Ind(1,1),Ind(2,1))}^{\theta_0} \tag{4.31}$$

$$\int_{Ang(Ind(1,1),Ind(2,1))}^{\theta_0}\cos\left[\left(\tfrac{\pi}{2}-\theta\right)t_{u,B}(\theta)\right]d\theta = \left(d_c-r_n-y(t)\right)\theta-r_n\cos[\theta]\Big|_{Ang(Ind(1,1),Ind(2,1))}^{\theta_0} \tag{4.32}$$

4.2.4 Development of the effective width of cut and effective undeformed chip thickness

Another important quantity in Figure 4-3 is the effective width of cut, w^* and effective undeformed chip thickness, t_u^*. Referring to the Oxley cutting force model in Chapter 3 used to describe the forces due to chip formation, w becomes w^* and t_u becomes t_u^*, thereby expressing an irregularly-shaped chip area as a simple equivalent rectangular area, as shown in Figure 4-3. w^* is chosen to be the length of the portion of the tool nose engaged in the workpiece, given by

$$w^* = r_n\left(\theta_0 - Ang\left(Ind(1,Q),Ind(2,Q)\right)\right) \tag{4.33}$$

The product of w^* and t_u^* will be such that it is the same as the sum of the areas from all potentially multiple type A regions and a single and type B regions (the total undeformed chip area). Therefore t_u^* can be thought of as the total undeformed total chip area divided by w^*, expressed as

$$t_u^* = \frac{\overbrace{\sum_{q=1}^{Q-1} \int_{Ang(Ind(1,q+1),Ind(2,q+1))} \int_{r_n - t_{u,A}(\theta, Ind(1,q)-1)}^{r_n} r dr d\theta}^{\text{Type A Region(s)}} + \overbrace{\int_{Ang(Ind(1,1),Ind(2,1))}^{\theta_0} \int_{r_n - t_{u,B}(\theta)}^{r_n} r dr d\theta}^{\text{Type B Region}}}{w^*} \tag{4.34}$$

where the integral associated with undeformed chip area contributions from type A regions is (neglecting the summation for conciseness purposes)

$$\int_{Ang(Ind(1,q+1),Ind(2,q+1))}^{Ang(Ind(1,q),Ind(2,q))} \int_{r_n - t_{u,A}(\theta, Ind(1,q)-1)}^{r_n} r dr d\theta = -\frac{1}{4}\left(2r_n^2 j \ln\left[2\left(\sqrt{r_n^2 - L_W \sin^2\left[\theta - \chi_W\right]} - j\sqrt{L_W} \sin\left[\theta - \chi_W\right] + \right) \right] + \right.$$
$$\left. 2\sqrt{L_W} \sin\left[\theta - \chi_W\right] \sqrt{r_n^2 - L_W \sin^2\left[\theta - \chi_W\right]} + L_W \sin\left[2\left(\theta - \chi_W\right)\right] \right) \Bigg|_{Ang(Ind(1,q+1),Ind(2,q+1))}^{Ang(Ind(1,q),Ind(2,q))} \tag{4.35}$$

and the undeformed chip area contribution from a type B region is

$$\int_{Ang(Ind(1,1),Ind(2,1))}^{\theta_0} \int_{r_n - t_{u,B}(\theta)}^{r_n} r dr d\theta = \frac{1}{2}\left(r_n^2 \theta + \frac{\left(d_c - r_n - y(t)\right)^2}{\tan\left[\theta\right]} \right) \Bigg|_{Ang(Ind(1,1),Ind(2,1))}^{\theta_0} \tag{4.36}$$

where j is $\sqrt{-1}$.

It should be noted that in the present application when Equation (4.35) is evaluated, the imaginary portion should cancel to give a real-valued area. However in numerical computer evaluation there will be a relatively small imaginary part due to round-off error, so it is necessary to take the real part of this area.

In Figure 4-7 are nine successive undeformed chip areas during a chatter simulation using the yet-to-be fully presented simplified dynamic cutting force model in this dissertation, with $D = 3$. Figure 4-7A-I corresponds to one sinusoidal period of vibration of the workpiece relative to the cutting tool, with Figure 4-7A occurring the earliest in time and Figure 4-7I occurring the latest in time. The shaded red region represents the undeformed chip area and the blue rectangle with sides that are dashed lines represents the effective undeformed rectangular chip area with dimensions w^* by t_u^*. Just as in Figure 4-3, the equivalent rectangular undeformed chip area is inclined at an angle of $\overline{\Omega}$ from the $\mathbf{Y}$ axis. The effective undeformed chip area changes its size and orientation as the actual undeformed chip area changes. It is interesting to note that during chatter the regenerative

position space is such that when the current RTWD is most engaged in the workpiece the relative tool position earliest in the delay space, $y(t-3\tau)$, is almost maximally engaged as well so it can exert influence on the undeformed chip area (e.g. Figure 4-7B and C).

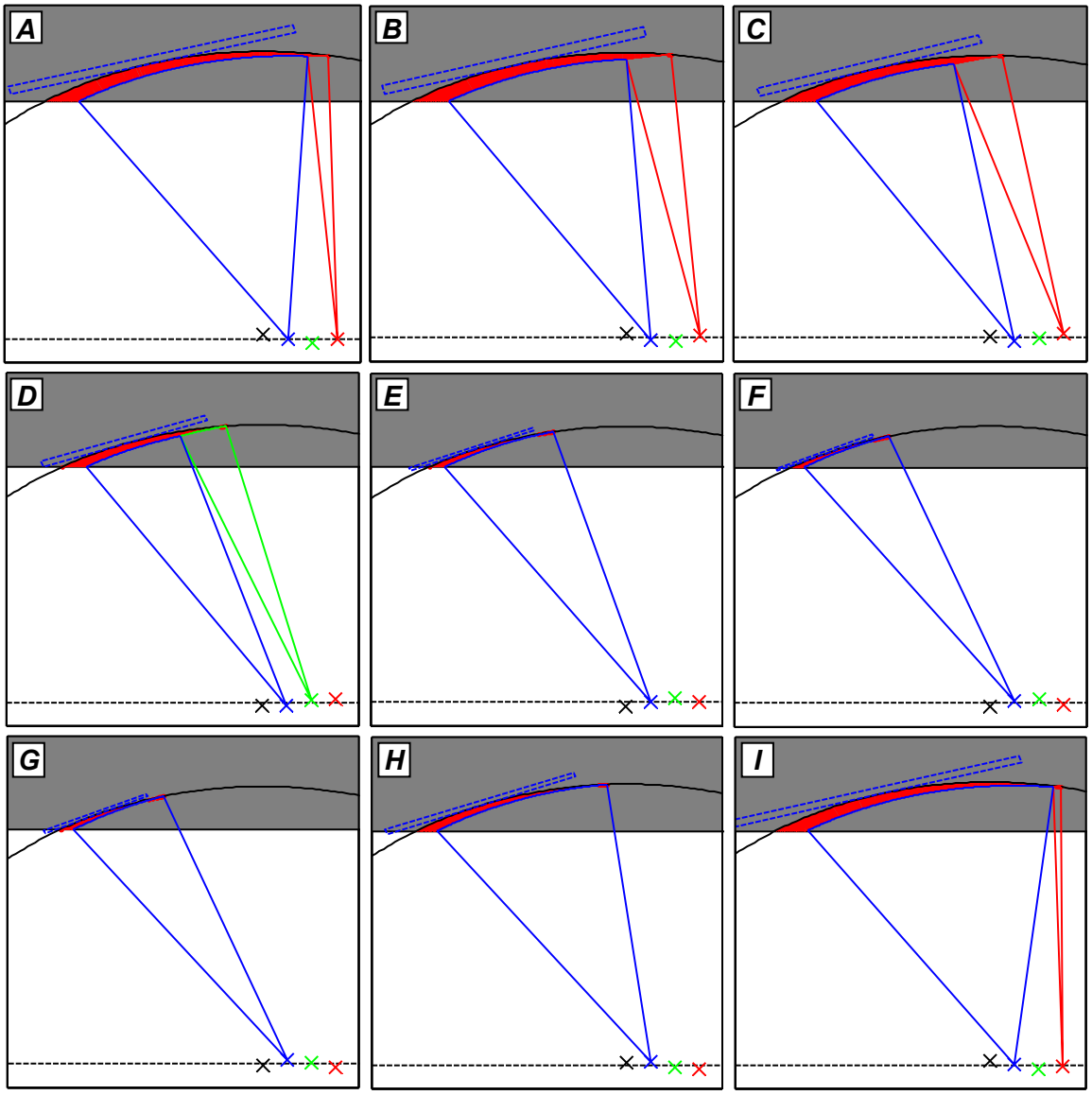

Figure 4-7: Nine progressive points in time taken from a chatter simulation using the simplified dynamic force model showing how the undeformed chip area, regenerative position space, w^*, and t_u^* change with time when there is relative tool-workpiece vibration. (A) Earliest in time; (I) latest in time.

4.2.5 Description of the forces due to chip formation in the simplified dynamic cutting force model

The final influence that the tool nose radius and vibration have on the equivalent orthogonal cutting process is the effective cutting velocity and rake angle. This idea is extended from [57], where

a single degree of freedom orthogonal model was used, and from [19] where a two degree of freedom orthogonal model was used, to the present case of oblique turning with a tool nose radius. Consider the following orthogonal machining operation depicted in Figure 4-8A, already transformed from the oblique nose radius cutting domain. As in the plowing and flank interference model, there is a relative velocity component in the cutting direction, V_C, and some instantaneous relative velocity in the thrust direction, V_T.

Previously described in Chapter 3, the Oxley orthogonal cutting force model only considers the component of the relative velocity parallel to the $\mathbf{C}$ axis in Figure 4-8A. However, this can be extended to the present scenario where the net relative velocity between the workpiece and the cutting tool is located at an acute angle of δ_V, as shown in Figure 4-8A. To do this, the entire system can be rotated clockwise by δ_V to yield the configuration depicted in Figure 4-8B. This is a standard configuration that can be input into the Oxley cutting force model since the net relative velocity, $\vec{V}_C$, is directed horizontally. Once the forces have been computed, an inverse rotation transformation can be applied. The forces per unit width of cut predicted by the Oxley cutting force model in the rotated $\mathbf{C}'\text{-}\mathbf{T}'$ reference frame are f_C' and f_T', and they are related to the total force in the $\mathbf{C}\text{-}\mathbf{T}$ reference frame by a simple rotation transformation and multiplication by w^*, given by

$$F_C = w^* f_C' \cos[\delta_v] - w^* f_T' \sin[\delta_v] \tag{4.37}$$

$$F_T = w^* f_C' \sin[\delta_v] - w^* f_T' \cos[\delta_v] \tag{4.38}$$

Based on the implementation of this rotation transformation, the $\mathbf{C}\text{-}\mathbf{T}$ reference frame in Figure 3-1 that was used in the derivation of Oxley's cutting force model should technically be labeled as the $\mathbf{C}'\text{-}\mathbf{T}'$ reference frame. This is because the Oxley model is applied instantaneously at points in time in the $\mathbf{C}'\text{-}\mathbf{T}'$ reference frame such that the net relative velocity between the workpiece and the cutting tool is directed horizontally. Therefore, the $\mathbf{C}'\text{-}\mathbf{T}'$ reference frame exists at various angles of orientation, δ_V, from the $\mathbf{C}\text{-}\mathbf{T}$ reference frame, and is used to obtain a quasi-static prediction of the forces due to chip formation.

It should be noted that the force component perpendicular to F_C and F_T, F_R, is also perpendicular to f_C' and f_T' since the rotation transformation given in Equations (4.37) and (4.38) is about an axis coinciding with F_R. Therefore F_R in Equation (4.7) can be found from F_C and F_T given in Equations (4.37) and (4.38), respectively.

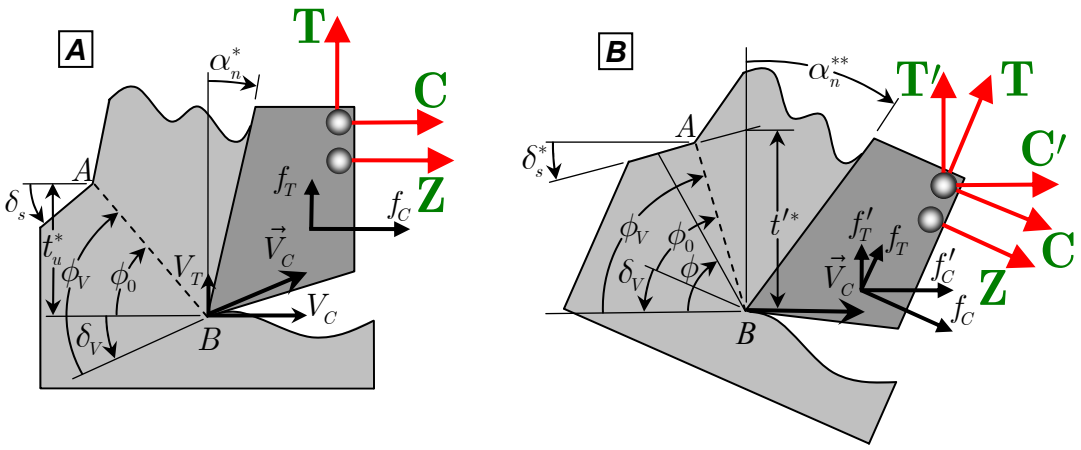

Figure 4-8: The influence of relative vibration on the effective cutting conditions. (A), An orthogonal cutting scenario with dynamic elements; (B), an equivalent quasi-static representation suitable for use in Oxley's cutting force model.

In finding f_C' and f_T' in the $\mathbf{C}'$ - $\mathbf{T}'$ reference frame, the effective cutting velocity, V_C^*, has become

$$V_C^* = \left|\vec{V}_C\right| = \sqrt{V_C{}^2 + \left(V_T^*\right)^2} \tag{4.39}$$

and the rake angle, α_n^*, has become α_n^{**}, as given by

$$\alpha_n^{**} = \alpha_n^* + \delta_V \tag{4.40}$$

where α_n^{**} is a further modified version of α_n^* due to dynamic effects and δ_V is given as

$$\delta_V = \tan^{-1}\left[\frac{V_T^*}{V_C}\right] \tag{4.41}$$

where

$$V_C = \bar{V}_C - \dot{z}(t) \tag{4.42}$$

The effective relative velocity in the thrust direction, V_T, will always be less than the relative velocity in the radial cutting direction, $\dot{y}(t)$, due to the tool nose radius effect. Referring to Figure 4-3, picture an infinite number of orthogonal cutting scenarios occurring all along the edge of the

tool nose, each with undeformed chip thickness, $t_u(\theta)$, and differential width of cut, $r_n d\theta$. At each angular position, θ, V_T is

$$V_T = -\sin[\theta]\dot{y}(t) \tag{4.43}$$

The effective velocity in the thrust direction, V_T^*, over the entire cutting region is therefore

$$V_T^* = -\varphi\dot{y}(t) \tag{4.44}$$

where φ is the tool nose radius scaling factor. φ captures the effective rate that the cutting tool is moving into the workpiece normal to the surface along the portion of the curved nose of the cutting tool that is engaged in the workpiece, and given as

$$\varphi = \int_{Ang(Ind(1,Q),Ind(1,Q))}^{\theta_0} \sin[\theta]\, d\theta \tag{4.45}$$

It should be noted that in Equation (3.28), V_T^* is used in place of V_T and the definition of V_C in Equation (4.42) is used to give a new formulation for the effective angle of material separation, $\beta_e^*(t)$

$$\beta_e^*(t) = \overline{\beta}_e + \tan^{-1}\left[\frac{\varphi\dot{y}(t)}{\overline{V}_C - \dot{z}(t)}\right] \tag{4.46}$$

It should be noted that a dependence on time has been indicated explicitly for $\beta_e^*(t)$ in order to facilitate later developments.

Because vibration is present, the definition of the shear angle needs to be expanded. Initially when the Oxley cutting force model was presented there was a single shear angle, ϕ_V, upon which the algorithm converged. Now that there is relative vibration between the cutting tool and workpiece, the shear angle will need to be addressed differently. As shown in Figure 4-8A, ϕ_0 will now be defined as the acute angle between the shear plane and the negative **C** axis and will be referred to as the "quasi-static shear angle" since it is a notion from quasi-static cutting force modeling. ϕ_V will be defined as the acute angle between the shear plane and the direction of net relative velocity with respect to the cutting tool and will be referred to as the "dynamic shear angle",

as shown in Figure 4-8B. In this way, ϕ_V will only equal ϕ_0 for $\delta_V = 0$. This new nomenclature will be used throughout the remainder of this dissertation.

Additionally the effective undeformed chip thickness, t_u^*, is now a function of the shear angle due to the nonzero effective workpiece surface slope, δ_s^*, in Figure 4-8B. As discussed previously, the undeformed chip thickness needs to be referenced from the tip of the cutting tool as the quantity t'^*. In the simplified cutting force model, it is assumed that the initial workpiece slope, δ_s, in Figure 4-8A is 0. The workpiece slope in the rotated reference frame is therefore

$$\delta_s^* = -\delta_V \tag{4.47}$$

regardless of the quasi-static shear angle, ϕ_0. In a later section it will be shown that for a nonzero δ_s, the choice of ϕ_0 will affect t'^*, and hence an iterative procedure is used to determine ϕ_0. The uncut chip thickness referenced from the tool tip, t'^*, as a function of the angle of net relative velocity is described by

$$t'^* = \frac{t_u^*}{\cos\left[\delta_V\right]} \tag{4.48}$$

where t_u^* was given in Equation (4.34). It should be noted that in the computation of f_C' and f_T', the regression surface fits for the Oxley model are employed, given by

$$f_C' = S_{F_C}\left(t'^*, \alpha_n^{**}, V_C^*, \delta_s^*\right) \tag{4.49}$$

$$f_T' = S_{F_T}\left(t'^*, \alpha_n^{**}, V_C^*, \delta_s^*\right) \tag{4.50}$$

In Equations (4.49) and (4.50), referring to the development of Oxley's cutting force model in Chapter 3, t'^*, α_n^{**}, V_C^*, and δ_s^* are used in place of t', α_n, $\left|\vec{V}_C\right|$, and δ_s, respectively, to describe an oblique nose radius cutting scenario with vibration equivalently in the orthogonal cutting domain.

4.3 Influence on plowing and flank interference forces

Previously, forces due to plowing and flank interference were developed for an orthogonal straight edge cutting condition and given in Equations (3.61) and (3.62). However, since turning

generally involves a cutting edge that has a radius, the equations need to be modified slightly. The thrust force per unit width of cut, as given in Equation (3.59), acts normal to the tool nose in the **XY** plane and therefore has components along the **X** and **Y** axes. The forces along the **X** axis are not being considered due the workpiece's large structural rigidity in that direction (this will be justified later by examining the stiffness in various directions of the actual workpiece used for experimental validation). The forces directed along the radial cutting direction (**Y** axis) are proportional to $\sin[\theta]$ and can be resolved by integrating along the tool nose over the angles that define the region of contact between the cutting tool's edge and the workpiece as given by

$$P_Y = \int_{Ang(Ind(1,Q),Ind(2,Q))}^{\theta_0} p_T \sin[\theta] r_n d\theta \quad = p_T \int_{Ang(Ind(1,Q),Ind(2,Q))}^{\theta_0} \sin[\theta] r_n d\theta \quad = K_{cf} A_i w^* \varphi \left(\cos[\gamma^*] + \mu \sin[\gamma^*]\right) \tag{4.51}$$

As defined in Equation (3.59), p_T is the force in the thrust direction per unit width of cut, making P_Y have units of force. The differential width of cut is taken to be $r_n d\theta$, and it is assumed that the following relation holds, since it simplifies the analysis greatly:

$$V_i \cong A_i \int_{Ang(Ind(1,Q),Ind(2,Q))}^{\theta_0} r_n d\theta \tag{4.52}$$

From Pappus's centroid theorem [58], the volume of a solid of revolution is the product of the area of its generating surface and the distance that its geometric centroid travels. Since the geometric centroid must lie somewhere in the region defined by the interference area, A_i, and based on the length scales shown in Figure 3-3A, it can be concluded that the geometric centroid has a normal distance to the origin of the global **XYZ** reference frame of approximately r_n regardless of the size and orientation of an interference area that would be encountered in a realistic machining simulation. Therefore we can assume that the distance to the geometric centroid of A_i is a constant, r_n. In a similar manner, the forces in the tangential cutting direction (**Z** axis) are

$$P_Z = \int_{Ang(Ind(1,Q),Ind(2,Q))}^{\theta_0} p_C r_n d\theta \quad = p_C \int_{Ang(Ind(1,Q),Ind(2,Q))}^{\theta_0} r_n d\theta \quad = K_{cf} A_i w^* \left(\mu \cos[\gamma^*] - \sin[\gamma^*]\right) \tag{4.53}$$

It is important to note that the differential force, p_C, does not vary along the path of integration since it is always in the **Z** direction. γ^* is taken to be 0° as was done previously when interference forces were derived in orthogonal cutting in order to keep the solution for the dynamic cutting force in closed-form. In later developments, the refined dynamic cutting force model will be presented and will have many elements that can not be evaluated in closed-form. It will employ an exact calculation for γ^* in hopes of obtaining an improved model of chatter.

Finally as an aside, it is generally thought that the "regenerative effect" only applies to the undeformed chip area and hence only affects the forces due to chip formation. From this model's formulation (as well as the refined cutting force model that will be introduced in a later chapter) it is clear that the regenerative effect influences the interference forces as well. This is evident by the integration limits in Equations (4.51) and (4.53) for the interference forces in the **Y** and **Z** directions, respectively. The limits in each case are the angles associates with the portion of the tool nose that is engaged in the workpiece. One limit is θ_0, which is clearly only associated with the RTWD at the current time. However one of them is $Ang\left(Ind(1,Q),Ind(2,Q)\right)$, which is always determined by a RTWD in the regenerative position space. For a graphical representation consider Figure 4-3, a case where the integration limits in Equations (4.51) and (4.53) would be from $\theta_{0,3}$ to θ_0. If the RTWD at time $t-2\tau$ was larger in the $-\bar{\mathbf{Y}}$ direction, the integration limits would instead be from $\theta_{0,2}$ to θ_0, and hence the manifestation of the regenerative effect in the interference forces– that is, the influence of previous RTWDs on the current state of cutting.

CHAPTER 5: COMPARISON WITH PREVIOUS WORK

"Science is facts; just as houses are made of stones, so is science made of facts; but a pile of stones is not a house and a collection of facts is not necessarily science."
–Henri Poincare

5.1 The Various Orthogonal Cutting Configurations

The analysis thus far for the simplified cutting force model has been built upon describing an equivalent representation of forces due to chip formation and interference in the plane, a so-called "orthogonal cutting force model." In the next chapter the refined cutting force model will be introduced and will still employ the orthogonal cutting force model paradigm. Therefore, for both the simplified and dynamic cutting force models, it is imperative that the behavior of the orthogonal models correlate well with previously published experimental work in the literature.

In the case of machining with vibration, there are two common scenarios that have been studied: wave generation [60]-[62], and wave removal [63]-[67]. In the case of wave generation, Figure 5-1A, the cutting tool has some relative sinusoidal vibration with respect to the workpiece in the thrust direction with amplitude, A_0, and a frequency, ω, in addition to the cutting velocity, $\bar{V}_C$. In the case of wave removal, Figure 5-1B, the cutting tool only has a velocity component in the cutting direction; however, the unmachined workpiece surface is sinusoidal with an amplitude A_0. In this way, for either wave generation or wave removal, the undeformed chip thickness, t_u, sinusoidally varies about some nominal depth of cut, d_c, at an amplitude, A_0. In short, for the case of wave generation the following equations hold:

$$t_u = d_c + A_0 \sin[2\pi\omega t] \tag{5.1}$$

$$V_T = 2\pi\omega A_0 \cos[2\pi\omega t] \tag{5.2}$$

where ω is in Hz. For the case of wave removal t_u is given in Equation (5.1) and $V_T = 0$.

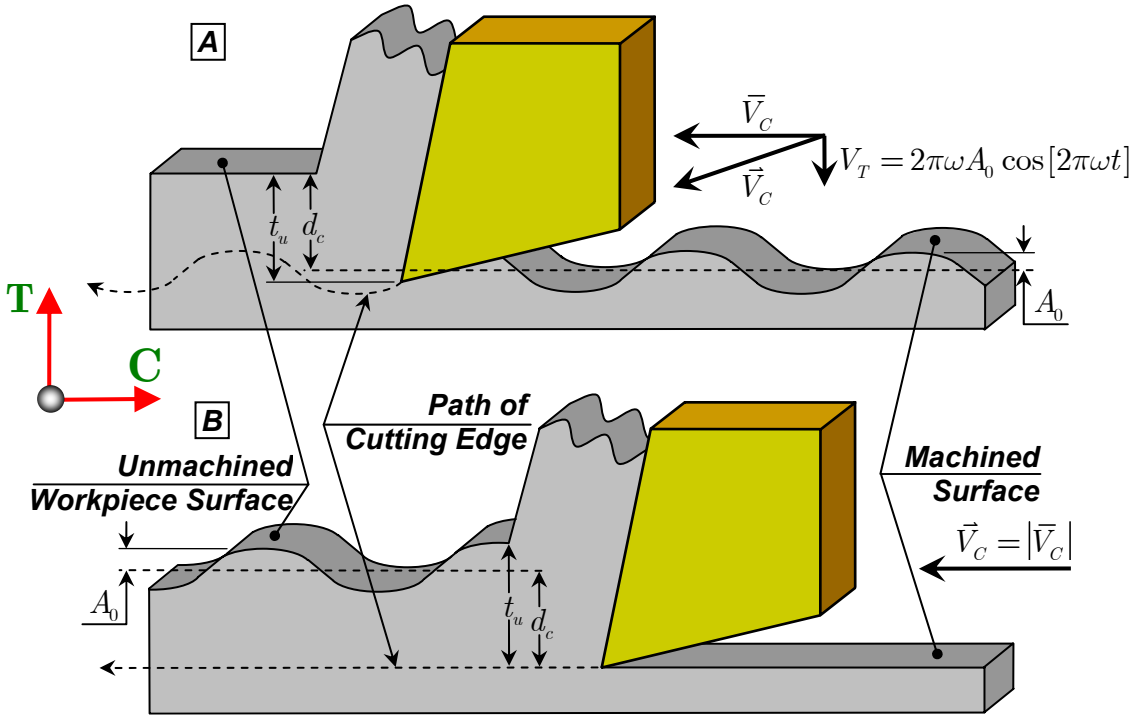

Figure 5-1: Examples of wave generation and wave removal in an orthogonal cutting scenario. (A) Wave generation; (B) wave removal.

5.2 Orthogonal Cutting Force Modeling of Wave Cutting

Consider first the case of wave generation, with a depth of cut d_c = 0.15 mm, cutting speed $\bar{V}_C$ =3.0 m/s, rake angle α_n = 7 deg, AISI 1018 steel workpiece material, vibration amplitude, A_0 = 0.05 mm, width of cut, w = 1 mm, and a RTWD oscillation frequency, ω, of 600 Hz. The forces due to chip formation are given in Figure 5-2, the shear angles in Figure 5-3, and the interference forces in Figure 5-4. It should be noted that all components except for the undeformed chip thickness have had their nominal values subtracted, i.e. the value when $\omega = 0$.

The forces due to chip formation in Figure 5-2 are nearly in phase with the waveform of the undeformed chip thickness, sinusoidal in nature, and exhibit approximately symmetric behavior about 0 N. For the case of the shear angles in Figure 5-3, the dynamic shear angle, ϕ_v, leads in phase by about 65°, whereas the quasi-static shear angle, ϕ_0, lags in phase by about 65°. Both waveforms are nearly sinusoidal in nature. Finally the interference forces are shown in Figure 5-4 and for each component they have about a 90° phase lead relative to the undeformed chip thickness. These

forces are highly asymmetric about 0 N and are less sinusoidal in nature than the waveforms for the shear angle and forces due to chip formation. As one would intuitively expect, they reach maximum values when the tool is traveling into the workpiece (i.e. undeformed chip thickness has a positive time rate of change). This was also demonstrated graphically in Figure 3-6.

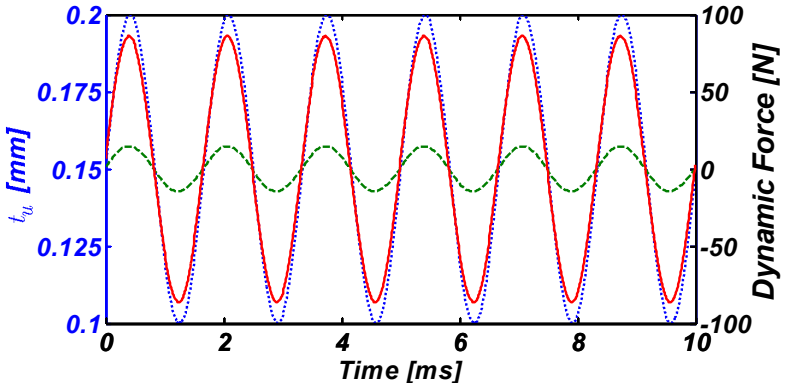

Figure 5-2: The dynamic forces due to chip formation during wave generation. ····, Undeformed chip thickness, t_u; ——, force in the cutting direction, F_C; ---, force in the thrust direction, F_T.

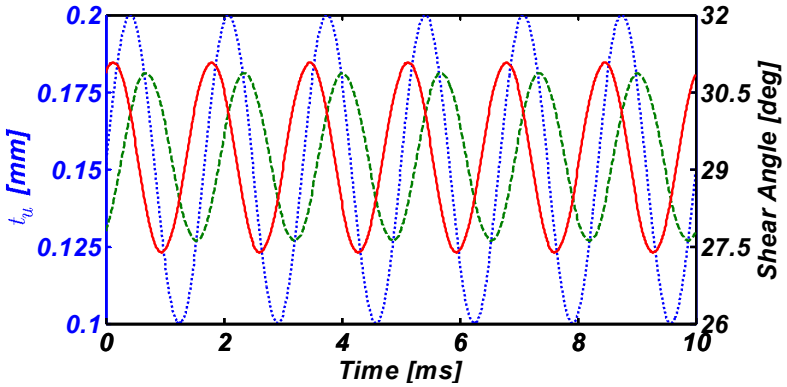

Figure 5-3: The shear angle during wave generation. ····, Undeformed chip thickness, t_u; ——, dynamic shear angle, ϕ_v; ---, quasi-static shear angle, ϕ_0.

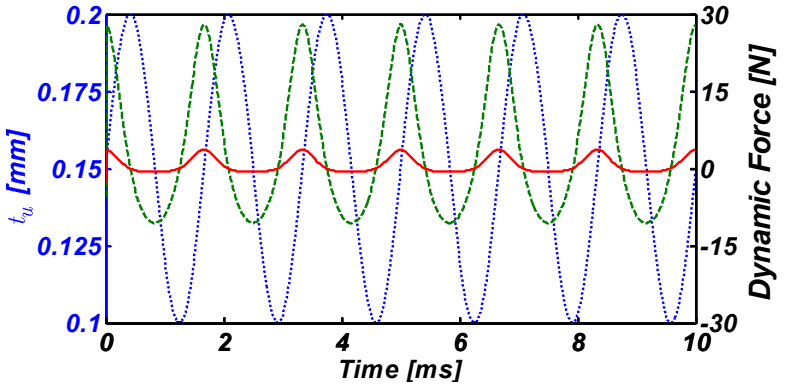

Figure 5-4: The dynamic interference forces during wave generation. ····, Undeformed chip thickness, t_u; ——, force in the cutting direction, P_C; ---, force in the thrust direction, P_T.

Finally, it is instructive to examine the total cutting force in the phase plane, shown in Figure 5-5, still using the same parameters. The total force in the thrust direction, $F_T + P_T$, does not exhibit odd symmetry about the mean operating point of (0.15 mm, 0 N). However, the total force in the cutting direction is more close to being odd-symmetric. This lack of symmetry in the thrust direction is caused by the large asymmetric waveform about 0 N for the interference force in the thrust direction in Figure 5-4. Since the asymmetric interference force in the cutting direction is much smaller, the total force in the cutting direction in Figure 5-5 is still close to being odd-symmetric. Both sets of forces exhibit hysteresis, as evident by the fact that the path of increasing chip thickness does not lie exactly on top of the path of decreasing chip thickness. However the force in the thrust direction exhibits much greater hysteresis, as evident by the larger deviation between paths of increasing and decreasing undeformed chip thickness. This same type of hysteresis for the forces in the thrust and cutting directions was also observed experimentally in [27].

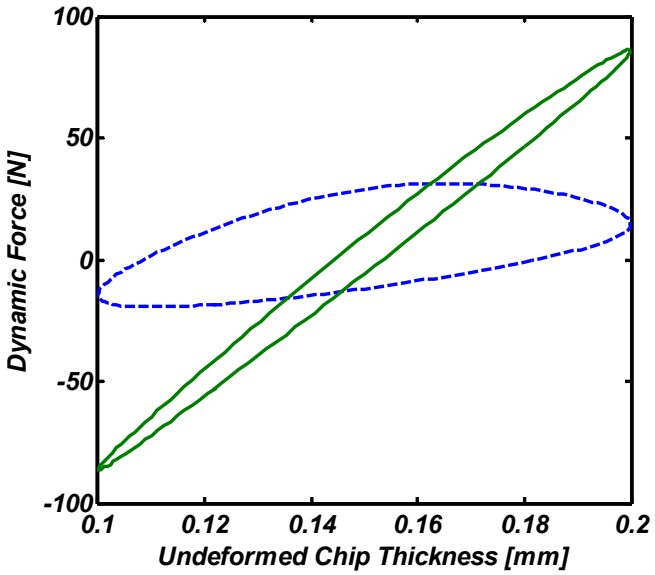

Figure 5-5: A phase portrait of the total dynamic force and undeformed chip thickness during wave generation. —, Total force in the cutting direction, $F_C + P_C$; ---, total force in the thrust direction, $F_T + P_T$.

The 600 Hz RTWD oscillation frequency was chosen for the previous example since it is the approximate chatter frequency of the workpiece used to experimentally validate the two dynamic cutting force models presented in this thesis. The phase difference between the undeformed chip

thickness and the forces and shear angles over a wider range of RTWD oscillation frequencies will now be explored.

In order to find the phase difference between two signals, the individual phase of each one over time must be found first. A so-called "analytic" signal, $q_A(t)$, is constructed from the original signal, $q(t)$, as

$$q_A(t) = q(t) + jq_H(t) \tag{5.3}$$

Where $q_H(t)$ is the Hilbert Transform, given as

$$q_H(t) = \frac{PV}{\pi}\int_{-\infty}^{\infty}\frac{q(t)}{t-\tau}d\tau \tag{5.4}$$

and PV is the Cauchy principle value. In the case of data in the discrete domain, a Discrete Hilbert transform is employed [68]. The envelope of the signal, $A(t)$, which is useful for estimating the signal oscillation amplitude comes directly from the analytic signal and is given as

$$A(t) = \sqrt{q(t)^2 + q_H(t)^2} \tag{5.5}$$

The instantaneous phase of the signal, $\theta(t)$, is now given as

$$\theta(t) = \tan^{-1}\left[\frac{q_H(t)}{q(t)}\right] \tag{5.6}$$

which for a physically meaningful instantaneous phase assumes that $q(t)$ is a zero mean signal with both narrow band and slowly changing frequency content. For a more rigorous definition of "physically meaningful", reference [69] can be consulted. In this way, the phase difference between two signals can be found by first finding their phases via Equation (5.6) and then taking the difference.

Consider Figure 5-6, which uses the same conditions as in the last example except that the undeformed chip thickness only oscillates at an amplitude of 0.025 mm instead of 0.05 mm. Frequencies in the range of 200-1800 Hz are considered for the RTWD oscillation frequency; a common range for chatter to materialize in practice. The phase difference relative to t_u for the forces due to chip formation, shear angle, interference forces, and the total cutting force are

presented in Figure 5-6A-D, respectively. The phase difference is calculated such that if it is positive for a certain quantity then it leads the undeformed chip thickness in phase and therefore occurs earlier in time. It should be noted that these plots contain two horizontal axes, one for the frequency of the RTWD, and the other for the wavelength of the machined workpiece surface, λ_w. This wavelength is given as

$$\lambda_w = \frac{2\pi}{\omega}\bar{V}_C \tag{5.7}$$

where ω is the oscillation frequency of the cutting tool relative to the workpiece in rad/s. As suggested by Equation (5.7), λ_w is inversely proportional to $2\pi\bar{V}_C$ times the RTWD oscillation frequency. Due to this inverse relationship to frequency, the values for λ_w are non-uniformly spaced in Figure 5-6.

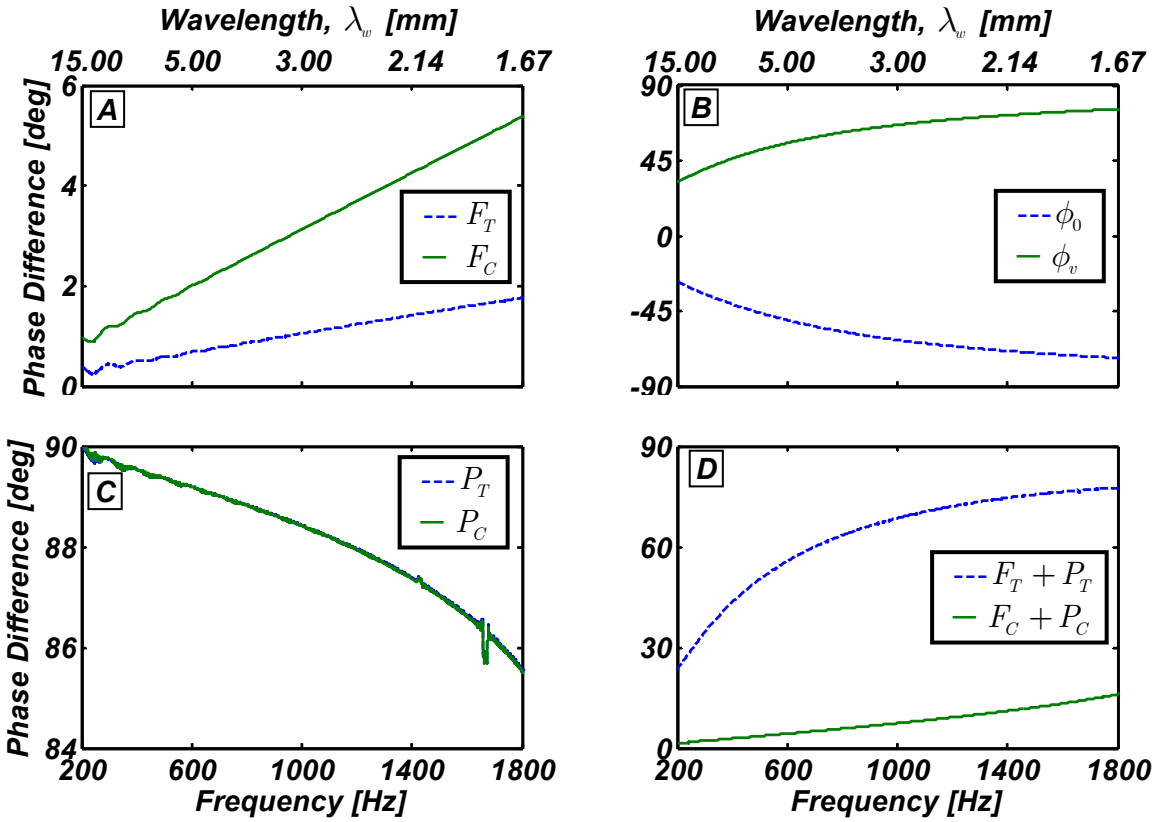

Figure 5-6: The shear angle and cutting forces as a function of the sinusoidal RTWD vibration frequency for wave generation. (A) Forces due to chip formation; (B) dynamic and quasi-static shear angles; (C) interference forces; (D) total force in the thrust and cutting directions.

Just as for the 600 Hz RTWD oscillation frequency in Figure 5-2, the forces due to chip formation in Figure 5-6A are nearly in phase with the undeformed chip thickness–only increasing slightly in phase with increases in the frequency of the RTWD. In Figure 5-6B, the quasi-static and dynamic shear angles are given. Just as in the specific case of the shear angle oscillation in Figure 5-3, the quasi-static shear angle, ϕ_0, generally tends to lag the undeformed chip thickness and approaches -90° from above as the RTWD oscillation frequency increases. This same type of phase lag behavior was also experimentally observed in [61] and [67] with hot finished mild steel (0.25% C) where it increased with increasing RTWD oscillation frequency. In Figure 5-6C, the interference forces are given. It should be noted that some of the "blips" in this plot are a consequence of the original signal violating some of the assumptions needed for a physically meaningful instantaneous phase. Specifically, the assumption of a narrow-band signal was violated since it is not dominated by a single sinusoid, as evident by 600 Hz waveform in Figure 5-4. Since the interference forces generally have between 45° and 90° of phase lead, they would tend to have more of a damping effect than a stiffening one. It is now clear why it has been reported that interference forces add process damping to the machining process [28].

It is normally difficult to isolate interference forces from those due to chip formation since the RTWD results in undeformed chip thickness variation and in turn changes in the chip formation forces. In [62] some "wave on wave" machining tests were conducted on with an aluminum alloy (HE-10-WP) workpiece material. This configuration would result if the two machining configurations shown in Figure 5-1 were combined such that there was both a sinusoidal RTWD as well as a sinusoidal unmachined workpiece surface. The phasing between the waves on the unmachined surface and those generated by the cutting tool on the machined surface was such that the undeformed chip thickness was held constant and forces due to chip formation were drastically reduced (there would still be some small force variation in the chip formation forces since the length of the shear plane would change). In this way, the interference forces were essentially isolated and in the thrust direction it was shown to have 70°-100° of phase lead, thus contributing to process

damping and agreeing with the model's results in Figure 5-6C. They also noted that there was a reduction in phase lead with increasing wavelength, λ_w (or decreasing RTWD oscillation frequency), which is again consistent with Figure 5-6C.

Finally, in Figure 5-6D, the phase difference between the total cutting force and the undeformed chip thickness is given. It should be noted that at higher frequencies the total thrust force, $F_T + P_T$, moves towards 90°, reaching a maximum value of about 80° at 1800 Hz. The total force in the cutting direction, $F_C + P_C$, increases in phase as well but stays much closer to 0°, only reaching a maximum value of 16° at 1800 Hz. This agrees with reports in [62] that showed for cutting speeds in the range of 0.25-6.10 m/s and RTWD oscillation frequencies in the range of 0-400 Hz in the machining of mild steel, the total machining force in the thrust direction led the undeformed chip thickness in phase. Specifically, with increasing frequency, increasing phase lead was observed. It was also shown that the total force in the cutting direction had a slight phase lead (less than ±2 deg). Although this does not entirely agree with the results in Figure 5-6D, the phase lead from 200-400 Hz is around 5-10 deg, which is not far from ±2 deg when considering the context of the current analysis.

At first glance it is not immediately apparent why there is an increase in phase lead of the total cutting force at higher RTWD oscillation frequencies, especially in the thrust direction. However, when the amplitudes of each force component as a function of frequency are examined in Figure 5-7 the reason becomes evident. In Figure 5-7A the amplitudes of the forces due to chip formation are plotted as a function of frequency and both components remain relatively constant. However, the interference forces in Figure 5-7B increase in amplitude dramatically with increases in frequency, especially in the thrust direction. This accounts for the increases in amplitude of the total cutting forces in Figure 5-7C, and phase shift of the total thrust force towards 90° in Figure 5-6D as the RTWD oscillation frequency increases.

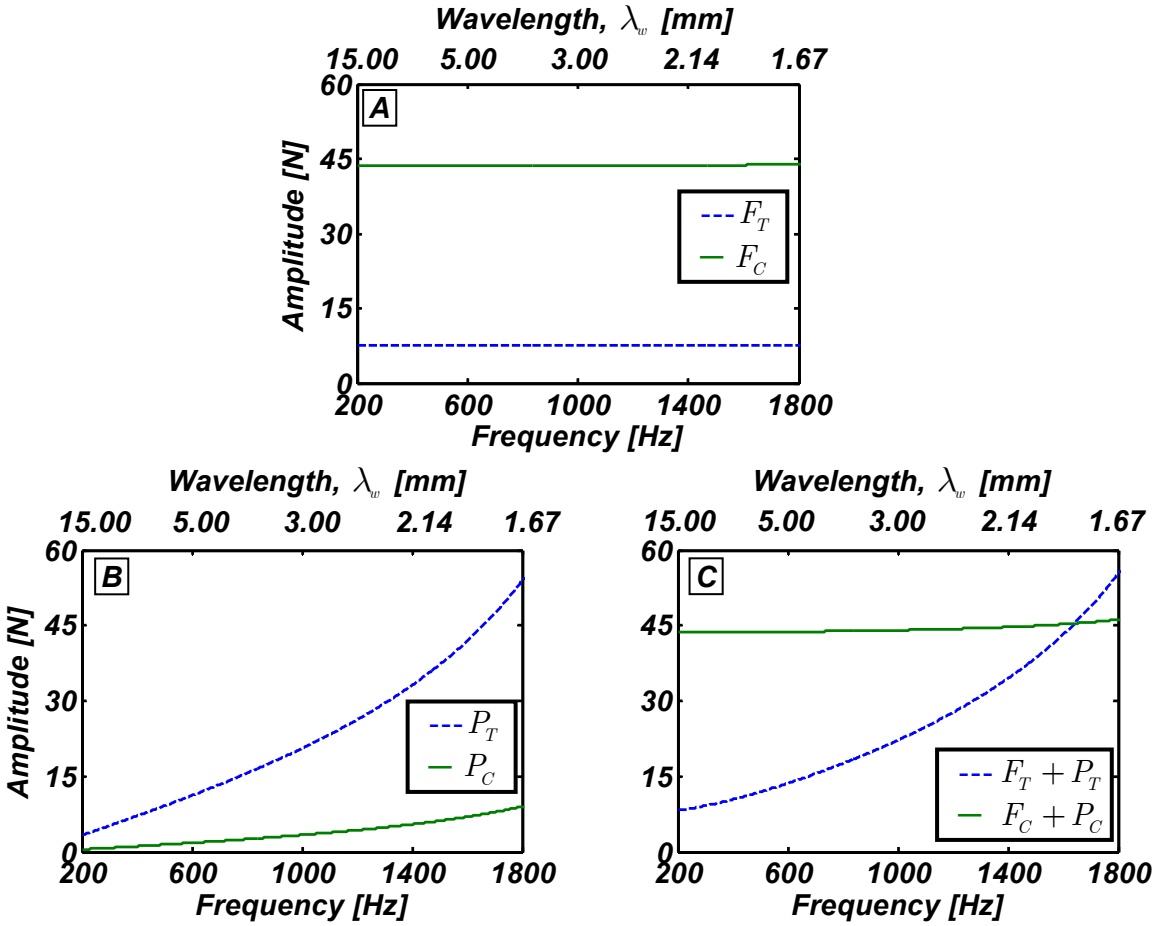

Figure 5-7: The amplitude of the forces as a function of the RTWD sinusoidal vibration frequency for wave generation. (A) Forces due to chip formation; (B) interference forces; (C) total cutting forces.

5.3 Orthogonal Cutting Force Modeling of Wave Removal

For the case of wave removing, the dynamic forces due to chip formation are given in Figure 5-8, and the shear angle in Figure 5-9. The same cutting conditions are used as in the example shown in Figures 5-2 to 5-4 except that now the unmachined workpiece surface is modulated at an amplitude of 0.05 mm about a nominal depth of cut of 0.15 mm, with $V_T = 0$. The interference forces are not shown, since they remain constant during wave removal because there is no relative motion in the thrust direction between the workpiece and the cutting tool. In the simulation, both the shear angle and the cutting force are in phase with the undeformed chip thickness at 600 Hz. This was also true when the frequency modulation of the unmachined workpiece surface was varied from 200-1800 Hz, and hence these results are not displayed.

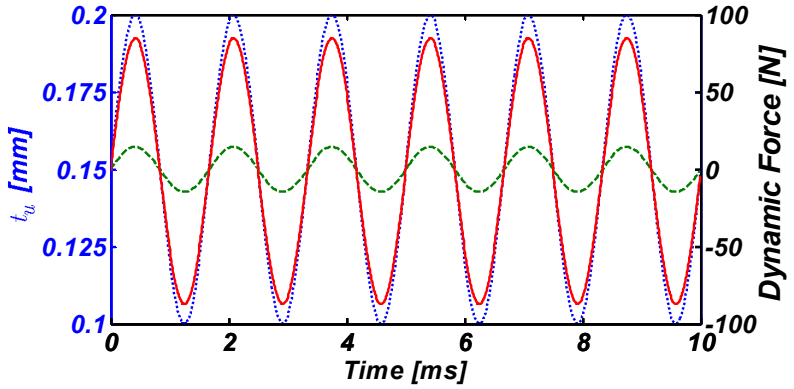

Figure 5-8: Dynamic force due to chip formation during wave removal. ····, Undeformed chip thickness, t_u; ——, force in the cutting direction, F_C; ---, force in the thrust direction, F_T.

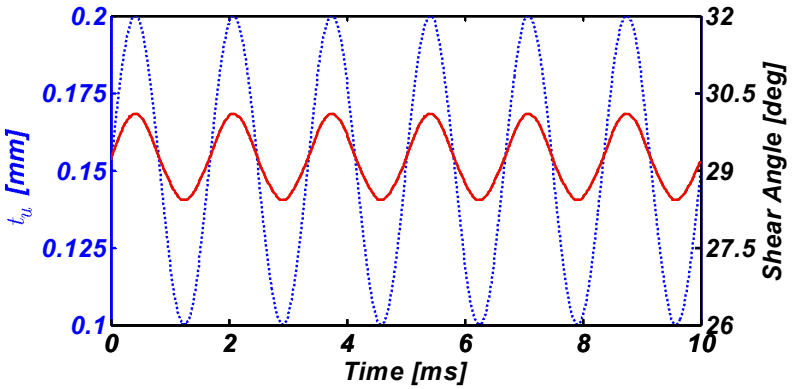

Figure 5-9: Shear angle during wave removal. ····, Undeformed chip thickness, t_u; ——, dynamic and quasi-static shear angles, ϕ_v and ϕ_0, respectively.

CHAPTER 6: THE REFINED DYNAMIC CUTTING FORCE MODEL

"The hypotheses we accept ought to explain phenomena which we have observed. But they ought to do more than this: our hypotheses ought to foretell phenomena which have not yet been observed."

–William Whewell

6.1 The General Formulation of the Forces Due to Chip Formation and Interference

Thus far, forces due to chip formation and interference between the tool and workpiece have been captured by a single "equivalent orthogonal cutting scenario." Historically this has been the approach in both quasi-static and dynamic cutting force modeling. This approach takes a relatively complicated cutting configuration and resolves it into a single simple oblique straight edge representation. This approach can be successful, especially if various "cutting force coefficients" are used to account for shortfalls in the geometric and material property modeling of the machining process. However, this type of approach will surely lead to a cutting force model that is application-specific because the cutting force coefficients are tuned to experimental data.

In this chapter a "refined cutting force model" will be introduced; this model employs a more rigorous description of dynamic cutting forces than was used in the simplified cutting force model. In general, this model relies upon integrating an "infinite" number of orthogonal cutting scenarios along the portion of tool nose that is engaged in the workpiece (e.g. the range $\theta_{0,3} \le \theta \le \theta_0$ in Figure 4-3), rather than attempting to resolve them into a single case. As a result, many parameters in the refined cutting force model have dependence on θ, where θ was defined along the region of the undeformed chip thickness (as was shown in Figure 4-3). These parameters have counterparts in the simplified cutting force model that have no dependence on θ since they were derived to describe the behavior of the entire cutting process with a single value.

As was discussed in the development of the previously presented simplified cutting force model, only forces along the **Y** and **Z** axes will be considered. These forces will be used in a dynamic simulation of a turning operation to excite a vibrating workpiece in order to study the

occurrence of chatter. This will be a separate effort from the dynamic cutting simulations using the forces generated by the simplified cutting force model introduced in Chapter 4, and comparisons between the two will be drawn in Chapter 8.

In the case of the refined dynamic cutting force model, the forces exerted upon the cutting tool due to chip formation along the **Y** and **Z** axes, refined versions of those in Equations (4.8) and (4.9), are given by

$$F_Y = \int_{Ang(Ind(1,Q),Ind(2,Q)}^{\theta_0} \left(f_{T,\theta} \sin\left[C_{S,\theta}^*\right] - f_{R,\theta} \cos\left[C_{S,\theta}^*\right] \right) r_n d\theta \tag{6.1}$$

$$F_Z = \int_{Ang(Ind(1,Q),Ind(2,Q)}^{\theta_0} f_{C,\theta} r_n d\theta \tag{6.2}$$

where for conciseness purposes, quantities with the subscript θ denote a dependence on θ and

$$f_{R,\theta} = \frac{f_{C,\theta}\left(\sin\left[i_\theta^*\right] - \cos\left[i_\theta^*\right]\sin\left[\alpha_{n,\theta}^*\right]\tan\left[\eta_{c,\theta}^*\right]\right) - f_{T,\theta}\cos\left[\alpha_{n,\theta}^*\right]\tan\left[\eta_{c,\theta}^*\right]}{\sin\left[i_\theta^*\right]\sin\left[\alpha_{n,\theta}^*\right]\tan\left[\eta_{c,\theta}^*\right] + \cos\left[i_\theta^*\right]} \tag{6.3}$$

$f_{C,\theta}$ and $f_{T,\theta}$ have units of force/length and are the cutting and thrust forces per unit width of cut (similar to F_C / w and F_T / w where F_C was given in Equation (4.37) and F_T in Equation (4.38)) and will be developed in the next section.

Now, the previously developed straight edge tool geometry given in Equations (4.1)-(4.6) for the simplified model (shown in red in Figure 4-1 and developed in [52]) is a function of θ given in Equations (6.4)-(6.9) (shown in blue in Figure 4-1). The direction of net force on a chip of differential width at an angle θ is measured relative to the side cutting edge and is given as

$$\eta_{0,\theta} = \pi - C_S - \theta \tag{6.4}$$

The projection of $\eta_{0,\theta}$ on the tool rake face is

$$\eta'_{0,\theta} = \cos^{-1}\left[\frac{\cot\left[\eta_{0,\theta}\right] - \tan\left[\alpha_n\right]\sin\left[i\right]}{\sqrt{\left(\cot\left[\eta_{0,\theta}\right]\sin\left[i\right] - \tan\left[\alpha_n\right]\right)^2 + \left(\csc\left[\eta_{0,\theta}\right]\cos\left[i\right]\right)^2}}\right] \tag{6.5}$$

and the effective side cutting edge at an angle, θ, is given as

$$C_{S,\theta}^{*} = C_S + \eta_{0,\theta} \tag{6.6}$$

The inclination angle is now

$$i_\theta^{*} = \sin^{-1}\left[\cos\left[\eta_{0,\theta}'\right]\sin[i] - \sin\left[\eta_{0,\theta}'\right]\sin[\alpha_n]\cos[i]\right] \tag{6.7}$$

with the rake angle being defined as

$$\alpha_{n,\theta}^{*} = \sin^{-1}\left[\frac{\sin[i] - \sin\left[i_\theta^{*}\right]\cos\left[\eta_{0,\theta}'\right]}{\sin\left[\eta_{0,\theta}'\right]\cos\left[i_\theta^{*}\right]}\right] \tag{6.8}$$

and the chip flow angle is given as

$$\eta_{c,\theta}^{*} = i_\theta^{*} \tag{6.9}$$

In Figure 6-1 the equivalent tool geometry parameters, i_θ^{*} and $\alpha_{n,\theta}^{*}$, are plotted as functions of θ on the interval $[0^\circ, 180^\circ]$ for the given tool geometry parameters: $\alpha_n = 5^\circ$, $i = 10^\circ$, and $C_S = 5^\circ$. The parameters were selected in order to describe how the equivalent tool geometry varies locally along the cutting tool. It should be noted that there is a discontinuity in both the inclination and rake angles at 175°, or more generally $180^\circ - C_S$. This is not a problem, however, since at this same angle, θ, there is a transition from the curved tool nose radius to the side cutting edge; hence the proposed approach is not valid anyway for the reasons discussed in Chapter 2. As stated in the assumptions in Chapter 2, the analysis in this dissertation is only being performed in machining operations along the tool nose; thus, this discontinuity will never be encountered. As a point of reference, the shaded red area in Figure 6-1 is a typical range of angles over which the nose of the cutting tool is engaged in the workpiece.

In a similar philosophy to the refinement of the forces due to chip formation, a more exact representation of the interference forces can be obtained by integrating along the portion of the tool edge engaged in the workpiece, given by

$$P_Y = \int_{Ang(Ind(1,Q),Ind(2,Q))}^{\theta_0} p_{T,\theta}\sin[\theta] r_n d\theta \tag{6.10}$$

$$P_Z = \int_{Ang(Ind(1,Q),Ind(2,Q))}^{\theta_0} p_{C,\theta} r_n d\theta \tag{6.11}$$

where the differential interference forces, $p_{C,\theta}$ and $p_{C,\theta}$ have units of force/length and will be described in a later section (similar to P_C / w and P_T / w with P_C and P_T given in Equation (3.61) and (3.62), respectively). It should be noted that all of the aforementioned quantities that have been denoted as having dependence on θ depend on many other parameters as well. However, for a given time step in a chatter simulation, all other quantities can be temporarily viewed as constant; hence there is sole dependence on θ when evaluating the dynamic cutting forces.

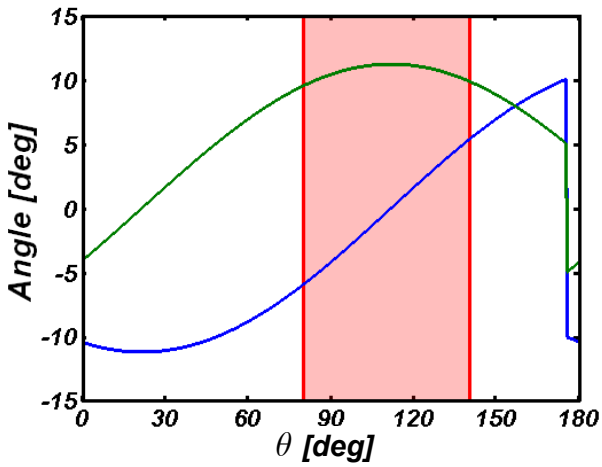

Figure 6-1: The equivalent tool geometry (not including C_S^*) as a function of the angle θ for $\alpha_n = 5^\circ$, $i = 10^\circ$, and $C_S = 5^\circ$. —, i_θ^*; —, $\alpha_{n,\theta}^*$.

6.2 Development of the Refined Approach to Describing Chip Formation Forces

Now the evaluation of the differential forces due to chip formation, $f_{C,\theta}$ and $f_{T,\theta}$, in Equations (6.1) and (6.2) will be presented in detail. This approach is slightly more involved than finding the forces due to chip formation in the simplified cutting force model because of the effect of a nonzero initial workpiece surface slope, δ_s. This is not to be confused with δ_s^*, which is the effective workpiece surface slope when relative vibration is present (resulting from the rotation transformation shown in Figure 4-8).

To motivate the need for an initial workpiece surface slope, first consider the diagram in Figure 4-3. Along the free surface of the chip, the majority of this boundary is prescribed by the previous three RTWDs of the tool: $y(t-\tau)$, $y(t-2\tau)$, and $y(t-3\tau)$. Only a small portion bounded by the angles θ_0 and θ_1 has a boundary that is defined by the unmachined surface of the workpiece. In the case of dynamic cutting with vibration, most of the machined surface will not have a slope of zero since when it was created the cutting tool likely had a nonzero vibration component in the radial ($\mathbf{Y}$) cutting direction. Based on this assertion, only the portion of the chip between θ_0 and θ_1 will have a zero initial workpiece slope.

Now consider the diagram in Figure 4-8A. If δ_s is nonzero then the quasi-static shear angle, ϕ_0, affects the undeformed chip thickness referenced from the tool tip, t', in the rotated quasi-static cutting representation in Figure 4-8B based on the following equation:

$$t'^* = \frac{t_u^* \sin[\delta_s + \phi_0]}{\sin[\phi_0]\cos[\delta_s^*]} \tag{6.12}$$

where δ_s^* in this case is no longer as it was presented in Equation (4.47) due to the nonzero initial workpiece surface slope, δ_s, and is given by

$$\delta_s^* = \delta_s - \delta_V \tag{6.13}$$

As discussed in the previous section, the refined approach integrates along the cutting zone to describe forces in a more precise manner, and hence t'^*, δ_s^*, δ_s, and ϕ_0 must now have dependence on θ. In addition, δ_s will be shown to have dependence on W as well, since it is defined by the relative velocity between the workpiece and the cutting tool at time, $t - W\tau$. Equations (6.12) and (6.13) now become

$$t'_\theta = \frac{t_u(\theta,W)\sin[\delta_s(\theta,W) + \phi_{0,\theta}]}{\sin[\phi_{0,\theta}]\cos[\delta_s^*(\theta,W)]} \tag{6.14}$$

where δ_s^* has become a function of W as well, and is given by

$$\delta_s^*(\theta,W) = \delta_s(\theta,W) - \delta_{V,\theta} \tag{6.15}$$

where $t_u(\theta,W)$ is either $t_{u,A}(\theta,W)$ or $t_{u,B}(\theta)$, depending on whether θ is in a type A or type B region, and $\delta_{V,\theta}$ is

$$\delta_{V,\theta} = -\tan^{-1}\left[\frac{\dot{y}(t)\sin[\theta]}{\bar{V}_C - \dot{z}(t)}\right] \tag{6.16}$$

It should be noted that $t_u(\theta,W)$ and t'_θ are not called $t^*_u(\theta,W)$ and t'^*_θ (akin to t^*_u and t'^* in Figure 4-8) since they are an exact representation of the undeformed chip thickness at an angle along the cutting zone, θ. They are not approximations based on trying to resolve the entire undeformed chip area into a single undeformed chip thickness, as was done for the simplified cutting force model.

The final element needed is the workpiece surface slope as a function of θ and W, $\delta_s(\theta,W)$. To derive this relationship, the exhibit shown in Figure 6-2 is used. Each picture depicts the same cutting scenario from a different viewing angle. At each time $t-W\tau$ ($0 \le W \le D$ and $D \in \mathbb{Z}$), based on the amount of relative tool-workpiece velocity in the $\mathbf{Y}$ direction, the entire surface generated by the curved tool edge will have the same radial complimentary workpiece surface slope, $\delta'_{s,comp}(W)$. It is taken to be the angle between a line tangent to the machined surface and the negative radial cutting direction (directed into the workpiece), as shown in detail for the tool position at $t-(W+1)\tau$ in Figure 6-2B. The subscript "$comp$" is used to denote a complimentary angle measurement.

In Figure 6-2B, a portion of a machined workpiece surface is shown over three revolutions. When the machined surface was generated at time $t-(W+1)\tau$, there was zero relative velocity in the $\mathbf{Y}$ direction between the cutting tool and the workpiece; hence, the complementary surface slope at all points along the machined surface at this time is 90°. However, when the cutting tool generated the machined surface at time $t-W\tau$, it had a velocity component in the $-\mathbf{Y}$ direction and created a sloped surface, with $\delta'_{s,comp}(W) \neq 0$. It should be noted that $\delta'_{s,comp}(W)$ is purely a function of W since all points on the free boundary of the undeformed chip area defined by a previous relative tool-workpiece velocity at a time in the regenerative delay space have the same slope

within the **YZ** plane. In fact, $\delta'_{s,comp}(W)$ is function of time as well, but as previously mentioned since so many parameters in the cutting model depend on time, it is not stated explicitly for conciseness.

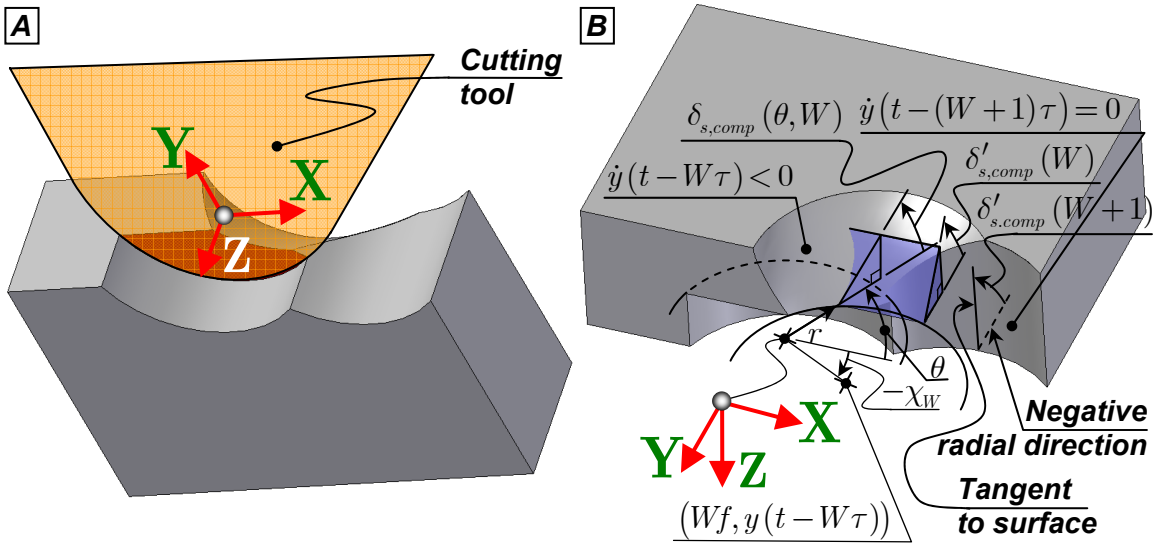

Figure 6-2: A schematic demonstrating the influence of vibration at times in the regenerative delay space on the workpiece surface slope, $\delta_{s,\theta}$. (A) A view from the bottom showing the chip area currently being removed in dark red; (B) a top view showing the geometry needed to find the complimentary radial workpiece surface slope, $\delta'_{s,comp}(W)$.

The complementary workpiece surface slope, $\delta'_{s,comp}(W)$, is purely a function of the tool behavior at the time that the surface was generated and is given as

$$\delta'_{s,comp}(W)=\begin{cases}-\tan^{-1}\left[\dfrac{\bar{V}_C-\dot{z}(t-W\tau)}{\dot{y}(t-W\tau)}\right] & \dot{y}(t-W\tau)<0\\ \pi-\tan^{-1}\left[\dfrac{\bar{V}_C-\dot{z}(t-W\tau)}{\dot{y}(t-W\tau)}\right] & \text{otherwise}\end{cases} \tag{6.17}$$

In Figure 6-2B the cylindrical coordinates, r, θ, and **Z** correspond to a particular point along the undeformed chip area with free boundary defined by the W^{th} previous RTWD at time $t-W\tau$. At this point, a right triangular prism having an angular elevation of $\delta'_{s,comp}(W)$ is tangent to the workpiece surface, as shown in the figure. The complementary polar workpiece surface slope, $\delta_{s,comp}(\theta,W)$, is the elevation of a cross section of the right triangular prism projected onto the $r-\mathbf{Z}$ plane at the polar coordinate θ and is given as

$$\delta_{s,comp}(\theta,W)=\begin{cases}\cos^{-1}\left[\dfrac{1}{\sqrt{1+\left(\sin[\theta]\tan\left[\delta'_{s,comp}(W)\right]\right)^2}}\right] & \delta'_{s,comp}(W)<\dfrac{\pi}{2}\\ \cos^{-1}\left[-\dfrac{1}{\sqrt{1+\left(\sin[\theta]\tan\left[\delta'_{s,comp}(W)\right]\right)^2}}\right] & \text{otherwise}\end{cases} \tag{6.18}$$

By definition, $\delta'_{s,comp}(W)$ is $\pi/2$ radians along the region of the undeformed chip area defined by the unmachined workpiece surface. Finally, it should be realized that the parameter that was originally needed before this analysis began, $\delta_s(\theta,W)$, is simply the complement of $\delta_{s,comp}(\theta,W)$, which is described by

$$\delta_s(\theta,W)=\frac{\pi}{2}-\delta_{s,comp}(\theta,W) \tag{6.19}$$

It should be noted that $\delta_s(\theta,W)$ could have been derived more directly by not finding complimentary angles, but it was easier to present the derivation graphically in this manner.

In order to compute Equation (6.14), the quasi-static shear angle at a given angular position, $\phi_{0,\theta}$, must be known. However it cannot be found until the system is rotated (e.g. Figure 4-8B) and the dynamic shear angle, $\phi_{V,\theta}$, is found by evaluating S_{ϕ_V}. In the development of the Oxley cutting force model in Chapter 3, S_{ϕ_V} was a function of t', α_n, $\left|\vec{V}_C\right|$, and δ_s. Now t'_θ, $\alpha^{**}_{n,\theta}$, $V^*_{C,\theta}$, and $\delta^*_s(\theta,W)$ are used in place of t', α_n, $\left|\vec{V}_C\right|$, and δ_s, respectively, to describe an oblique nose radius cutting scenario with vibration by using the quasi-static Oxley orthogonal cutting force model located at an angle along the undeformed chip area, θ. The effective cutting speed, $V^*_{C,\theta}$ is given as

$$V^*_{C,\theta}=\sqrt{\left(\bar{V}_C-\dot{z}(t)\right)^2+\left(\dot{y}(t)\sin[\theta]\right)^2} \tag{6.20}$$

and the effective rake angle modified by dynamic effects, $\alpha^{**}_{n,\theta}$, is given as

$$\alpha^{**}_{n,\theta}=\alpha^{*}_{n,\theta}+\delta_{V,\theta} \tag{6.21}$$

Hence, an iterative procedure is used to find $\phi_{0,\theta}$ and is depicted as a flowchart in Figure 6-3.

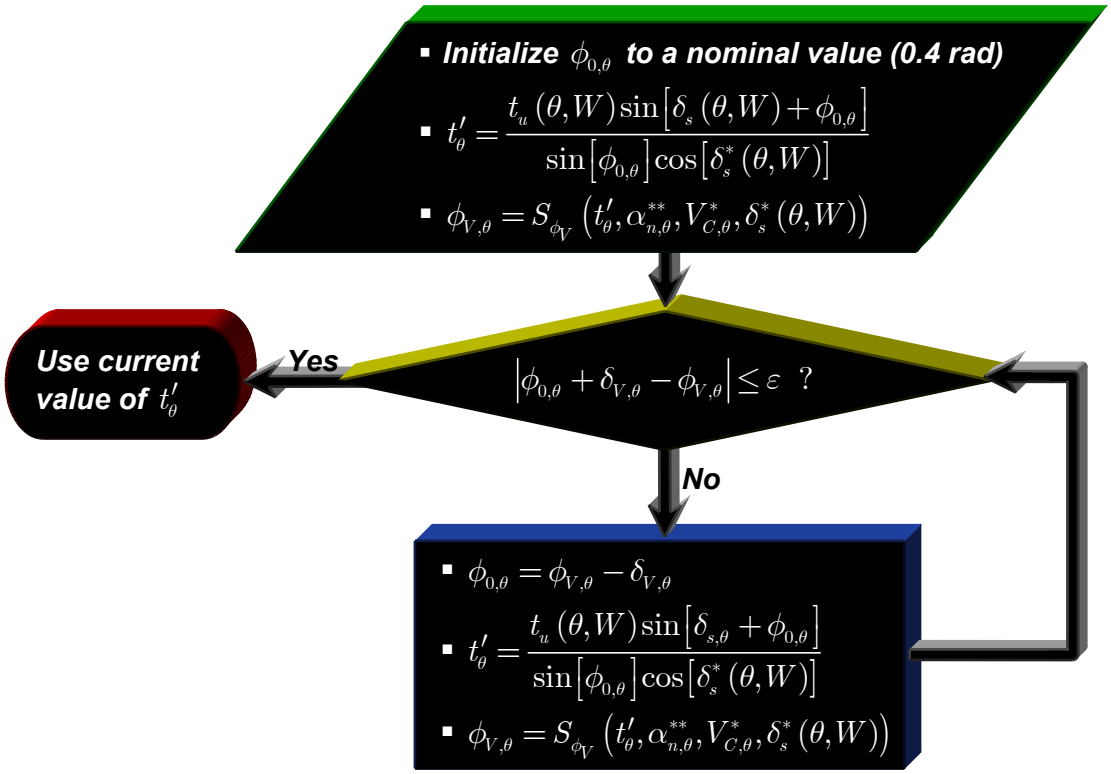

Figure 6-3: Flowchart for determining t'_θ with a initial workpiece surface slope.

The iteration begins by initializing a value of 0.4 radians for $\phi_{0,\theta}$ and using it to compute t'_θ, which is then used as an input to the regression surface S_{ϕ_V} (the other input parameters, $\alpha_{n,\theta}^{**}$, $V_{C,\theta}^*$, and $\delta_s^*(\theta,W)$ are known at this point). The output of S_{ϕ_V} is $\phi_{V,\theta}$, the shear angle measured from the direction of net relative velocity between the workpiece and the cutting tool. Now with initial guesses for $\phi_{0,\theta}$ and $\phi_{V,\theta}$, the iteration begins.

The decision box in the flow chart calculates the absolute error between the right and left hand sides of the following equation

$$\phi_{V,\theta} = \phi_{0,\theta} + \delta_{V,\theta} \tag{6.22}$$

which is how these angles were defined originally in Figure 4-8. If Equation (6.22) is satisfied within a specified tolerance, ε, then $\phi_{0,\theta}$ is sufficiently accurate and the iteration terminates, using the current value of t'_θ for future calculations. It should be noted that for a zero initial workpiece surface slope, $\delta_s = 0$, the algorithm converges in a single iteration. This explains why in the

simplified cutting force model that assumed δ_s to be zero, it was not necessary to iterate when determining ϕ_0.

With the value of t'_θ determined, the differential thrust and cutting forces per unit width of cut at an angle, θ, can be found, which are given as

$$f_{C,\theta} = f'_{C,\theta} \cos\left[\delta_{v,\theta}\right] - f'_{T,\theta} \sin\left[\delta_{v,\theta}\right] \tag{6.23}$$

$$f_{T,\theta} = f'_{C,\theta} \sin\left[\delta_{v,\theta}\right] + f'_{T,\theta} \cos\left[\delta_{v,\theta}\right] \tag{6.24}$$

where $f'_{C,\theta}$ and $f'_{T,\theta}$ are differential cutting and thrust forces per unit width of cut along the $\mathbf{C}'$ - $\mathbf{T}'$ axes in a rotated, quasi-static orthogonal modeling configuration, described by

$$f'_{C,\theta} = S_{f_C}\left(t'_\theta, \alpha^{**}_{n,\theta}, V^*_{C,\theta}, \delta^*_s(\theta, W)\right) \tag{6.25}$$

$$f'_{T,\theta} = S_{f_T}\left(t'_\theta, \alpha^{**}_{n,\theta}, V^*_{C,\theta}, \delta^*_s(\theta, W)\right) \tag{6.26}$$

To understand how the force exerted upon the cutting tool varies with θ along the cutting zone, three cutting scenarios with different regenerative position spaces are presented in Figure 6-4. These three configurations all occurred at a point in time during a chatter simulation using the refined dynamic cutting force model. The corresponding differential forces due to chip formation as well as the dynamic shear angle are plotted as a function of θ in Figure 6-4A,C, and E, with the undeformed chip area showing influence from various RTWDs in the regenerative position space as depicted in Figure 6-4B,D, and F. The differential forces in the $\mathbf{Y}$ and $\mathbf{Z}$ directions, $\partial F_Y / \partial\theta$ and $\partial F_Z / \partial\theta$, would be found by taking the partial derivative with respect to θ of Equations (6.1) and (6.2), respectively. For the differential force exerted in each direction as well as the dynamic shear angle, there are three traces; each one is for a different relative velocity in the $\mathbf{Y}$ direction at the current time, t, all with $\dot{z}(t) = 0$: $\dot{y}(t) = -0.3\ [m/s]$, $\dot{y}(t) = 0\ [m/s]$, and $\dot{y}(t) = 0.3\ [m/s]$. From the definition of $y(t)$ (and in turn $\dot{y}(t)$ through differentiation) a positive value indicates that the cutting tool is moving away relative to the workpiece. As one would intuitively expect, for the

three different cutting conditions shown in Figure 6-4A,C, and E, when the tool is moving away the differential forces are smaller, and vice versa.

Figure 6-4A and B illustrate the case that would exist for zero vibration cutting. Figure 6-4C and D depicts a case where there has been nonzero relative vibration in the regenerative position space, and the differential forces due to chip formation are much higher than in the case of Figure 6-4A due to the larger undeformed chip area. Figure 6-4E and F shows another case of nonzero relative vibration in the regenerative position space; this time it has a much smaller undeformed chip area and corresponding differential forces.

It is important to note that the derivatives of $\partial F_Y / \partial \theta$ and $\partial F_Z / \partial \theta$ are only sectionally smooth. This will be important in future developments when numerical integration of Equations (6.1) and (6.2) is discussed in Chapter 7. The number of discontinuities is equal to one less than the total number of angular intersections between tool nose positions in the regenerative delay space that are relevant to the description of the undeformed chip area, or the quantity Q, which was developed previously in the algorithm shown in Figure 4-6.

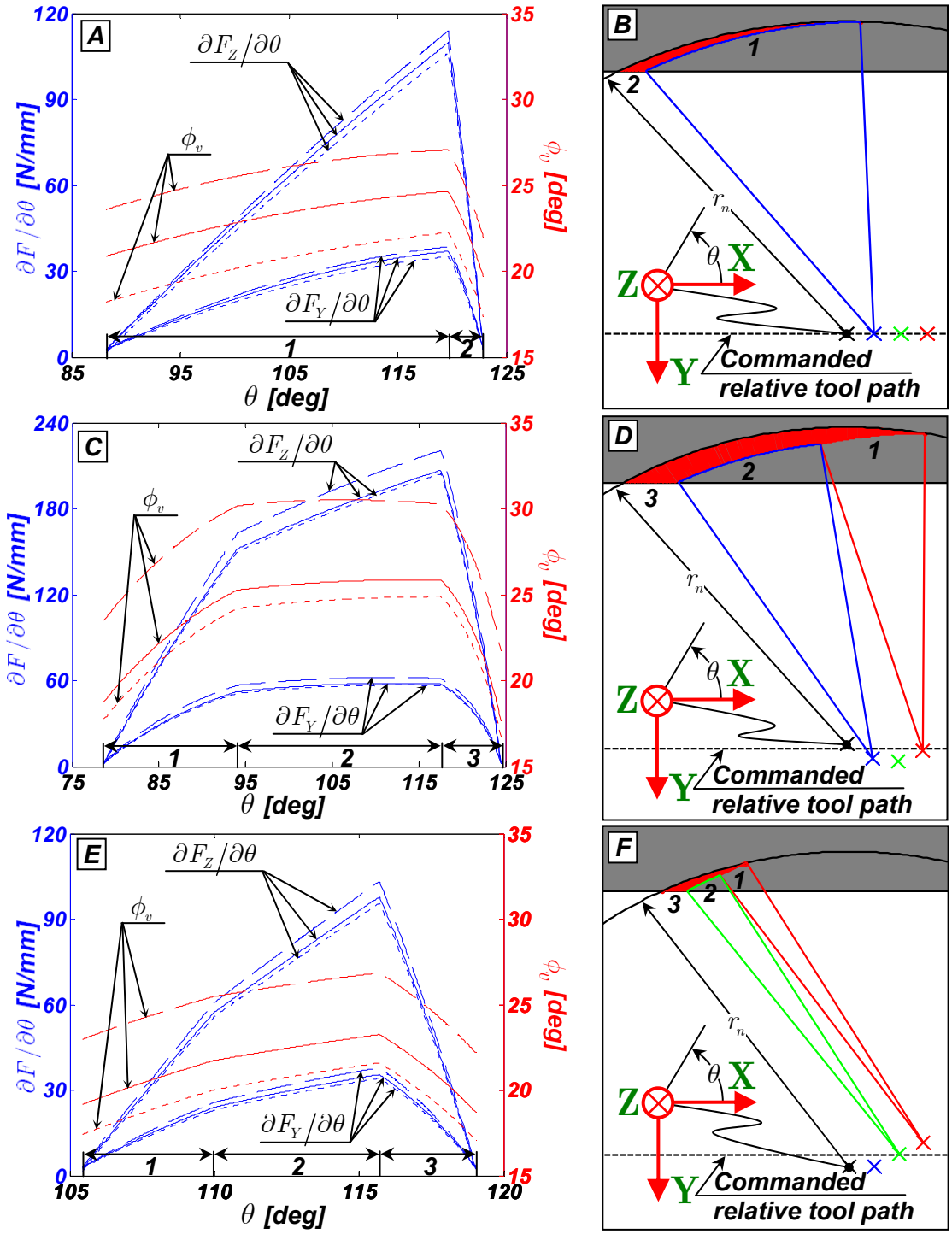

Figure 6-4: $\partial F_Z/\partial\theta$, $\partial F_Y/\partial\theta$, and ϕ_V as a result of various conditions on the relative radial velocity, $\dot{y}(t)$. Cutting conditions used: $\bar{V}_C = 3.30[m/s]$, $f = 0.0762$ $[mm]$, $d_c = 0.191$ $[mm]$, $r_n = 1.19$ $[mm]$, $\alpha_n = -3^\circ$, $i = 10^\circ$, and $C_s = 5^\circ$. The forces are shown in **blue** and the dynamic shear angle in **red**; ---, $\dot{y}(t) = -0.3$ $[m/s]$; —, $\dot{y}(t) = 0$ $[m/s]$; — — —, $\dot{y}(t) = 0.3$ $[m/s]$. (A),(B), The differential forces due to chip formation and the dynamic shear angle for zero relative vibration history; (C),(D) the differential forces due to chip formation and the dynamic shear angle for a nonzero regenerative position space. (E),(F) the differential forces due to chip formation and the dynamic shear angle for a nonzero regenerative position space.

6.3 Development of the Refined Approach to Describing Interference Forces

Similar in philosophy to what was done for the forces due to chip formation, a higher fidelity model for describing the interference forces by integrating along the chip formation zone will now be presented. This is in contrast to the simplified approach that resolved the cutting scenario into a single equivalent orthogonal cutting process that was used to derive interference forces. Figure 6-5B shows a diagram of the turning process along with a magnification of the portion along the cutting tool where plowing and flank interference occur.

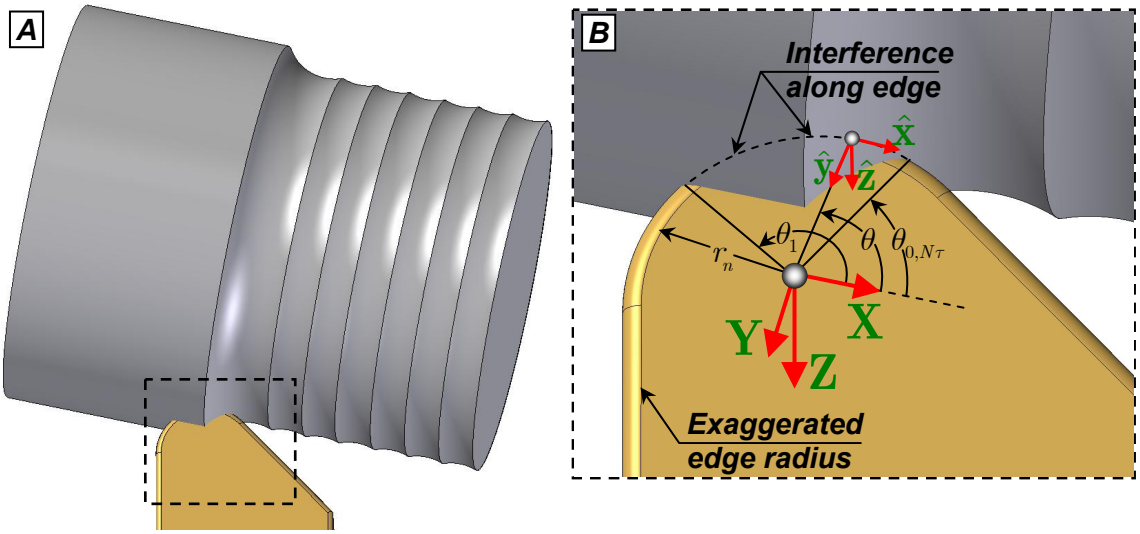

Figure 6-5: A schematic showing the region where plowing and flank interference occur along the tool edge. (A), A wide-field view of a partially machined workpiece; (B), a close-up view of the cutting zone.

Previously, a 2nd order polynomial was generated based on the relative vibration history used to describe the undeformed workpiece surface in $\hat{y}-\hat{z}$ coordinates; this was given in Equation (3.32). However, there is one fundamental error with this approach. The lack of dependence on θ, suggests that the cross section of the interference volume, i.e. the interference area, between the cutting tool and the workpiece is constant along the entire portion cutting zone. In Figure 6-5B, the cutting zone is defined from $\theta_{0,N}$ to θ_0, where the range for N was given in Equation (4.12) with the particular value of N depending on the nature of the regenerative position space. In the straight edge orthogonal cutting scenario depicted in Figure 3-2, the assumption of a constant interference area was valid since there is a one to one correspondence between the RTWDs, $y(t)$ and $z(t)$, and

the undeformed workpiece surface, $y_{sur}(\hat{z})$, along the entire length of the entire tool edge. In the case of machining with a tool nose radius this is no longer true, as will be shown by using the exhibit in Figure 6-6.

A cutting edge having a tool nose radius of r_n, shown as a solid line, is engaged in the workpiece and removes a semicircular slot as it travels in the **Z** direction. For the sake of keeping this a planar analysis, assume that the cutting tool instantaneously jumps a distance of $-a$ into the workpiece to assume the position denoted by the dashed line (a has a negative value in this example).

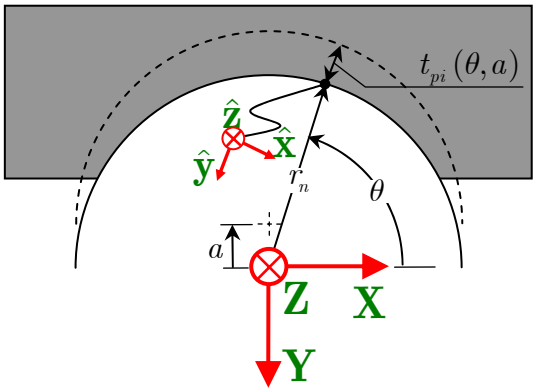

Figure 6-6: A diagram showing how penetration varies with the angle along the cutting edge, θ.

The planar interference, $t_{pi}(\theta,a)$, as denoted in Figure 6-6, between the cutting tool and the workpiece is given by

$$t_{pi}(\theta,a)=\sqrt{r_n^2-\frac{a^2}{2}(\cos[2\theta]+1)}-a\sin[\theta]-r_n=\hat{y}_{pi}(\theta,a) \tag{6.27}$$

which can be interpreted as the equation for the solid semicircle subtracted from the equation for the dashed semicircle. The $\hat{\mathbf{x}}\hat{\mathbf{y}}\hat{\mathbf{z}}$ reference frame is oriented at an angle, θ, and a distance, r_n, from the **XYZ** reference frame. Therefore Equation (6.27) is equivalent to the planar interference between the two semicircles along the $\hat{y}$ axis, $\hat{y}_{pi}(\theta,a)$. In this way, a relationship is established between the RTWD in the radial direction, a, and the interference in $\hat{y}$ coordinates as a function of θ. However, this equation requires modification because for positive values of a, $t_{pi}(\theta,a)$ can become negative and it is not physically valid for the cutting tool to have negative interference with the

workpiece. In addition, when applied to the interference between the cutting tool and the undeformed workpiece surface, Equation (6.27) needs to be reformulated to reflect displacements in the tangential cutting direction, **Z** (or $\hat{z}$ direction in Figure 3-5 or Figure 6-5).

If there is no relative vibration between the workpiece and the cutting tool, then the same interference area exists along the entire portion of the tool nose that is engaged in the workpiece. Therefore the equation describing the undeformed workpiece surface in $\hat{y}-\hat{z}$ coordinates has no dependence on θ or $\hat{z}$, and is given by

$$\hat{y}_{sur,static} = -r_e \cos\left[\overline{\beta}_e\right] \tag{6.28}$$

and would correspond to the undeformed workpiece surface pictured in Figure 3-2A at all angles, θ. The subscript "*static*" denotes the workpiece interference that exists during quasi-static, zero relative vibration cutting.

What needs to be captured by an equation having the general form of Equation (6.27) is the deviation from the undeformed workpiece surface in zero vibration cutting (given in Equation (6.28)) from $\theta = \pi/2$ as a function of θ. To accomplish this, the coefficient, a_0, in Equation (3.32) can be separated into two components

$$a_0 = \underbrace{a_{0,dyn}}_{\substack{\text{deviation from} \\ \text{zero vibration}}} + \underbrace{\hat{y}_{sur,static}}_{\text{zero vibration}} \tag{6.29}$$

where $a_{0,dyn}$ represents the portion that is a deviation from $\hat{y}_{sur,static}$ when there is relative tool-workpiece vibration. It should be noted that $a_{0,dyn}$ as well as the other previously developed coefficients, a_1 and a_2, take on nonzero values only when there is relative tool workpiece vibration. Therefore, the polynomial representing the component of the undeformed workpiece surface that is a deviation from zero vibration cutting, $\hat{y}_{sur,dyn}(\hat{z})$, can be input into Equation (6.27) in place of a to yield

$$\hat{y}_{sur,exact}(\theta,\hat{z}) = \hat{y}_{pi}\left(\theta, \hat{y}_{sur,dyn}(\hat{z})\right) + \hat{y}_{sur,static} = \sqrt{r_n^2 - \frac{\hat{y}_{sur,dyn}(\hat{z})^2}{2}\left(\cos[2\theta]+1\right)} + \hat{y}_{sur,dyn}(\hat{z})\sin[\theta] - r_n + \hat{y}_{sur,static} \tag{6.30}$$

where the subscript "dyn" in $\hat{y}_{sur,dyn}(\hat{z})$ denotes dynamic cutting with relative tool workpiece vibration and is defined as

$$\hat{y}_{sur,dyn}(\hat{z}) = a_0 - \hat{y}_{sur,static} + a_1\hat{z} + a_2\hat{z}^2 \tag{6.31}$$

This new expression for the undeformed workpiece surface is called "$\hat{y}_{sur,exact}(\theta,\hat{z})$" because it is an exact geometric representation of the undeformed workpiece surface along the cutting zone, assuming that the undeformed workpiece surface at $\theta = \pi/2$ can be represented by a second order polynomial. The problem with this description is that it is no longer a polynomial in $\hat{z}$ like in Equation (3.32), so previously derived equations will become drastically more complicated and more elements will have to be numerically evaluated. Fortunately, a relatively good approximation can be made to obtain a polynomial approximation of Equation (6.30) because of practical constraints on its constitutive parameters.

Typically $r_n \gg \left|\hat{y}_{sur,dyn}(\hat{z})\right|$ over the range of value in the $\hat{z}$ direction where it is defined, which means that $\hat{y}_{sur,exact}(\theta,\hat{z})$ can be approximated as $\hat{y}_{sur}(\theta,\hat{z})$, given as

$$\hat{y}_{sur,exact}(\theta,\hat{z}) \approx \hat{y}_{sur}(\theta,\hat{z}) = \hat{y}_{sur,dyn}(\hat{z})\sin[\theta] + \hat{y}_{sur,static} \tag{6.32}$$

which can be expanded to be rewritten as a polynomial in $\hat{z}$ as

$$\hat{y}_{sur}(\theta,\hat{z}) = \left(a_0 - \hat{y}_{sur,static} + a_1\hat{z} + a_2\hat{z}^2\right)\sin[\theta] + \hat{y}_{sur,static} = a_{0,\theta} + a_{1,\theta}\hat{z} + a_{2,\theta}\hat{z}^2 \tag{6.33}$$

where

$$a_{0,\theta} \triangleq \left(a_0 + r_e\cos\left[\overline{\beta}_e\right]\right)\sin[\theta] - r_e\cos\left[\overline{\beta}_e\right]$$

$$a_{1,\theta} \triangleq a_1\sin[\theta]$$

$$a_{2,\theta} \triangleq a_2\sin[\theta]$$

To determine the accuracy of this approximation, it is compared to the exact formulation in Equation (6.30) for a given undeformed workpiece surface. The relative percent error between them is given by

$$100\left|\frac{\hat{y}_{sur,exact}(\theta,\hat{z})-\hat{y}_{sur}(\theta,\hat{z})}{\hat{y}_{sur,exact}(\theta,\hat{z})}\right|$$

and is plotted as a function of θ and $\hat{z}$ in Figure 6-7.

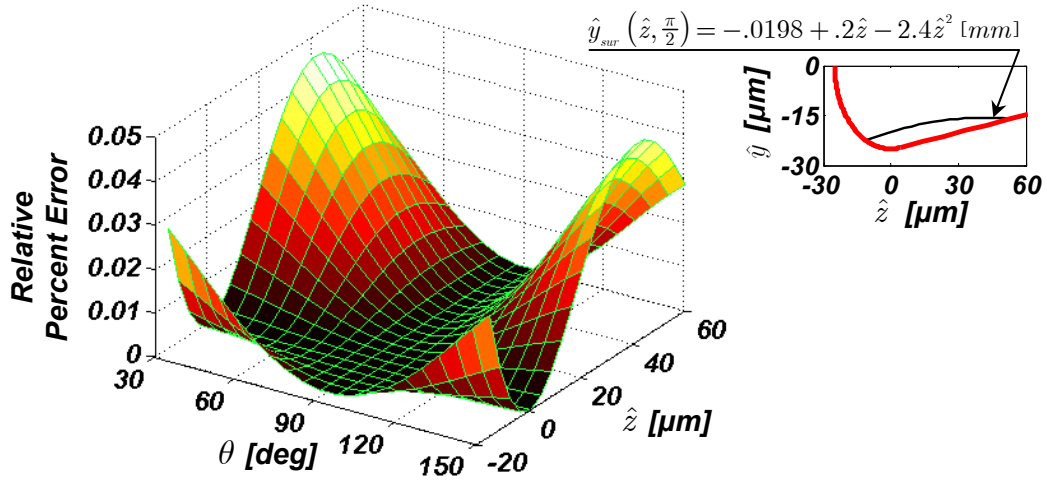

Figure 6-7: The relative percent error by using Equation (6.33) to approximate Equation (6.30) with an inset showing the undeformed workpiece surface at $\theta = 90^\circ$.

The undeformed workpiece surface used is shown as an inset in Figure 6-7, and r_n was taken to be 0.79 mm, a nominal value for typical turning applications. It should be noted that the error is the lowest for values of θ near 90° because both equations reduce to Equation (3.32) at this angle. This is the angle along the tool nose where the undeformed workpiece surface coefficients, a_0, a_1, and a_2, were defined originally. For a larger tool nose radius (1.19 mm) the entire plot would look similar except that the errors improve and would be scaled such that the largest error is around 0.03%. A smaller tool nose radius of 0.40 mm would scale the entire plot such that the largest error is around 0.1%. It should be noted that the type of undeformed workpiece surface shown in the inset is a relatively large departure from $\hat{y}_{sur,static}$ and represents an extreme case. In order to obtain an undeformed workpiece surface like this in a simulation, an extremely low cutting speed and large displacements in the radial cutting direction would have to occur. Consequently this plot represents an upper bound on the type of error to expect from this approximation when used to simulate practical machining scenarios.

Based on the confirmed validity of the approximation, Equation (6.33) is now used for the description of the undeformed workpiece surface in the refined approach to the description of the interference forces. If there is any relative tool-workpiece vibration present, there will be a departure from describing the undeformed workpiece surface with Equation (6.28) and the interference volume will be comprised of variable interference area cross sections. To better understand how the cross section of the interference volume changes with varying angle, θ, consider Figure 6-8. The scaling of the tool edge radius relative to the tool nose radius has been increased dramatically for illustration purposes. Typically the ratio r_n / r_e is on the order of 20-40:1 or higher, and in Figure 6-8 it is 8:5. Additionally, the interference volume has been plotted over the range $0 < \theta < \pi$, which typically is larger than would be encountered in a practical machining scenario.

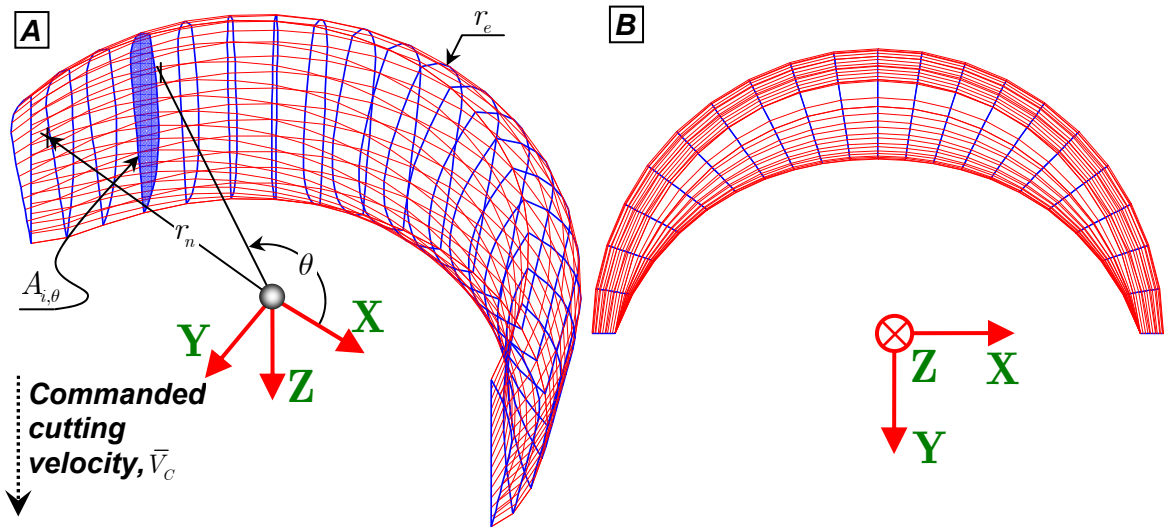

Figure 6-8: An example of an interference volume, V_i, along the cutting edge with an exaggerated tool edge radius. (A) Isometric view; (B) top view.

Figure 6-8A is an isometric view of an interference volume, V_i. The interference cross section of the interference volume at $\theta = 0, \pi$ is the same as the one that exists in an orthogonal cutting scenario with zero vibration, e.g. Figure 3-2A. This conceptually makes sense because regardless of how much the tool vibrates, there is no component of that velocity traveling in the workpiece at $\theta = 0, \pi$. In this example, at $\theta = \pi / 2$ the interference area, $A_{i,\theta}$, is maximum based on the vibration history.

In Figure 6-9 are cross sections of the interference volume in Figure 6-8 superimposed on one another. Each cross section is defined in the $\hat{y}-\hat{z}$ plane as the area between the undeformed workpiece surface and the boundary of the cutting tool at a particular angle, θ. The darkest lines represent the undeformed workpiece surface close to $\theta = 0^\circ$, 180° and the lightest ones are for $\theta = 90^\circ$. The direction and relative magnitude of the net differential interference force (force per unit width of cut, i.e. Equations (3.59) and (3.60)) for each interference volume cross section are shown as well, with the color matching that of its respective cross sectional interference area. The lengths of the vectors are all scaled relative to one another. It should be noted that because vibration along the axis of the workpiece has been neglected, there is symmetry in the differential forces developed along the interference volume. In this case, the amount of penetration into the region of the cutting tool by the undeformed workpiece surface is much larger than would be encountered in practice.

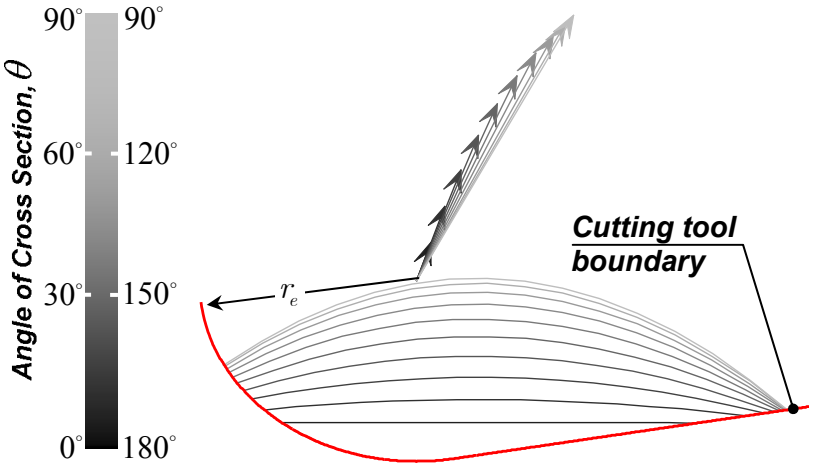

Figure 6-9: Cross-sections of the interference volume in Figure 6-8 superimposed on one another as well as the net interference force vectors shown as arrows.

Another interference volume is shown in Figure 6-10 along with its corresponding cross-sections in Figure 6-11 based on a different undeformed workpiece surface. However, the amount of interference between the undeformed workpiece surface and the cutting tool in Figure 6-11 is far more realistic than that in Figure 6-9.

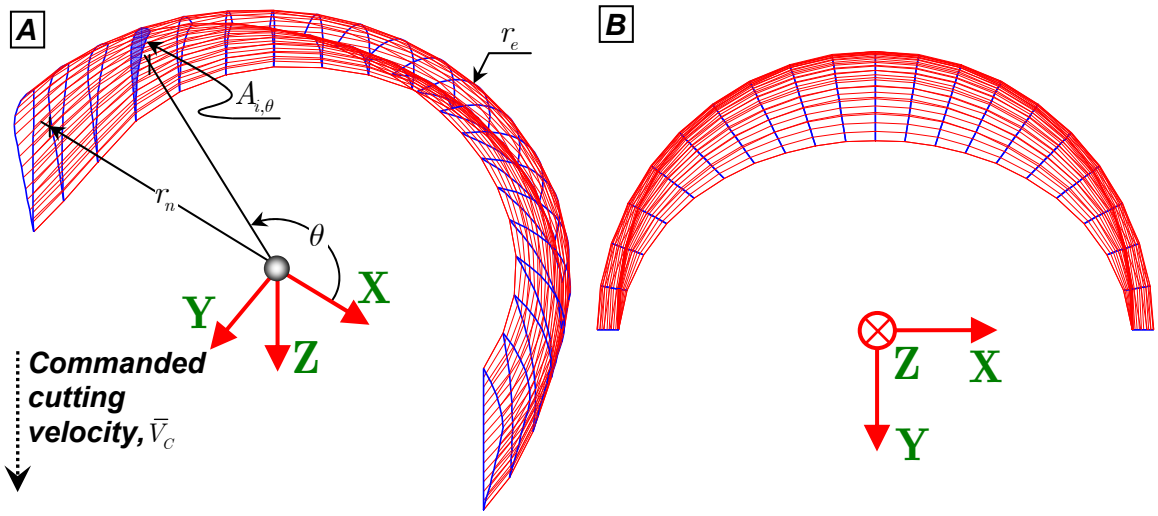

Figure 6-10: Another example of an interference volume, V_i, along the cutting edge with an exaggerated scaling of the tool edge radius. (A) Isometric view; (B) top view.

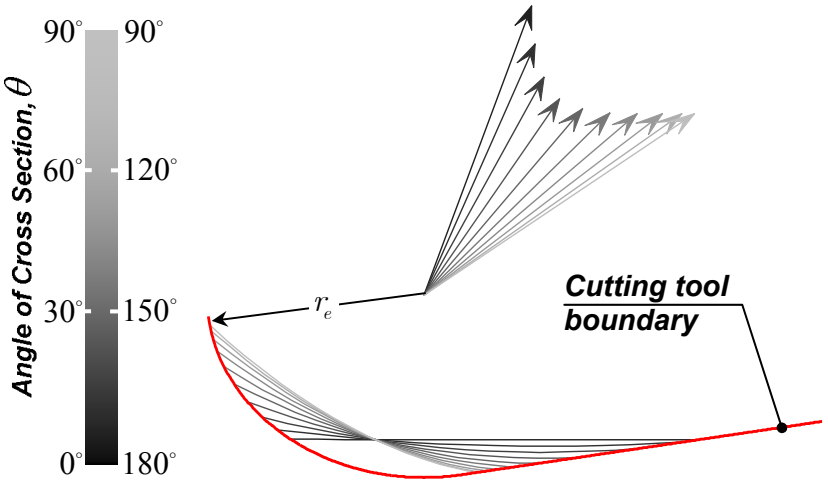

Figure 6-11: Cross-sections of the interference volume in Figure 6-10 superimposed on one another as well as the net interference force vectors shown as arrows.

Another parameter that needs to be modified in this analysis is the angle of material separation, β_e. Previously when presenting results in the simplified dynamic cutting force model, β_e was derived through the process of trying to obtain a single approximation to the interference occurring along the entire tool edge (Equation (4.46)). For the refined cutting force model, it is desirable to fit a second order polynomial to the undeformed workpiece surface at $\theta = \pi/2$, the point along the cutting edge where there is a one to one correspondence between relative tool motion and interference with the workpiece. In this case, the angle of material separation is given as

$$\beta_e(t) = \overline{\beta}_e + \tan^{-1}\left[\frac{\dot{y}(t)}{\overline{V}_C - \dot{z}(t)}\right] \tag{6.34}$$

Previously Equations (3.29) and (3.30) were developed to describe the interference forces by resolving the cutting process into a single orthogonal cutting scenario in Equations (4.51) and (4.53). In the more refined approach, differential interference forces will be resolved at an infinite number of angular coordinates, θ, around the cutting zone, and the net interference force will be computed via integration. In this way, differential interference forces, $p'_{C,\theta}$ and $p'_{T,\theta}$ in a reference frame rotated by γ^*_θ with units of force/length are

$$p'_{C,\theta} = \mu K_{cf} A_{i,\theta} \tag{6.35}$$

$$p'_{T,\theta} = K_{cf} A_{i,\theta} \tag{6.36}$$

By employing a rotation transformation similar to that used to generate Equations (3.59) and (3.60) in the simplified cutting force model, the differential forces in the thrust and cutting directions are given as

$$p_{T,\theta} = K_{cf} A_{i,\theta} \left(\cos\left[\gamma^*_\theta\right] + \mu \sin\left[\gamma^*_\theta\right]\right) \tag{6.37}$$

$$p_{C,\theta} = K_{cf} A_{i,\theta} \left(\mu \cos\left[\gamma^*_\theta\right] - \sin\left[\gamma^*_\theta\right]\right) \tag{6.38}$$

where the effective clearance angle, γ^*_θ, is now a function of θ and is

$$\gamma^*_\theta = \begin{cases} \dfrac{\overbrace{\int_{\beta_{1,\theta}}^{\beta_{2,\theta}} t_{i-te}(\theta,\beta)\left(\beta - \dfrac{3\pi}{2}\right) r_e d\beta}^{\text{tool edge}}}{\underbrace{\int_{\beta_{1,\theta}}^{\beta_{2,\theta}} t_{i-te}(\theta,\beta)\, r_e d\beta}_{\text{tool edge}}} & \hat{z}_{2,\theta} \le \hat{z}_{te-cf} \\ \dfrac{\overbrace{\int_{\beta_{1,\theta}}^{3\pi/2+\gamma} t_{i-te}(\theta,\beta)\left(\beta - \dfrac{3\pi}{2}\right) r_e d\beta}^{\text{tool edge}} + \overbrace{\int_0^{\tilde{z}_{2,\theta}} t_{i-cf}(\theta,\tilde{z})\,\gamma d\tilde{z}}^{\text{clearance face}}}{\underbrace{\int_{\beta_{1,\theta}}^{3\pi/2+\gamma} t_{i-te}(\theta,\beta)\, r_e d\beta}_{\text{tool edge}} + \underbrace{\int_0^{\tilde{z}_{2,\theta}} t_{i-cf}(\theta,\tilde{z})\, d\tilde{z}}_{\text{clearance face}}} & \text{otherwise} \end{cases} \tag{6.39}$$

which is similar to the formulation in Equation (3.49) except that many parameters are now functions of θ. $t_{i-te}(\theta,\beta)$, $t_{i-cf}(\theta,\tilde{z})$, $\hat{z}_{1,\theta}$, $\hat{z}_{2,\theta}$, $\beta_{1,\theta}$, $\beta_{2,\theta}$, and $\tilde{z}_{2,\theta}$ are the same as $t_{i-te}(\beta)$, $t_{i-cf}(\tilde{z})$, $\hat{z}_1$, $\hat{z}_2$, β_1, β_2, and $\tilde{z}_2$, given in Equations (3.50), (3.55) or (3.56), (3.42), (3.43), (3.51), (3.52), and (3.53), respectively, with all instances of a_0, a_1, and a_2 set equal to $a_{0,\theta}$, $a_{1,\theta}$, and $a_{2,\theta}$, respectively. Additionally, in the case of $\tilde{z}_{2,\theta}$, $\hat{z}_2$ becomes $\hat{z}_{2,\theta}$ as well. Just as in Equation (3.49), the integrations performed along the tool edge in the numerator and denominator in Equation (6.39) are evaluated numerically in a vectorized fashion. The results of the integration along the clearance face are similar to that given in Equation (3.50) with all aforementioned constituent parameters now functions of θ.

The interference area, previously A_i in Equation (3.46), is now a function of θ and denoted as $A_{i,\theta}$, described by

$$A_{i,\theta} = \begin{cases} A_{i-te}\left(\hat{z}_{1,\theta}, \hat{z}_{2,\theta}, \theta\right) & \hat{z}_{2,\theta} \le \hat{z}_{te-cf} \\ A_{i-te}\left(\hat{z}_{1,\theta}, \hat{z}_{te-cf}, \theta\right) + A_{i-cf}\left(\hat{z}_{2,\theta}, \theta\right) & \text{otherwise} \end{cases} \tag{6.40}$$

where $A_{i-te}\left(\hat{z}_{1,\theta}, \hat{z}_{te-cf}, \theta\right)$ and $A_{i-cf}\left(\hat{z}_{2,\theta}, \theta\right)$ are similar to $A_{i-te}\left(\hat{z}_{1,\theta}, \hat{z}_{te-cf}\right)$ and $A_{i-cf}\left(\hat{z}_{2,\theta}\right)$, given in Equations (3.44) and (3.45), with all instances of a_0, a_1, and a_2 set equal to $a_{0,\theta}$, $a_{1,\theta}$, and $a_{2,\theta}$, respectively.

CHAPTER 7: NUMERICAL IMPLEMENTATION

"A man's accomplishments in life are the cumulative effect of his attention to detail."
– John Foster Dulles

7.1 Equations of Motion for Machining a Compliant Workpiece with a Rigid Cutting Tool

As previously discussed, it was deemed necessary to model the chattering process in two dimensions–the directions commonly referred to the "tangential" and "radial" cutting directions (the $\mathbf{Y}$ and $\mathbf{Z}$ directions shown in Figure 6-5B). Although some investigators have modeled chatter in three dimensions [30], it makes little sense in the current application to model the third spatial dimension, the "axial" cutting direction, since it is directed along the axis of the workpiece. The workpiece is extremely rigid along its axis compared to its other two directions and consequently any axial vibrations are negligible (this will be demonstrated in a later section). More commonly, chatter problems are formulated with one degree of freedom, only considering motion in the radial cutting direction, since it directly influences the undeformed chip thickness. However, the inclusion of a degree of freedom in the tangential direction is usually critical for accurate predictions. The bulk of the motion during either stable or unstable cutting is generally in the tangential cutting direction, since it has greatest amount of cutting force [27],[34]. Motion in this direction is also impeded less by interaction between the cutting tool and the workpiece. Since there is coupling between the motions in the radial and tangential cutting directions (e.g. Equations (4.39), (4.40), (4.46), and many others), they both must be modeled and the minimum number of degrees of freedom for an accurate dynamic cutting force model is two. The only place where this assertion could be false is in a laboratory condition where a chattering toolholder is intentionally designed to only vibrate appreciably in one direction [57].

In Figure 7-1 various quantities related to the position of the cutting tool and the geometry of the workpiece are shown. The workpiece has a length, L, initial diameter, d_w, and machined diameter, d_m. A new reference frame with a single axis, the $\widehat{\mathbf{X}}$ reference frame, is located where the

workpiece meets the spindle. It is fixed in space and is used to locate the axial position of the cutting tool along the workpiece. The cutting tool starts machining at some axial position, $\hat{x}_0$, and moves along the workpiece as it performs a turning cut. At any point in time, the axial position of the cutting tool is $\hat{x}_t(t)$, which is given by

$$\hat{x}_t(t) = \hat{x}_0 + \frac{ft}{\tau} \tag{7.1}$$

where it is assumed that the tool moves from the cantilevered end of the workpiece to the free end and τ was given in Equation (2.13). For the remainder of this work, $\hat{x}_t(t)$ can be referred to as simply $\hat{x}_t$ for conciseness purposes. During the experiments presented in Chapter 8, for most cutting conditions chosen there was a point along the workpiece where a transition from stable cutting to chatter was observed.

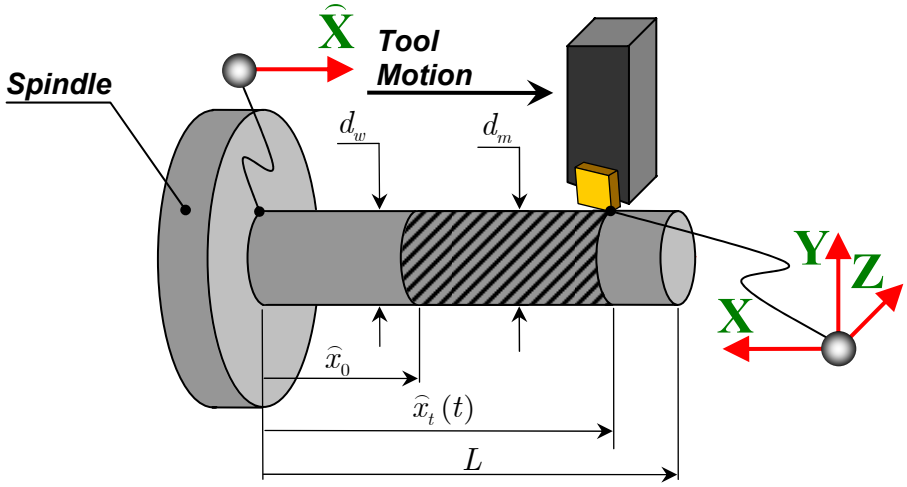

Figure 7-1: A diagram showing various quantities related to the position of the cutting tool and the geometry of the workpiece.

The equations of motion of the workpiece in the radial and tangential cutting directions are

$$\ddot{y}_w(t) + 2\zeta\omega_n\dot{y}_w(t) + \omega_n^2 y_w(t) = -\psi\left(\hat{x}_t(t), d_c\right)\left(F_Y + P_Y - F_{Y,static} - P_{Y,static}\right) \tag{7.2}$$

$$\ddot{z}_w(t) + 2\zeta\omega_n\dot{z}_w(t) + \omega_n^2 z_w(t) = -\psi\left(\hat{x}_t(t), d_c\right)\left(F_Z + P_Z - F_{Z,static} - P_{Z,static} + 0.05(2u-1)\right) \tag{7.3}$$

where F_Y, F_Z, P_Y, and P_Z can come from either of the aforementioned simplified or refined dynamic cutting force models, $F_{Y,static}$, $F_{Z,static}$, $P_{Y,static}$, and $P_{Z,static}$ are the forces in the **Y** and **Z**

directions due to chip formation and interference in the when there is zero RTWD for all time, respectively. $\psi(\hat{x}_t(t), d_c)$ is a coefficient that reflects the change in stiffness of the workpiece at the cutting zone as a function of the axial position of the cutting tool, $\hat{x}_t(t)$, and the nominal depth of cut, d_c. $y_w(t)$ and $z_w(t)$, along with their time derivatives, can be obtained from Equations (2.2)-(2.5).

The subtraction of the forces, $F_{Y,static}$, $F_{Z,static}$, $P_{Y,static}$, and $P_{Z,static}$, in Equations (7.2) and (7.3) is used in order to guarantee that the system has no transient response when the simulation begins. If these were not present during the first time step in the simulation, the system would receive a "step" input of the magnitude of the entire cutting force when there is no vibration. This would cause the system to oscillate considerably and contaminate the solution. In essence, the subtraction of these forces only allows the workpiece to be excited by dynamic cutting forces. Since the workpiece is modeled as a linear system, this shift in operating point should not affect its stability.

The argument could be made that if the workpiece were compliant enough, and if the tool were far enough away from the cantilevered end, the mean cutting force value (the quasi-static component) would be important since it would cause the effective depth of cut to become larger as the workpiece deflected away from the tool. This could be encountered in other scenarios, but with respect to the workpiece used to validate the proposed dynamic cutting force models in this dissertation, it is not a significant effect since the maximum deflection for the largest depth of cut used in this study was around 0.02 mm. If the mean deflection of the workpiece was significant and could not be neglected, a way around producing a large transient response would be to initialize the position of the workpiece in the $\hat{y}$ and $\hat{z}$ directions to be such that it is the static amount of deflection when subjected to $F_{Y,static} + P_{Y,static}$ and $F_{Z,static} + P_{Z,static}$, respectively.

A minus sign has been placed outside the forcing terms in both Equations (7.2) and (7.3) because in the development of the dynamic cutting model, forces were described with respect to the cutting tool in order to stay with convention in the literature. By Newton's third law, there must be

equal and opposite forces exerted on the cutting tool and workpiece as long as there is contact. If through excessive vibration the tool looses contact with the workpiece, both aforementioned cutting force models will predict zero force. This no longer represents a pair of bodies with equal and opposite reactions, but $-0=0$ so Equations (7.2) and (7.3) still hold in the case of contact loss. There is an extra forcing term in the Equation (7.3), $0.05(2u-1)$, this represents the stochastic nature of the cutting process in that small variations in force exist during either stable or unstable cutting. u is a sample from the uniform distribution, U, which is

$$u \sim U(0,1) \tag{7.4}$$

In this way, there will be uniformly distributed forces on the interval $(-0.05, 0.05)$ Newtons. Since the system dynamics are changing as cutting processes (via the $\psi(\widehat{x}_t(t), d_c)$ term), the system can transition from a stable equilibrium point to an unstable one during the simulation of a cut. The random excitation ensures that the system does not "sit" on an unstable equilibrium point, which is something that would never happen in practice. In reality, the random component of forces during machining is more similar to a Gaussian distribution [34]. The random excitation used in this case is for purely numerical reasons, and it requires fewer steps in computer code to produce uniformly distributed random numbers. It makes no difference whether the random excitation is present in both Equation (7.2) and (7.3) or just one of them.

To numerically solve the equations of motion in Equations (7.2) and (7.3), they should be put in state space form, which is

$$\begin{aligned}\frac{d}{dt}\begin{Bmatrix} y_w(t) \\ \dot{y}_w(t) \\ z_w(t) \\ \dot{z}_w(t) \end{Bmatrix} = &\begin{bmatrix} 0 & 1 & 0 & 0 \\ -\omega_n^2 & -2\zeta\omega_n & 0 & 0 \\ 0 & 0 & 0 & 1 \\ 0 & 0 & -\omega_n^2 & -2\zeta\omega_n \end{bmatrix}\begin{Bmatrix} y_w(t) \\ \dot{y}_w(t) \\ z_w(t) \\ \dot{z}_w(t) \end{Bmatrix} \\ &- \psi(\widehat{x}_t(t))\begin{bmatrix} 0 \\ F_Y(\cdot)_1 + P_Y(\cdot)_2 - F_{Y,static}(\cdot)_3 - P_{Y,static}(\cdot)_4 \\ 0 \\ F_Z(\cdot)_1 + P_Z(\cdot)_2 - F_{Z,static}(\cdot)_3 - P_{Z,static}(\cdot)_4 + 0.05(2u-1) \end{bmatrix}\end{aligned} \tag{7.5}$$

where

$$(\cdot)_1 \triangleq (t, t-\tau, ..., t-D\tau)$$

$$(\cdot)_2 \triangleq (t, t-\tau, ..., t-D\tau, t-\tau_1, t-\tau_2)$$

$$(\cdot)_3 \triangleq (t, t-\tau_1)$$

$$(\cdot)_4 \triangleq (t, t-\tau_1, t-\tau_2, t-\tau)$$

and τ_1 and τ_2 are delays associated with data points used to generate the undeformed workpiece surface that will be defined in a later section. These four states are used to obtain the absolute velocities and positions of the workpiece in the **Y** and **Z** directions, as given in Equations (2.2)-(2.5). Although it appears from Equation (7.5) that the $y_w(t)$ and $\dot{y}_w(t)$ states are decoupled from the $z_w(t)$ and $\dot{z}_w(t)$ states because of the zero entries in the off-diagonal 2×2 block matrices in the square matrix, they are in fact coupled because the forcing terms, $F_Y(\cdot)_1$, $F_Z(\cdot)_1$, $P_Y(\cdot)_2$, and $P_Z(\cdot)_2$ (i.e. $F_Y(\cdot)_1$ and $F_Z(\cdot)_1$ depend on $y_w(t)$, $\dot{y}_w(t)$, and $\dot{z}_w(t)$ at various times, and $P_Y(\cdot)_2$, and $P_Z(\cdot)_2$ depend on all four states at various times). The time dependence for all the terms in Equation (7.5) has been explicitly shown in order to facilitate developments in the numerical methods section.

7.2 Justification for a Two Degree of Freedom Modal of the Workpiece

In actuality, a point along the workpiece has 6 degrees of freedom-three for rotation and three for displacement. However, due to the inherent stiffness distribution of the workpiece, certain motions contribute negligibly to the total amount of vibration at the cutting zone. It is desirable to use the minimum number of degrees of freedom that capture the bulk of the workpiece dynamics since every degree of freedom adds two states to the system in Equation (7.5) and results in longer computational times. Referring to Figure 7-1, consider a point along a workpiece, $\widehat{x}_t$, having a diameter, d_m, of 37.87 mm, and length, L, of 170.4 mm (the length and nominal diameter for the workpiece used in this study). The axial stiffness, k_x, with units of force/length is given as

$$k_x = \frac{\pi d_m^2 E}{4\widehat{x}_t} \tag{7.6}$$

the torsional stiffness about the **X** axis, $k_{\theta x}$, with units of force·length/rad is given as

$$k_{\theta x} = \frac{\pi d_m^4 G}{32 \hat{x}_t} \tag{7.7}$$

where G is the shear modulus and the stiffness in either the **Y** or **Z** directions, $k_{y,z}$, with units of force/length is

$$k_{y,z} = \frac{3\pi d_m^4 E}{64 \hat{x}_t^3} \tag{7.8}$$

For a force, F_{Ax}, applied along the axis of the workpiece, the displacement, δ_x, is

$$\delta_x = \frac{F_{Ax}}{k_x} \tag{7.9}$$

For a force applied tangentially, F_{Tan}, the magnitude of the linear deflection at the edge of the workpiece, $\delta_{y,z-\theta x}$, is

$$\delta_{y,z-\theta x} = \frac{d_m^2 F_{Tan}}{4 k_{\theta x}} \tag{7.10}$$

and for a force, F_{Rad}, applied radially towards the center of the workpiece, the magnitude of the displacement is

$$\delta_{y,z} = \frac{F_{Rad}}{k_{y,z}} \tag{7.11}$$

To compare the effects of the stiffnesses in given in Equations (7.6)-(7.8) on the static displacement of the workpiece, the ratio of each displacement to each force in Equations (7.9)-(7.11), known as the compliance, is plotted as a function of axial position along the workpiece, $\hat{x}_t$, in Figure 7-2. The compliance in the **Y** or **Z** directions of the workpiece due to a radially applied load is dominant for all axial positions greater than about 60 mm. At the end of the workpiece, an axial position of 170 mm, this compliance is 22 times greater than the compliance due to torsion and 107 times greater than the workpiece's axial compliance. The fact that the compliance due to a radially applied force is dominant allows certain motions to be neglected, namely, axial vibrations of the workpiece and angular vibration about the its axis. This is because in all of the cutting experiments

conducted in this investigation, chatter always materialized at least an axial position of around 70 mm. This supports the form of the model used for the workpiece in Equations (7.2) and (7.3), and allows for a state space formulation in Equation (7.5) with only four states.

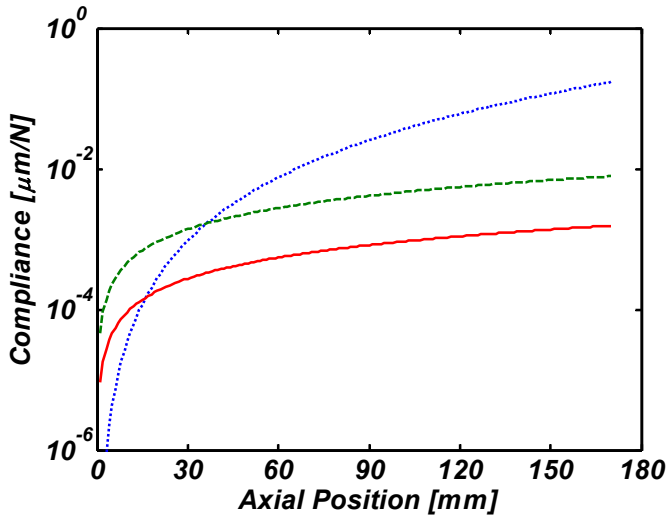

Figure 7-2: Various compliances of the workpiece as a function of axial position, $\hat{x}_t$. ····, The compliance in the radial direction of the workpiece in the **Y** or **Z** directions; ---, the compliance of the workpiece in the **Y** or **Z** direction due to torsion from a tangentially applied load; ——, the compliance along the axis of the workpiece in the **X** direction.

7.3 A Computationally Efficient Implementation of Oxley's Orthogonal Cutting Force Model

As previously mentioned, one of the strengths of the Oxley cutting force model is that no knowledge of the deformed chip thickness, t_d, is required to calculate the forces due to chip formation. However, one drawback is that this model is relatively slow in finding the shear angle due to the algorithm's iterative nature. In most applications of the Oxley model this is not a problem since only one cutting condition is simulated at a time. In the case of stable turning for a constant commanded depth of cut, this force value is typically valid for all time because it is assumed that there is minimal relative tool-workpiece vibration. Clearly this is not the case in the present application where chatter is being considered and the cutting force model is evaluated at every time step of a dynamic cutting simulation (potentially tens of millions of times in the present application).

This problem is compounded because in order to get the resolution necessary the potential shear angles, ϕ, must be evaluated many more times than it would for traditional quasi-static cutting force prediction. Chatter arises because of deviations from a nominal cutting force, and at its inception these deviations can be very small. In order to predict small changes in cutting force, the shear angle resolution must be very high, since it is directly related to the forces due to chip formation (e.g. in Equations (3.4) and (3.5)).

To make a dynamic simulation using the Oxley cutting force model tractable, a four dimensional regression surface is evaluated instead. To perform the regression, the Oxley cutting force model is evaluated over the anticipated parameter space with a unity width of cut, w, in order to generate many data points. The independent variables are the following aforementioned parameters in the orthogonal cutting domain: t', the effective depth of cut referenced at the tip of the cutting tool, α_n, the normal rake angle, $\left|\vec{V}_C\right|$, the magnitude of the cutting velocity, and δ_s, the workpiece surface slope. The outputs are the shear angle, ϕ_V, and the differential forces due to chip formation, f_C and f_T. As previously presented, three regression surfaces are fit to the outputs of Oxley's cutting force model:, S_{f_C}, S_{f_T}, and S_{ϕ_V}. The general form for each regression surface, S_{reg}, is

$$S_{reg}\left(t',\alpha_n,\left|\vec{V}_C\right|,\delta_s\right)=\sum_{p=0}^{4}\sum_{q=0}^{4}\sum_{r=0}^{4}\sum_{s=0}^{4}\begin{cases}C_{p.q.r.s}\left(t'\right)^p\left(\alpha_n\right)^q\left(\left|\vec{V}_C\right|\right)^r\left(\delta_s\right)^s & p+q+r+s\le 4\\ 0 & \text{otherwise}\end{cases} \tag{7.12}$$

where $C_{p.q.r.s}$ is a coefficient to be determined by least squares. The sum of the squared error, E, is computed by summing over DP data points, and is given as

$$E=\sum_{dp=1}^{DP}\left(O_{dp}-S_{dp}\right)^2 \tag{7.13}$$

where O_{dp} and S_{dp} are outputs from the Oxley model and the regression surface at a given data point, dp, in the four dimensional space, $\left(t',\alpha_n,\left|\vec{V}_C\right|,\delta_s\right)$. Now the least squares problem can be

formulated by taking the partial derivative with respect to the unknown coefficients and equating to zero as such:

$$0 = \sum_{p=0}^{4}\sum_{q=0}^{4}\sum_{r=0}^{4}\sum_{s=0}^{4}\begin{cases}\dfrac{\partial}{\partial C_{p,q,r,s}}\left[\sum_{dp=1}^{DP}\left(O_{dp}-S_{dp}\right)^2\right] & p+q+r+s\le 4 \\ 0 & \text{otherwise}\end{cases} \tag{7.14}$$

If each partially differentiated term, $\partial/\partial C_{p,q,r,s}[\cdot]$, in Equation (7.14) is required to be zero individually, then it creates a system of equations that can be solved to find the coefficients $C_{p,q,r,s}$ $\forall\ p+q+r+s\le 4$. These results are given in Appendix C.

Some representative plots showing the fit between the regression surfaces and the outputs from the Oxley cutting force model will now be presented. Each plot can be envisioned as taking a slice out of the four dimensional parameters space, $\left(t',\alpha_n,\left|\vec{V}_C\right|,\delta_s\right)$, while holding three parameters constant and varying the fourth. In Figure 7-3A and B the effect of varying t' is shown, while holding the other independent parameters constant. In Figure 7-3B and C the cutting velocity, $\left|\vec{V}_C\right|$, is varied with the other parameters held constant. In Figure 7-3D and E the rake angle, α_n, is varied as other parameters are held constant, and in Figure 7-3F and G the workpiece surface slope, δ_s, is varied. The range on each plot for the parameter being varied corresponds to the anticipated parameter space that would be encountered during a dynamic simulation using the cutting parameters in this study. It should be noted that in the case of t', the smallest value that was simulated in the Oxley cutting force model is 0.01 mm, since below this value erratic results were obtained. Based on obvious intuition, artificial data points predicting forces of 0 N along all the dimensions where $t' = 0$ mm were added to the data that was used to generate S_{F_C} and S_{F_T}. For S_{ϕ_V} the shear angles predicted at $t' = 0.01$ mm were extrapolated to $t' = 0$ mm. Due to slight errors in the regression surface fits, a force of 0 N was not necessarily predicted at $t' = 0$ mm, as evident in Figure 6-4A, C, and E where the differential interference forces do not quite go to zero at the endpoints of the undeformed chip area.

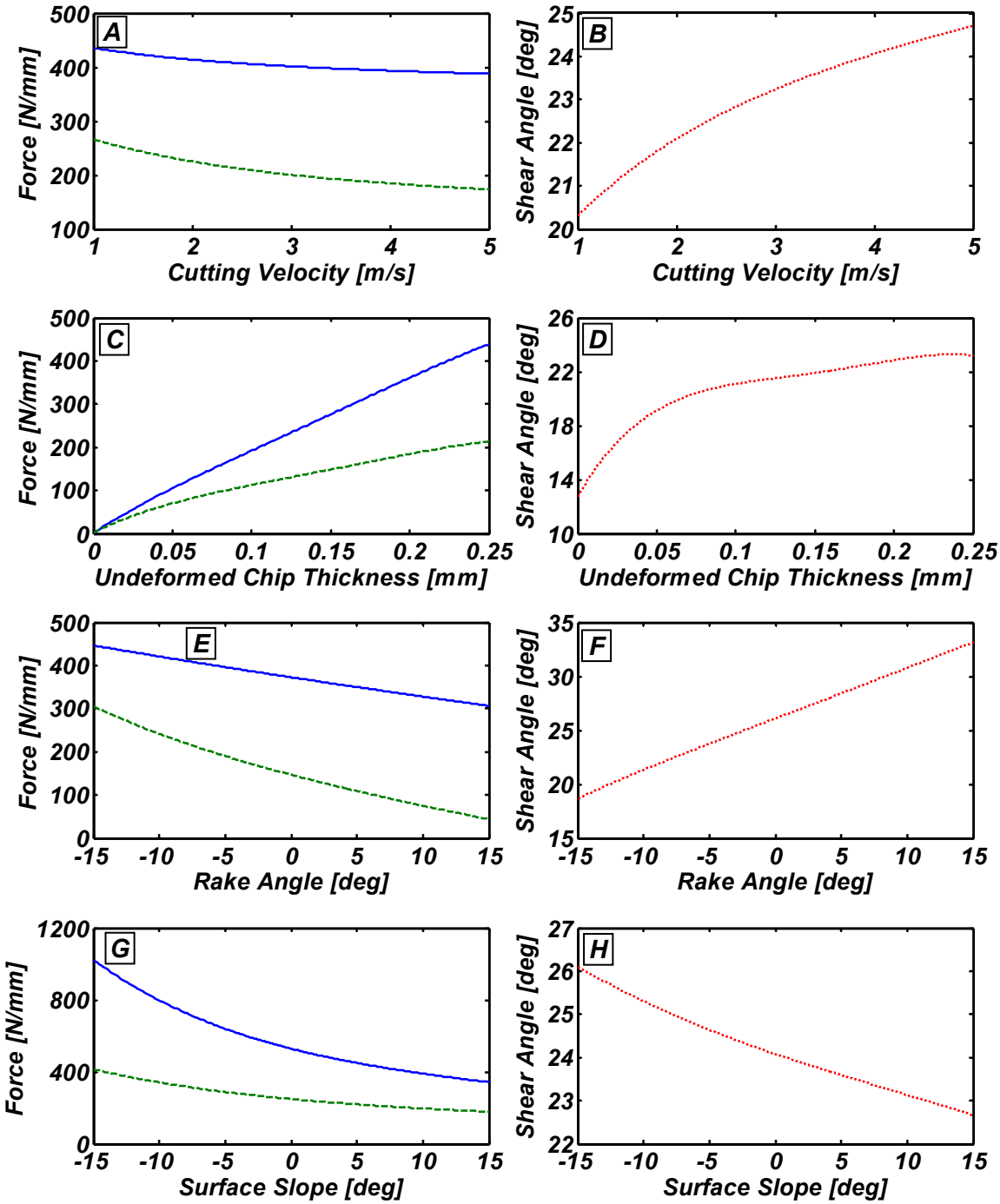

Figure 7-3: Outputs from regression surface fits to outputs of the Oxley cutting force model with one parameter varied and others held constant. (A), (B) $\left|\vec{V}_C\right|$ is varied with t' = 0.22 mm, α_n = -6.11°, and δ_s = 8.97°; (C), (D) t' is varied with $\left|\vec{V}_C\right|$ = 3.48 m/s , α_n = -6.11°, and δ_s = 8.97°; (E), (F) α_n is varied with $\left|\vec{V}_C\right|$ = 3.48 m/s , t' = 0.22 mm, and δ_s = 8.97°; (G), (H) δ_s is varied with $\left|\vec{V}_C\right|$ = 3.48 m/s , t' = 0.22 mm, and α_n = -6.11°. ——, Differential force due to chip formation in the cutting direction, f_C ; ----, differential force due to chip formation in the thrust direction, f_T ; ····, dynamic shear angle, ϕ_V .

7.4 Numerical Evaluation of the Integrals in the Refined Dynamic Cutting Force Model

There have been two approaches presented to describe the cutting forces in dynamic cutting. In the simplified dynamic cutting force model, all of the integrals can be evaluated in closed form, so there are no numerical issues in this case. However for the refined dynamic cutting force model there are multiple integrals that need to be evaluated numerically because this cutting force model is to be used during a dynamic simulation–potentially being evaluated tens of millions of times to simulate a turning operation. Consequently, the computation time of the dynamic cutting force model must be kept to a minimum, and special care must be taken in choosing accurate and efficient algorithms to perform the numerical integration.

Specifically, there are five integrals that need to be numerically evaluated in the refined cutting force approach. The first two are for the cutting forces in the **Y** and **Z** directions, Equations (6.1) and (6.2), respectively. They have similar behaviors in terms of their error dynamics because they are integrated over the same undeformed chip area, e.g., the shaded grey regions in Figure 4-3. Along the free boundary of the undeformed chip area there exist discontinuities in the differential force (more specifically a cusp singularity), with the number of discontinuities depending on the regenerative position space. This was graphically shown in Figure 6-4. Based on this realization, it will be shown that better accuracy can be obtained by breaking up the integrals in Equations (6.1), (6.2) and evaluating them along each region of the chip area that has a smooth free boundary.

Shown in Figure 7-4 are the errors in numerical integration using Simpson's 1/2 rule, a single-application Gaussian Quadrature applied over the entire undeformed chip area, and a multiple-application Gaussian Quadrature applied over each region of the undeformed chip with a free boundary that has a continuous derivative. For the latter two cases consider Figure 4-3 in the following example. If a 5 point single-application Gaussian Quadrature is used over the entire area, then 5 total function evaluations are needed; however, if a 5 point multiple-application Gaussian Quadrature is used than 20 function evaluations are needed, since there are four intervals that have a

continuous spatial derivative at the free boundary, namely: $[\theta_{0,3}, \theta_{2,3}]$, $[\theta_{2,3}, \theta_{1,2}]$, $[\theta_{1,2}, \theta_1]$, and $[\theta_1, \theta_0]$. To perform all numerical calculations in this section, double precision floating point arithmetic was used, with all length units in millimeters and all forces expressed in Newtons.

To find the errors associated with each approach, an average of all errors in numerically integrating Equations (6.1) and (6.2) was found from 10,000 random regenerative delay spaces, $[t \quad t-\tau \quad \cdots \quad t-3\tau]$, with each term in the range of [-100, 100] μm using nominal values for the depth of cut, feed rate, and tool nose radius in this study. Second through seventeenth order Gaussian Quadrature was considered, as well Simpson's rules using 10-6000 steps. From the results in Figure 7-4, it is clear that multiple-application Gaussian Quadrature outperforms the other two approaches in terms of the number of function evaluations needed to achieve a specified error tolerance.

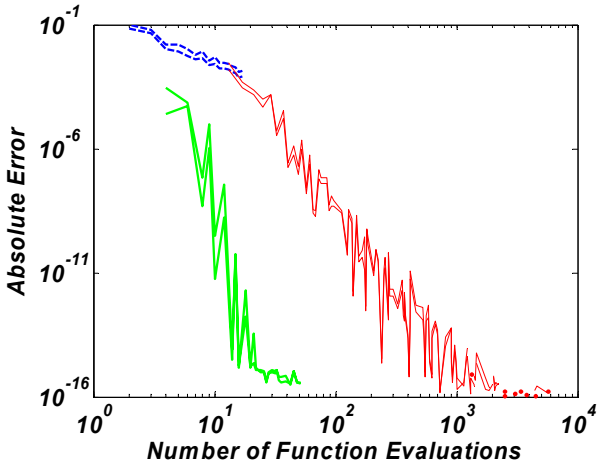

Figure 7-4: The absolute error for three numerical integration strategies to evaluate the cutting forces in Equations (6.1) and (6.2). —, Simpson's 1/2 rule; ---, single-application Gaussian Quadrature applied over the entire interval; —, multiple-application Gaussian Quadrature applied along regions with a smooth free boundary.

Figure 7-5 shows the error in evaluating Equations (6.1) and (6.2) versus the order of the multiple-application Gaussian Quadrature, once again by averaging over 10,000 random sets of tool positions. Based on the plot, eight point Gaussian Quadrature is used since the error approaches the noise floor with the smallest number of function evaluations.

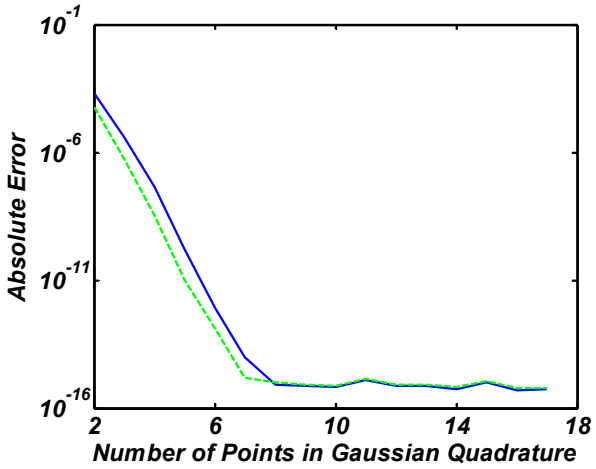

Figure 7-5: The absolute error for various orders of multiple-application Gaussian Quadrature applied over regions of the undeformed chip area with a smooth free boundary in Equations (6.1) and (6.2). —, The absolute error in finding F_Y, Equation (6.1); - - -, the absolute error in finding F_Z, Equation (6.2).

Based on this realization, Equations (6.1) and (6.2) are now evaluated over regions in the undeformed chip area that have a sectionally smooth free boundary. The intervals for each integration are the same as those used to find the angle of the chip flow direction in Equation (4.28). The forces due to chip formation are now given as

$$F_Y = \sum_{q=1}^{Q-1} \int_{Ang(Ind(1,q+1),Ind(2,q+1))}^{Ang(Ind(1,q),Ind(2,q))} \left(f_{T,\theta} \sin\left[C_{s,\theta}^*\right] - f_{R,\theta} \cos\left[C_{s,\theta}^*\right] \right) r_n d\theta + \int_{Ang(Ind(1,1),Ind(2,1))}^{\theta_0} \left(f_{T,\theta} \sin\left[C_{s,\theta}^*\right] - f_{R,\theta} \cos\left[C_{s,\theta}^*\right] \right) r_n d\theta \tag{7.15}$$

$$F_Z = \sum_{q=1}^{Q-1} \int_{Ang(Ind(1,q+1),Ind(2,q+1))}^{Ang(Ind(1,q),Ind(2,q))} f_{C,\theta} r_n d\theta + \int_{Ang(Ind(1,1),Ind(2,1))}^{\theta_0} f_{C,\theta} r_n d\theta \tag{7.16}$$

where there are Q intervals where Gaussian Quadrature is applied ($Q-1$ for a type a region and 1 for a type B region). It should be noted that Equations (7.15) and (7.16) can be solved in a vectorized fashion since they share the same limits of integration.

The next integrals that need to be numerically evaluated are those associated with the interference forces in Equations (6.10) and (6.11). Contained within these equations was γ_θ^*, which needs to be numerically evaluated as well. Whether the interference area, $A_{i,\theta}$, only exists along the tool edge ($\hat{z}_{2,\theta} < \hat{z}_{ce-cf}$) or along both the cutting edge and the clearance face ($\hat{z}_{2,\theta} \geq \hat{z}_{ce-cf}$), there are always two integrations performed along the edge of the cutting tool that have no closed-form solution when solving for γ_θ^*: one in the numerator and one in the denominator. The errors for

various numbers of points used for Gaussian Quadrature are given in Figure 7-6. One of the integrals approaches the noise floor with only five sample points and the other with nine; however a nine point quadrature is used for both. This is because they have the same limits and in computer code implementation they are evaluated in a vectorized fashion.

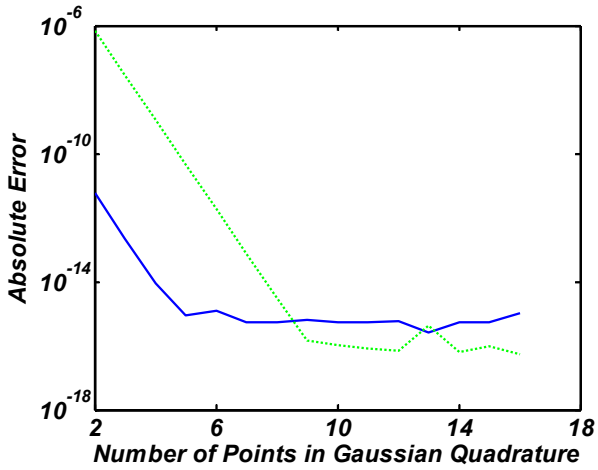

Figure 7-6: The absolute error for various orders of Gaussian Quadrature when used to perform the integrations in Equation (6.39) along the tool edge. —, The absolute error in the integral in the denominator; - - -, the absolute error in the integral in the numerator.

The numerical error for using various numbers of points for the Gaussian Quadrature in evaluating the interference forces in Equations (6.10) and (6.11) is given in Figure 7-7. In order to ensure that the most accurate forces are calculated 5 point Gaussian Quadrature is used.

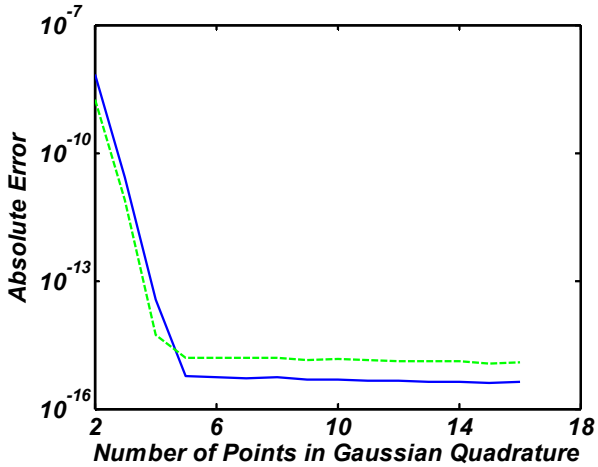

Figure 7-7: The absolute error for various orders of Gaussian Quadrature when used to perform the integrations for the interference forces. —, The absolute error calculating the force in the **Y** direction, P_Y, Equation (6.10); - - -, the absolute error calculating the force in the **Z** direction, P_Z, Equation (6.11).

Now the details of how to implement Gaussian Quadrature will be presented. Recall that a P point Gaussian Quadrature is a weighted sum of P function values at specified nodes, x_p, within the domain of integration, yielding exact results when integrating polynomials of degree $2P-1$, or less. In other words, the integral of a function, $f(x)$, can be approximated by

$$\int_{-1}^{1} f(x)\,dx \approx \sum_{p=1}^{P} w_p f\left(x_p\right) \tag{7.17}$$

where the weights, w_p, and sample points, x_p, are defined for integration over the interval $[-1,1]$. More generally, integrations are performed over an arbitrary interval, $[a,b]$, so the Gaussian Quadrature in Equation (7.17) becomes

$$\int_{a}^{b} f(x)\,dx \approx \sum_{p=1}^{P} w_p' f\left(x_p'\right) \tag{7.18}$$

where

$$w_p' = \frac{w_p\,(b-a)}{2} \tag{7.19}$$

$$x_p' = \left(\frac{b-a}{2}\right) x_p + \frac{a+b}{2} \tag{7.20}$$

In summary there are five integrals that must be evaluated and the number of Gaussian Quadrature sample points needed for each one is given in Table 7-1.

Table 7-1: The number of Gaussian sample points (number of function evaluations) needed for each integral that needs to be numerically evaluated in the refined dynamic cutting force model.

Equation Number	***Quantity***	***Number of Points in Gaussian Quadrature, P***
6.1	Cutting force, F_Y	8*
6.2	Cutting force, F_Z	8*
6.38 (numerator)	Effective clearance angle, γ^*	9
6.38 (denominator)	Effective clearance angle, γ^*	9
6.9	Interference force, P_Y	5
6.10	Interference force, P_Z	5

*per region of undeformed chip area with a smooth free boundary

The weights, w_p, and sample points, x_p, are defined in Appendix C.

7.5 Curve Fitting of the Undeformed Workpiece Surface

In the previous equations that predict the plowing and flank interference forces, both in the simplified and refined dynamic cutting force models, a second or first order polynomial was used to describe the undeformed workpiece surface. To generate this polynomial, the recent relative vibration history between the cutting tool and the workpiece needs to be known. Since a second order polynomial requires a minimum of three points, two previous points in addition to the one at the current time will be used to define the undeformed workpiece surface. Considering the length scales in Figure 3-3A, it would be desirable to have the points in time spaced out in time in the way depicted in Figure 7-8. As previously discussed, the point on the undeformed workpiece surface at the current time, t, is known as the chip separation point. It is purely a function of the current velocity of the tool relative to the workpiece and the tool edge geometry, since it depends on β_e, which was defined in Equation (6.34).

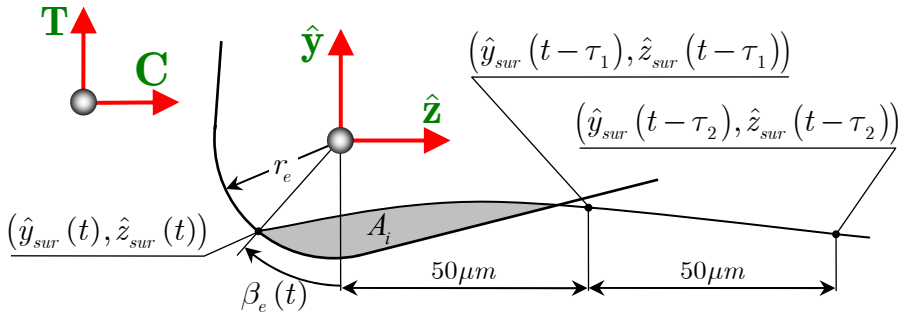

Figure 7-8: A schematic showing how the two points on the undeformed workpiece surface at times $t-\tau_1$ and $t-\tau_2$ relate to the geometry of the cutting edge.

The other two points located at times $t-\tau_1$ and $t-\tau_2$ are spaced at increments of 50 μm from the origin of the $\hat{\mathbf{y}}$ - $\hat{\mathbf{z}}$ reference frame. The 50 μm spacing was found to work well in most cutting conditions (based on the 38 μm edge radius tool used in all experiments and simulations). It is just large enough to capture subtle curvatures in the undeformed workpiece surface, yet not so small that it makes the solver take an inordinate amount of time. In solving delay differential equations, the solver cannot take larger steps than the smallest delay, or else the numerical solver will have to *extrapolate* rather than *interpolate* the solution in order to find values for the smallest delay. In

order to insure that the approximate spacing of the two points at times $t-\tau_1$ and $t-\tau_2$ is invariant under various cutting velocities, they must occur at the delays

$$\tau_1 = \frac{50\times10^{-6}}{\bar{V}_C} \tag{7.21}$$

$$\tau_2 = \frac{100\times10^{-6}}{\bar{V}_C} \tag{7.22}$$

where the nominal cutting speed, $\bar{V}_C$, is in units of m/s. The coordinates of the three points used to fit a polynomial to describe the undeformed workpiece surface will now be given. The coordinates of the undeformed workpiece surface at the current time are

$$\hat{y}_{sur}(t) = -r_e \cos\left[\beta_e(t)\right] \tag{7.23}$$

$$\hat{z}_{sur}(t) = -r_e \sin\left[\beta_e(t)\right] \tag{7.24}$$

where $\beta_e(t)$ was defined in Equation (6.34) for the refined cutting force model and in Equation (4.46) for the simplified cutting force model. The coordinates for undeformed workpiece in the refined cutting force model at times $t-\tau_V$, where V can take on the value of 1 or 2, are

$$\hat{y}_{sur}(t-\tau_V) = -r_e \cos\left[\beta_e(t-\tau_V)\right] - y(t) + y(t-\tau_V) \tag{7.25}$$

$$\hat{z}_{sur}(t-\tau_V) = -r_e \sin\left[\beta_e(t-\tau_V)\right] - z(t) + z(t-\tau_V) + \bar{V}_C\tau_V \tag{7.26}$$

and for the simplified cutting force model the coordinates in the $\hat{z}$ direction, $\hat{z}_{sur}(t-\tau_V)$, are the same while using the following coordinates in the $\hat{y}$ direction:

$$\hat{y}_{sur}(t-\tau_V) = -r_e \cos\left[\beta_e(t-\tau_V)\right] - \varphi y(t) + \varphi y(t-\tau_V) \tag{7.27}$$

Once the three points on the undeformed workpiece surface at times, t, $t-\tau_1$, $t-\tau_2$, are determined, the coefficients for the polynomial representing the undeformed workpiece surface in Equation (3.32) be generated. These coefficients are given as

$$\begin{Bmatrix} a_0 \\ a_1 \\ a_2 \end{Bmatrix} = \begin{bmatrix} 3 & \sum_{k=1}^{3} \hat{\mathbf{z}}_{\mathbf{sur}}(k) & \sum_{k=1}^{3} \hat{\mathbf{z}}_{\mathbf{sur}}(k)^2 \\ \sum_{k=1}^{3} \hat{\mathbf{z}}_{\mathbf{sur}}(k) & \sum_{k=1}^{3} \hat{\mathbf{z}}_{\mathbf{sur}}(k)^2 & \sum_{k=1}^{3} \hat{\mathbf{z}}_{\mathbf{sur}}(k)^3 \\ \sum_{k=1}^{3} \hat{\mathbf{z}}_{\mathbf{sur}}(k)^2 & \sum_{k=1}^{3} \hat{\mathbf{z}}_{\mathbf{sur}}(k)^3 & \sum_{k=1}^{3} \hat{\mathbf{z}}_{\mathbf{sur}}(k)^4 \end{bmatrix}^{-1} \begin{Bmatrix} \sum_{k=1}^{3} \hat{\mathbf{y}}_{\mathbf{sur}}(k) \\ \sum_{k=1}^{3} \hat{\mathbf{y}}_{\mathbf{sur}}(k)\hat{\mathbf{z}}_{\mathbf{sur}}(k) \\ \sum_{k=1}^{3} \hat{\mathbf{y}}_{\mathbf{sur}}(k)\hat{\mathbf{z}}_{\mathbf{sur}}(k)^2 \end{Bmatrix} \tag{7.28}$$

where

$$\hat{\mathbf{y}}_{\mathbf{sur}} \triangleq \begin{bmatrix} \hat{y}_{sur}(t) & \hat{y}_{sur}(t-\tau_1) & \hat{y}_{sur}(t-\tau_2) \end{bmatrix}$$

$$\hat{\mathbf{z}}_{\mathbf{sur}} \triangleq \begin{bmatrix} \hat{z}_{sur}(t) & \hat{z}_{sur}(t-\tau_1) & \hat{z}_{sur}(t-\tau_2) \end{bmatrix}$$

and $\hat{\mathbf{y}}_{\mathbf{sur}}(k)$ and $\hat{\mathbf{z}}_{\mathbf{sur}}(k)$ refer to the k^{th} entry in $\hat{\mathbf{y}}_{\mathbf{sur}}$ and $\hat{\mathbf{z}}_{\mathbf{sur}}$, respectively. If a value of a_2 in Equation (7.28) smaller than 1×10^{-4} mm^{-1} is obtained, it suggests that there is a very small amount of curvature in the undeformed workpiece surface. Since a value this small has a much higher percentage of round-off error, it can lead significant errors when computing the intersections between the undeformed workpiece surface and the tool edge (e.g. in Equations (3.38) and (3.39)). To mitigate this, a first order polynomial is used instead for small values of a_2, whose coefficients are given as

$$\begin{Bmatrix} a_0 \\ a_1 \end{Bmatrix} = \begin{bmatrix} 2 & \sum_{k=1}^{2} \hat{\mathbf{z}}_{\mathbf{sur}}(k) \\ \sum_{k=1}^{2} \hat{\mathbf{z}}_{\mathbf{sur}}(k) & \sum_{k=1}^{2} \hat{\mathbf{z}}_{\mathbf{sur}}(k)^2 \end{bmatrix}^{-1} \begin{Bmatrix} \sum_{k=1}^{2} \hat{\mathbf{y}}_{\mathbf{sur}}(k) \\ \sum_{k=1}^{2} \hat{\mathbf{y}}_{\mathbf{sur}}(k)\hat{\mathbf{z}}_{\mathbf{sur}}(k) \end{Bmatrix} \tag{7.29}$$

with $a_2 = 0$.

7.6 Method of Solving the Equations of Motion

As previously mentioned, the equations of motion associated with chatter are referred to as Delay Differential Equations (DDEs) since they involve states that are delayed version of others. Numerous delay differential equation solvers have been developed for equations with both constant and variable delays. Initially, the delay equation solver in MATLAB, dde23 [59] was used. This is an

all-purpose variable step size solver, meant to handle DDEs with fixed or variable delays, stiff or non-stiff behavior, and events (the vanishing of a delayed state). In addition, it tracks discontinuities in the solution and incorporates these points into the solution mesh in order to improve the error. It was adequate for a single cutting condition using the dynamic cutting force model, simulating 40 seconds of cutting for a workpiece that has a natural frequency of about 600 Hz in about 9 hours on a 2.92 GHz PC with 2 GB of RAM. For the purposes of this investigation, more speed was needed in order to generate stability lobe diagrams because they rely on thousands of simulations in order to sufficiently resolve the stability limits.

At this point some physical insight into the present system being modeled is in order. A workpiece during a machining process vibrates about a fixed point in space in a sinusoidal fashion, undergoing relatively gradual changes in amplitude (no step-like "jumps"). Even when there is a transition from stable cutting to chatter, it is a smooth increase in amplitude, all the while maintaining sinusoidal oscillations with approximately the same period (close to the natural frequency of the workpiece). This is a non-stiff system with consistent sinusoidal behavior, and thus a solver that exploits variable step sizes is likely wasting resources with extra function evaluations to ensure the error satisfies a given tolerance. A fixed step solver with a sufficiently small time step is much more computationally efficient since it does not waste function evaluations checking the error. In addition, it was found that it is unnecessary to track discontinuities in the solution when solving the chatter equations of motion, since as previously mentioned the system undergoes smooth changes in its states. This agrees with intuition as well as testing against the MATLAB variable step solver, dde23. Based on this, a fourth order Runge-Kutta fixed step solver was written in FORTRAN 90 in order to solve the DDEs. The solution proceeds in a fashion very similar to the solution of an ODE except that certain states are delayed versions of others. These delayed states can simply be viewed as a time-dependant input to the system and are determined by piecewise cubic Hermite interpolation of the solution history.

Equation (7.5) can be rewritten as

$$\dot{\mathbf{y}}(t) = \mathbf{G}\mathbf{y}(t) + \psi(x)\mathbf{F}\left(t, t-\tau, ..., t-D\tau, t-\tau_1, t-\tau_2\right) \tag{7.30}$$

where

$$\mathbf{y}(t) = \left[\dot{y}_w(t) \quad y_w(t) \quad \dot{z}_w(t) \quad z_w(t)\right]^T$$

and $\mathbf{G}$ and $\mathbf{F}$ are remaining and 4x1 matrices in the right hand side of Equation (7.5), respectively. $\mathbf{F}$ can contain forces from either the simplified or refined dynamic cutting force models. The fourth order Runge-Kutta Method uses a fixed step size Δt in time in order to generate the solution at the next time step, $\mathbf{y}_{n+1}$, from the current time step, $\mathbf{y}_n$, and is given as

$$\mathbf{y}_{n+1} = \mathbf{y}_n + \frac{1}{6}\left(\mathbf{k}_1 + 2\mathbf{k}_2 + 2\mathbf{k}_3 + \mathbf{k}_4\right) \tag{7.31}$$

where $\mathbf{k}_1, \mathbf{k}_2, \mathbf{k}_3$, and $\mathbf{k}_4$ are 4x1 matrices given by

$$\mathbf{k}_1 = \Delta t\left[\mathbf{G}\mathbf{y}_n + \psi\left(\hat{x}_t(t), d_c\right)\mathbf{F}\left(t, t-\tau, ..., t-D\tau, t-\tau_1, t-\tau_2\right)\right]$$

$$\mathbf{k}_2 = \Delta t\left[\mathbf{G}\left[\mathbf{y}_n + \tfrac{1}{2}\mathbf{k}_1\right] + \psi\left(\hat{x}_t\left(t+\tfrac{\Delta t}{2}\right), d_c\right)\mathbf{F}\left(t+\tfrac{\Delta t}{2}, t-\tau+\tfrac{\Delta t}{2}, ..., t-D\tau+\tfrac{\Delta t}{2}, t-\tau_1+\tfrac{\Delta t}{2}, t-\tau_2+\tfrac{\Delta t}{2}\right)\right]$$

$$\mathbf{k}_3 = \Delta t\left[\mathbf{G}\left[\mathbf{y}_n + \tfrac{1}{2}\mathbf{k}_2\right] + \psi\left(\hat{x}_t\left(t+\tfrac{\Delta t}{2}\right), d_c\right)\mathbf{F}\left(t+\tfrac{\Delta t}{2}, t-\tau+\tfrac{\Delta t}{2}, ..., t-D\tau+\tfrac{\Delta t}{2}, t-\tau_1+\tfrac{\Delta t}{2}, t-\tau_2+\tfrac{\Delta t}{2}\right)\right]$$

$$\mathbf{k}_4 = \Delta t\left[\mathbf{G}\left[\mathbf{y}_n + \mathbf{k}_3\right] + \psi\left(\hat{x}_t(t+\Delta t), d_c\right)\mathbf{F}\left(t+\Delta t, t-\tau+\Delta t, ..., t-D\tau+\Delta t, t-\tau_1+\Delta t, t-\tau_2+\Delta t\right)\right]$$

and Δt is the step size, which should be taken to be the smallest delay in the system, τ_1, or $\frac{\pi}{40\omega_n}$, whichever is smaller. The latter of the two, $\frac{\pi}{40\omega_n}$, guarantees that the solver generates a mesh of at least 80 points per sinusoidal period of oscillation (the dominant frequency of vibration during the cutting simulation is only slightly higher than the open loop natural frequency of the workpiece, ω_n).

When numerically solving Equation (7.30) with the proposed Runge-Kutta algorithm on a single core of a 2.2 GHz computer a significant speed increase was seen in using the simplified cutting force model. When coded in FORTRAN 90, it could be evaluated 140,000 times per second as opposed to the refined cutting force model which could only be evaluated 28,000 times per second. In MATLAB, the simplified cutting force model was executed 2500 times per second and

the refined cutting force model was solved 500 times per second. In both the MATLAB and FORTRAN 90 computing environments, the simplified cutting force model ran 5 times faster.

7.7 Summary of the Steps Taken to Implement Both Proposed Dynamic Cutting Force Models

Due to the relatively large number of equations associated with the both of the previously developed simplified and refined dynamic cutting forces models, the steps needed to implement them will now be outlined. Since they share a number of steps between them, a single outline is presented. The parts where they differ are denoted by the portions of the outline enclosed in rectangular boxes, where those shaded with a grey background represent steps specific to the simplified model, and those enclosed in a box with a white background are specific to the refined model.

- Input the cutting conditions and material properties, i.e. depth of cut, d_c, feed rate per revolution, f, commanded cutting speed, $\bar{V}_C$, and cutting tool geometry, tool nose radius, r_n, normal rake angle, α_n, inclination angle, i, side cutting edge angle, C_S, and clearance angle, γ
- Find all forces in the **Y** and **Z** directions due to chip formation and interference, $F_{Y,static}$, $F_{Z,static}$, $P_{Y,static}$, and $P_{Z,static}$ when there is zero vibration (quasi-static cutting)
- Choose appropriate initial conditions on the state vector, $\mathbf{y}(t)$, (typically 0 for all time, $t<0$), and temporal range of the solution vector, $[0, t_f]$
- Let $t = \Delta t$, where Δt is the step size of the Runge-Kutta solver
- **While** $t < t_f$
  - Find $\mathbf{k_1}$, $\mathbf{k_2}$, $\mathbf{k_3}$, and $\mathbf{k_4}$ in that order by solving for the force vector, $\mathbf{F}$, at times t, $t+\frac{\Delta t}{2}$, $t+\frac{\Delta t}{2}$, and $t+\Delta t$ by taking the state vector, $\mathbf{y}(t)$, to be $\mathbf{y_n}$, $\mathbf{y_n}+\frac{1}{2}\mathbf{k_1}$, $\mathbf{y_n}+\frac{1}{2}\mathbf{k_2}$, $\mathbf{y_n}+\mathbf{k_3}$, respectively, in Equation (7.31)
  - To find each force vector, $\mathbf{F}$
    - Find all angles of intersection between the unmachined workpiece surface and tool nose radii in the regenerative position space, θ_W in Equation (4.25)
    - Check to make sure cutting is taking place, i.e. test all inequalities in Equation (4.26)
    - If cutting *is not* taking place, let $F_Y = F_Z = P_Y = P_Z = 0$
    - If cutting *is* taking place:
      - Find all angles of intersection between tool nose radii in the regenerative position space, $\theta_{M,N}$ in Equation (4.24)

- Assemble the matrix Ang in Equation (4.27), containing all angles $\theta_{M\tau,N\tau}$ and θ_W
- Find the matrix Ind that contains indices that reference angles of intersection in the matrix Ang relevant to the undeformed chip area using the flowchart in Figure 4-6
- Determine values for a_0, a_1, and a_2 using either Equation (7.28) or (7.29)

- Solve for the forces due to chip formation, F_Y and F_Z in closed-form
  - ◇ Solve for the angle of the chip flow direction, $\bar{\Omega}$, via Equation (4.28)
  - ◇ Calculate the effective width of cut and undeformed chip thickness, w^* and t_u^*, by means of Equations (4.33) and (4.34), respectively
  - ◇ Find the effective tool geometry, C_S^*, i^*, α_n^*, given in Equations (4.3)-(4.5), and η_c^*, given in Equation (4.6)
  - ◇ Obtain the effective cutting parameters δ_s^*, V_C^*, α_n^{**}, and t' using Equations (4.46), (4.39) , (4.40), and (4.47), respectively
  - ◇ Find f_C' and f_T' by evaluating the regression surfaces $S_{F_C}\left(t',\alpha_n^{**},V_C^*,\delta_s^*\right)$ and $S_{F_T}\left(t',\alpha_n^{**},V_C^*,\delta_s^*\right)$, multiplying each one by w^*
  - ◇ Solve for F_R, F_C, and F_T in Equations (4.7), (4.37), and (4.38), respectively
  - ◇ Calculate the forces F_Y and F_Z via Equations (4.8) and (4.9), respectively

- Numerically solve for the forces due to chip formation, F_Y and F_Z in Equations (7.15) and (7.16) by evaluating the integrals in a vectorized fashion using the Gaussian Quadrature given in Equation (7.18), where Equations (7.19) and (7.20) transform the 8th order weights and nodes given in Appendix C to the integrals' shared range if integration
  - ◇ In the numerical evaluation at each node, x_i, which represents a particular value of θ the following steps must be performed:
    - ◆ Find t_θ using either Equation (4.18) or (4.21), depending on whether θ is in a type A or B region of the undeformed chip thickness
    - ◆ Find the effective tool geometry, $C_{S,\theta}^*$, i_θ^*, $\alpha_{n,\theta}^*$, given in Equations (6.6)-(6.8) respectively, and $\eta_{c,\theta}^*$ given in Equation (6.9)
    - ◆ Find the effective cutting parameters $\delta_s^*(\theta,W)$, $V_{C,\theta}^*$, and $\alpha_{n,\theta}^{**}$, using Equations (6.15), (6.20), and (6.21) respectively
    - ◆ Iterate to find t_θ' using the flowchart in Figure 6-3
    - ◆ Find $f_{R,\theta}$, $f_{C,\theta}$ and $f_{T,\theta}$ using Equations (6.3), (6.23), and (6.24) respectively

- Solve for the interference forces, P_Y and P_Z in Equations (4.48) and (4.50) in closed-form:
  - ◇ Curve fit the undeformed workpiece surface using Equation (7.28) or (7.29), with the points in Equations (7.26) and (7.27) using the separation angle in Equation (4.46)
  - ◇ Determine the interference area, A_i, according to Equation (3.41)
  - ◇ Take γ^* to be 0° to maintain a closed-form solution
  - ◇ Solve for the interference forces, P_Y and P_Z in Equations (4.48) and (4.50)

- Numerically solve for the interference forces, P_Y and P_Z in Equations (6.10) and (6.11) by evaluating the integrals in a vectorized fashion using the Gaussian Quadrature given in Equation (7.18), where Equations (7.19) and (7.20) transform the 5th order weights and nodes given in Appendix C to the integrals' particular range if integration
  - Curve fit the undeformed workpiece surface using Equation (7.28) or (7.29), with the points in Equations (7.25) and (7.26) using the separation angle in Equation (6.34)
  - In the numerical evaluation at each node, x_i, which represents a particular value of θ the following steps must be performed:
    - Solve for $a_{0,\theta}$, $a_{1,\theta}$, and $a_{2,\theta}$, using Equation (6.33)
    - Determine the cross sectional interference area, $A_{i,\theta}$, according to Equation (6.40)
    - Find the effective clearance angle, γ_θ^*, using Equation (6.39)
      - Numerically evaluate the integral in the numerator and denominator along the tool edge in a vectorized fashion using the Gaussian quadrature given in Equation (7.18), where Equations (7.19) and (7.20) transform the 9th order weights and nodes given in Appendix C to the integral's shared range of integration
      - If the interference exists along the clearance face ($\hat{z}_{2,\theta} > \hat{z}_{te-cf}$), then use the antiderivative given in Equation (3.50) with all instances of a_0, a_1 and a_2 set equal to $a_{0,\theta}$, $a_{1,\theta}$, and $a_{2,\theta}$, respectively
      - Solve for the differential interference forces, $p_{C,\theta}$ and $p_{T,\theta}$ in Equations (6.37) and (6.38), respectively
- Combine the machining forces at the current time step in the radial cutting direction, F_Y and P_Y, with the forces present during zero vibration, $F_{Y,static}$ and $P_{Y,static}$, and the forces in the tangential direction, F_Z and P_Z, with the forces present during zero vibration, $F_{Z,static}$ and $P_{Z,static}$, and use them to find $\mathbf{k_1}$, $\mathbf{k_2}$, $\mathbf{k_3}$, or $\mathbf{k_4}$ in Equation (7.5)

- $t = t + \Delta t$

End of simulation

CHAPTER 8: EXPERIMENTAL VALIDATION

"An experiment is a question which science poses to Nature, and a measurement is the recording of Nature's answer."

–Max Planck

8.1 Overview of the Chapter

As presented in the introduction, there are four methods by which a chatter model can be verified: frequency domain content, point of chatter instability, time domain chatter amplitude growth over time, and machined surface topography. These four metrics comprise some sections of this chapter and will each be investigated separately. To the author's knowledge, accurate correlation of time domain chatter amplitude growth and machined surface topography between an analytical model and experimental measurements has yet to be established in turning. However Li and Shin [71], did obtain satisfactory agreement for predicted machined surface topography in milling during chatter. Although predicting time domain amplitude growth and surface topography during chatter could be viewed as academic and having little practical merit, it is nevertheless important since it determines whether the true physics of the process are being accurately captured.

Comparisons between the predictions of both the simplified and refined dynamic cutting force models to experimental results are only made for the point of chatter instability along the workpiece. For the other three comparisons to experimental data, time domain amplitude growth, frequency domain content, and chattered surface topography, only the refined cutting force model is used. The justification for this is two-fold. The first reason is for conciseness. Secondly, the motivation for deriving the simplified cutting force model in closed-form was such that it could be used as a fast simulation tool for process planning (avoiding chatter). The reasons for developing the refined cutting force model were less in the interest of computational speed and had more to do with modeling the process in a physically rigorous manner. This is why the comparisons of time domain amplitude growth, frequency domain content, and chattered surface topography, which are only

useful for verifying if the true physics of the process is being captured, are exclusive to the refined cutting force model.

8.2 Experimental Setup

To validate both of the proposed dynamic cutting force models, cutting tests were performed on a cantilevered-free AISI 018 steel workpiece with Hardinge Conquest T42SP ultra-precision CNC horizontal lathe. Numerous depths of cut and cutting speeds were considered and the point along the workpiece where a transition from stable cutting to chatter was recorded (determined by the occurrence of chatter marks) and compared to predictions from both of the dynamic cutting force models. For every cut, a fresh tool insert was used in order to eliminate the effects of tool wear in this study, since it has been shown to drastically influence the point of chatter stability [26]. For a small subset of the machining conditions, two laser displacement sensors were used to record the workpiece's position such that time and frequency domain comparisons could be made between the predicted and actual motion of the workpiece. In Figure 8-1 is a picture of the actual experimental setup and in Figure 8-2 is a schematic of the same setup annotated with dimensions.

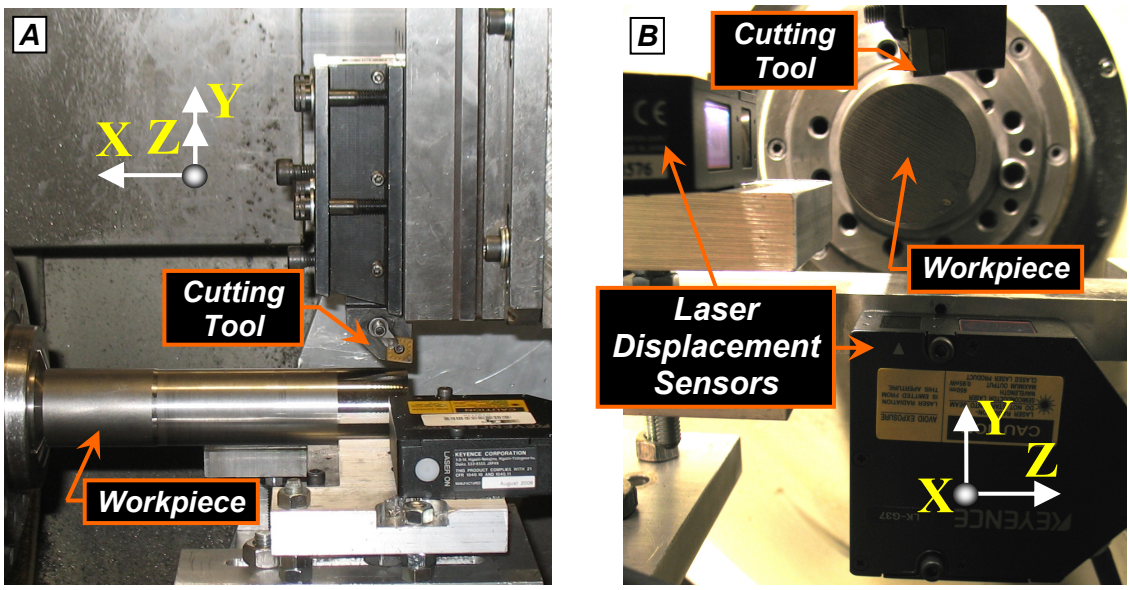

Figure 8-1: The experimental setup used to measure the workpiece displacement over time during turning. (A) Front view; (B) side view.

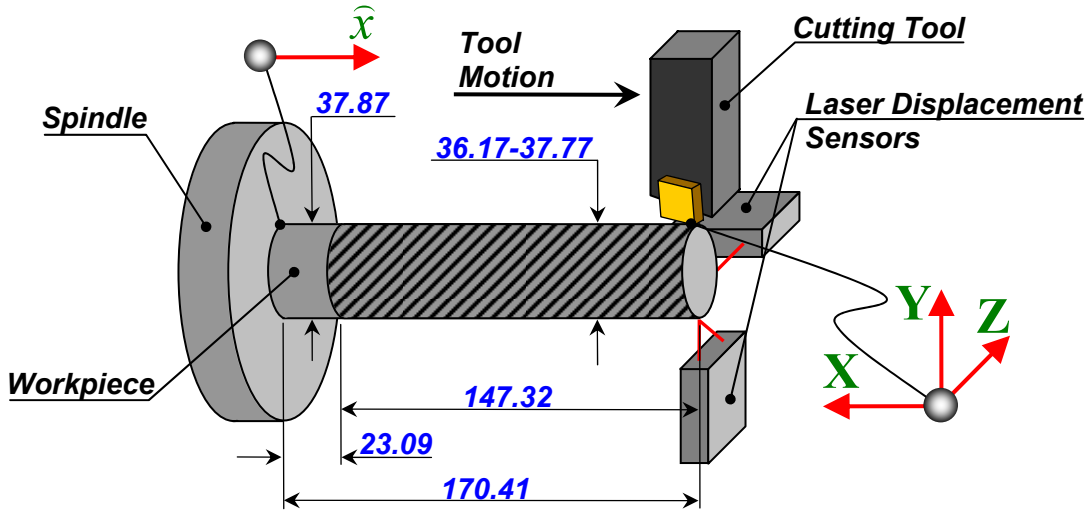

Figure 8-2: A schematic of the experimental setup for measuring the workpiece displacement during machining annotated with the actual machined dimensions of the workpiece (in mm).

As shown in Figure 8-1, the linear displacement of the workpiece in the radial and tangential cutting directions was measured using two Keyence LK-G37 laser displacement sensors with a 50 kHz bandwidth and 10 nm resolution. The sensors were mounted on a custom machined bracket that attached to the toolholder turret and positioned at 90° and 180°, 2-3 mm ahead of the cutting zone along the workpiece's axis of rotation. In this way, the absolute displacement of the workpiece at the cutting zone could be accurately measured throughout an entire cut without chips blocking the laser beam. Because of the spot size of the beam, it had a spatial averaging effect in that it tended to respond to the bulk motion of the workpiece rather then any inherent variation of its surface topography.

8.3 Description of the Open Loop Workpiece Dynamics

Owing to the flowchart in Figure 1-2 showing the general way in which a dynamic turning process is simulated, the final element needed is a dynamic model of the workpiece. As was introduced in Equations (7.2) and (7.3), the parameters that capture this are the damping ratio, ζ, natural frequency, ω_n, and a function that reflects the changing stiffness of the workpiece at the cutting zone, $\psi(\hat{x}_t(t), d_c)$ (although the units of $\psi(\hat{x}_t(t), d_c)$ are kg^{-1}, it varies along the axis of the workpiece because the stiffness varies). $\psi(\hat{x}_t(t), d_c)$ depends on both the axial position of the

cutting tool in the $\hat{\mathbf{x}}$ direction as well as the nominal depth of cut. At larger depths of cut $\psi(\hat{x}_t(t), d_c)$ is greater because the removed material causes the workpiece to be more compliant. Also, as the tool cuts and is fed from the cantilevered end to the free end of the workpiece the value of $\psi(\hat{x}_t(t), d_c)$ gets larger as well. This intuitively makes sense since the compliance at the tool-workpiece interface is increasing, as suggested by Figure 7-2.

To obtain $\psi(\hat{x}_t(t), d_c)$, a series of driving-point impact tests were performed along the length of the workpiece at various axial positions and at various stages of material removal. The input was a modal impact hammer and the output was a uniaxial piezoelectric accelerometer. Four depths of cut, 0.05, 0.32, 0.58, and 0.85 mm, at five axial positions, $\hat{x}_t$, along the workpiece, 23.09, 68.81, 102.59, 136.63, and 170.41 mm were measured. At each axial position, the amount of material that would have been removed during the cutting configuration depicted in Figure 8-2 was replicated. This range of axial positions and depths of cut was chosen to fully encompass all of the simulated and experimental cutting conditions.

In Figure 8-3A, experimentally measured receptance Frequency Response Functions (FRFs) are shown for five axial positions and four depths of cut. From these experimental FRFs, $\psi(\hat{x}_t(t), d_c)$ was determined in a least squares fashion based on a frequency domain model:

$$FRF(\hat{x}_t, d_c, \omega) = \frac{\psi(\hat{x}_t(t), d_c)}{2\zeta\omega_n\omega j + \omega_n^2 - \omega^2} \tag{8.1}$$

where FRF is the frequency response function as a function of $\hat{x}_t$, d_c, and frequency, ω. The curve-fitted FRFs are plotted in Figure 8-3B. The choice of the model having the form of Equation (8.1) was based on the fact that both the damping ratio and the natural frequency did not shift appreciably from one impact test to another; therefore the only varying coefficient needed was $\psi(\hat{x}_t(t), d_c)$. Also, before and during the occurrence of chatter the vast majority of the vibration energy of the workpiece is concentrated at its first natural frequency of 600 Hz. Consequently its second natural frequency at around 3000 Hz was not modeled because it represents a very small

contribution dynamic response of the workpiece. It should be noted that since acceleration measurements were used and receptance FRFs were desired, the measured FRFs in Figure 8-3A have been twice numerically integrated in frequency to obtain units of mm/N. This operation resulted in near division by zero at low frequencies and hence the rapid increase in the FRF value near 0 Hz. These data points were not used in the curve fitting of the model in Equation (8.1).

It should be noted that although the workpiece is rotating, there need be no consideration of gyroscopic effects since the rotational frequency is relatively low and the displacement at any point along the workpiece is small. Consequently, open loop dynamic properties of the workpiece determined via model impact testing are assumed to apply during cutting. This same notion was experimentally validated in [29]. The FRF in Equation (8.1) using the values found for $\psi(\hat{x}_t(t), d_c)$ is plotted in Figure 8-4 as a function of $\hat{x}_t(t)$ and d_c with the exact numerical formulation for $\psi(\hat{x}_t(t), d_c)$ given in Appendix E.

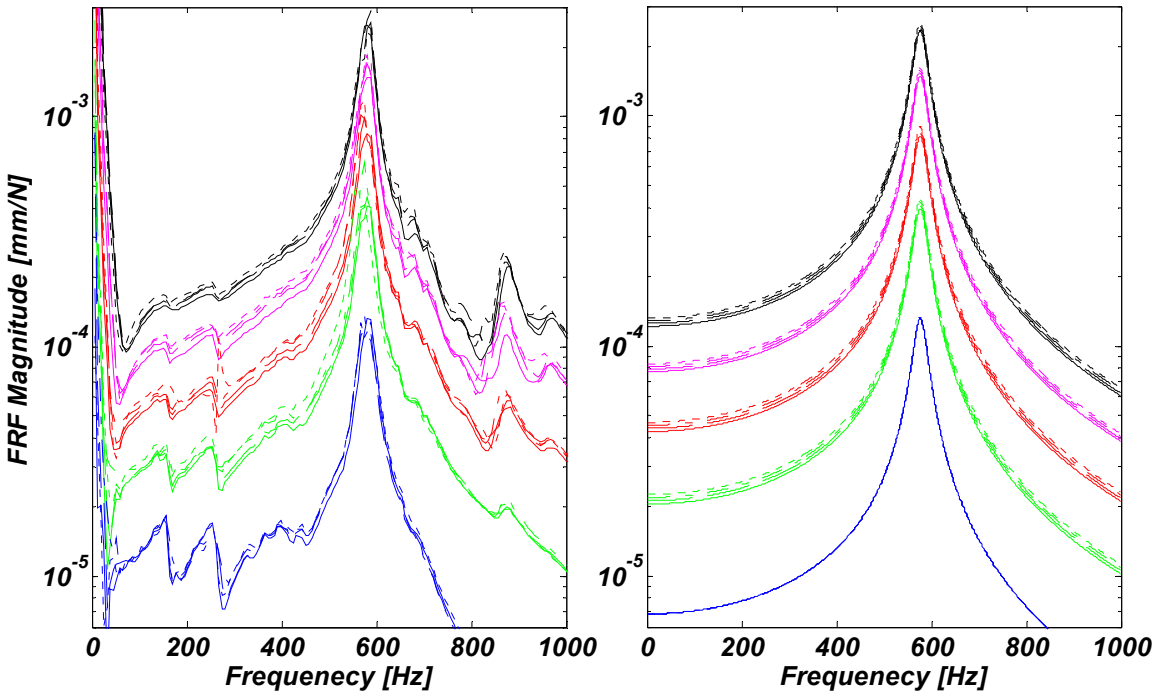

Figure 8-3: Frequency response functions of the workpiece at various axial positions and with varying amounts of material removal. **Blue** traces denote $\hat{x}_t$ =23.09 mm; **green** traces denote $\hat{x}_t$ =68.81 mm; **red** traces denote $\hat{x}_t$ =102.59 mm; **magenta** traces denote $\hat{x}_t$ =136.63 mm; **black** traces, denote $\hat{x}_t$ =170.41. For a solid line, ——, d_c =0.05 mm; for a dashed line, – – –, d_c =0.32 mm; for a long and short dashed line, – - – -, d_c =0.58 mm; for a short dashed line, ----, d_c =0.85mm.

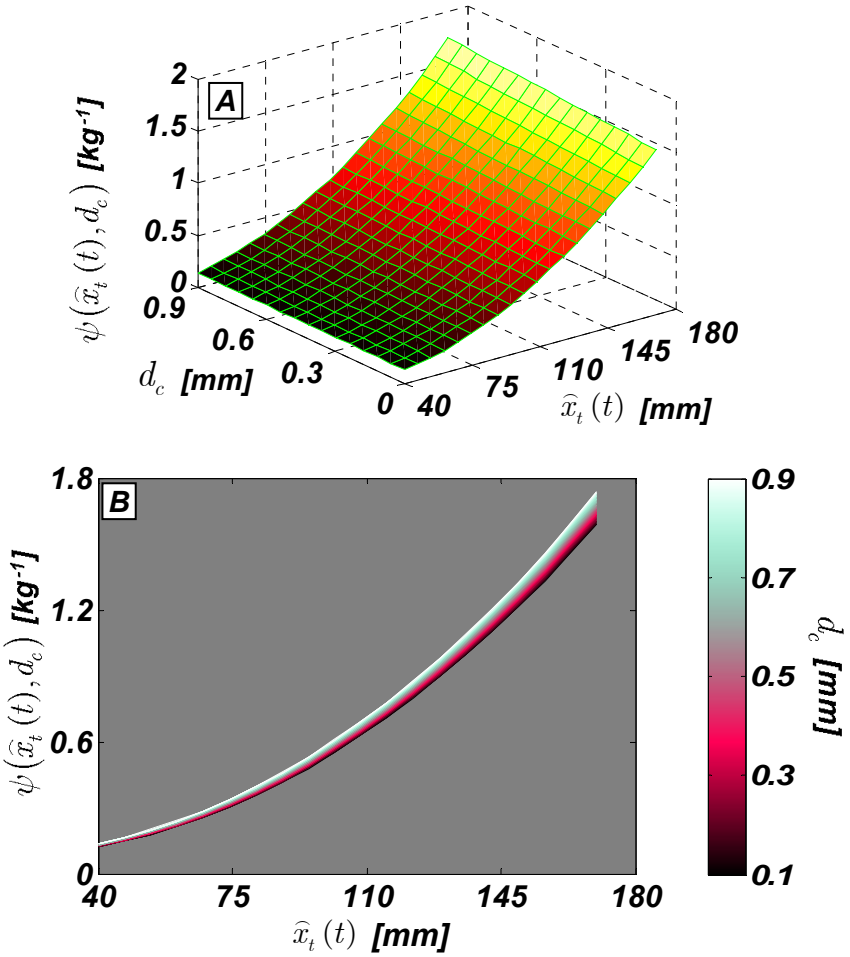

Figure 8-4: The function, $\psi(\widehat{x}_t(t), d_c)$, that reflects the varying compliance of the workpiece at the cutting zone as a function of the axial tool position and depth of cut. (A), A 3D surface plot; (B) a 2D projection.

8.4 Machining Tests to Validate Stability Limits

8.4.1 Presentation of results

For many investigations a single stability lobe diagram like that in Figure 2-2 is first generated by an analytical model. Then machining tests are conducted at a fixed cutting velocity, increasing the depth (or width) of cut until chatter is observed and thereby verifying the boundary of the stability lobe. However, with respect to the system being simulated in Figure 7-1, there is a third dimension in the stability diagram that reflects the position of the cutting tool along the workpiece's axis where chatter occurred. Typically, chatter models describe a compliant cutting tool and a rigid workpiece, a system that has constant stiffness at the cutting zone for all time and therefore a simple "yes" or "no" for the occurrence of chatter would suffice. In this dissertation, since a compliant

workpiece is being simulated, the stiffness of the system at the cutting zone changes over time and depending on the cutting conditions chatter can materialize at various positions along the workpiece. This was done intentionally since it becomes a dynamically more interesting problem than in the case of constant system stiffness. In the results that follow an increase in chatter stability is equivalent to chatter occurring later along the axis of the workpiece towards the free end.

For the previously mentioned reasons, the stability lobe diagrams in this work are not lines, but surfaces in three dimensions: depth of cut, cutting velocity, and the axial position along the workpiece where chatter materialized (measured from the cantilevered end of the workpiece in Figure 8-2). For the simulation, a value of 3.81×10^5 N/mm^3 was originally chosen for the force-interference volume constant, K_{cf}, given in Equation (3.31), as was derived in [66]. It was found that the rapid increase in stability observed in the experimental data was not adequately captured with this value of K_{cf}. However when the value was increased to 6.00×10^5 N/mm^3 an adequate increase in predicted low speed chatter stability was observed. The justification for this can be explained as follows. K_{cf} is inversely proportional to the extent of plastic deformation in the workpiece caused by the stress field around edge of the cutting tool, ρ. Since ρ has been observed to vary between 0.508 and 5.08 mm in other machining tests [70] (assuming that AISI 1018 steel has a Young's Modulus of 200 GPa and a Poisson's ratio of 0.300), by Equation (3.31) K_{cf} could be in the range 7.63×10^4 to 7.63×10^5 N/mm^3. Additionally in [51], Endres presented a semi-empirical model which allows K_{cf} to vary as a free parameter as it was calibrated to predict machining forces in turning experiments on SAE 1112. The range of values for K_{cf} that Endres found for a wide range of cutting conditions was about 9.2×10^4 to 1.1×10^6 N/mm^3, which encompasses the value used in this study, 6.00×10^5 N/mm^3. It is interesting to note that the range of values empirically derived by Endres is close to that suggested by Equation (3.31) when using the aforementioned values of ρ.

In this investigation, two different tool nose radii, 0.79 and 1.19 mm, were used as the parameter space consisting of the depth of cut and cutting vacuity was explored. The specific

machining and simulation parameters used are given in Table 8-1 and Table 8-2. It should be noted that the range for the depth of cut is greater for the larger tool nose radius. This is due to one of the simplifying assumptions made in both of the models' development in that there is no cutting along the straight edge of the cutting tool. Based on the side cutting edge angle and the nose radius of the cutting tool the largest depth of cut that the model is valid for, $d_{c,\max}$, is

$$d_{c,\max} = r_n \cos[C_S] \tag{8.2}$$

which for the 0.79 mm tool nose radius works out to $d_{c,\max}$ = 0.608 mm and for the 1.19 mm tool nose radius $d_{c,\max}$ = 0.912 mm. This explains why the maximum depth of cut in the experiments for the 1.19 mm tool nose radius was 0.85 mm and the largest depth of cut for the 0.79 tool nose radius was 0.55 mm.

To generate the experimental data for each tool nose radius, six depths of cut were used at six different cutting velocities for a total of 36 unique cutting conditions. All of these conditions are given in Table 8-3, and as shown there are six different depths of cut for each tool nose radius and six common cutting velocities. It was identified early in the machining tests that there was a great deal of variability in the point of chatter along the workpiece when the same cutting test was repeated (sometimes as a much as 20-25 mm over a 170 mm length workpiece). Therefore, it was necessary to repeat each cutting condition multiple times in order to obtain an interval of possible chatter locations. Specifically, each cut was repeated three times, and in the plots that follow containing experimental chatter instability point measurements, three data points are given for each cutting condition: a maximum chatter location, a minimum chatter location, and an average chatter location. Because each data point was repeated 3 times, to generate 36 unique cutting conditions for each tool nose radius it took a total of 216 total machining tests. For each test a new workpiece was used with the same initial machined dimensions since the act of removing material causes its dynamic properties to change.

Table 8-1: The cutting conditions used in the simulations and machining experiments.

Cutting Parameter	*Value*
Depth of cut, d_c	0.01-0.6 [mm] for r_n =0.79 [mm] 0.01-0.9 [mm] for r_n =1.19 [mm]
Tool nose radius, r_n	0.79 or 1.19 [mm]
Cutting velocity, $\overline{V}_C$	1.0-5.0 [m/s]
Feed rate, f	0.076 [mm]
Side cutting edge angle, C_S	40 [deg]
End cutting edge angle, C_E	50 [deg]
Rake angle, α_n	-6.0 [deg]
Inclination angle, i	-10.8 [deg]
Clearance angle, γ	7 [deg]
Edge radius, r_e	0.038 [mm]
Initial workpiece diameter, d_w	37.87 [mm]
Workpiece length, L	170.41 [mm]
Material	AISI 1018 cold rolled steel
Cutting insert	Kennametal CNMG432FW or CNMG433FW

Table 8-2: The simulation parameters used for both cutting force models

Simulation Parameter	*Value*
Separation angle, $\overline{\beta}_e$	30 [deg]
Coefficient of friction, μ	0.3 [--]
Natural frequency, ω_n	577 [Hz]
Damping ratio, ζ	0.030 [--]
Force-interference volume constant, K_{cf}	6.0×10^5 [N/mm^3]

Table 8-3: The cutting conditions used for experiments.

Tool Nose Radius [mm]	*Depth of cut [mm]*	*Cutting Velocities [m/s]*
0.79	0.05	1.08, 1.3, 2.25, 3.08, 3.92, 4.75
	0.15	
	0.25	
	0.35	
	0.45	
	0.55	
1.19	0.05	
	0.21	
	0.37	
	0.53	
	0.69	
	0.85	

A total of four distinct sets of results will be presented in the following order: chatter stability prediction from the simplified cutting force model for the 0.79 mm nose radius tool, prediction from the simplified cutting force model for the 1.19 mm nose radius tool, prediction from the refined cutting force model for the 0.79 mm nose radius tool, and a prediction from the refined cutting force model for the 1.19 mm nose radius tool. Each of the four predictions consist of three figures and two tables. The first figure contains six graphs, each one for a constant depth of cut and plotting the point of chatter along the workpiece as a function of cutting velocity. The second and third figures come purely from either of the theoretical models and are the three dimensional stability lobe surfaces discussed earlier. In one plot the third dimension is contoured in a two dimensional plane and in the other plot it is shown in three dimensions. These stability lobe surfaces were created by interpolating between 10,000 simulations that used various combinations of the depth of cut and cutting velocity. Finally in the two tables, one gives average errors in the model's prediction of the point of chatter as a function of cutting velocity and the other gives it as a function of the depth of cut.

First consider the experimental results of the point of chatter instability along the workpiece for the 0.79 mm tool nose radius compared to the prediction from the simplified cutting force model in Figure 8-5. The general trend of the model is to predict chatter to occur sooner along the workpiece than it was experimentally measured. Additionally the increase in low speed stability, especially in the 0.25, 0.35, 0.45, and 0.55 mm depths of cut is smaller than what is suggested by the experimental data. In Figure 8-6 and Figure 8-7 are the stability surfaces predicted by the simplified cutting force model. At very light depths of cut and at low cutting speeds the model predicts a rapid increase in stability. It is clear that the simplified model has reproduced the characteristic lobes present in the classical stability diagram in Figure 2-2.

In Table 8-4 and Table 8-5 is the average error and standard deviation between the prediction of the simplified cutting force model and the experimental measurements. For Table 8-4 it should be noted that there are two sets of average errors and standard deviations for the cutting

velocities: one for all the depths of cut, and the other for all the depths of cut except the lightest one at 0.05 mm. This is because the error in the prediction for the lightest depth of cut is very large and felt to be outside the predictive range of the model (this will be come increasingly apparent after the three other sets of results for the point of chatter instability predicted along the workpiece). The best predictions in each table are shown in bold and indicate that the most accurate one as a function of the cutting velocity occurs at of 4.75 m/s, having an average error of 18.62 mm. If the lightest depth of cut is neglected than the average error for the best prediction drops to 11.00 mm at 2.25 m/s. The most accurate prediction as a function of the depth of cut occurs at the largest one, 0.55 mm, having an average error of 13.01 mm.

Finally, in each table there is a column labeled "predictions in range." A prediction by the analytical model was determined to be "in range" of the experimental measurements if it was within ±8.5 mm from the average experimentally measured value, or within the range of the error bars, whichever one was larger. The interval ±8.5 mm was chosen since the entre range is 17 mm, which is roughly 10% of the workpiece's length. For this set of results as well as the next three, it should be noted that if the position of chatter is 170.41 mm, the length of the workpiece, then there was no chatter observed. For this particular case of the simplified cutting force model predicting chatter for the 0.79 mm nose radius cutting tool, the largest number of predictions in range as a function of the cutting velocity was 2 out of 6 at 2.25 m/s and the largest number as a function of the depth of cut was 2 out of 6 at both 0.35 and 0.55 mm.

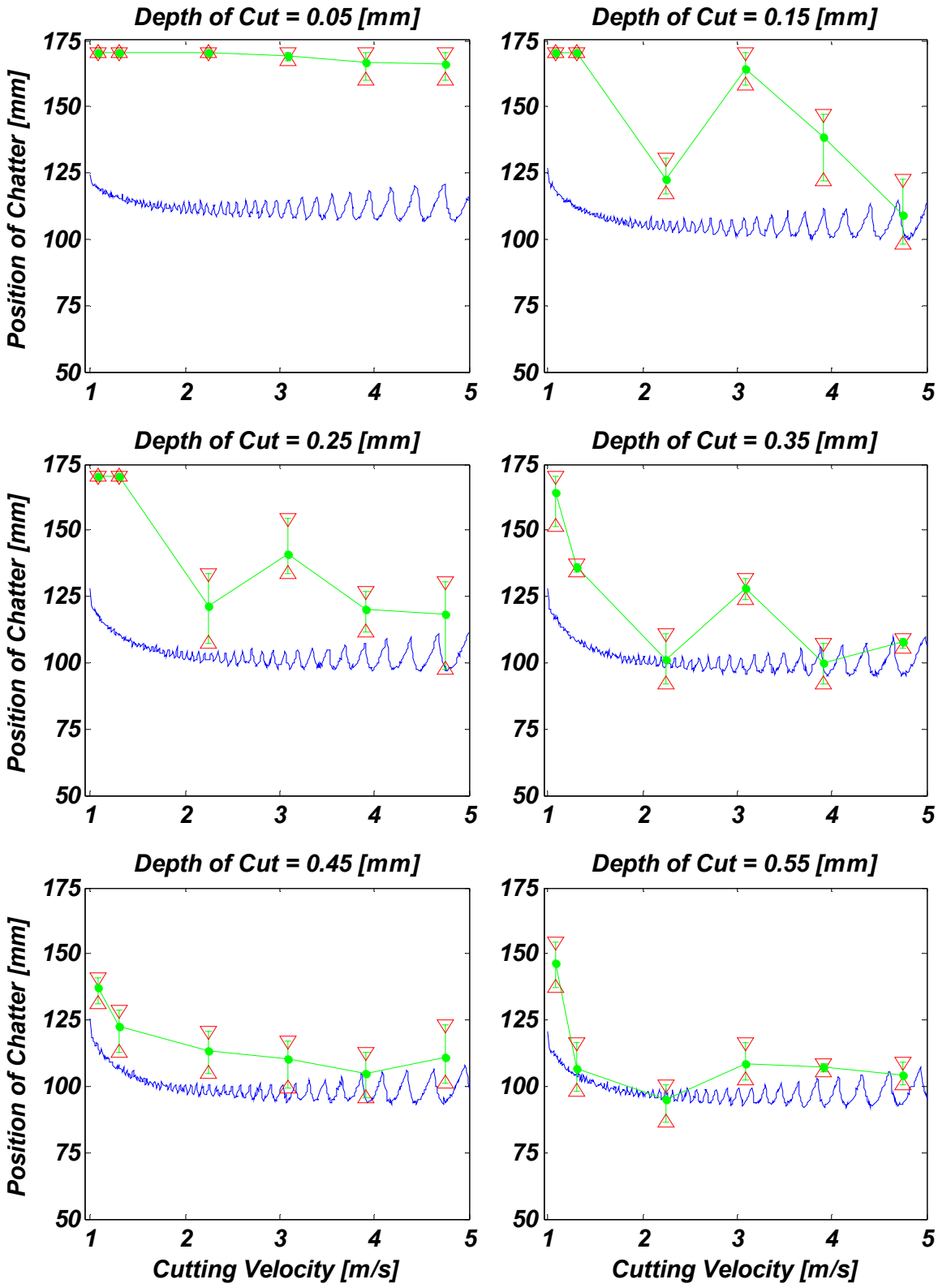

Figure 8-5: Simplified cutting force model predictions and experimental measurements of the position of chatter for a 0.79 mm nose radius cutting tool. Δ, ∇, and ●, the minimum, maximum, and mean position of chatter for a specific cutting condition, respectively; —, model prediction.

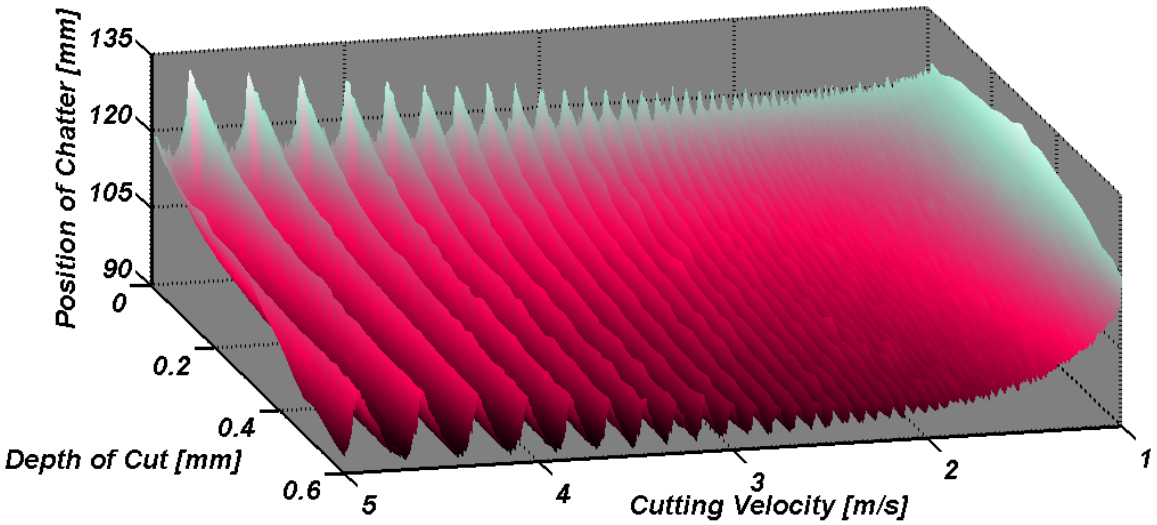

Figure 8-6: Stability diagram using the simplified dynamic cutting force model for the 0.79 mm nose radius cutting tool showing the distance along the workpiece where chatter began (3D view).

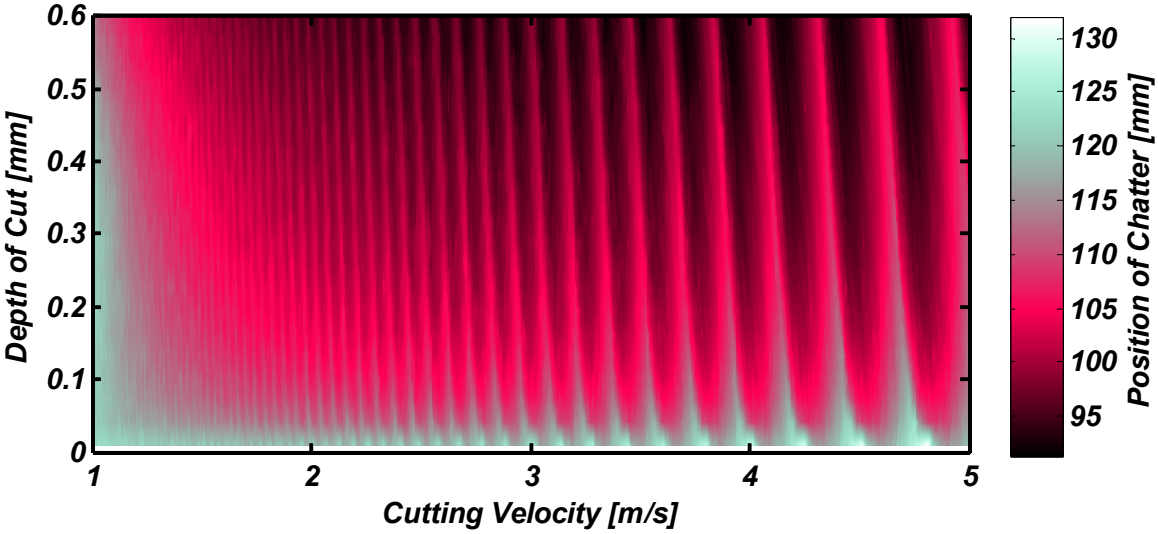

Figure 8-7: Stability diagram using the simplified dynamic cutting force model for the 0.79 mm nose radius cutting tool showing the distance along the workpiece where chatter began (2D view).

Table 8-4: Comparison of the simplified dynamic cutting force model to experimental results when machining with a 0.79 mm tool nose radius (along various cutting velocities).

Cutting Velocity [m/s]	*All Depths of Cut*		*Neglecting Lightest Depth of Cut*		*Predictions in Range [out of 6]*
	Average Error [mm]	*Standard Deviation [mm]*	*Average Error [mm]*	*Standard Deviation [mm]*	
1.08	43.39	11.98	41.90	12.76	0/6
1.30	36.44	24.90	32.69	25.87	1/6
2.25	19.17	21.76	**11.00**	9.59	2/6
3.08	35.81	18.82	31.86	18.04	0/6
3.92	20.29	17.65	13.93	9.26	1/6
4.75	**18.62**	14.01	13.34	6.00	1/6

Table 8-5: Comparison of the simplified dynamic cutting force model to experimental results when machining with a 0.79 mm tool nose radius (along various depths of cut).

Depth of Cut [mm]	*Average Error [mm]*	*Standard Deviation [mm]*	*Predictions in Range [out of 6]*
0.05	53.13	5.09	0/6
0.15	36.62	22.40	1/6
0.25	35.17	18.53	0/6
0.35	20.03	18.51	2/6
0.45	15.76	4.41	0/6
0.55	**13.01**	12.02	2/6

In Figure 8-8 are the experimental results for the point of chatter instability along the workpiece when using a 1.19 mm nose radius tool compared to the prediction from the simplified cutting force model. Similar to the prediction of the 0.79 mm nose radius cutting tool, the model predicts a slight increase in stability at low cutting speeds. However in this case, the degree of increased stabilization suggested by the experimental results appears to agree much better with the model. In Figure 8-9 and Figure 8-10 are the stability surfaces predicted by the simplified cutting force model for the 1.19 mm tool nose radius.

From Table 8-6 and Table 8-7, it can be seen that predictions of chatter for the 1.19 mm tool nose radius were slightly better than those for the 0.79 mm nose radius tool. Once again, the most accurate prediction as a function of cutting velocity occur at of 4.75 m/s, having an average error of 17.09 mm over all the depths of cut. When neglecting the lightest depth of cut, the best prediction improves has 13.39 mm of average error at a cutting velocity of 2.25 m/s. The most accurate predictions as a function of cutting depth once again occurred at the largest value tested, 0.85 mm, having an average error of 11.37 mm. The largest number of predictions by the simplified model that were in range as a function of the cutting velocity was 3 out of 6 at 2.25 m/s and the largest number as a function of the depth of cut was 4 out of 6 at 0.85 mm.

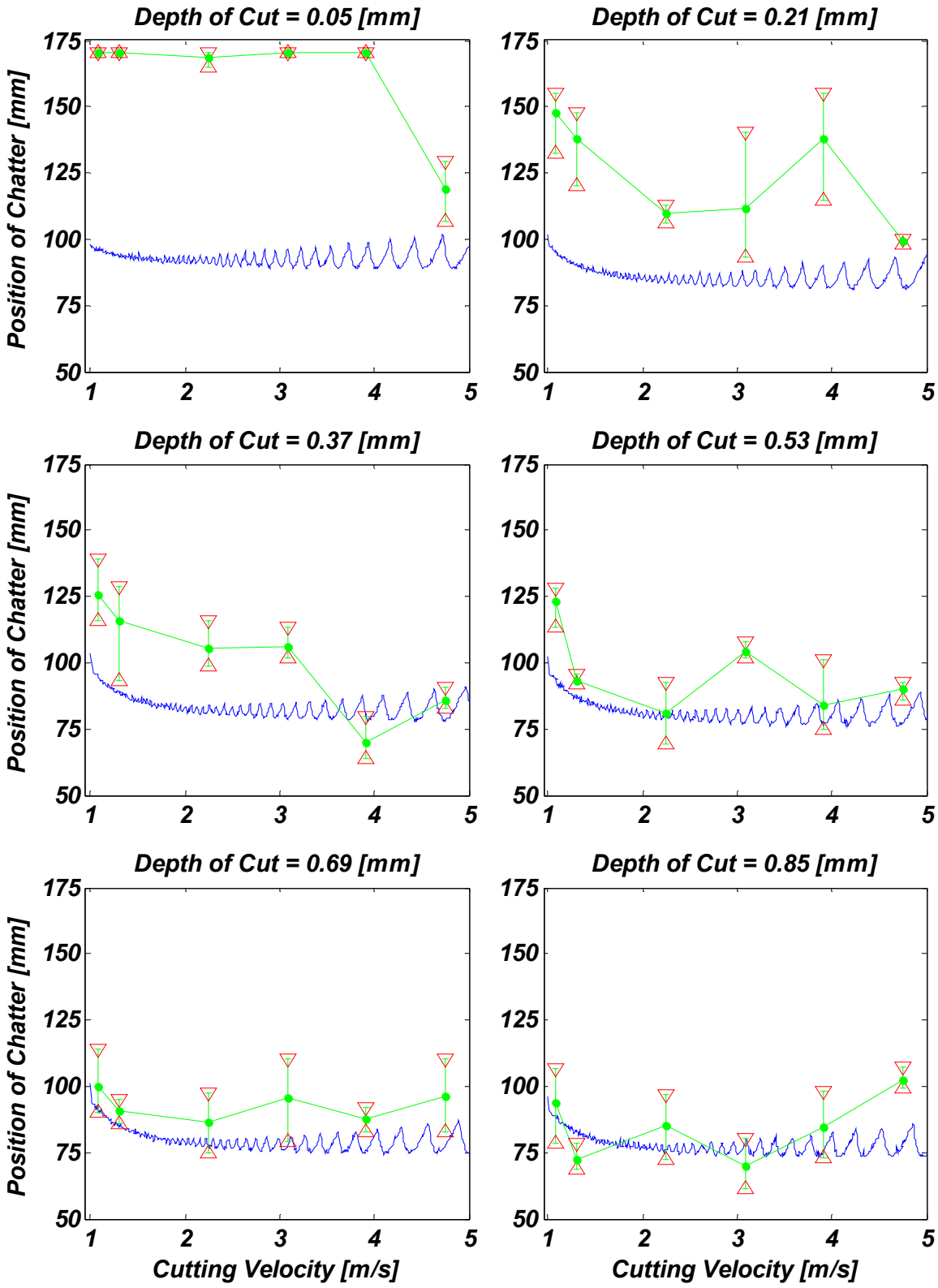

Figure 8-8: Simplified cutting force model predictions and experimental measurements of the position of chatter for a 1.19 mm nose radius cutting tool. Δ, ∇, and ●, the minimum, maximum, and mean position of chatter for a specific cutting condition, respectively; —, model prediction.

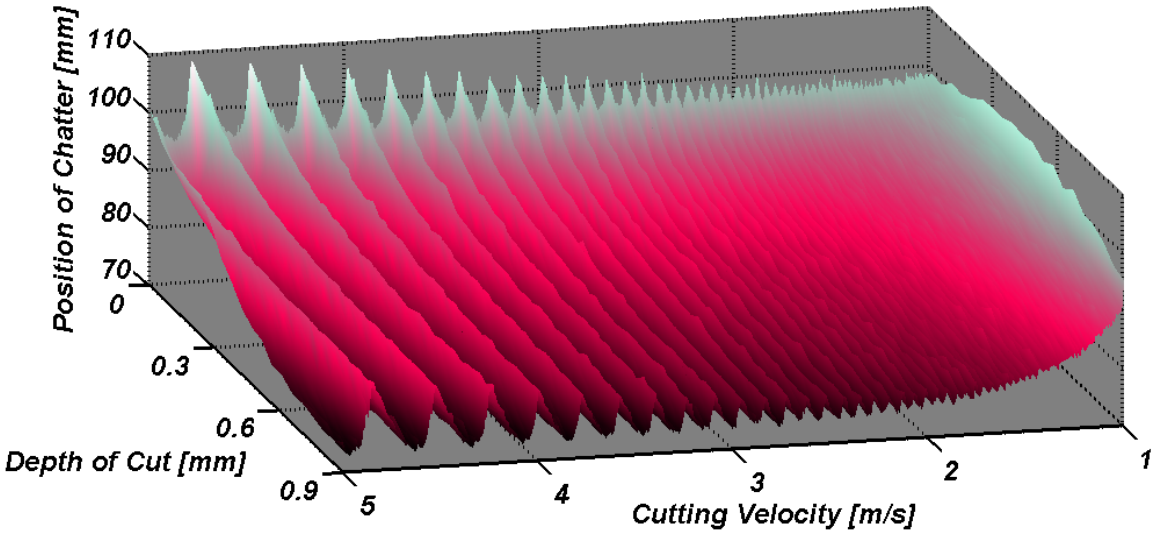

Figure 8-9: Stability diagram using the simplified dynamic cutting force model for the 1.19 mm nose radius cutting tool showing the distance along the workpiece where chatter began (3D view).

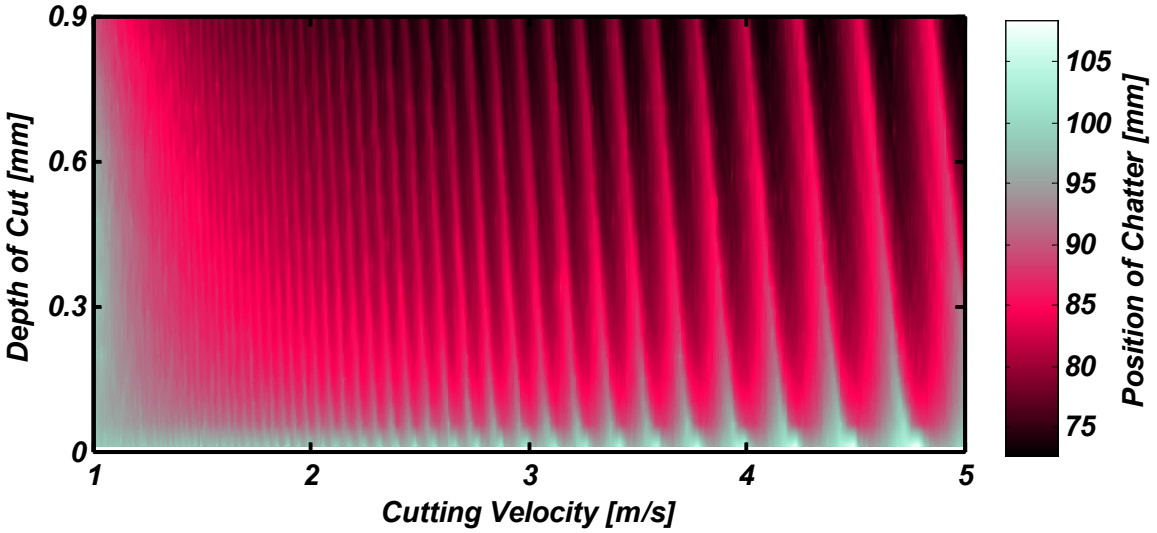

Figure 8-10: Stability diagram using the simplified dynamic cutting force model for the 1.19 mm nose radius cutting tool showing the distance along the workpiece where chatter began (2D view).

Table 8-6: Comparison of the simplified dynamic cutting force model to experimental results when machining with a 1.19 mm tool nose radius (along various cutting velocities).

Cutting Velocity [m/s]	*All Depths of Cut*		*Neglecting Lightest Depth of Cut*		*Predictions in Range [out of 6]*
	Average Error [mm]	*Standard Deviation [mm]*	*Average Error [mm]*	*Standard Deviation [mm]*	
1.08	33.69	25.99	25.51	18.51	2/6
1.30	29.21	28.21	19.68	17.70	2/6
2.25	24.15	27.88	**13.39**	10.13	3/6
3.08	30.61	22.75	21.84	8.37	1/6
3.92	27.13	28.25	17.78	18.46	2/6
4.75	**17.09**	6.19	15.83	6.00	1/6

Table 8-7: Comparison of the simplified dynamic cutting force model to experimental results when machining with a 1.19 mm tool nose radius (along various depths of cut).

Depth of Cut [mm]	*Average Error [mm]*	*Standard Deviation [mm]*	*Predictions in Range [out of 6]*
0.05	66.87	21.35	0/6
0.21	36.65	15.06	0/6
0.37	20.93	9.82	1/6
0.53	13.73	11.69	3/6
0.69	12.34	4.94	3/6
0.85	**11.37**	6.25	4/6

In Figure 8-11 are the predictions from the refined cutting force model in comparison to the experimental point of chatter instability along the workpiece for the 0.79 mm tool nose radius. In comparison to the simplified cutting force model, the refined model appears to be capturing the trends of the data much better. For depths of cut greater than 0.15 mm, the rapid increase in low speed chatter stability suggested by the experimental data is adequately captured. In Figure 8-12 and Figure 8-13 are the stability surfaces predicted by the refined cutting force model. The numerical results in Table 8-8 and Table 8-9 indicate that the errors between the refined cutting force model and measurements are generally quite good, especially for cutting velocities greater than 1.3 m/s and depths of cut larger than 0.15 mm. Once again just as for the simplified model, there are very large errors at the 0.05 mm depth of cut. The best agreement between the experimental results and the model's prediction as a function of cutting velocity occurs at 4.75 m/s, having an average error of 10.28 mm for all depths of cut and just 4.99 mm when excluding the smallest depth of cut. 9.76 mm was the lowest error as a function of the cutting depth, occurring at 0.45 mm. The largest number of predictions by the refined cutting force model that were in range as a function of the cutting velocity was 5 out of 6 at 4.75 m/s and the largest number as a function of the depth of cut was 3 out of 6 at 0.15, 0.25, 0.35, 0.45 and 0.55 mm.

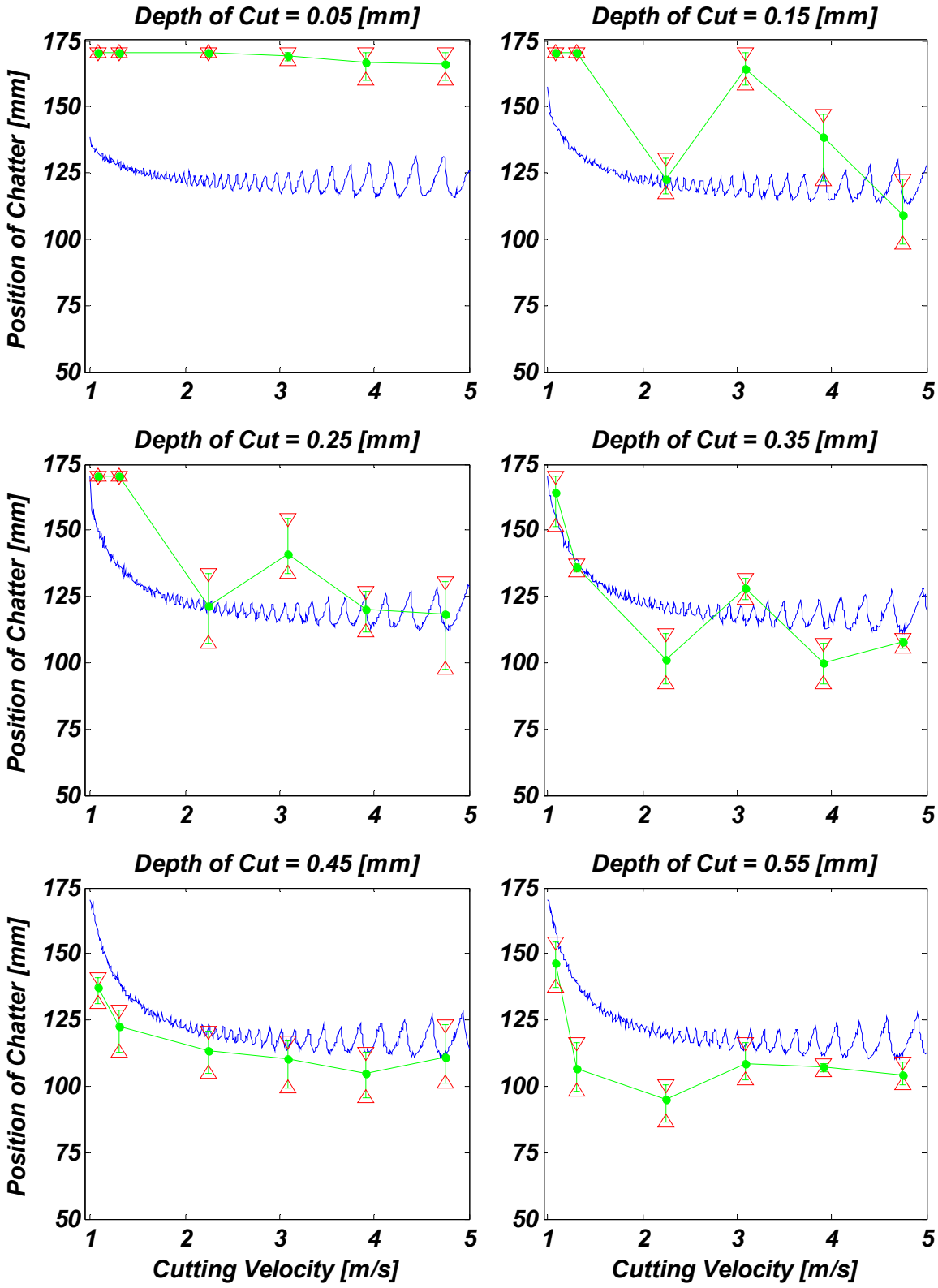

Figure 8-11: Refined cutting force model predictions and experimental measurements of the position of chatter for a 0.79 mm nose radius cutting tool. Δ , ∇ , and ●, the minimum, maximum, and mean position of chatter for a specific cutting condition, respectively; —, model prediction.

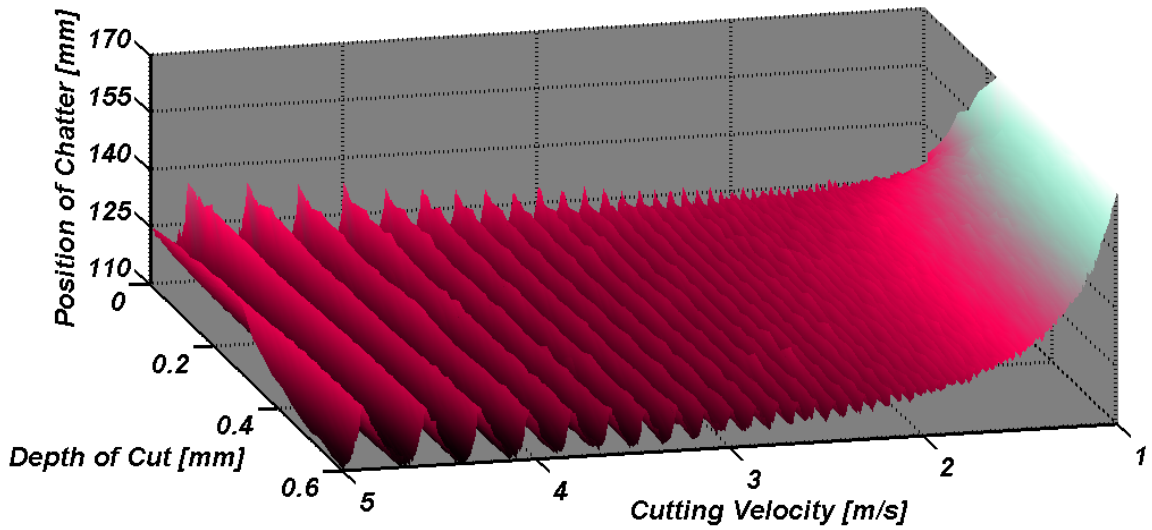

Figure 8-12: Stability diagram using the refined dynamic cutting force model for the 0.79 mm nose radius cutting tool showing the distance along the workpiece where chatter began (3D view).

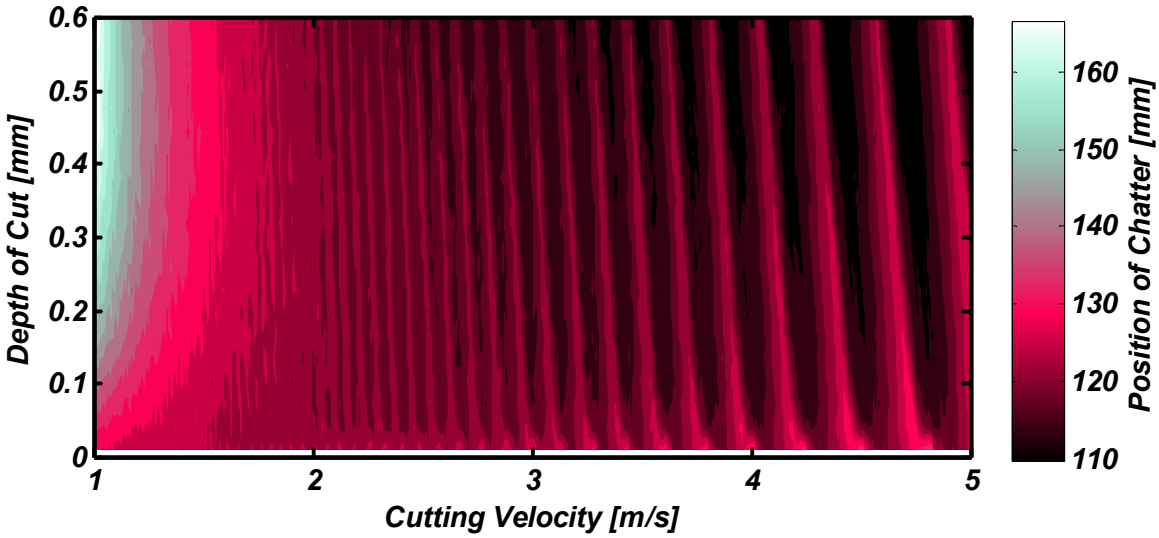

Figure 8-13: Stability diagram using the refined dynamic cutting force model for the 0.79 mm nose radius cutting tool showing the distance along the workpiece where chatter began (2D view).

Table 8-8: Comparison of the refined dynamic cutting force model to experimental results when machining with a 0.79 mm tool nose radius (along various cutting velocities).

Cutting Velocity [m/s]	*All Depths of Cut*		*Neglecting Lightest Depth of Cut*		*Predictions in Range [out of 6]*
	Average Error [mm]	*Standard Deviation [mm]*	*Average Error [mm]*	*Standard Deviation [mm]*	
1.08	20.98	10.82	17.60	7.79	1/6
1.30	27.88	14.98	24.95	14.70	1/6
2.25	18.01	17.72	11.73	9.84	2/6
3.08	22.18	18.15	17.50	15.74	2/6
3.92	13.66	14.83	7.91	5.20	4/6
4.75	**10.28**	13.19	**4.99**	2.73	5/6

Table 8-9: Comparison of the refined dynamic cutting force model to experimental results when machining with a 0.79 mm tool nose radius (along various depths of cut).

Depth of Cut [mm]	*Average Error [mm]*	*Standard Deviation [mm]*	*Predictions in Range [out of 6]*
0.05	42.42	4.72	0/6
0.15	21.56	16.69	3/6
0.25	14.37	13.60	3/6
0.35	10.16	6.18	3/6
0.45	**9.76**	7.56	3/6
0.55	14.72	11.22	3/6

Finally, in Figure 8-14 are the predictions from the refined cutting force model in comparison to measured points of chatter along the workpiece when using a 1.19 mm tool nose radius. Just as in the case for the 0.79 mm tool nose radius, there is much better agreement with the experimental results then in the case of the simplified cutting force model. In Figure 8-15 and Figure 8-16 are the stability surfaces predicted by the refined cutting force model. They look qualitatively very similar to the ones for the 0.79 mm tool nose radius in Figure 8-12 and Figure 8-13.

The numerical results in Table 8-10 and Table 8-11 indicate that the errors between the refined cutting force model and the experimental measurements are generally good, especially for cutting velocities greater than 1.3 m/s and depths of cut larger than 0.21 mm. The best agreement in the model's predictions as a function of cutting velocity occur at 4.75 m/s, having an average error of 6.46 mm for all depths of cut and just 4.54 mm when excluding the smallest depth of cut. Additionally, five out of six cutting conditions are predicted in range. The lowest error as a function of cutting depth occurs as 0.37 mm, having as average error of 9.57 mm with predictions for 4 out of the 6 cutting conditions being in range.

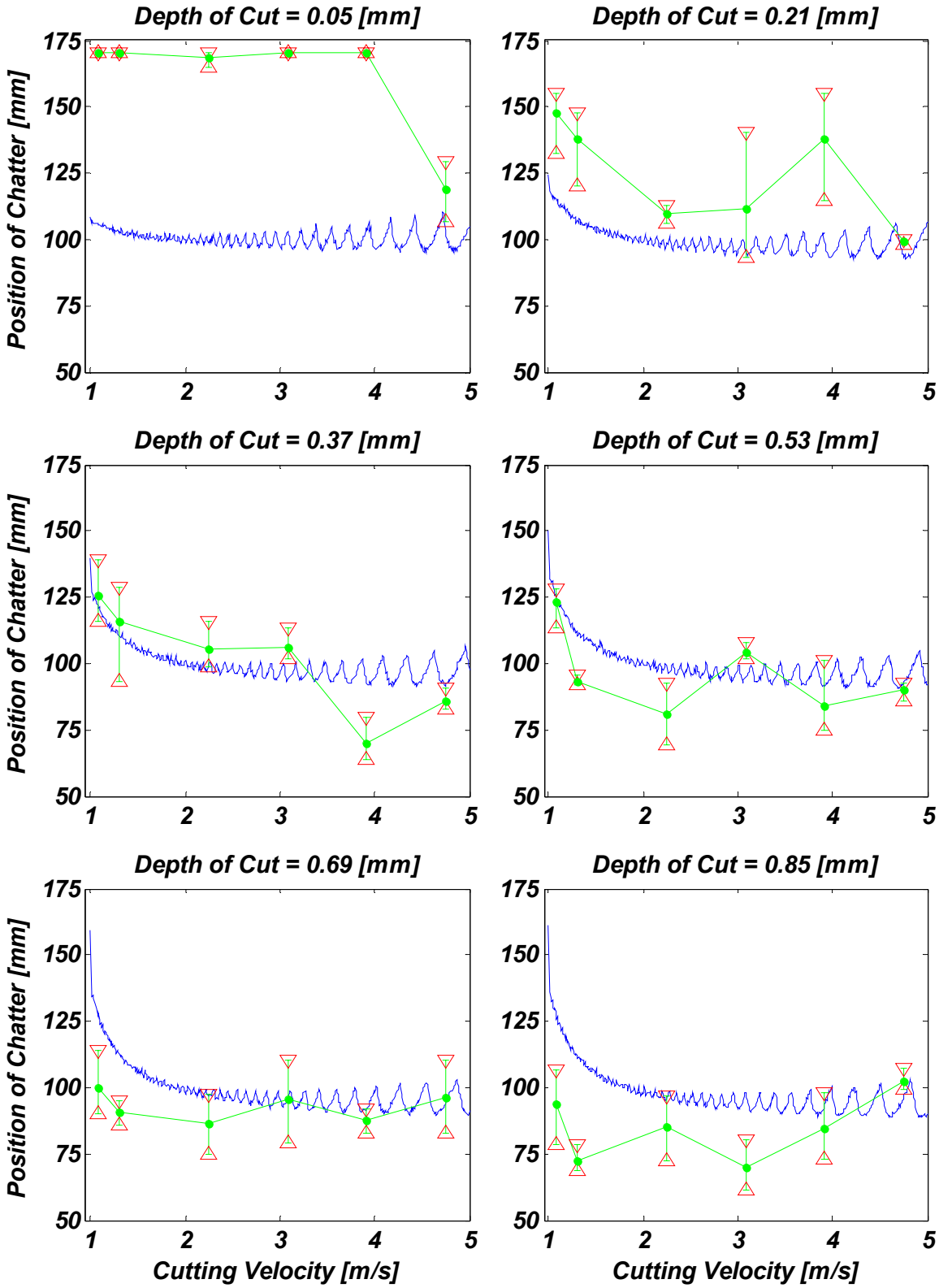

Figure 8-14: Refined cutting force model predictions and experimental measurements of the position of chatter for a 1.19 mm nose radius cutting tool. Δ , ∇ , and ●, the minimum, maximum, and mean position of chatter for a specific cutting condition, respectively; —, model prediction.

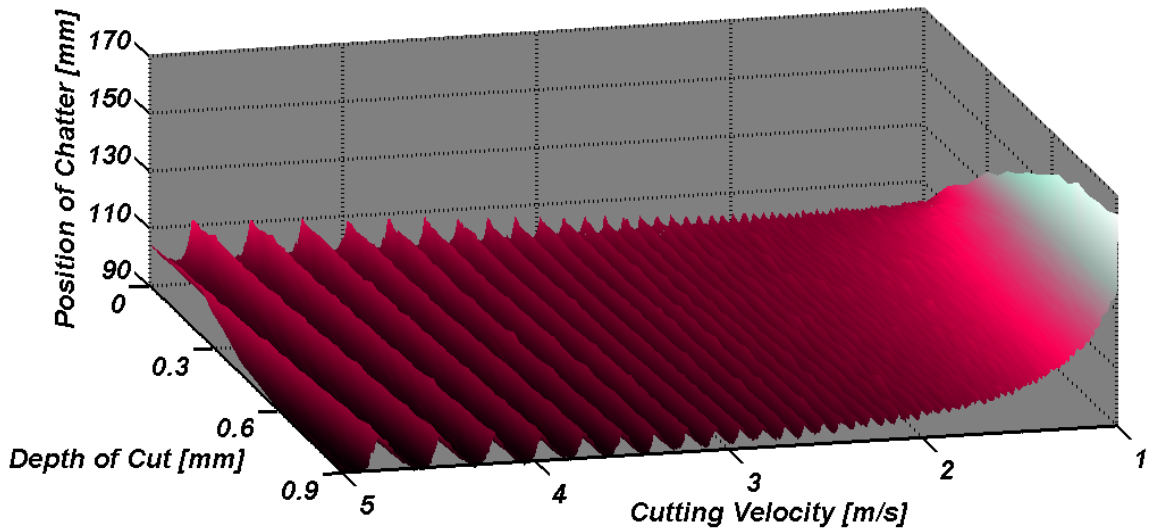

Figure 8-15: Stability diagram using the refined dynamic cutting force model for the 1.19 mm nose radius cutting tool showing the distance along the workpiece where chatter began (3D view).

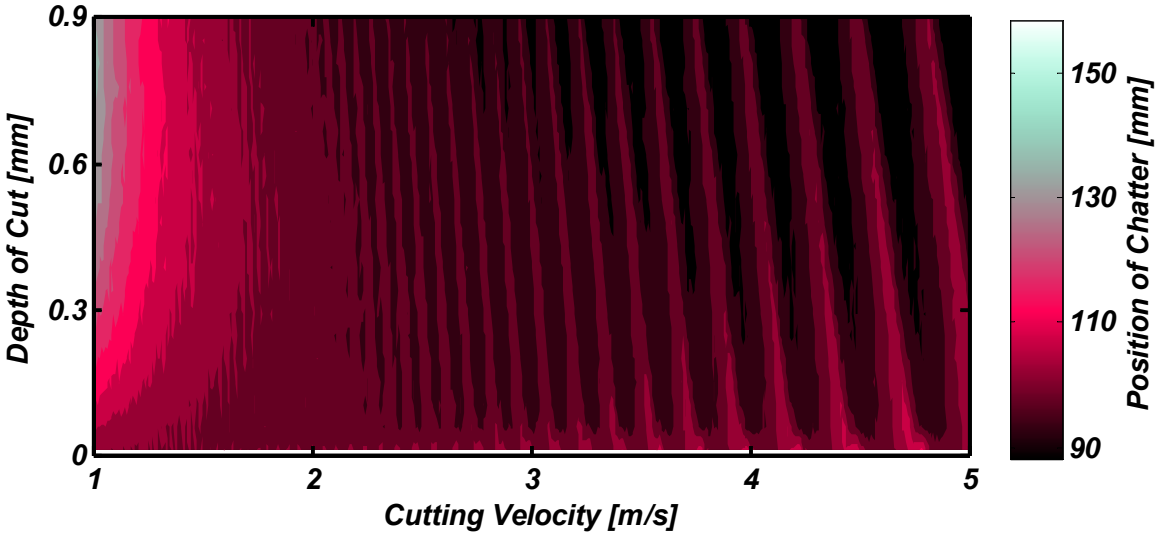

Figure 8-16: Stability diagram using the refined dynamic cutting force model for the 1.19 mm nose radius cutting tool showing the distance along the workpiece where chatter began (2D view).

Table 8-10: Comparison of the refined dynamic cutting force model to experimental results when machining with a 1.19 mm tool nose radius (along various cutting velocities).

Cutting Velocity [m/s]	*All Depths of Cut*		*Neglecting Lightest Depth of Cut*		*Predictions in Range [out of 6]*
	Average Error [mm]	*Standard Deviation [mm]*	*Average Error [mm]*	*Standard Deviation [mm]*	
1.08	27.27	23.05	19.69	15.30	2/6
1.30	30.53	21.56	23.07	12.79	1/6
2.25	21.10	24.37	11.29	4.48	3/6
3.08	22.36	23.84	13.36	10.17	2/6
3.92	24.73	24.17	16.36	14.34	3/6
4.75	**6.46**	4.96	**4.54**	1.76	5/6

Table 8-11: Comparison of the refined dynamic cutting force model to experimental results when machining with a 1.19 mm tool nose radius (along various depths of cut).

Depth of Cut [mm]	*Average Error [mm]*	*Standard Deviation [mm]*	*Predictions in Range [out of 6]*
0.05	58.84	21.02	0/6
0.21	22.27	13.38	2/6
0.37	**9.57**	7.05	4/6
0.53	9.70	7.26	3/6
0.69	11.25	11.41	4/6
0.85	20.81	14.05	3/6

8.4.2 Summary of results, explanation of trends, and limitations of the current approach

The average errors and standard deviations for each model used in conjunction with each tool nose radius are summarized in Table 8-12. The refined cutting force model exhibits much lower errors in the prediction of the point of chatter instability along the axis of the workpiece than that of the simplified cutting force model. Neglecting the lightest depth of cut, the average error for the refined cutting force model is 14.11 mm when using the small tool nose radius and 14.72 mm for the large tool nose radius. The simplified cutting force model on the other hand has an average error of 24.12 mm for the small tool nose radius and 19.00 mm when using the large tool nose radius. This means that on average, regardless of the tool nose radius used in this study, the average error in the point where chatter is predicted by the refined cutting force model is 8.6% of the workpiece's overall length. For the simplified cutting force model, 11 out of 36 cutting conditions for the large tool nose radius tool were predicted in range and 5 out of 36 were predicted in range for the small tool nose radius. However, the refined cutting force model predicted 15 out of 36 cutting conditions in range for the small tool nose radius and 16 out of 36 in range for the large tool nose radius.

For both cutting force models, predictions of the point of chatter instability along the workpiece at very low depths of cut were universally inaccurate (chatter was predicted too soon). It is felt that the main reason for this is because it is more difficult to separate the forces due to plowing and flank interference from those due to chip formation at these low depths of cut. This is a

fundamental assumption on which this approach is built–that is using two separate analyses to capture both chip formation and interference forces.

The claim that there is coupling between the plowing and chip formation mechanisms has been substantiated in numerous experimental studies [72]. At very low depths of cut on the order of the tool edge radius, the effective rake angle of the tool becomes more negative, thus causing the shear angle to decrease (as suggested by Figure 7-3F). Geometrically, this will cause the shear plane to become longer by some percentage and since the flow stress changes by smaller percentage (in general), the total amount of force along the shear plane increases. This larger amount of force along the shear plane will in turn cause the forces due to chip formation to increase (as suggested by Figure 7-3E).

Additionally at extremely low depths of cut, on the order of half of the tool edge radius, chip formation ceases and the machining process become purely a plowing operation. When cutting with a tool nose radius, there will always be a point along the undeformed chip area where the undeformed chip thickness transitions to zero because of its crescent-shaped nature (e.g. in Figure 6-4). However, the current modeling approach assumes that chip formation is always possible, regardless of the size of the undeformed chip thickness.

Finally, the nature of the plowing force can change at low depths of cut . It was observed that at low depths of cut, on the order of the tool edge radius, the nominal separation angle ,**Error! Objects cannot be created from editing field codes.**, decreases [72]. In the current modeling approach this would cause the size of the interference area to decrease and reduce the magnitude of the interference force (as suggested by Figure 3-4).

Although the predictions for the simplified model are less accurate, on a positive note they do exhibit the classic stability lobes that have been suggested by the more simplistic, traditional chatter models introduced in the literature review. One of the assumptions in the simplified cutting force model was that the effective clearance angle, γ^*, remains at zero degrees for all time. This was done in order to maintain a closed-form description of the interference forces. However at low

cutting velocities, for a fixed RTWD oscillation frequency and amplitude, γ^* will oscillate with a larger amplitude and higher frequency. This was demonstrated graphically in Figure 2-3 and represented by Equation (5.7). The fact that γ^* remains at 0° in the simplified cutting force model is one reason it does not show more drastic increases in stability at low cutting velocities.

Table 8-12: A comparison of errors between experiments and both the refined and simplified cutting force models.

Model and Tool Nose Radius	*All Depths of Cut*		*Neglecting Lightest Depth of Cut*		*Predictions in Range [out of 36]*
	Average Error [mm]	*Standard Deviation [mm]*	*Average Error [mm]*	*Standard Deviation [mm]*	
Simplified 0.79 mm	28.95	20.02	24.12	18.28	5/36
Simplified 1.19 mm	26.98	23.32	19.00	13.51	11/36
Refined 0.79 mm	**18.83**	15.20	**14.11**	11.70	15/36
Refined 1.19 mm	22.07	21.34	14.72	11.73	16/36

8.5 Frequency Domain Validation

With the most important attribute of a chatter model's validation complete, attention can now shift to other metrics used to determine the degree to which the proposed approach captures the physics of the process. From this point forward, only results from the refined cutting force model will be presented for conciseness and for the reasons stated in the first section of this chapter.

As mentioned in Chapter 1, the least rigorous metric to validate a chatter model is by comparing its content in the frequency domain to that measured experimentally. In Figure 8-17 are Discrete Fourier Transforms of a simulated and experimentally measured time series during chatter. The cutting conditions and simulation parameters were the same as those listed in Table 8-1 and Table 8-2 except that the depth of cut was 0.25 mm, the cutting velocity was 2.25 m/s, and the tool nose radius used was 0.79 mm. The dominant frequency of the workpiece's response during chatter was the same in the radial and tangential directions and for the simulation it was 609.9 Hz and for the experiment it was 608.8 Hz. These frequencies are both above the workpiece's open-loop natural

frequency, ω_n, of 577 Hz. This increase in frequency is due to the fact that the cutting tool imposes a boundary condition on the workpiece that has a stiffening effect. Additionally, the analytical model has strongly pronounced harmonics at 608.8 Hz, whereas these harmonics in the experimental data are only barely noticeable. This agreement in frequency is a good sign of the refined model capturing the physics of chatter in turning.

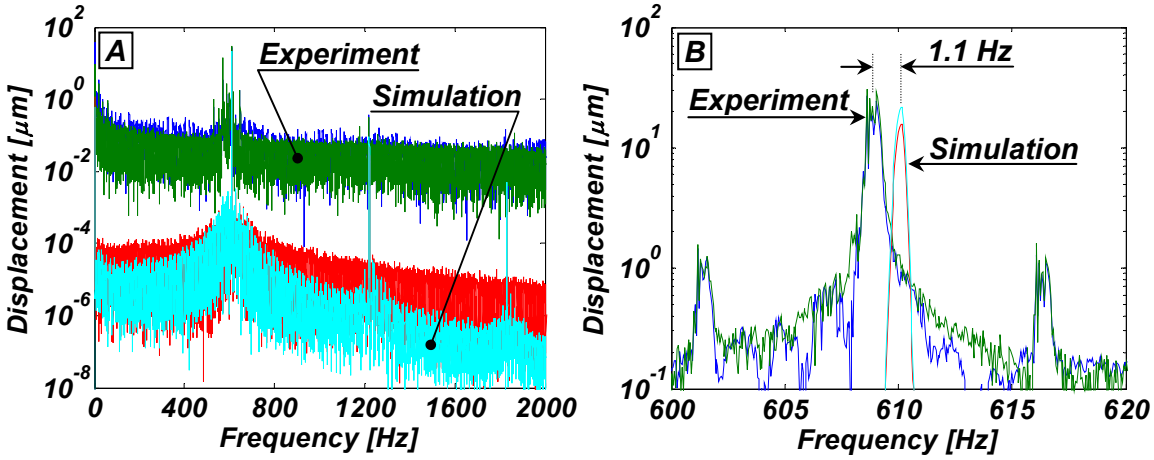

Figure 8-17: The Discrete Fourier Transform of simulation and experimental time histories. (A) Reponses in the range of 0-2000 Hz; (B) responses in the range 600-620 Hz showing the dominant frequency of the workpiece's response. ——, Measured displacement in the radial cutting direction; ——, measured displacement in the tangential cutting direction; ——, simulated displacement in the radial cutting direction; ——, simulated displacement in the tangential cutting direction.

8.6 Time Domain Validation

8.6.1 Comparison with Experimental Data

With comparisons to experimental data of the point of chatter instability along the workpiece and the content of the vibration in the frequency domain complete, the focus now shifts to predicting the amplitude of the vibrations in the time domain. If the dynamic cutting force model can successfully predict this, then it is likely valid over two distinct operating points. That is, describing forces accurately for both the case when the vibration amplitudes are relatively low (pre-chatter, useful for predicting stability limits) and relatively high (after the inception of chatter, useful for time domain amplitude growth prediction). To the author's knowledge, there is yet to be a model

for turning that has shown agreement with experimental data for both the point of chatter instability as well as its amplitude growth over time.

Shi and Tobias conducted an interesting experiment where a face milling cutter was fed at a constant rate and cutting velocity along the top of a workpiece that was inclined [73]. This provided for either a slowly increasing or slowly decreasing depth of cut over time. A picture of their experimental setup is in Figure 8-18 and their results have been reproduced in Figure 8-19. When slowly increasing the depth of cut, chatter occurs at a 4.15 mm depth of cut. However when starting at a large depth of cut where chatter is already present and slowly decreasing the depth of cut, stable cutting does not materialize until 3.00 mm. In both cases there is a very distinct "jump" between stable cutting and chatter as well as a hysteresis effect in chatter amplitude versus the depth of cut.

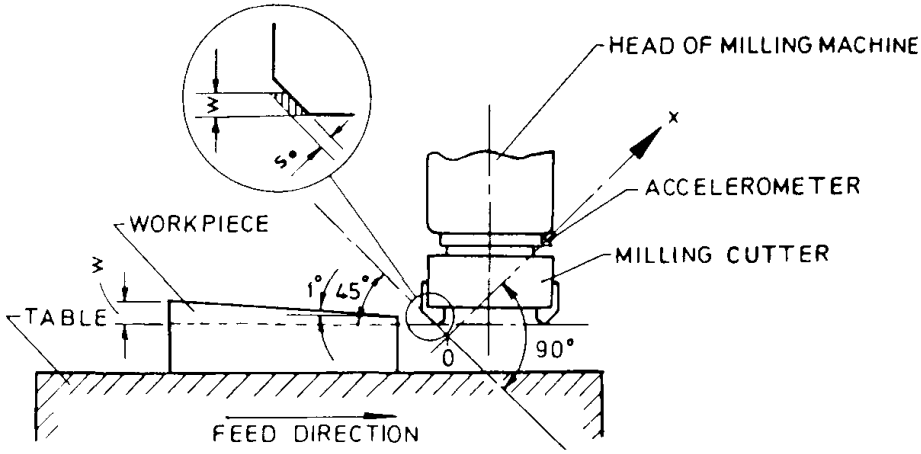

Figure 8-18: Experimental setup used by Shi and Tobias (re-presented from [73]).

Experiments and simulations were conducted in order to see if slowly varying a parameter that controls the onset of chatter, in this case the position of the cutting tool along the workpiece, would reproduce the hysteresis effect that Shi and Tobias observed in face milling. Two cases using the same cutting conditions but feeding the tool in opposite directions were experimentally measured with the setup in Figure 8-1, using the parameters as listed in Table 8-1 and Table 8-2 except that the depth of cut was 0.25 mm, the cutting velocity was 2.25 m/s, and the tool nose radius was 0.79 mm.

In Figure 8-20A is the experimentally measured workpiece displacement when the tool is fed from the cantilevered end to the free end of the workpiece, and Figure 8-20B is the simulated

version. The experiment shows chatter occurring at around 128 mm and the simulation predicts it at around 120 mm with good agreement in the predicted vibration amplitude. In Figure 8-20C is the experimentally measured case where the tool is being fed in the opposite direction along the workpiece (from the free end to the cantilevered end), and Figure 8-20D is the corresponding simulation. The experiment indicates stable cutting starting at 95 mm and the simulation predicts it at around 111 mm. In this case the error in the predicted vibration amplitude is larger, however a completely counter-intuitive effect in the experimental measurements has been captured by the simulation.

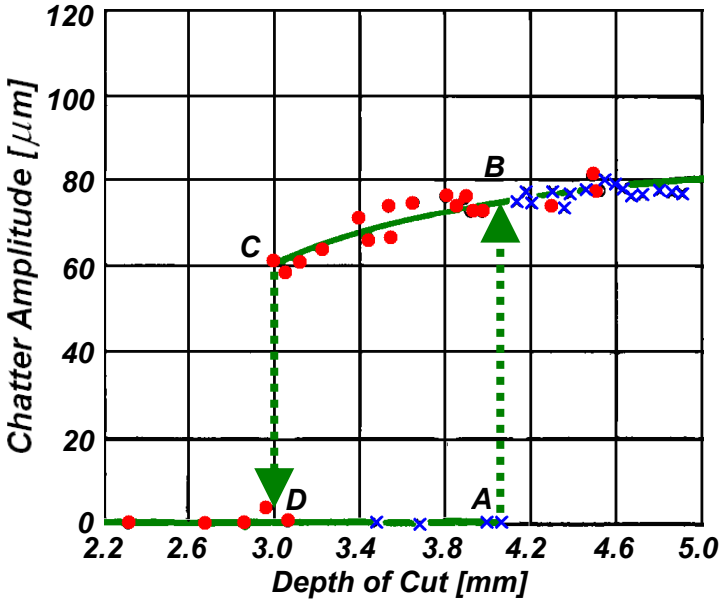

Figure 8-19: Relationship between the chatter amplitude and depth of cut determined experimentally using the setup in Figure 8-18, re-presented from [73]. ×, increasing depth of cut; ●, decreasing depth of cut; the green arrows show the direction of the jump between stable cutting and chatter.

In Figure 8-20C and D, when the tool is cutting near the free end of the workpiece, the system is very flexible and chatter occurs for both the experiment and the simulation. As the tool moves towards the cantilevered end, the stiffness at the tool-workpiece interface increases and in turn causes the vibration amplitude to decrease. However, at a certain point along the cut the vibrations momentarily increase and then decrease again until the system transitions to stable cutting with low levels of vibration. This is contrary to what would be expected because there should be a consistent decreases in vibration amplitude as the stiffness of the system at the cutting zone

increases. In general, it can be said that this system is undergoing a bifurcation–abruptly transitioning from one limit cycle amplitude to another. Finally, from comparing Figure 8-20A and B to Figure 8-20C and D, it is clear that there is a hysteresis of the vibration amplitude versus the axial position of the cutting tool. This is similar to the hysteresis observed by Shi and Tobias for face milling introduced earlier [73].

To further emphasize the occurrence of the hysteresis effect, consider the chatter amplitude versus tool position for both the simulation and experiment in Figure 8-21. There is a plot for vibration in the radial cutting direction as well as in the tangential cutting direction, with the width of the hysteresis annotated in each graph. The experimental results show a larger width of the hysteresis (34 mm) than in the case of the simulation (17 mm). Additionally, as shown in Figure 8-20C and D, there is some peculiar behavior present in both the simulated and measured data when the tool is being fed from the free end of the workpiece to the cantilevered end. As time progresses, the chatter amplitude decreases, then increases, and then decreases again towards the low levels of vibration present in stable cutting. The fact that the model is reproducing this complicated phenomenon in the experimental data is an important step forward in chatter modeling because it means that the actual physics of the process are being described with a high level of accuracy. Also noteworthy for the simulated data in Figure 8-21 of tool being fed from the free end to the cantilevered end, when the system undergoes a jump to a larger vibration amplitude, it follows the same trajectory that it does for the case where the tool was moving from the cantilevered end to the free end, except in reverse.

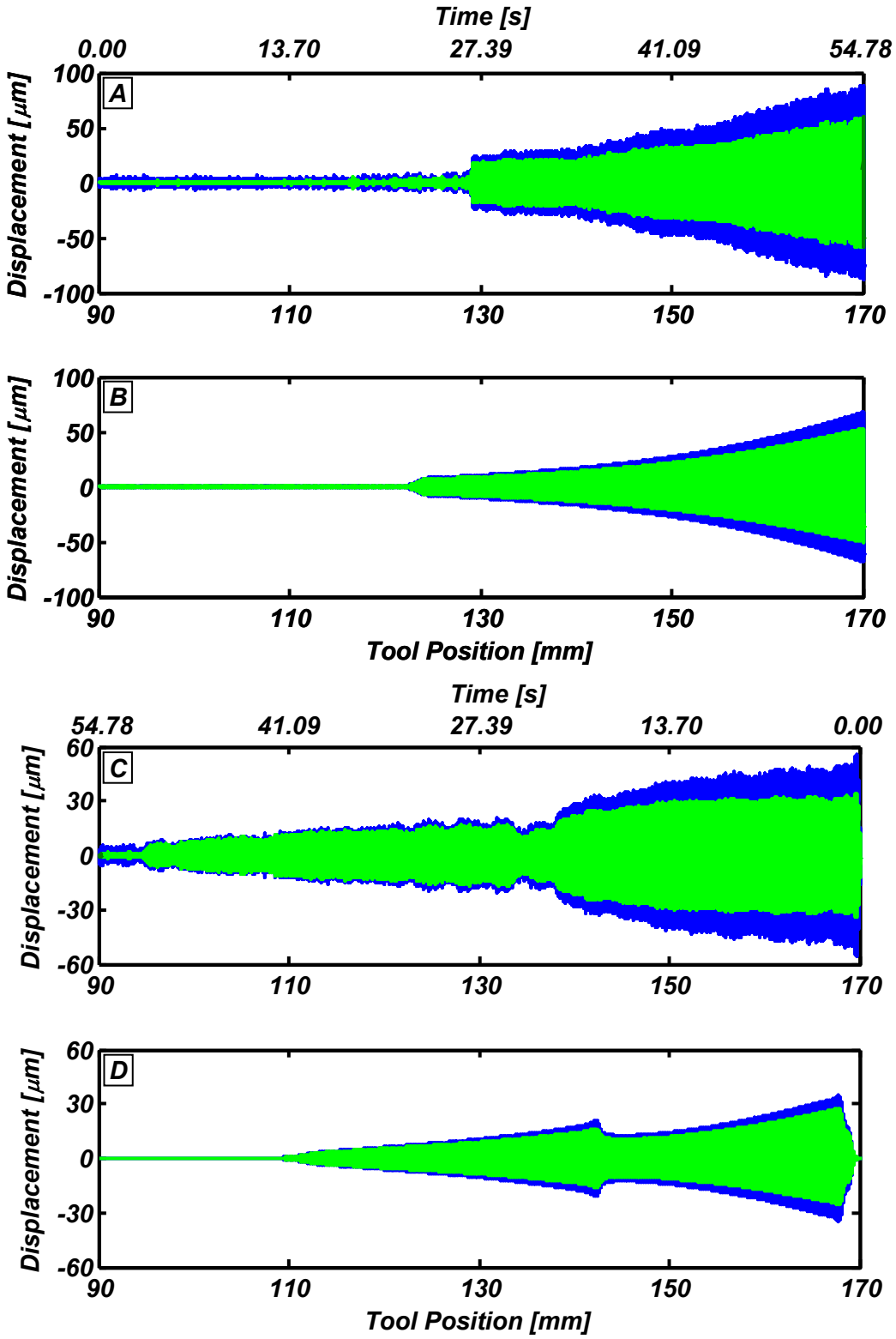

Figure 8-20: A demonstration of the hysteresis of chatter amplitude versus axial tool position. (A) and (B), experiment and simulation, respectively, of a turning cut starting at the cantilevered end and moving towards the free end; (C) and (D) experiment and simulation, respectively, of a turning cut starting at the free end and moving towards the cantilevered end. ——, displacement in the tangential cutting direction; ——, displacement in the radial cutting direction.

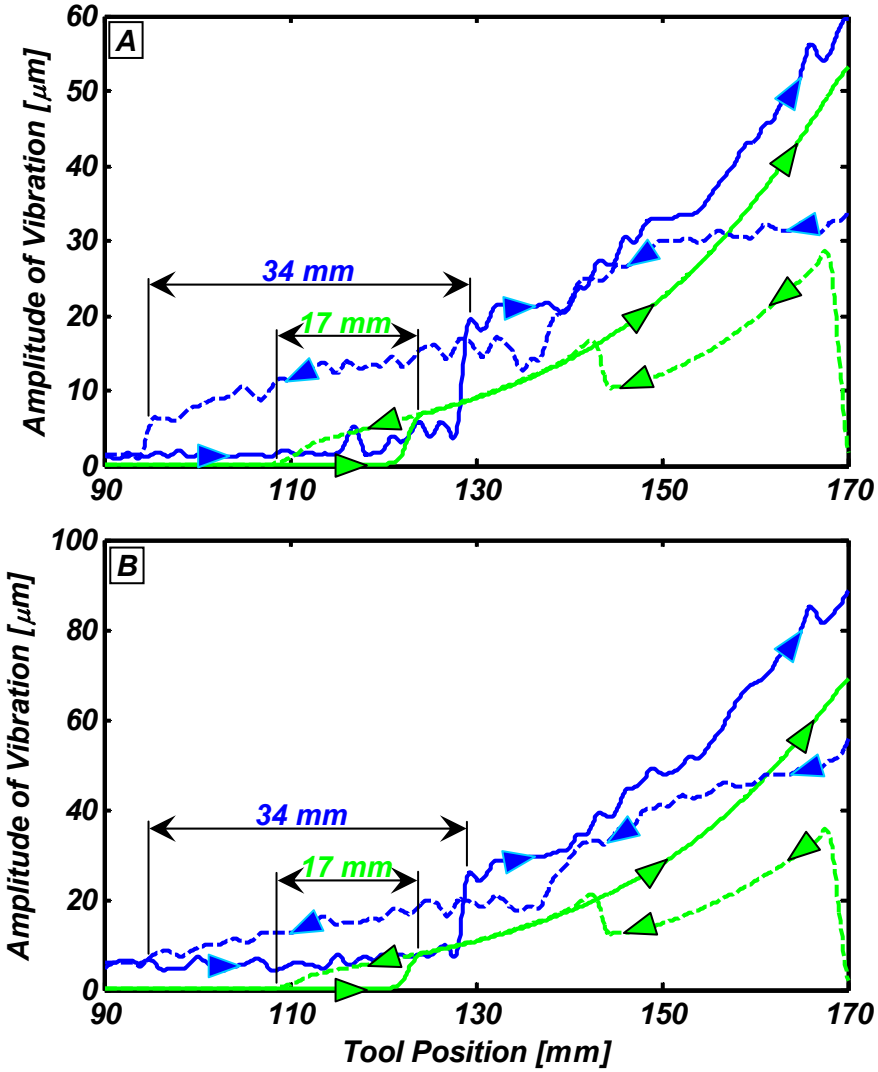

Figure 8-21: Graphs showing the hysteresis of the chatter vibration amplitude vs. axial position along the workpiece with arrowheads denoting the direction of the system's behavior. (A) Vibration in the radial (**Y**) direction; (B) vibration in the tangential (**Z**) direction. **Blue** lines represent experimentally measured displacements; **green** lines come from simulations; solid (——) lines represent turning from the cantilevered end to the free end (Figure 8-20A and B); dashed (---) lines represent turning from the free end to the cantilevered end (Figure 8-20C and D).

8.6.2 A note on the inclusion of plowing and flank interference forces in an analytical chatter model

As identified in the literature review in Chapter 2, despite the overwhelming experimental evidence that plowing and flank interference forces are intimately linked with chatter stability, there are still a number of analytical modeling approaches that choose to neglect it. In Figure 8-22, is a simulation for the vibration of the workpiece using the same cutting conditions as were used to generate the time series in Figure 8-20B. In Figure 8-22A is a time series with a simulation only

considering forces due to chip formation, F_Y and F_Z, and Figure 8-22B is one that only has interference forces, P_Y and P_Z.

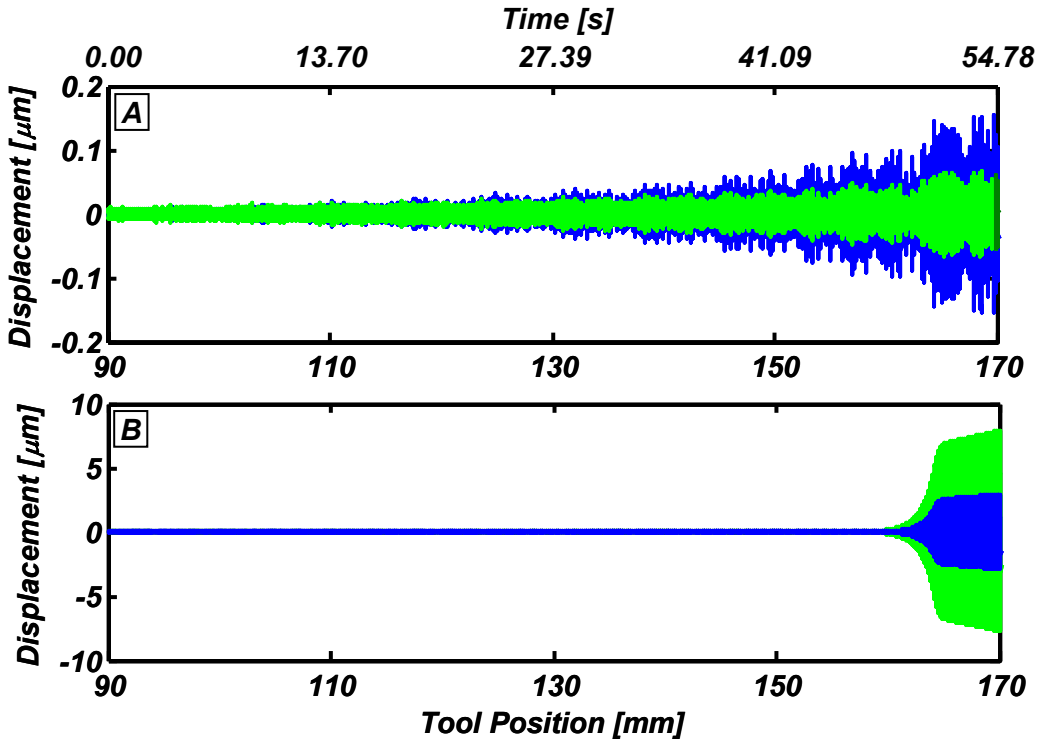

Figure 8-22: Time domain simulations with the refined cutting force model. (A) Simulation with no interference forces; (B) simulation with no forces due to chip formation. ——, displacement in the tangential (**Z**) cutting direction; ——, displacement in the radial (**Y**) cutting direction.

There are a number of interesting observations that can be drawn from these results. First, it is quite obvious that the point of chatter instability is very different than in the case where both types of forces were included in the simulation (Figure 8-20B). For the case of no interference forces in Figure 8-22A, chatter never materializes along the workpiece. The only reason that the vibration amplitude grows is because of the fixed level of the random excitation in conjunction with the increase in compliance at the cutting zone as the tool moves towards the free end of the workpiece. The time series in Figure 8-22B is a simulation with no forces due to chip formation, and in this case chatter sets in much later and at a smaller amplitude than it did in Figure 8-20A. Also when chatter does occur, the vibration in the radial direction is larger than the vibration in the tangential direction, which is contrary to that suggested by the all time histories in Figure 8-20.

Based on these results it is clear that there is some interplay between the forces due to chip formation and interference since collectively they produce something unique from their individual parts. The lack of chatter instability appearing in Figure 8-20A suggests once again that including plowing and flank interference forces is a requirement for a model that is trying to capture the true physics of the dynamic cutting process.

8.7 Surface Topography Validation

The final and most rigorous metric that can be used to validate a chatter model is to compare the actual machined surface topography to that predicted by the analytical model. It is the author's opinion that this represents the greatest challenge in chatter modeling because if this can be predicted then the following three elements are being captured: the point of instability, the amplitude of the growth, and the phasing of the terms in the regenerative delay space, $[y(t) \;\; y(t-\tau) \;\; \cdots \;\; y(t-N\tau)]$. The exact procedure for generating the surface topography from a machining simulation was developed solely by the author, but will not be presented here since it is just an exercise in geometry and not integral to the theme of this work.

Consider some simulated surface topography as well as a picture of the actual machined surface in Figure 8-23 using the parameters as listed in Table 8-1 and Table 8-2 except that the depth of cut was 0.25 mm, the cutting velocity was 2.25 m/s, and the tool nose radius was 0.79 mm. To get a sense of orientation, the direction of cutting would progress along the vertical axis of each plot starting at 15 mm and going to 0 mm. The interesting part of this comparison is that the simulation was able to reproduce the "scalloped" chatter marks observed on the actual machined workpiece surface. This is also true in Figure 8-24, which used the same cutting conditions as in Figure 8-23 except that depth of cut was 0.15 mm.

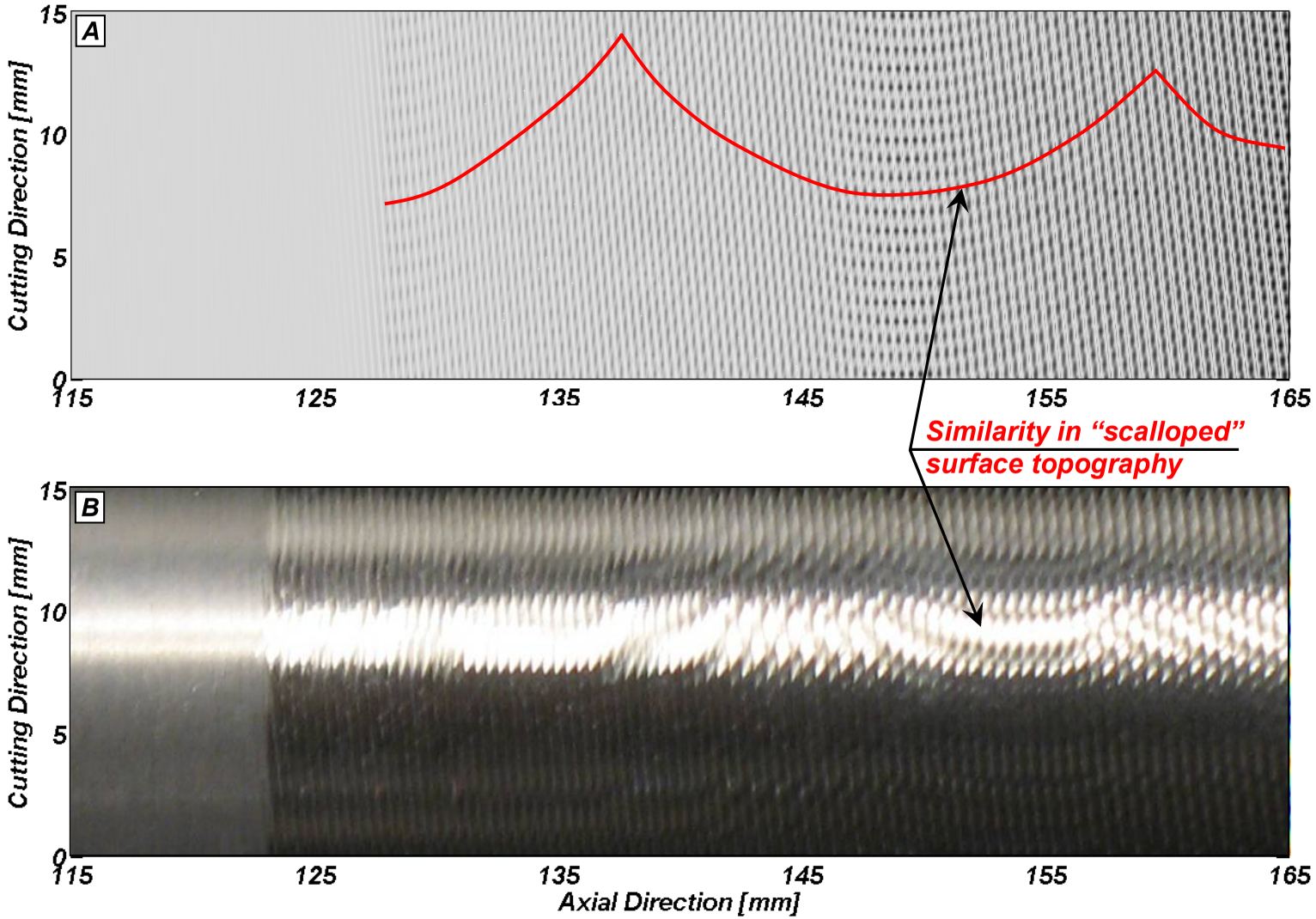

Figure 8-23: Workpiece surfaces generated during unstable cutting showing chatter marks. (A) Simulation; (B) picture of the actual machined workpiece surface.

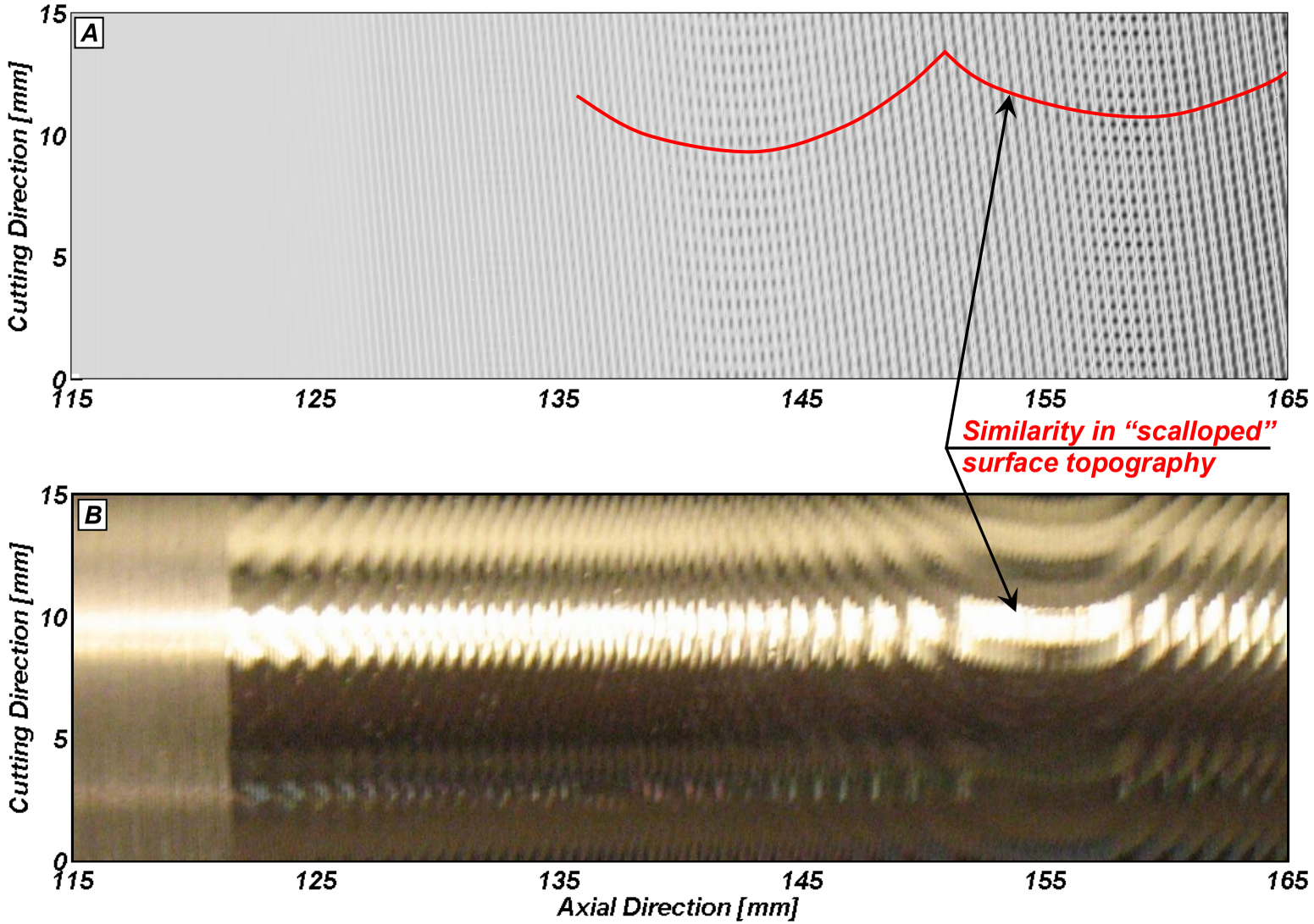

Figure 8-24: Workpiece surfaces generated during unstable cutting showing chatter marks. (A) Simulation; (B) picture of the actual machined workpiece surface.

8.8 Sensitivity Study

Whenever an analytical model is presented, it is instructive to explore its sensitivity to its constitutive parameters. This is done for two reasons; first, any parameter that is overly sensitive and not known with a high level of confidence is problematic. Second, the trends in the model behavior when varying each parameter should agree with prior work. With respect to this study, inputs to the refined dynamic cutting force model were varied in order to explore their influence on the position along the workpiece where chatter occurred. The nominal machining parameters are given in Table 8-13 and are used while each parameter under study is varied.

Table 8-13: The nominal cutting conditions used in the sensitivity study.

Cutting Parameter	*Value*
Depth of cut, d_c	0.35 [mm]
Tool nose radius, r_n	0.79 [mm]
Cutting velocity, $\bar{V}_C$	3.0 [m/s]
Feed rate, f	0.076 [mm]
Side cutting edge angle, C_S	0 [deg]
End cutting edge angle, C_E	0 [deg]
Rake angle, α_n	0 [deg]
Inclination angle, i	0 [deg]
Clearance angle, γ	10 [deg]
Edge radius, r_e	0.038 [mm]
Initial workpiece diameter, d_w	37.87 [mm]
Workpiece length, L	170.41 [mm]
Separation angle, $\bar{\beta}_e$	30.0 [deg]
Coefficient of friction, μ	0.3 [--]
Natural frequency, ω_n	577 [Hz]
Damping ratio, ζ	0.030 [--]
Force-interference volume constant of proportionality, K_{cf}	6.0×10^5 [N/mm^3]
Material	AISI 1018 steel

In Figure 8-25 the sensitivity of 10 various parameters is plotted. The position of chatter using the nominal values in Table 8-13 is 124.6 mm and has been denoted in each plot with a dashed red line. Some parameters are known with a high level of certainty: the tool nose radius, r_n, the feed rate, f, the inclination angle, i, the clearance angle, γ, the natural frequency, ω_n, and the damping

ratio, ζ. Other parameters are not known with a high level of certainty: the edge radius, r_e, the nominal separation angle, $\overline{\beta}_e$, the coefficient of friction, μ, and the force-interference volume constant, K_{cf}. Of these uncertain parameters, the model is sensitive to all of them except for the coefficient of friction. The edge radius of the cutting tool is generally an uncertain parameter since the nature of tool wear or built up edge can give rise to a time varying "effective" tool edge radius. Although the nominal value of $\overline{\beta}_e$ was taken from prior experimental work [49], it still is not fully understood and is assumed that it can vary from the value of 30° used in this study. From the sensitivity plots, K_{cf} could be viewed as the one problematic parameter in this model in that it was not based rigorous physical modeling. As previous discussed although the value used in this study, 6.0×10^5 N/mm^3, is within the ranges suggested by Equation (2.23) it is nevertheless a tuned parameter.

As demonstrated in [33] and [55], increasing the tool nose radius will decrease stability limits and hence provide for the earlier materialization of chatter. This agrees with the sensitivity plot for the tool nose radius in Figure 8-25A. In [74] it was shown that in milling the stability of the process increased as the feed per tooth was increased. This is analogous to the present scenario of turning since increasing the feed rate decreases the amount of overlap between successive tool passes, thereby diminishing the regenerative effect and increasing stability. This agrees with the sensitivity plot for the feedrate in Figure 8-25B. Since in the sensitivity study C_S was taken to be 0°, varying the inclination angle is similar to varying the rake angle in an orthogonal cutting force model. It has been experimentally suggested in [25] that the rake angle has little effect on the point of chatter stability. Theoretically it was suggested in [57] that increasing the rake angle can add stability to the process, as suggested by the refined cutting force model's sensitivity plot in Figure 8-25C as well. Intuitively it seems that increasing the rake angle could stabilize the process based on the following logic. At a certain point, if the rake angle of the cutting tool is positive enough the thrust force can actually reverse directions and pull the tool towards the workpiece. Based on this coarse analysis this

would seem to have a stabilizing effect in that it would reduce the *relative* motion between the workpiece and the cutting tool; however further experiments would be needed to confirm this.

Next, the clearance angle in Figure 8-25D has a stabilizing effect at values less than 7°, which agrees with prior experimental orthogonal turning work in [25]. It was also remarked in the same source that it has been common in machine shops to encounter chatter when a fresh tool is used and for the chatter to spontaneously disappear when the tool "wears in." When the tool wears a "clearance land" is developed behind the cutting edge (also called flank wear). This essentially decreases the effective clearance angle and therefore agrees with the trends of the proposed model and prior work. Next the edge radius of the model was found to decrease stability at larger values. The author is not aware of any experimental studies on varying the edge radius in chatter, but it is a well-known fact that a large edge radius increases the average forces in machining [75].

Finally the position of chatter was found to be quite sensitive to the damping ratio, as suggested in Figure 8-25I. This intuitively makes since because damping dissipates energy and would therefore delay the occurrence of high energy chatter vibrations. Additionally, this also agrees with the author's experience. It was observed that when turning large, thin-walled tubes, chatter was a frequent problem. To mitigate this, machinists often tossed rags and shop towels inside the rotating workpiece and could then take deeper depths of cut without chattering. In essence they were adding damping to the system in order to increase the stability limit.

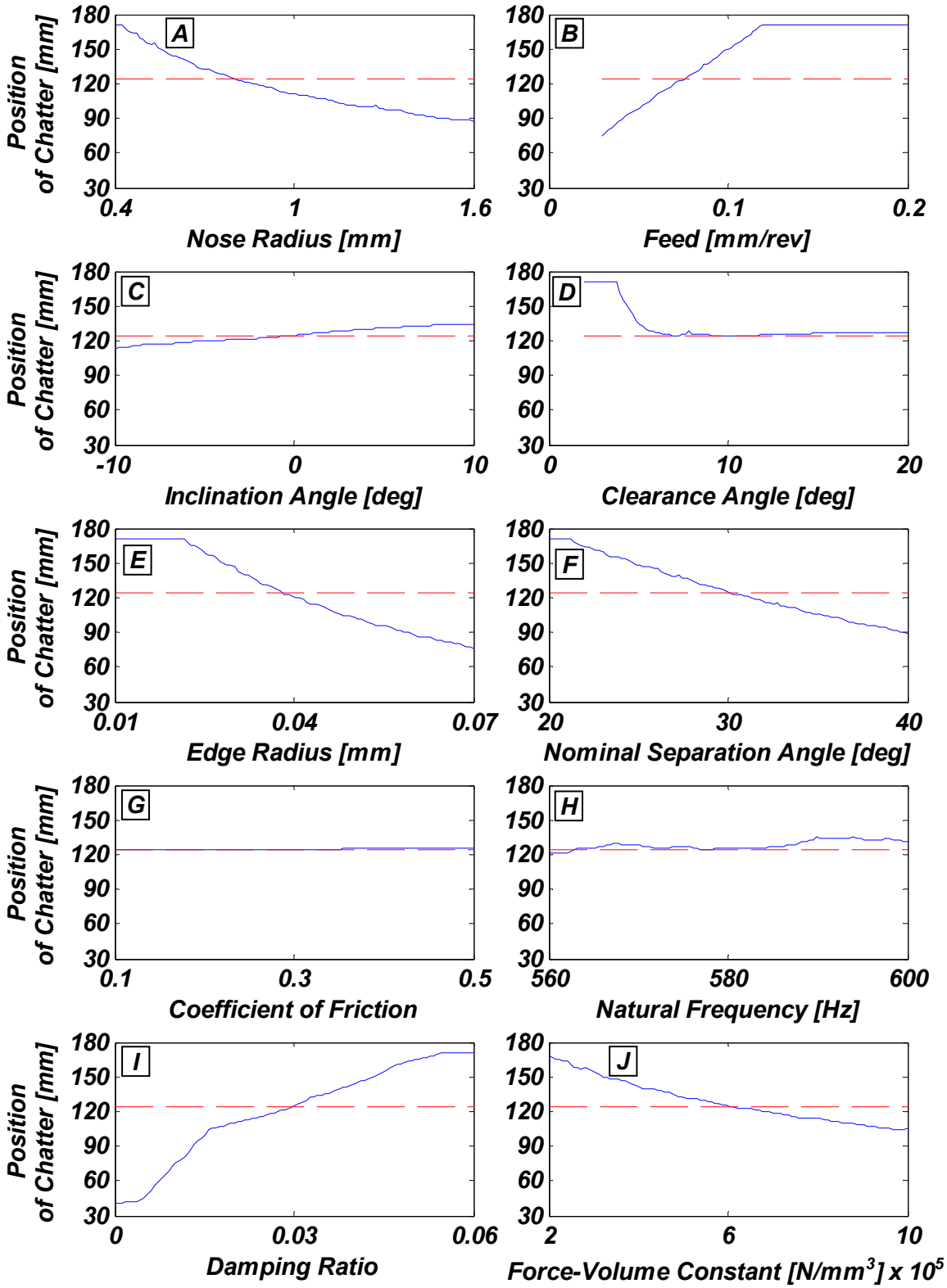

Figure 8-25: Sensitivity plots for the refined dynamic cutting force model. (A) Varying nose radius; (B) varying feed rate; (C) varying inclination angle; (D) varying clearance angle; (E) varying edge radius; (F) varying separation angle; (G) varying coefficient of friction; (H) varying natural frequency; (I) varying damping ratio; (J) varying the force-interference volume constant. —, Point of chatter as a function of the parameter being varied; – – –, point of chatter using the nominal parameters in Table 8-13.

CHAPTER 9: CONCLUSIONS AND FUTURE WORK

"Science never solves a problem without creating ten more."
–George Bernard Shaw

9.1 Summary

This dissertation presents a method of predicting chatter in a turning operation from true process parameters. The modeling techniques are extensions of work performed in quasi-static cutting force modeling as well as dynamic cutting force modeling. Two models were derived: a simplified model to describe dynamic cutting forces in a closed-form manner, and a refined cutting force model, which employed a more rigorous geometric formulation to describe the dynamic cutting forces in a non-closed form fashion.

In Chapter 3, the Oxley orthogonal cutting force model was introduced in order to describe the forces due to chip formation. The model captured the effect of strain, strain rate, and temperature on the chip formation forces. Additionally, the effects of a nonzero workpiece surface slope were incorporated into the model such that it could be used in a dynamic cutting scenario. Next, forces due to plowing and flank interference were modeled in the orthogonal cutting domain. By tracking the vibration history of the workpiece, the amount of material displaced by the cutting tool's edge and clearance face could be determined. Through various geometric relations and assumptions made about the stress field around the tool edge, forces can be calculated based on the amount of displaced material.

Chapter 4 dealt with capturing the effect that the tool geometry commonly used in practice and vibration have on the machining forces. Effects such the oblique cutting geometry and the tool nose radius were incorporated into the model. The simplified cutting force model was fully developed in this chapter by deriving a single equivalent orthogonal cutting representation for the forces due to chip formation and another orthogonal representation for the interference forces.

Comparisons between the current orthogonal modeling approach and previous experimental work in dynamic cutting force analysis were conducted in Chapter 5. The behavior of the interference forces, the forces due to chip formation, and the shear angle were explored as a function of the oscillation frequency of both the cutting tool and the unmachined workpiece surface.

In Chapter 6, the refined cutting force model was presented by deriving the geometry of the cutting process in a more rigorous fashion. Improvements were made over the simplified cutting force model in the way that forces due to chip formation as well as plowing and flank interference were calculated by integrating infinite number of cutting scenarios along the entire cutting zone.

Actual numerical implementation of both of the proposed models was presented in Chapter 7. The equations of motion were developed and a Runge-Kutta integration solution procedure was presented. Additionally, methods for numerically evaluating integrals in the refined cutting force model were covered.

Finally in Chapter 8, the simplified and refined dynamic cutting force models were experimentally validated. Both were used to predict the point of chatter instability along the workpiece and compared with machining experiments for a wide range of cutting conditions. In addition, the refined cutting force model was compared with experimental measurements in the frequency and time domains as well as the actual machined surface topography. A sensitivity study was also conducted whereby general trends in the model's output were explained and correlated with real-world machining observations and prior work in the literature.

9.2 Conclusions

The research in this dissertation was driven by the need for a more physics-based modeling approach in the description of dynamic cutting forces in turning. Previous models were oversimplified or used too many parameters to curve fit experimental data. By incorporating many of the true process parameters in turning and modeling forces due to plowing and flank interference as well as chip formation, accurate stability predictions over a wide range of machining conditions

were made. Additionally, predictions of the time domain chatter amplitude growth showed good agreement with experimental results. Finally, trends in the experimentally machined surface topography were captured by the analytical model which is proof that the physics of the process are being captured.

9.3 Contributions

The modeling approaches in this work provided improvement to the current state of the art in the analytical modeling of chatter in turning. The intellectual contributions of the research presented are as follows:

- Extended Oxley's cutting force model to apply in a dynamic cutting environment by accounting for vibration effects
- Developed a set of equations to describe the undeformed chip area during vibration with influence from an arbitrary number of previous relative tool-workpiece positions
- Fused an oblique cutting force model with Oxley's cutting force model and developed a simple way to integrate along the undeformed chip area to find forces due to chip formation
- Extended an interference volume model for describing forces due to plowing and flank interference in the orthogonal cutting domain to the 3D cutting domain that incorporates the effect of the tool nose radius
- Explained physically why the cutting process stabilizes at low cutting velocities
- Validated the orthogonal cutting force model on which both the simplified and refined cutting force models were built upon by comparing it with previously published work
- Validated the refined and simplified cutting force models by predicting the point of instability over wide range of cutting conditions
- Validated the refined cutting force model against experimental results in the time and frequency domains as well as comparisons of the machined surface topography during chatter
- Performed a sensitivity analysis of the refined cutting force model on the point of chatter instability along the workpiece

9.4 Future Work

The proposed approach provides a solid foundation for the prediction of chatter in turning based on true process parameters and rigorous modeling of physical mechanisms present in metal

cutting. However, there are opportunities for improving the predictive capability further. The following areas for future research will help address limitations in the current modeling approach and improve the state of chatter modeling.

In the orthogonal cutting force modeling, which served as the backbone for both the simplified and dynamic cutting force models, steady state conditions were always assumed. In reality, any material is viscoelastic to some extent and therefore can only change its state of stress in a finite amount of time. As discussed earlier, the system is assumed to be memoryless and therefore can react immediately to any condition, i.e. it produces the steady state force for a given cutting condition instantaneously regardless of its history.

In addressing the forces due to chip formation with the Oxley cutting force model, Johnson-Cook coefficients for AISI 4340 (an alloy steel with a relatively high yield strength) were used instead of those that would be more similar to the AISI 1018 (a low carbon steel with a relatively low yield strength) used in this study. The justification for this was that since a linear model for the workpiece is used, only deviations from the average force due to chip formation are of interest. The exact effect of the Johnson-Cook coefficients on the proposed model's prediction of chatter remains an open question.

In the small depth of cut regime, chatter stability predictions were vastly underestimated (predicted chatter much earlier along the workpiece than was observed experimentally). It is felt that the primary reason for this is the assumption that the mechanism producing chips and that producing the plowing and flank interference can be analyzed separately. At very small depths of cut, the undeformed chip thickness is on the order of the edge radius, and hence it is difficult to separate these two types of forces. This is an ongoing issue in machining cutting force and remains an area of research.

Finally, there is the issue with how the plowing and flank interference forces were calculated. Pivotal in this was the force-interference volume coefficient, K_{cf}. The value used in this study fell within the range suggested in its derivation (7.63×10^4 to 7.63×10^5 N/mm^3), however a more

rigorous formulation is needed in order to narrow this range or determine what additional parameters control its location within this range.

With the aforementioned modifications to the current modeling approach, the methodologies presented here can progress towards becoming a more highly reliable model that is valid over a wider parameter space. The results of this would be realized in a more useful tool for process planning and optimization of machining operations.

APPENDIX A: JOHNSON-COOK COEFFCIENTS USED TO MODEL THE FLOW STRESS OF THE WORKPIECE

As discussed in the text, Johnson-Cook coefficients for AISI 1006 steel were originally used to model the AISI 1018 steel of the workpiece since they are both carbon steels. However, the lack of convergence of the Oxley cutting force model necessitated the use AISI 4340 coefficients instead. The justifications for this are given in text and the parameters for AISI 4340 steel are given below in Table A-1.

Table A-1: The Johnson-Cook parameters for AISI 4340 steel used in the Oxley cutting force model.

Parameter	*Value*	*Units*
A	792	MPa
B	510	MPa
C	0.014	dimensionless
m	1.03	dimensionless
n	0.26	dimensionless
$\dot{\varepsilon}_0$	1	1/s

APPENDIX B: A CLOSED-FORM SOLUTION TO THE INTERSECTION BETWEEN THE UNDEFORMED WORKPIECE SURFACE AND THE BOUNDARY OF THE CUTTING TOOL

The equation that must be satisfied for the two intersections between the undeformed workpiece surface and the cutting edge is

$$a_0 + a_1\hat{z} + a_2\hat{z}^2 = -\sqrt{r_e^2 - \hat{z}^2}$$

which can be rewritten as the quartic equation

$$\hat{z}^4 + A\hat{z}^3 + B\hat{z}^2 + C\hat{z} + D = 0$$

where

$$A \triangleq \frac{2a_1}{a_2}, \qquad B \triangleq \frac{\left(2a_0a_2 + a_1^2 + 1\right)}{a_2^2}, \qquad C \triangleq \frac{2a_0a_1}{a_2^2}, \qquad D \triangleq \frac{a_0^2 - r_e^2}{a_2^2}$$

There are four solutions to this quartic equation, given as

$$\left\{\hat{z}_1, \hat{z}_2, \hat{z}_3, \hat{z}_4\right\} = -\frac{A}{4} + \frac{1}{2}\left(\pm_1 W \pm_2 \sqrt{-\left(3\alpha + 2y \pm_1 \frac{2\beta}{W}\right)}\right)$$

where the $\pm_1$ and $\pm_2$ are evaluated separately over all possible combinations to obtain four roots, specifically, $++$, $--$, $+-$, and $-+$, respectively, and W, α, y, and β are given as

$$W = \sqrt{\alpha + 2y}, \qquad \alpha = B - \frac{3A^2}{8}, \qquad y = -\frac{5}{6}\alpha - U + \begin{cases} 0 & U = 0 \\ \dfrac{P}{3U} & U \neq 0 \end{cases}, \qquad \beta = \frac{A^3}{8} - \frac{AB}{2} + C$$

where U and P are

$$U = \sqrt[3]{\frac{Q}{2} - \sqrt{\frac{Q^2}{4} + \frac{P^3}{27}}}, \quad P = -\frac{\alpha^2}{12} - \gamma$$

where Q and γ are

$$Q = -\frac{\alpha^3}{108} + \frac{\alpha\gamma}{3} - \frac{\beta^2}{8}, \quad \gamma = \frac{BA^2}{16} - \frac{3A^4}{256} - \frac{AC}{4} + D$$

Due to physical constraints on the parameters, there will always be two real roots of the quartic equation and two complex ones. However, numerical round off errors can cause all roots to be complex, but there will be two of them with a much smaller imaginary part than the other two

(perhaps having a magnitude of $< 10^{-9}$ mm if units of mm are used for all length measures), and the real parts of these roots should be taken as the intersection between the undeformed workpiece surface and a semicircle coincident with the tool edge. $\hat{z}_{1,quart}$ and $\hat{z}_{2,quart}$ should be assigned the values of these two roots, where $\hat{z}_{1,quart} < \hat{z}_{2,quart}$.

APPENDIX C: REGRESSION SURFACES FOR S_{f_C}, S_{f_T}, AND S_{ϕ_V}

Three regressions surface were used to capture the output of the Oxley cutting force model: the force due to chip formation in the cutting direction, S_{f_C}, the force due to chip formation in the thrust direction, S_{f_T}, and the shear angle, S_{ϕ_V}. S_{f_C} and S_{f_T} are in units of N/mm, and S_{ϕ_V} is in units of radians. t', α_n, $\left|\vec{V}_C\right|$, δ_s are in units of mm, rad, m/s, and rad respectively. It should be noted that t'_θ, $\alpha^{**}_{n,\theta}$, $V^*_{C,\theta}$, and $\delta^*_s(\theta, W)$ can be used in place of t', α_n, $\left|\vec{V}_C\right|$, and δ_s, respectively, when calculating forces due to chip formation in refined cutting force model. Likewise, t', α^{**}_n, V^*_C, and δ^*_s can be used in place of t', α_n, $\left|\vec{V}_C\right|$, and δ_s, respectively, when calculating forces due to chip formation in simplified cutting force model. Since this model is based on a regression fit it is only valid in the following ranges along each dimension:

$$\left|\vec{V}_C\right| \in [1,5] \qquad t' \in [0, 0.25] \qquad \alpha_n \in [-0.26, 0.26] \qquad \delta_s \in [-0.26, 0.26]$$

Outside of this range, accurate outputs are not guaranteed. To facilitate the copying and pasting of the regression surfaces the following variables have been defined as

$$\mathrm{w} \triangleq \left|\vec{V}_C\right| \qquad \mathrm{x} \triangleq t' \qquad \mathrm{y} \triangleq \alpha_n \qquad \mathrm{z} \triangleq \delta_s$$

$S_{F_C} =$

```
+2.00273405296216470e+001-4.63469146195298550e+001*w*x*y^2
-8.19175412434860560e+000*w^2*x*y-6.81504727455204030e+001*w*x^2*y
+1.48277159318001740e+002*w*x*y-3.70668482097132430e+002*w*x*z^2
+6.81703867677821500e+000*w^2-1.04463484659382370e+004*x^2
-8.27709655850682860e+000*w^2*x^2+3.01648219263662830e+001*w^2*x
+3.43938849852420280e+002*w*x^2-2.49946684572255750e+002*w*x
+9.52356984581838190e+001*y^2+3.26503406654477150e+000*w^2*y^2
-4.80628117829383900e+000*w^2*y-3.63118227076233000e+001*w*y^2
+2.15100612906134150e+001*w*y-1.55518795745546840e+003*x^2*y^2
+5.13372746107541930e+003*x^2*y+1.99798744658071110e+003*x*y^2
-3.07904438962259470e+003*x*y+3.36262533470492200e+002*z^2
+1.39423291606700750e+001*w^2*z^2-1.37418790714646160e+001*w^2*z
-9.94886798565023310e+003*x^2*z^2+1.66146422987746850e+004*x^2*z
+4.34388143662097080e+003*y^2*z^2-9.17267397618007290e+002*y^2*z
+9.94591032349608390e+003*x*z^2+2.30858221996324460e+002*w*y*z^2
-1.55736275520511040e+004*x*y*z^2-4.68754758565204720e+002*w*x^2*z
+5.96897974717220110e+002*w*x*z+1.01423722348616860e+002*w*y^2*z
-1.05229023750443340e+004*x^2*y*z+1.18961963912514000e+004*x*y*z
-7.18654257179744130e+003*x*z-1.96501768390951160e+003*y*z^2
+2.66076883111566930e+002*y*z-1.46043902519321510e+002*w*z^2
+5.77466767003836030e+001*w*z-8.85281591371842040e+001*y^3
-1.56988982222292760e+000*w^3*x-5.32808850816563220e+002*w*x^3
+3.32222235525570290e-001*w^3*y+1.79305555602587500e+001*w*y^3
```

-8.750778398182421400e+003*x^3*y-1.221035871384173600e+003*x*y^3
-1.069635120786441900e+000*w^3+4.275414391476970200e+004*x^3
-1.248550194239244300e+003*z^3+1.614733935059201300e+003*y^3*z
+1.016567289644386900e+000*w^3*z-2.750608662735272800e+004*x^3*z
-9.257972305535417000e+003*x*z^3+5.369089288130310700e+003*y*z^3
+1.442675656226037100e+002*w*z^3+6.057313842288512800e-002*w^4
-6.701917593407759000e+004*x^4-1.105571347047178800e+002*y^4
+2.619608367116076800e+003*z^4-8.630520993776275600e+003*x*y^2*z
+3.441681610282635600e+003*x-2.991710480035526100e+001*y
-1.175211658421256100e+002*w*y*z-3.638435028407805300e+001*w^2*x*z
-7.798548371848366400e+001*z+1.153375405840101600e+001*w^2*y*z
-4.470855738743954400e+002*w*x*y*z-1.855261612589438200e+001*w

S_{F_T} = +2.862648252481102800e+001-1.196691179959435200e+002*w*x*y^2
-2.174526148502844700e+001*w^2*x*y-2.568908691327029600e+002*w*x^2*y
+3.608452065646085300e+002*w*x*y-1.533498081694830800e+002*w*x*z^2
+9.624869031655043400e+000*w^2-1.340632962055034300e+004*x^2
-1.989329296232041200e+001*w^2*x^2+4.533231832692426600e+001*w^2*x
+5.885657908866948000e+002*w*x^2-3.705667509085134300e+002*w*x
+1.190824107819106700e+002*y^2+4.333308947708745900e+000*w^2*y^2
-7.704603937678856900e+000*w^2*y-4.889351856694352700e+001*w*y^2
+3.303941849357651300e+001*w*y-3.156671145508201300e+003*x^2*y^2
+1.024950073386705700e+004*x^2*y+3.981003046970767200e+003*x*y^2
-4.900803965681165200e+003*x*y+2.173515003199956400e+002*z^2
+7.870684787820945200e+000*w^2*z^2-1.096391470249827500e+001*w^2*z
-4.718193460562900300e+003*x^2*z^2+1.168821780606573200e+004*x^2*z
+3.037404090681246500e+003*y^2*z^2-1.062089902501370300e+003*y^2*z
+2.970175430124544600e+003*x*z^2+1.560278880180986500e+002*w*y*z^2
-6.957999064516137900e+003*x*y*z^2-3.823436712137782900e+002*w*x^2*z
+4.150228570250707200e+002*w*x*z+1.194679319871972300e+002*w*y^2*z
-9.503909435256973700e+003*x^2*y*z+8.875283076603147500e+003*x*y*z
-3.380118723099065400e+003*x*z-1.374067497929282400e+003*y*z^2
+3.634638692669838600e+002*y*z-8.716660181864107000e+001*w*z^2
+4.852704822901053200e+001*w*z-3.816624231723554300e+002*y^3
-2.325237151974345600e+000*w^3*x-8.303923437234376500e+002*w*x^3
+5.657456651424084300e-001*w^3*y+3.030046041656583400e+001*w*y^3
-1.698635128584182500e+004*x^3*y-2.560279947962768800e+003*x*y^3
-1.513632922234512000e+000*w^3+5.405520426372809000e+004*x^3
-5.526832803049534300e+002*z^3+1.779093757865704200e+003*y^3*z
+7.761228544360595500e-001*w^3*z-1.909510222282762700e+004*x^3*z
-1.409751142187487900e+003*x*z^3+2.333080149571726900e+003*y*z^3
+6.318164859975553300e+001*w*z^3+8.609963462834238600e-002*w^4
-8.385705769522380400e+004*x^4+8.496938918229751600e+002*y^4
+6.805605660908169100e+002*z^4-7.928137688331222300e+003*x*y^2*z
+2.532140373588086700e+003*x-4.508285566870123500e+001*y
-1.409488784348095900e+002*w*y*z-2.407089827432878700e+001*w^2*x*z
-6.947346224115145200e+001*z+1.325487570353130100e+001*w^2*y*z
-3.572655420934917200e+002*w*x*y*z-2.628130505137906800e+001*w

S_{ϕ_v} = +1.504567718932745300e-001-3.441684206335461300e-001*w*x*y^2
+3.674047336496059200e-002*w^2*x*y+1.135053677446926000e+000*w*x^2*y
-6.160308145658717200e-001*w*x*y-4.491116464783224300e-002*w*x*z^2
-1.993811840496868800e-002*w^2-3.551736156854453000e+001*x^2
-5.420023964440721900e-002*w^2*x^2+3.566755273325105500e-002*w^2*x
+1.103344555511292000e+000*w*x^2-2.813888275076258900e-001*w*x
-4.220074767899037500e-001*y^2-7.715128046203874000e-003*w^2*y^2
-1.670530174790635000e-002*w^2*y+1.102452102776056300e-001*w*y^2
+1.071407443092215200e-001*w*y-7.814703616493203800e+000*x^2*y^2
-1.866564810453276400e+001*x^2*y+3.458732084767735000e+000*x*y^2
+3.661491275278608600e+000*x*y+1.368230981680825200e-001*z^2
+9.889101788621496600e-004*w^2*z^2-1.368956655672926000e-002*w^2*z
+1.308722599151748400e+000*x^2*z^2-1.620177213192137700e+001*x^2*z

```
+4.63982574186493910e-001*y^2*z^2-9.19628214487606450e-001*y^2*z
-4.30390626608777300e-001*x*z^2+1.47796785960035910e-002*w*y*z^2
+1.19193357234079600e+000*x*y*z^2+8.11855530561722880e-001*w*x^2*z
-4.56875198605102010e-001*w*x*z+8.93988439404687920e-002*w*y^2*z
-6.93346593841519180e+000*x^2*y*z+3.31295588787089600e+000*x*y*z
+3.17177786846452700e+000*x*z-4.45264373284451840e-001*y*z^2
-3.26575521476109460e-001*y*z-7.62098263767405950e-003*w*z^2
+8.96069748478764690e-002*w*z-1.93041105972289850e-001*y^3
-1.67879269081176840e-003*w^3*x-1.59246860474268860e+000*w*x^3
+9.00770192253482730e-004*w^3*y+4.65749762641606490e-002*w*y^3
+3.25804462231827400e+001*x^3*y+1.50898321521231660e+000*x*y^3
+2.36018651818432290e-003*w^3+1.49153909880575640e+002*x^3
-9.33447307771548130e-002*z^3-7.37698430957740010e-002*y^3*z
+7.23565064688485160e-004*w^3*z+2.84973522182707550e+001*x^3*z
+1.88748040512449450e-001*x*z^3+6.82471285371356600e-001*y*z^3
-1.53705640825847950e-002*w*z^3-1.09563917951264940e-004*w^4
-2.31446385075119790e+002*x^4-7.68226379312835880e-001*y^4
-5.26437431728405820e-002*z^4+2.99266247265365150e+000*x*y^2*z
+4.04887411049617270e+000*x+1.73972639844676170e-001*y
+1.27405585768466310e-001*w*y*z+2.78837279917821190e-002*w^2*x*z
-3.47966803005979710e-001*z-9.29846191305617330e-003*w^2*y*z
-4.01152213867914890e-001*w*x*y*z+8.79568719265774180e-002*w
```

APPENDIX D: NODES AND WEIGHTS USED FOR GAUSSIAN QUADRATURE

Table D-1: Nodes and weights for 5th order Gaussian Quadrature.

Nodes, x_p	***Weights,*** w_p
0.90617984593866396	8.2444001768938353
0.53846931010568311	-2.9110668435605040
0.00000000000000000	2.2500000000000000
-0.53846931010568311	-2.9110668435605040
-0.90617984593866396	8.2444001768938353

Table D-2: Nodes and weights for 8th order Gaussian Quadrature.

Nodes, x_p	***Weights,*** w_p
0.96028985649753629	17.922771464432078
0.79666647741362673	-5.5818790601306656
0.52553240991632899	3.3388096902387669
0.18343464249564981	-2.6874218067243119
-0.18343464249564981	2.6874218067243119
-0.52553240991632899	-3.3388096902387669
-0.79666647741362673	5.5818790601306656
-0.96028985649753629	-17.922771464432078

Table D-3: Nodes and weights for 9th order Gaussian Quadrature.

Nodes, x_p	***Weights,*** w_p
0.96816023950762609	22.018133995029626
0.83603110732663577	-6.7380614436617821
0.61337143270059047	3.8972854718701457
0.32425342340380892	-2.9721880659817645
0.00000000000000000	2.7343750000000000
-0.32425342340380892	-2.9721880659817645
-0.61337143270059047	3.8972854718701457
-0.83603110732663577	-6.7380614436617821
-0.96816023950762609	22.018133995029626

APPENDIX E: REGRESSION SURFACE FOR THE FUNCTION REFLECTING THE CHANGE IN STIFFNESS OF THE WORKPIECE AT THE CUTTING ZONE

The function, $\psi(\hat{x}_t(t), d_c)$, depends on parameters: $\hat{x}_t(t)$, the axial position along the workpiece (in mm) and the depth of cut, d_c (in mm). It is only valid over the following ranges of its two independent parameters since it was fit over a set of discrete data points:

$$\hat{x}_t(t) \in [40.0, 170.4] \qquad d_c \in [0.0, 0.9]$$

Outside of this range, accurate outputs are not guaranteed. To facilitate the copying and pasting of the regression surface the following variables have been defined as

$$\mathtt{x} \triangleq \hat{x}_t(t) \qquad \mathtt{d} \triangleq d_c$$

and it is given as

$\psi(\hat{x}_t(t), d_c)$ =
```
+1.07388070038387800e-001-2.06837819557895760e-003*x
+6.30768446259903540e-005*x^2+3.76143268387440420e-008*x^3
-1.85335326483720310e-001*d+9.30937436967210100e-001*d^2
-8.38341712323297020e-001*d^3+8.85141772408948310e-003*x*d
-7.18598682073097200e-005*x^2*d+1.03563107151336680e-007*x^3*d
-5.31189868602970350e-002*x*d^2+4.84882426133448900e-002*x*d^3
+6.94742008806131100e-004*x^2*d^2-6.46673270434819020e-004*x^2*d^3
+1.03563294047738140e-007*x^3*d-2.46777698739201700e-006*x^3*d^2
+2.31745519819898390e-006*x^3*d^3
```

REFERENCES

[1] Ota, H., and Kono, K., 1974, On Chatter Vibrations of Machine Tool or Work Due to Regenerative Effect and Time Lag, *Journal of Engineering for Industry*, **96**, pp. 247-255.

[2] Gurney, J. P., and Tobias, S. A., 1962, A graphical analysis of regenerative machine tool instability, *Transactions of the ASME Journal for Engineering Industry*, pp. 103-112.

[3] Tlusty, J. A., 1965, A method of analysis of machine tool stability, *International Journal of Machine Design and Research*, **6**, pp. 5-14.

[4] Tobias, S. A., 1965, Machine Tool Vibration, London, England: Blackie and Sons Ltd.

[5] Tlusty, J., 1984, Dynamics of High Speed Milling, *ASME Journal of Engineering for Industry*, **118**, pp. 59-67.

[6] Jayaram, S., Kapoor, S. G., and DeVor, R. E., 2000, Analytical Analysis of Variable Speed Machining, *Journal of Manufacturing Science and Engineering*, **122**, pp. 391-397.

[7] Sweeney, G. and Tobias, S. A., 1969, Survey of Basic Machine Tool Chatter Research, *International Journal of Machine Design and Research*, **9**, pp. 217-238.

[8] Srinivasan, K. and Nachtigal, C. L., 1978, Investigation of the Cutting Process Dynamics in Turning Operations, *ASME Journal of Engineering for Industry*, **100**, pp. 323-331.

[9] Moriwaki, T. and Iwata, K., 1976, In-Process Analysis of Machine Tool Structure Dynamics and Prediction of Machining Chatter, *ASME Journal of Engineering for Industry*, **98**, pp. 301-305.

[10] Endre, W. and Ozdoganlar, 2002, Existence and Effects of Overlap Factors Greater than Unity and Less than Zero, *Journal of Manufacturing Processes*, **4**(1), pp. 67-76.

[11] Chen, C. K., and Tsao, Y. M., 2005, A Stability Analysis of turning a Tailstock Supported Flexible Work-piece, *International Journal of Machine Tools and Manufacture*, **46**, pp. 18-25.

[12] Olgac, N., and Hosek, M., 1998, A New Perspective and Analysis for Regenerative Machine Tool Chatter, *International Journal of Machine Tools and Manufacture*, **38**, pp. 783-798.

[13] Nayfeh, A. H., Chin, C.-M., and Pratt, J. R., 1997, Perturbation methods in nonlinear dynamics - applications to machining dynamics, *ASME Journal of Manufacturing Science and Engineering*, **119**, pp. 485-493.

[14] Pratt, J. R., Davies, M. A., Evans, C. J., and Kennedy, M. D., 1999, Dynamic interrogation of a basic cutting process, *Annals of the CIRP*, **48**, pp. 39-42.

[15] Gradisek, J., Govekar, E., and Grabec, I., 2001, Chatter onset in non-regenerative cutting - A numerical study *Journal of Sound and Vibration*, **242**(5), pp. 829-838.

[16] Gradisek, J., and Grabec, I., 2002, Stochastic Dynamics of Metal Cutting: Bifurcation Phenomena in Turning, *Mechanical Systems and Signal Processing*, **16**(5), pp. 831-840.

[17] Hanna, N. A., and Tobias, S. A., 1974, A Theory of Nonlinear Regenerative Chatter, *ASME Journal of Engineering for Industry*, **35**, pp. 247-255.

[18] Moon, F. C., Kalmar-Nagy, T., Nonlinear Models for Complex Dynamics in Cutting Materials, *Phil. Trans. R. Soc. A,* **359**, pp. 695-711.

[19] Chandiramani, N.K., Pothala, 2006, Dynamics of 2-Dof Regenerative Chatter During Turning, *Journal of Sound and Vibration*, **290**(1-2), pp. 448-464.

[20] Fofana, M. S., 2002, Effect of Regenerative Process on the Sample Stability of a Multiple Delay Differential Equation, *Chaos, Solitons and Fractals*, **14**, pp. 301-309.

[21] Demir, A., Hasanov, A., and Namachchivaya, N. S., 2006, Delay Equations with fluctuating Delay Related to the Regenerative Chatter, *International Journal of Non-Linear Mechanics*, **41**, pp. 464-474.

[22] Fofana, M. S., and Ryba, P. B., 2004, Parametric Stability of Non-Linear Time Delay Equations, *International Journal of Non-Linear Mechanics*, **39**, pp. 79-91.

[23] Fofana, M. S., 2003, Delay Dynamical Systems and Applications to Nonlinear Machine-Tool Chatter, *Chaos, Solutions and Fractals*, **17**, pp. 731-747.

[24] Altintas, Y., Eynian, M., and Onozuka, H., 2008, Identification of Dynamic Cutting Force Coefficients and Chatter Stability with Process Damping, *CIRP Annals – Manufacturing Technology*, **57**, pp. 371-374.

[25] Sisson, T. R., Kegg, R. L., 1969, An Explanation of Low Speed Chatter Effects, *Journal of Engineering for Industry*, **91**(4), pp. 951-958.

[26] Chiou, A. Y., and Liang, S. Y., 1997, Chatter Stability of a Slender Cutting Tool in Turning with Tool Wear Effect, *International Journal of Machine Tools and Manufacture*, **38**(4), pp. 315-327.

[27] Marui, E., Ema, S., and Kato, S., 1983, Chatter Vibration of Lathe Tools Part 1: General Characteristics of Chatter Vibration, *Journal of Engineering for Industry*, **105**, pp. 100-106.

[28] Marui, E., Ema, S., and Kato, S., 1983, Chatter Vibration of Lathe Tools Part 2: On the Mechanism of Exciting Energy Supply, *Journal of Engineering for Industry*, **105**, pp. 107-113.

[29] Rao, B. C., and Shin, Y. C., 1999, A Comprehensive Dynamic Cutting Force Model for Chatter Prediction in Turning, *International Journal of Machine Tools and Manufacture*, **39**, pp. 1631-1654.

[30] Clancy, B. E, and Shin, Y. C., 2002, A Comprehensive Chatter Prediction Model for Face Turning Operation Including Tool Wear Effect, *International Journal of Machine Tools and Manufacture*, **42**, pp. 1035-1044.

[31] Budak, E., and Ozlu, E., 2007, Analytical Modeling of Chatter Stability in Turning and Boring Operations: A Multi-Dimensional Approach*, Annals of the CIRP*, pp. 401-404.

[32] Ozlu, E., and Budak, E., 2007, Analytical Modeling of Chatter Stability in Turning and Boring Operations-Part 1: Model Development, *Journal of Manufacturing Science and Engineering*, **129**(4), pp. 726-732.

[33] Ozlu, E., and Budak, E., 2007, Comparison of One-Dimensional and Multi-Dimensional Models in Stability Analysis of Turning Operations, *International Journal of Machine Tools and Manufacture*, **47**, pp. 1875-1883.

[34] Cardi, A. A., Bement, M. T., and Liang, S. Y., 2008, "Workpiece Dynamics During Stable Cutting in a Turning Operation," *International Journal of Machine Tool Research*, **3**(4), p. 406-424.

[35] Oxley, P.L.B., 1989, The Mechanics of Machining: An Analytical Approach to Assessing Machinability, New York: E. Horwood; Halsted Press, 242 pp.

[36] Lazogly, I., and Liang, S. Y., Analytical Modeling of Force System in Ball-End Milling, *Machining Science and Technology*, **1:2**, pp. 219-234.

[37] Li, H. Z., Zhang, W. B., and Li, X. P., 2001, Modeling of Cutting Forces in Helical end Milling Using a Predictive Machining Theory, *International Journal of Mechanical Sciences*, **43**, pp. 1711-1730.

[38] Marui, E, Hashimoto, M., Kato, S., 1995, Regenerative Chatter Vibration Occurring in Turning with Different Side Cutting Edge Angles, *ASME Journal of Engineering for Industry,* **117**, pp. 551-558.

[39] Tounsi, N., and Otho, Alain, 2000, Dynamic Cutting Force Measuring, *International Journal of Machine Tools and Manufacture*, **40**, pp. 1157-1170.

[40] Tarng, Y. S., Young, H. T., and Lee, B. Y., 1991. An Analytical Model of Chatter Vibration in Metal Cutting, *International Journal of Machine Tools and Manufacture*, **24**(2), pp. 183-197.

[41] Schimmel, R. J., Endres, W. J., and Stevenson, R., 2000, The Effect of Zero-Clearance Lands in Orthogonal Machining in Light of an Internally Consistent Material Model, *Machining Science and Technology*, **4**(1), pp. 101-125.

[42] Merchant, M. E., 1945, Mechanics of the Metal Cutting Process. Ii. Plasticity Conditions in Orthogonal Cutting, *Journal of Applied Physics*, **16**, pp. 318-324.

[43] Johnson, G. R., and Cook, W. H., 1983, "A Constitutive Model and Data for Metals Subject to Large Strains, High Strain Rates and High Temperatures," *Proceedings of the Seventh International Symposium on Ballistics*, Hague, Netherlands, pp. 541-547.

[44] Wang, Z.G., et al., 2005, A Hybrid Cutting Force Model for High-Speed Milling of Titanium Alloys, *CIRP Annals - Manufacturing Technology*, **54**(1), pp. 71-74.

[45] Waldorf, D. J., DeVor, R. E., and Kapoor, S. G., 1998, A Slip-Line Field for Ploughing During Orthogonal Cutting, *ASME Journal of Manufacturing Science and Engineering*, **120**(4), pp. 693-699.

[46] Waldorf, D. J., 2006, A Simplified Model for Ploughing Forces in Turning, *Journal of Manufacturing Process*, **8**(2), pp. 76-82.

[47] Wu, D. W, 1988, Application of a comprehensive Dynamic Cutting Force Model to Orthogonal Wave Generating Processes, *International Journal of Mechanical Sciences*, **30**(8), pp. 581-600.

[48] Endres, W. J., DeVor, R. E, and Kapoor, S. G., 1995, A Dual-Mechanism Approach to the Prediction of Machining Forces, Part 1: Model Development, *ASME Journal of Engineering for Industry*, **117**, pp. 526-533.

[49] Basuray, P. K., Mistra, B. K., and Lal, G. K., 1977, Transition from Ploughing to Cutting During Machining with Blunt Tools, *Wear*, **43**, pp. 341-349.

[50] Shaw, M. C., and DeSalvo, G. J., A New Approach to Plasticity and its Application to Blunt Two Dimensional Indenters, *ASME Journal of Engineering for Industry*, **92**, pp. 472-479.

[51] Endres W., 1992, A Dual Mechanism Approach for the Prediction of Machining Forces for Metal Cutting Processes, Ph.D. Dissertation, University of Illinois.

[52] Arsecularatne, J. A., Fowle, R. F., and Mathew, P., 1996, Nose Radius Oblique Tool: Cutting Force and Built up Edge Prediction, *International Journal of Machine Tools and Manufacture*, **36**(5), pp. 585-595.

[53] Stabler, G. V., 1951, The Fundamental Geometry of Cutting Tools, *Proceedings of the Institution of Mechanical Engineers*, **165**, pp. 14-21.

[54] Armarego, E. J. A, and Wiriyacosol, S., 1969, The Machining of Metals, Prentice Hall, Englewood Cliffs, NJ.

[55] Cardi, A. A., Bement, M. T., and Liang, S. Y., 2007, "Effect of Tool Nose Radius on the Chatter Instability of Oblique Machining," *Proceeding of the International Conference on Advanced Manufacturing Technology (ICAM-2007)*, Tainan, Taiwan.

[56] Brown, R. H., and Armarego, E. J. A., 1964, Oblique Machining with a Single Cutting Edge, *International Journal of Machine Tool Design and Research*, **4**, pp. 9-25.

[57] Moufki, A., Devillez, A., Segreti, M., and Dudzinski, D., 2006, A Semi-analytical Model of Non-linear Vibrations in Orthogonal Cutting and Experimental Validation, *International Journal of Machine Tools and Manufacture*, **46**, pp. 436-449.

[58] Weisstein, E. W., 2003, "Pappus's Centroid Theorem", CRC Concise Encyclopedia of Mathematics, New York, CRC Press, p. 2131.

[59] Shampine, L.F. and S. Thompson, 2001, Solving DDEs in MATLAB, *Applied Numerical Mathematics*, **37**, pp. 441-458.

[60] Boothroyd, G., 1970, Effect of Surface Slope on Shear Angle in Metal Cutting, *ASME Journal of Engineering for Industry*, **92**(1), pp. 115-118.

[61] Nigm, M. M., and Sadek, M. M., 1977, Experimental Investigation of the Characteristics of Dynamic Cutting Process, *ASME Journal of Engineering for Industry*, pp. 410-418.

[62] Wallace, P. W. and Andrew, C., 1965, Machining Forces: Some Effects of Tool Vibration, *Journal of Mechanical Engineering Science*, **7**(2), pp. 152-162.

[63] Rubenstein, C., 1971, An Analysis of Dynamic Cutting when a Plane Surface is Cut with an Oscillating Tool-I: General Equations, *International Journal of Machine Design and Research*, **12**, pp. 179-191.

[64] Wu, D. W., 1986, Governing Equations of the Shear Angle Oscillation in Dynamic Orthogonal Cutting, *ASME Journal of Engineering for Industry*, **108**(4), pp. 280-287.

[65] Tarng, Y. S., Young H. T., and Lee, B. Y., An Analytical Model of Chatter Vibration in Metal Cutting, *International Journal of Machine Tools and Manufacture*, **34**(2), pp. 183-197.

[66] Wu. D. W., 1988, Application of a Comprehensive Dynamic Cutting Force Model for Orthogonal Wave-Generating Processes, *International Journal of Mechanical Sciences*, **30**(8), pp. 581-600.

[67] Wu D. W., 1987, Development of a Dynamic Shear Angle Model for Wave-Generating Processes Based on Work-Hardening Slip-Line Field Theory, *International Journal of Mechanical Sciences*, **29**(6), pp. 407-424.

[68] Oppenheim, A. V., and Schafer, R. W, 1999, Discrete-Time Signal Processing, Upper Saddle River, New Jersey: Prentice Hall.

[69] Boashash, B., 1992, Estimating and Interpreting the Instantaneous Frequency of a Signal – Part I: Fundamentals, *Proceedings of the IEEE*, **80**(4), pp. 520-538.

[70] Liu, C. R., and Barash, M. M., 1978, Variables Governing Patterns of Mechanical Residual Stress in a Machined Surface, *Journal of Engineering for Industry*, **104**, pp. 257-264.

[71] Li, H., and Shin, Y-C., 2006, A Comprehensive Dynamic End Milling Simulation Model, *Journal of Manufacturing Science and Engineering*, **128**, pp. 86-95.

[72] Waldorf, D. J., DeVor, R. E., and Kapoor, S. G., 1999, An Evaluation of Ploughing Models for Orthogonal Machining, *Journal of Manufacturing Science and Engineering*, **121**, pp. 550-558.

[73] Shi, H. M., and Tobias, S. A., 1983, Theory of Finite Amplitude Machine Tool Instability, *International Journal of Machine Tool Design and Research*, **24**(1), pp. 45-69.

[74] Landers, R. G., and Ulsoy, A. G., 2008, Nonlinear Effect in Machining Chatter Analysis, *Journal of Manufacturing Science and Engineering*, **130**(1).

[75] Endres, W. J., and Kountanya, R. K., 2002, The Effect of Corner Radius and Edge Radius on Tool Flank Wear, *Journal of Manufacturing Processes*, **4**(2), pp. 89-96.

VITA

Adam Cardi was born August 30, 1983, in Boston, Massachusetts, son of Dr. Michael and Linda Cardi. He grew up in Cincinnati, Ohio, and graduated from Wyoming High School in 2002. After that, he attended Purdue University and graduated in 2005. During his senior year he worked under Dr. Douglas Adams and developed load identification algorithms for body armor. In the Fall of 2005, he began work on his Ph.D. at Georgia Tech while working under the co-advisement of Professor Steven Liang and Dr. Matthew Bement of Los Alamos National Laboratory. At Georgia Tech, he primarily focused on developing dynamic cutting force models for metal turning operations. After graduation in May, 2009, he plans to begin work at Exponent, an engineering and scientific consulting firm.